Shock Wave Propagation in Periodically Layered Composites

Thesis by
Shiming Zhuang

In Partial Fulfillment of the Requirements
for the Degree of
Doctor of Philosophy

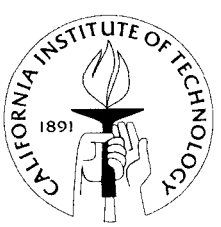

California Institute of Technology
Pasadena, California

2002
(Defended June 14, 2001)

Dedicated to my family

Acknowledgments

First and foremost I wish to thank my advisor, Professor G. Ravichandran for everything he has done for me. This thesis would not have been written without his guidance, support and encouragement. His devotion and spirit in performing scientific research has inspired my own dedication. I have benefited tremendously from his knowledge and insight in science. I am greatly indebted to him for his giving me freedom to do research, his advice and help whenever needed, his enthusiasm when there was a big progress, his understanding when progress was little. I would also like to sincerely express my thanks to Professor and Mrs. Ravichandran for their friendship and hospitality, which made my life here at Caltech especially enjoyable and memorable.

I wish to also thank Dr. Dennis E. Grady, Professors Wolfgang G. Knauss, Ares J. Rosakis and Joseph E. Shepherd for taking their time to be my Ph.D. committee and offering their valuable comments. Dr. Grady was actively involved in my graduate research work from the beginning of the project and gave me many valuable suggestions and advice.

I am grateful to Professor Thomas J. Ahrens for his generosity for letting me share instruments in his lab and inviting me to join his fruitful Shock Wave Reading Group from which I greatly benefited. My special thanks go to Professor Sun Chengwei for introducing me to the field of shock waves and giving me invaluable advice. I would like to thank Dr. David M. Owen and Dr. Jon Hodowany for all help they provided to me. They helped me in getting familiar with all the facilities in the lab. David is also the first person at Caltech I collaborated with on a project under Dr. Rosakis and Dr. Ravichandran. I wish to especially thank Dr. Changli Liu and Ms. Ling Cui for their friendship and hospitality. They helped my family and I adapt quickly in this new society.

I am deeply indebted to Eric N. Burcsu, who is one of most creative people I have ever known. Besides contributing to my knowledge of computers, to me, he is somewhat like a

dictionary. Whenever I had trouble to understand an idiom, slang in English, cultural and social issues, he is the 'book' I checked. I also want to thank my fellow student, Ioannis Chasiotis, for sharing with me his understanding of graduate study, scientific research, life, and many other things through many long, late night discussions. Both Eric and Ioannis spent their valuable time reading my manuscripts and providing constructive criticism. It was a pleasure to work with so many creative people as Mr. Jun Lu, Mr. Nitin Deshpande, Dr. Kenji Oguni, Dr. Sangwook Lee, Dr. Sunil Yadav, Dr. Daniel Rittel, Dr. Murat Vural, Dr. Yann Tamim Carin, Dr. Ben Chow and Ms. Rongjing Zhang. I truly thank them for the help they provided and value the friendship I developed with them through the years, which will be in my deep memory for all my life.

Through the years of my stay at Caltech, I had the privilege of working, learning and playing with my fellow students in the other research groups of Solid Mechanics. I thank Mr. Petros Arakelian, our lab technician, Mr. Joseph A. Haggerty in Aeronautics Shop, Mr. Michael A. Gerfen in Central Engineering Service, Mr. Michael A. Long in Professor Thomas Ahrens' Lab for the help they provided. I would also like to thank Professor Ravichandran's secretary Ms. Denise Thobe for her patience and help on countless administrative requests.

Words cannot express my thanks to the members of my family to whom this thesis is dedicated. The support and encouragement from my parents has always been the driving force for me to keep moving forward. My brothers and sisters cheered with me through the good times and encouraged me through the bad times. My wife, Jianhua, endured my mood swings, failures and rejoiced in my successes. Without many years of her understanding, support and sacrifice I do not think I could get to this point of my life. Since being born, our lovely daughter Claire has always been the source of joy and happiness for the family.

The research presented in this dissertation was made possible by the Solid Mechanics program (Dr. M. A. Zikry, Program Manager) of the Army Research Office through a grant (DAAG55-98-1-0237) to the California Institute of Technology and is gratefully acknowledged.

Abstract

Mathematically, a shock wave is treated as a discontinuity in a medium. In reality, however, a shock wave is always structured, i.e., its front takes a finite time to rise from an initial material state to the final shocked state. The structuring of a shock front is due to the competition between the nonlinearity of material behavior and the dissipation processes occurring during the wave propagation. There are many mechanisms which may be responsible for the dissipation and/or dispersion of shock wave energy. In homogeneous media, such as metals, one common interpretation for the structuring of a shock wave is that the viscoplasticity processes (dislocation, twinning, etc.) are responsible for the dissipation of energy. While in heterogeneous composites, besides the viscous dissipative processes existing in each of its constituents, due to the existence of internal interfaces, the scattering induced by the interface during shock compression could be another important mechanism.

In this study, the interface scattering effects on shock wave propagation in heterogeneous media were investigated by subjecting periodically layered composites to planar impact loading with a flyer plate. The flyer plate was accelerated to a desired velocity using a powder gun loading system. In order to measure shock particle velocity time history at an internal or the free surface of the specimen, the so-called VISAR (Velocity Interferometry System for Any Reflector) diagnostic system was constructed and used during shock compression experiments. Manganin stress gages were embedded inside the specimen at selected internal interfaces to measure shock stress time history. To study the scattering mechanisms of the interface to waves, two-component composite specimens with different interface mechanical properties and heterogeneity were prepared and tested. Different types of composites were prepared with differing mechanical impedance. Specimens with different heterogeneity were obtained by

changing the geometrical configuration (length scale) of the layered stack. Two-dimensional numerical simulations were also carried out to understand the process of shock wave evolution in the layered composites.

Experimental and numerical studies show that periodically layered composites support steady structured shock waves. The influence of internal interfaces on the shock wave propagation is through the scattering mechanism, i.e., multiple reflection of waves in the layers and their interaction with the shock wave. The interface scattering affects both the bulk and the deviatoric response of the composite to shock compression. The influence of scattering on the bulk behavior is to slow down the velocity of the shock wave in the composites, while its influence on the deviatoric response is to structure the shock wave profile. If all the dissipative and dispersive effects are collectively termed as viscosity, which causes the shock front structuring, i.e., the shock front rise-time increasing, then the effective shock viscosity increases with the increase of interface impedance mismatch and decreases with the increase of interface density (interface area per unit volume) and shock loading strength. The existing mixture model for constructing the constitutive relation for composites based on the known properties of its component materials can only, at best, reasonably predict the response of the composites under strong shock loading conditions. In order to fully describe the response of a heterogeneous composite to shock compression loading, accurate physics-based constitutive relations need to be formulated to take into account the scattering effects induced by the heterogeneous microstructure.

Contents

List of Figures

List of Tables

Chapter 1

Introduction

1.1 Motivation

Shock wave propagation and its effects on solids have been extensively investigated in the past few decades[1-8]. Progress in experimental measurement techniques and theoretical work makes it possible to develop insights regarding details of the compression process during shock wave propagation in solids. Mathematically, the front of a shock wave can be, and has been, treated as a discontinuity with zero rise time, but the real shock front always has a finite rise time (for metals, ranging from the order of several to hundreds of nanoseconds) corresponding to the compression of the material from its initial state to the final shocked state, and the slope of the shock front varies with shock amplitude. One common interpretation for the observed finite rise-time in the steady structured shock waves propagating in homogeneous metals is that the underlying physics of time-dependent plasticity processes (dislocations, twinning, etc.) are responsible for dissipation and dispersion of the waves. Based on the formalisms of viscoplasticity, many descriptive constitutive models have been developed and have been reasonably successful in interpreting the experimental data[9-12].

Wave propagation in heterogeneous materials has received considerable attention and earlier efforts have resulted in a sound understanding of many of the fundamental issues. Nevertheless, most of the consequences of wave dispersion in composite materials were brought to light through investigations of the linear elastic analysis of ideal periodic composites[13-15]. Relatively little is known regarding finite amplitude shock wave propagation in heterogeneous media. Much

of the attention of the earlier work has been paid to the geometric dispersion of elastic waves, but almost no insight exists on the role of interface scattering effects on the dispersion and dissipation of shock (finite amplitude) waves in heterogeneous solids.

With high-performance heterogeneous materials such as fiber reinforced, woven composites and functionally graded materials finding increasing use in systems and structures designed to function in the severe shock environments, the assessment and evaluation of the response of those systems to complex loading conditions is essential. To do so, the advanced computational method relying on accurate physics-based material constitutive models is required, although such kinds of models can not be correctly formulated without fully understanding the physical mechanisms of dissipation and dispersion of shock waves propagating in heterogeneous solids. Small-scale heterogeneity, e.g., grain boundaries in polycrystalline metals, fiber or particle reinforcement in polymer and metallic composites, could lead to scattering of waves which may be reflected in the rise time of a shock wave. The relative importance of scattering increases with the severity of the heterogeneity. Therefore, in order to obtain an accurate physically based constitutive relation to properly describe the dynamic response of heterogeneous materials and assess the performance of the composite material structures and systems in the shock related environments, it is critical to evaluate the role played by scattering induced by the heterogeneous microstructure as a shock wave propagates in the composite materials.

This provides the motivation to experimentally investigate the dispersion and attenuation of shock wave propagation in layered heterogeneous composites, and the influence of length scales associated with the heterogeneity (e.g., fiber diameter) and material properties on the wave propagation. Scattering as a mechanism for structured shock waves in metals, as well as in heterogeneous composite materials, has been recently proposed by Grady[16,17]. Based on the quasi-harmonic representation of scattered acoustic energy in solids, he proposed a continuum constitutive model to describe finite-amplitude nonlinear wave propagation in heterogeneous

solids. The results of this investigation is expected to establish a basis for formulating a physically based constitutive model which accounts for the scattering effects of internal interfaces to the wave propagation. Such a model can then be implemented in computational code for simulating and assessing the performance of heterogeneous systems and structures under impact shock environment.

1.2 Review

1.2.1 Shock Compression of Homogeneous Solids

Shock loading to a solid body is usually generated through high velocity planar impact or high energy explosive detonation[1-3,7]. The process of a shock wave compressing a solid from its initial state to the high pressure final state is completed in the time scale of shock front rise period which may range from several to hundreds of nanoseconds, though the shock pulse may be as long as up to tens of microseconds. The shock front rise time depends on the loading condition and the properties of material that is compressed. Roughly, the impulsive shock loading may be divided into three regimes: strong shock or high pressure, weak shock or intermediate pressure and elastic or low pressure; the corresponding behavior of solids are respectively hydrodynamic, finite-strain plastic and linear elastic[2,7,18].

In the strong shock loading regime, stress or pressure is many times larger than the yield stress of the material. Material strength effects may be neglected and solids may be treated as an inviscid compressible fluid, which is the so called hydrodynamic approximation for the response of solids to strong shock wave loading. The main feature of the shock compression phenomena in this regime is characterized by a single shock front that brings the material from its initial state to a new high pressure, high temperature state. The shock compressed state will sustain a time

period of shock pulse duration which is determined by the loading boundary condition and material properties, and follows by an isentropic unloading process which brings the material back to an ambient pressure, elevated temperature and zero kinetic energy state[2]. The constitutive description of material response in this regime is through the equation of state (EOS) which relates three state variables. Many theoretical and experimental studies on the EOS of solids have been carried out since the pioneering experimental measurement of shock wave velocity of steel and lead loaded by high explosives[19]. The theories on shock compression of solids have been studied extensively and the progress in various aspects have been reviewed[20-26]. Courant and Friedrichs' "Supersonic flow and shock waves" is a standard reference book for shock waves[27]. A thorough collection of Hugoniot data by Marsh[28], along with Steinberg's subset of EOS and material properties[29], serves as a valuable sources of experimental data on shock compression of solids.

In the elastic regime, upon being loaded, material deforms in a completely reversible manner. The response of the material is described by a linearly elastic constitutive model, i.e., Hooke's law. Because of the linearity of both the governing equations and the constitutive relations, most dynamic problems in the elastic regime can be analytically solved, or can at least be much simplified. Comparatively, the theories on elastic wave propagation in solids are most fully developed[30-32].

The most complex phenomena happen at loading stresses ranging from the Hugoniot elastic limit to the stress value at which the elastic precursor wave is overtaken by the plastic wave. In this regime, material strength plays a dominant role during dynamic deformation. Elastic-plastic structured double wave front is one of the typical features observed in this stress regime. Phase transformation, strain hardening, and rate-dependent viscoplasticity add to the complication of wave propagation phenomena in solids, and the difficulty in modeling them. Since the deformation is large and strength effects dominate the process, one common way to describe response of solids to shock is that the bulk response and deviatoric response are considered

separately. The bulk response is modeled by EOS, while deviatoric response is described by a constitutive relation for the shear strength of material[33,34]. Much effort and progress have been made in diagnostic techniques, experimental observations and theoretical analyses since the first experimental measurement of shock wave velocity by Pack et al.[19], the first measurement of elastic-plastic wave profile by Minshill[35], and the early continuum theoretical analysis by Wood[36]. Early pioneering work on the elastic-plastic wave propagation in the wire or thin rod was carried out by Rakhmatulin[67], Taylor[68], von Karman and Duwez[69], and others. Clifton[70] performed detailed analysis of plane wave propagation in plastic and elastic-plastic solids. The review papers by Herrmann[33], Murri et al.[37], Doran and Linde[38], Cristescu[39], Davison and Graham[1] summarized the progress in the field of plane shock compression of solids dated up to the end of 1970s. The most up-date and thorough review on the progress in this field was given by Graham[2]. In this book, besides the mechanics aspect of shock compression solids, the electrical, magnetic and optical properties of solids under high pressure shock compression, shock induced solid-state chemistry, shock modification, shock activation and shock chemical synthesis, as well as experimental methods, were also discussed.

Historically, the shock wave study may be traced back at least 200 years to the work of Poisson who tried to solve the propagation of a finite-amplitude wave in fluid[40]. Stokes probably was the first person studying the motion of fluid with the concept of propagating discontinuity[41]. In the early 20th century the concept of shock wave propagating in fluid as a discontinuity and fluid dynamics theory had already been fully developed through the pioneering work of Riemann, Rankine, Hugoniot, Rayleigh, Taylor, and others[40].

Nevertheless, the study of shock wave propagation in solids did not start until at the middle of the 20th century when the needs for defense applications served as a driving force[33]. Since then, tremendous progress has continuously been made in theory, experimental measurements and techniques for shock-compression solids, and on the scientific and engineering applications. The papers marked as milestones in the study of shock compression science were outlined in a recent

review paper by Johnson and Cheret[40]. The recently published series of collections and books[2-8] summarized all aspects of the field of shock compression solids, including the fundamental concepts, theories, experimental methods, diagnostic techniques, observations, scientific and engineering applications and much more.

1.2.2 Shock Propagation in Heterogeneous Media

So far, only a limited number of experiments have been carried out that concern the finite-amplitude wave propagation in composite materials for the loading stress in the intermediate regime. Barker et al.[42] performed experiments on periodic laminates and found that below certain critical input amplitude, the stress wave amplitude decayed exponentially with distance and formed a structured shock wave above that critical amplitude. Lundergan and Drumhellar[43] and Oved et al.[44] also conducted limited shock wave experiments on layered stacks, which showed resonance phenomena due to layering. There has been a lack of systematic study of stress wave propagation in either layered systems or fiber reinforced composites, which would be valuable in development or validation of physically based models for transient (pulse) loading.

In developing theoretical models for finite-amplitude shock wave propagation in composites, several approaches for calculating the high-pressure Hugoniot of composites have been proposed[24,45-48]. One approach is to consider the composite or mixture as a laminated structure and calculate an average shock velocity based on the shock transit time through the various layers. This method is straightforward, but the calculated velocity represents the fastest possible disturbance wave speed neglecting the delay effects due to the interactions between the interfaces and shock wave. The other approach is to interpolate the experimental shock velocity-particle velocity Hugoniot relations by mass averaging based on the assumption that the particle velocity of each component is the same[8]. These two methods most likely overpredict the response of composite to shock compression. The additive approximation approach developed by Dremin

and Karpukhin[48] can more reasonably predict the experimentally measured Hugoniot relation. The basis of this approach is that the rule of additivity is assumed to be met sufficiently. The local pressure in each component is assumed to be the same as the mean pressure of the composite, and the volume of the shock-compressed mixture is equal to the sum of the volumes of its components under the same pressure in the homogeneous monolithic samples[49]. McQueen et al.[24] also used the additive approximation to formulate the EOS of composites, but in a different approach, in which 0 K isotherms of components are calculated first by Mie-Gruneisen equation from their shock Hugoniots to obtain the 0 K isotherm of the mixture on the additive basis of mass fraction, then the shock Hugoniot of the mixture is calculated from the 0 K mixture isotherm using the Mie-Gruneisen EOS. All these models deal with the bulk response of a composite compressed by shock wave.

Theoretical models for predicting the structure of the profile of shock wave propagating in composites is not yet available. A few simplified models have been proposed[50-53]. Barker[50] proposed a viscous type EOS to describe the stress wave propagation in layered composites, in which the dispersive effects due to the interactions of wave with interfaces and reflected waves are accounted for by direct analogy with the viscosity effect existing in the viscoelastic materials. Chen and Gurtin's model[51] deals with the condition for an acceleration wave propagating in layered composites to grow into a shock or decay, and to calculate the effective moduli for the composites. Kanel et al.[52] proposed an empirical constitutive relation for describing the dispersive effects in composites. These models account for dispersion through a time-dependent relaxation process assuming the existence of a steady shock wave. In the model proposed by Johnson et al.[53] the dissipation and dispersion due to both the viscoplasticity and interface reflection are considered. Recently, based on nonequilibrium phonon energy induced by scattering of waves within heterogeneous microstructure, Grady et al.[54] proposed a continuum anelastic response model for finite amplitude wave propagation in the heterogeneous media. In this model the energy state of the matter behind the shock wave is decomposed into two parts:

one is the lattice strain energy and the other is the kinetic energy corresponding to a field of acoustic phonon energy caused by wave scattering within the heterogeneous microstructure. The acoustic phonon energy is modeled through a normal mode of representation of the heterogeneous solid which addresses the wave dispersion process.

1.3 Structured Shock Profile

Due to the nature of material properties and the existence of dissipative mechanisms during wave propagation, the profile of a shock, if it forms, is always structured. Rayleigh[55] discussed the nature of the shock profile and gave an analysis for the shock (permanent regime) solution. Lighthill[56] proposed a theory for the structure of shock in a compressible fluid, which treats the balance achieved between the effect of convection, which tends to steepen a compressive wave, and the effect of viscosity, which tends to smear out the steepness of wave front. Band[57] was probably the first one to discuss in detail the existence and structuring of a steady shock profile in viscoelastic shear yielding solids. The concept of steady shocks in solids were further treated by the later work of Band and Duvall[58], Bland[59], and Swan, Duvall and Thornhill[60], and others.

1.3.1 Shock Viscosity

The structuring of shock wave profile is due to various dissipative phenomena which may be generally termed as viscosity of the medium. The action of viscosity is to produce a drag pressure exerting in opposition to the driving pressure of the wave, so that the momentum transportation in the wave propagation direction is slowed down. As a result, the particle velocity gradient is reduced and the shock front width increases. Experimental results show that in general the viscosity increases with shock pressure, or particle velocity gradient, and decreases

with temperature[61-63]. Therefore, with the increase in shock pressure, the drag pressure also increases. The balance between the drag pressure from the viscosity and the shock driving pressure from the boundary, results in the formation of a steady shock wave with a definite rise time.

The shock front width or rise time can be related to the shock viscosity[58,59,62]. By measuring the rise time of a shock profile the effective shock viscosity can be calculated, or at least, comparatively estimated. Through a set of experimental data that are systematically measured, the corresponding constitutive model can be formulated and used to predict the profile of a large-amplitude shock-wave propagation[9,64].

There are many irreversible processes responsible for the formation of a steady shock profile. In solids, there exist various sources of viscosity, such as viscoelasticity, thermal diffusion, phonon scattering, and viscoplastic effects[57,64,65]. Gilman[65] investigated different dissipation in metals due to dislocation motion, electron-electron, electron-phonon, and phonon-phonon interactions and concluded that among all dissipation systems, dislocation motion is the most dissipative. This is because the motion of dislocations through solid medium changes its density and simultaneously relaxes the shear strain that would otherwise exist behind the front. Due to the dislocations that move with shock front, the viscosity associated with them is proportional to the shock velocity. The experimental measurements, theoretical interpretation of shock viscosity, and its applications in earth science have been thoroughly reviewed by Miller and Ahrens[66]. In heterogeneous solids (ceramics, composites, etc.), besides the dissipative mechanisms discussed above, due to the existence of a large amount of internal interfaces, the microstructure scattering of shock wave induced by them could be another dominant dissipative source, or dispersion, which will contribute to the structuring of shock wave propagation in heterogeneous media.

1.3.2 Scattering as a Mechanism of Dissipation

Scattering as a dissipative mechanism exists in many dynamic equilibrium and nonequilibrium processes such as scattering effects of atom-electron, atom-photon, atom-phonon, particle-waves, flaw-waves, etc., which lead the initial state to eventually transition to a steady state. When a finite amplitude shock wave propagates through a heterogeneous solid, due to the mismatch in mechanical properties between matrix and inclusions or flaws, the wave will be partially reflected and partially transmitted. The directions of reflected and transmitted waves, which are determined by the geometric orientation of interface and wave reflection and transmission laws, are randomly oriented, and hence the process is known as scattering.

Upon the arrival of the wave front, no matter whether scattering occurs or not, strong or weak, the material experiences a compression process, and would achieve some level of lattice strain energy. Therefore, as a shock wave passes through a heterogeneous solid, the energy state of the matter behind the shock wave will include a component due to the lattice strain energy and a kinetic component corresponding to a field of acoustic phonon energy caused by wave scattering within the heterogeneous microstructure. Such phonon energy can be characterized through a harmonic normal mode representation of a solid[16,17].

The inducement of a kinetic component of acoustic phonon energy during the dynamics of the shock compression process results in unique consequences. During passage of a structured shock, dispersion due to wave scattering leads to the production of phonon energy within a limited spectrum of normal mode coordinates in the shock front. This non-equilibrium acoustic phonon energy accounts for the excess stress on the Rayleigh line above the Hugoniot during passage of the shock wave (see Fig. 2.4). Diffusion of this energy to an equilibrium configuration throughout the acoustic normal modes is achieved as the final shock state is approached. Ultimately, continued diffusion throughout the full thermal spectrum occurs until complete thermoelastic equilibrium is achieved. These processes account for entropy production within the

shock process in the heterogeneous solid. Details of the steady shock wave profile structure are determined by characteristic relaxation times associated with specifics in the acoustic energy diffusion processes.

1.4 Objectives and Approach

The objective of this work is to study the influence of scattering effects induced by internal interfaces on shock wave propagation in heterogeneous media. To do so, experiments are designed and conducted in order to evaluate the role of interface heterogeneity, i.e., impedance mismatch, multiple length scales, and the interface characteristics on stress wave dispersion and attenuation; numerical simulations are performed to understand the process of interface induced scattering and to study the response of heterogeneous solids to the shock compression. The ultimate goal is to develop physically based models accounting for the microstructure scattering effects on the wave propagation that can be implemented in computational codes for simulating and assessing the performance of heterogeneous systems and structures exposed to an impact related shock environment.

An ideal model system to investigate the effect of heterogeneous materials on wave propagation is to consider stress wave propagation through layered media made of isotropic materials. Such a system offers a unique opportunity for designing of interpretable experiments, as well as for providing insights into wave propagation in much more complicated microstructures, e.g., fiber reinforced, particulate and woven composites. In such a system the length scales, e.g., thickness of individual layers, and other measures of heterogeneity, e.g., impedance mismatch, are well defined. Such a heterogeneous material is amenable to the analysis of wave propagation and provides an ideal system for conducting experiments for which one-dimensional measurements would be sufficient.

The specimens used in the shock compression experiments are periodically layered two-component composites. In order to study the influence of length scales and interface impedance mismatch on shock propagation, four different materials, polycarbonate, 6061-T6 aluminum alloy, 304 stainless steel and glass, are chosen as components, and two thicknesses of each component layer are used except aluminum for which only one thickness layer is available. The component layers are alternately bonded to form the specimen. Shock compression experiments were conducted by employing a powder gun loading system, which can accelerate a flat plate flyer to a velocity in range of 400 m/s to about 2000 m/s. In order to measure the particle velocity history on the specimen window surface, a velocity interferometry system for any reflector, the so called VISAR, is constructed, and to measure the shock stress history at selected internal interfaces, manganin stress technique is adopted. The details of shock wave experimental method and each experimental technique are described in Chapter 3. Relevant basic theories for describing shock wave propagation in solids is given in Chapter 2. The details of specimen structure, preparation, experiment and the results are described in Chapter 4. In Chapter 5 the numerical simulation methods are introduced and the results from the computation are compared with experiments. Finally, directions for future work are suggested in Chapter 6.

1.5 References

1. Davson, L. and Graham, R.A. Shock compression of solids, *Phys. Rep.***55**, 255 (1979).
2. Graham, R.A. *Solids under High-Pressure Shock Compression: Mechanics, Physics, and Chemistry*, Springer-Verlag, New York (1993).
3. Asay, J.R. and Shahinpoor, M. *High-Pressure Shock Compression of Solids*, Springer-Verlag, New York (1993).
4. Davison, L., Grady, D.E., and Shahinpoor. M. *High-Pressure Shock Compression of Solids II: Dynamic Fracture and Fragmentation*, Springer, New York (1996).
5. Davison, L. and Shahinpoor, M. *High-Pressure Shock Compression of Solids III*, Springer, New York (1998).
6. Davison, L., Horie, Y., and Shahinpoor. M. *High-Pressure Shock Compression of Solids IV: Response of Highly Porous Solids to Shock Loading*, Springer, New York (1997).
7. Chou, P.C. and Hopkins, A.K. *Dynamic Response of Materials to Intense Impulse Loading*, Air Force Materials Laboratory, Wright Patterson AFB, Ohio (1972).
8. Meyers, M.A. *Dynamic Behavior of Materials*, John Willey & Sons, Inc., New York (1994).
9. Swegle, J.W. and Grady, D.E. Shock viscosity and the prediction of shock wave rise times, *J. Appl. Phys.* **58**, 692 (1985).
10. Rubin, M.B. Analysis of weak shocks in 6061-T6 aluminum, in *Shock Waves in Condensed Matter-1989*, edited by Schmidt, S.C., Johnson, J.N., and Davison, L.W., American Institute of Physics, New York, p321 (1990).
11. Partom, Y. Understanding the Swegle-Grady fourth power relation, in *Shock Waves in Condensed Matter-1989*, edited by Schmidt, S.C., Johnson, J.N., and Davison, L.W., American Institute of Physics, New York, p317 (1990).
12. Johnson, J.N. Calculation of path-dependent wave shock hardening, *J. Appl. Phys.* **72**, 797 (1992).

13. Sun, C.T., Achenbach, J. D., and Hermann, G. Continuum theory for a laminated medium, *J. Appl. Mech.* **35**, 467 (1968).

14. Ben-Amoz, M. On wave propagation in laminated composites-II. Propagation Normal to the Laminates, *Int. J. Engng Sci.* **13**, 57 (1975).

15. Nayfeh, A.H. *Wave Propagation in Layered Anisotropic Media: with Applications to Composites*, Elsevier Science, Amsterdam (1995).

16. Grady, D.E. Physics and modeling of shock-wave dispersion in heterogeneous composite, *J. Phys IV FRANCE* **7**, C3-669 (1997).

17. Grady, D.E. Scattering as a mechanism for structured shock waves in metals, *J. Mech. Phys. Solids* **46**, 2017 (1998).

18. Duvall, G.E. and Fowles, G.R. Shock Waves, in *High Pressure Physics and Chemistry*, edited by Bradley, R.S., Academic Press, London and Now York, Vol. **2**, p209 (1963).

19. Pack, D.C., Evans, W.M., and James, H.J. The propagation of shock wave in steel and lead, *Proc. Phys. Soc.* **60**, 1 (1948).

20. Rice, M.H., Mcqueen, R.G., and Walsh, J.M. Compression of solids by strong shock waves, in *Solid State Physics*, edited by Seitz, F. and Turnbull, D., Academic Press Inc., Publishers, New York and London, Vol. **6**, p1 (1958).

21. Al'tshuler, L.V. Use of shock waves in high-pressure physics, *Soviet Physics USPEKHI* **8**, 52 (1965).

22. Zel'Dovich, Ya.B. and Raizer, Yu.P. *Physics of shock waves and high-temperature hydrodynamic phenomena*, Academic Press, New York (1967).

23. Zhakov, V.N. and Kalinin, V.A. *Equations of state for solids at high pressures and temperatures*, Consultants Bureau, New York (1971).

24. McQueen, R.G., Marsh, S.P., Taylor, J.W., Fritz, J.N., and Carter, W.J. The equation of state of solids from shock wave studies, in *High Velocity Impact Phenomena*, edited by Kinslow, R., Academic Press, New York, p293 (1970).

25. Royce, E.B. High-pressure equations of state from shock-wave data, in *Proceedings of the International School of Physics <<Enrico Fermi>> Course XLVIII: Physics of High Energy Density*, edited by Caldirola, P. and Knoepfel, H., Academic Press, New York, p80 (1971).

26. Duvall, G.E. Shock waves and equations of state, in *Dynamic Response of Materials to Intense Impulsive Loading*, edited by Chou, P.C. and Hopkins, A.K., Air Force Materials Laboratory, Wright Patterson AFB, Ohio, p89 (1972).

27. Courant, R. and Friedrichs, K.O. *Supersonic flow and shock waves*, Interscience Publishers, Inc., New York (1948).

28. Marsh, S.P. *LASL Shock Hugoniot Data*, University of California Press, Berkeley and Los Angeles (1980).

29. Steinberg, D.J. *Equation of state and strength properties of selected materials*, Lawrence Livermore National Laboratory, UCRL-MA-106439 (1996).

30. Kolsky, H. *Stress Waves in Solids*, Clarendon Press, Oxford (1953).

31. Achenbach, J.D. *Wave propagation in elastic solids*, North-Holland Pub. Co., Amsterdam (1973).

32. Graff, K.F. *Wave motion in elastic solids*, Ohio State University Press, Columbus (1975).

33. Herrmann, W. Nonlinear stress waves in metals, in *Wave Propagation in Solids*, edited by Miklowitz, J., ASME, p129 (1969).

34. Wilkins, M.L. Calculation of Elastic-Plastic Flow, in *Methods in Computational Physics*, edited by Alder, B., Vol. **3**, 211 (1964).

35. Minshall, S. *J. Appl. Phys.* **26**, 463 (1955).

36. Wood, D.S. *J.Appl. Mech.* **19**, 521 (1952).

37. Murri, W.J., Curran, D.R., Peterson, C.F., and Crewdson, R.C. Response of solids to shock waves, in *Advances in High-Pressure Research*, edited by Wentorf, R.H., Jr., Academic Press, London and New York, Vol. **4**, 2 (1974).

38. Doran, D.G. and Linde, R.K. Shock effects in solids, in *Solid State Physics*, edited by Seitz, F. and Turnbull, D., Academic Press Inc., Publishers, New York and London, Vol. **6**, 230 (1966).

39. Cristescu, N. *Dynamic plasticity*, North-Holland Publishing Company, Amsterdam (1967).

40. Johnson, J.N. and Cheret, R. *Classic Papers in Shock Compression Science*, Springer-Verlag, New York, p3 (1998).

41. Johnson, J.N. and Cheret, R. *Classic Papers in Shock Compression Science*, Springer-Verlag, New York, p71 (1998).

42. Barker, L.M., Lundergan, C.D., Chen, P.J., and Gurtin, M.E. Nonlinear viscoelasticity and the evolution of stress waves in laminated composites: a comparison of theory and experiment, *J. Appl. Mech.* **41**, 1025 (1974).

43. Lundergan, C.D. and Drumheller, D.S. Dispersion of shock waves in composite materials, in *Shock Waves and the Mechanical Properties of Solids*, edited by Burke, J. and Weiss, V., Syracuse University Press, New York, p141 (1971).

44. Oved, Y., Luttwak, G.E., and Rosenberg, Z. Shock wave propagation in layered composites, *J. Comp. Mat.* **12**, 84 (1978).

45. Tsou, F.K. and Chou, P.C. Analytical study of Hugoniot in unidirectional fiber reinforced composites, *J. Comp. Mat.* **3**, 500 (1969).

46. Tsou, F.K. and Chou, P.C. The control-volume approach to Hugoniot of macroscopically homogeneous composites, *J. Comp. Mat.* **4**, 536 (1970).

47. Torvik, O.J. Shock propagation in a composite material, *J. Comp., Materials* **4**, 296 (1970).

48. Dremin, A.N. and Karpukhin, I.A. Method for determining the shock adiabatic curves for the disperse substances, *Zh. Prikl. Mekhan, i Teck. Fiz.* **1**, No.3 (1960).

49. Alekseev, Yu.F., Al'tshuler, L.V., and Krupnikova, V.P. Shock compression of two-component paraffin-tungsten mixture, *Zh. Prikl. Mekhan, i Teck. Fiz.* **12**, No.4 (1971).

50. Barker, L.M. A model for stress-wave propagation, *J. Comp. Mat.* **5**, 140 (1971).

51. Chen, P.J. and Gurtin, M.E. On the propagation of one-dimensional acceleration waves in laminated composites, *J. Appl. Mech.* **40**, 1055 (1973).

52. Kanel, G.I., Ivanov, M.F., and Parshikov, A.N. Computer simulation of the heterogeneous materials response to the impact loading, *Int. J. Impact Engng.* **17**, 455 (1995).

53. Johnson, J.N., Hixson, R.S., and Gray, G.T.III Shock-wave compression and release of aluminum/ceramic composites, *J. Appl. Phys.* **76**, 5706 (1994).

54. Grady, D.E., Ravichandran, G., and Zhuang, S., Continuum and subscale modeling of heterogeneous media in the dynamic environment, in *Proceedings of the AIRPAT Conference*, Honolulu, Hawaii, edited by Manghani, M., Oxford University Press (1999).

55. Rayleigh, Lord, Aerial plane waves of finite amplitude, *Proc. Roy. Soc.* **A84**, 247 (1910).

56. Lighthill, M.J. *Survey in Mechanics*, Cambridge University Press, p250 (1965).

57. Band, W. Studies in the theory of shock propagation in solids, *J. Geophys. Res.* **65**, 695 (1960).

58. Band, W. and Duvall, G.E. Physical nature of shock propagation, *Amer. J. Phys.* **29**, 780 (1961).

59. Bland, D.R. On shock structure in a solid, *J. Inst. Maths Applics* **1**, 56 (1965).

60. Swan, G.W., Duvall, G.E., and Thornhill, C.K. On steady wave profiles in solids, *J. Mech. Phys. Solids* **21**, 215 (1973).

61. Mineev, V.N. and Savinov, E.V. Viscosity and melting point of aluminum, lead, and sodium chloride subjected to shock compression, *Soviet Physics JETP* **25(3)**, 411 (1967).

62. Mineev, V.N. and Zaidel, R.M. The viscosity of water and mercury under shock loading, *Soviet Physics JETP* **27(6)**, 874 (1968).

63. Godunov, S.K. and Deribas, A.A. Influence of material viscosity on the jet formation process during collisions of metal plates, *Combustion, Explosion, and Shock Waves* **11(1)**, 1 (1975).

64. Johnson, J.N. and Barker, L.M. Dislocation dynamics and steady plastic wave profiles in 6061-T6 aluminum, *J. Appl. phys.* **40(11)**, 4321 (1969).

65. Gillman, J.J. Resistance to shock-front propagation in solids, *J. Appl. Phys.* **50(6)**, 4059 (1979).

66. Miller, G.H. and Ahrens, T.J. Shock-wave viscosity measurement, *Rev. Mod. Phys.* **63(4)**, 919 (1991).

67. Rakhmatulin, H.A. *Prikl. Mat, Mech.* **10**, 333 (1946).

68. Taylor, G.I. The use of flat-ended projectiles for determining dynamic yield stress, *Proc. Roy. Soc. Ser.* **A 194**, 289 (1948).

69. Von Karman, T. and Duwez, P.E. The propagation of plastic deformation in solids, *J. Appl. Phys.* **21**, 987 (1950).

70. Clifton, R.J. On the analysis of elastic/visco-plastic waves of finite uniaxial strain, in *Shock Waves and the Mechanical Properties of Solids*, edited by Burke, J.J. and Weiss, V., Syracuse University Press, New York, p73 (1971).

Chapter 2

Shock Wave Phenomenon in Solids

The characteristics of solids such as shear strength, polymorphic phase transformation, heterogeneous structure, anisotropy, and viscoplasticity, etc., which distinguish them from liquids and gases, make shock wave propagation in solids and the induced effects much more complicated and much more difficult to be fully described and modeled. Nevertheless, due to the sustained efforts of experimentalists, engineers and scientists in the past several decades, considerable progress has been made in experimental techniques, theories, numerical analyses and applications toward fully describing the complicated mechanical response of solids to shock compression and understanding physical effects (such as electric, magnetic and optical properties) in solids under shock loading[1-8].

In this chapter, for the purpose of conceptual completeness of the study of shock wave propagation in the layered heterogeneous composites, only some basic descriptions of mechanical response of solids to shock compression have briefly been cited, i.e., the equation of state for the bulk response and shear strength for deviatoric response.

2.1 Jump Conditions

When a shock propagates in a homogenous, isotropic solid (see Fig. 2.1), ignoring the influence of heat conduction, viscosity and material heterogeneity on the compression process of the shock front, treating the shock front as a mathematical discontinuity in density, pressure, energy and entropy, assuming that steady state condition exists and the initial and final states are equilibrium

states, the conservation laws of mass, momentum and energy across a shock front for one-dimensional plane wave can be written as[1,9-13]

$$\frac{\rho_0}{\rho_1} = 1 - \frac{u_1 - u_0}{U - u_0}, \tag{2.1}$$

$$\sigma_1 - \sigma_0 = \rho_0 (U - u_0)(u_1 - u_0), \tag{2.2}$$

$$E_1 - E_0 = \frac{1}{2}(\sigma_1 + \sigma_0)(V_0 - V_1), \tag{2.3}$$

where U is shock wave velocity; subscripts 0 and 1 represent the quantities in the initial and final states (ahead and behind the shock front); u, ρ, σ, E are particle velocity, density, normal stress and internal energy, respectively; $V = 1/\rho$ is the specific volume. Since there exists a discontinuity in density, stress (or pressure), energy, entropy, and as well as particle velocity, between the material states before and after shock wave, equations (2.1), (2.2) and (2.3) relating the final state to the initial state, are the so called shock jump conditions. The internal energy jump condition, equation (2.3) is also called as Rankine-Hugoniot equation.

If the initial state of material is specified, i.e., $u_0, \rho_0, \sigma_0, E_0$ are known, there remains five unknown variables, u, ρ, σ, E and U, in the jump equations describing the shock. Upon specifying the boundary loading producing the shock, one more variable is reduced, so in order to determine the variables in the shocked state, an additional equation is needed. This additional equation, containing the information of material behavior, which distinguishes one from another, is called equation of state (EOS).

2.2 Equation of State (EOS)

For the sake of simplification, it is assumed that the stress range concerned here is high enough such that the shear stresses in the compressed material are small relative to the average value of

principal stress components, i.e., the equation of state for hydrodynamic approximation, and the shocked state is a single phase state.

Among the variables in the shock jump equations, kinematic quantities, shock velocity U and particle velocity u_1, are the two which can be easily measured through shock-wave experiments. Experimental measurements are normally made relative to coordinates chosen so that $u_0 = 0$, and $U > 0$. The relation between U and u_1 can empirically be described by a polynomial equation[13,14],

$$U = C_0 + su_1 + s_1 u_1^2 + \cdots, \tag{2.4}$$

where C_0 is the bulk sound speed at ambient pressure, and s, s_1 are positive constants. This equation is often known as the Hugoniot curve[15], or shock-wave equation of state, which represents the locus of associated values of U and u_1 determined from a set of experiment involving shocks of varying strength. For most metals, $s_1 = 0$, and equation (2.4) reduces to a linear relationship[16],

$$U = C_0 + su_1 . \tag{2.5}$$

Combining equation (2.5) or (2.4) with shock jump equations, totally 10 pairs of Hugoniot relationships, in turn, 20 equations can be obtained between pairs of variables in the set $\{U, u_1, V_1, \sigma_1, E_1\}$. One of them, in the pressure-volume form, is

$$P_H = \frac{\rho_0 C_0^2 \eta}{(1 - s\eta)^2}, \tag{2.6}$$

$$\eta = 1 - \frac{V_1}{V_0} = \frac{u_1}{U}, \tag{2.7}$$

or, expressing specific volume in terms of Hugoniot pressure,

$$V_1 = \frac{C_0^2}{2s^2 P_H}\left[\sqrt{1 + \frac{4sV_0}{C_0^2}P_H} + \frac{2s(s-1)V_0}{C_0^2}P_H - 1\right]. \tag{2.6'}$$

In obtaining the equations (2.6)-(2.7), the normal stress σ in jump conditions has been substituted by the Hugoniot pressure P_H or P_I in order to be consistent with hydrodynamic

assumption made at the beginning of this section. The Hugoniot curve depends on the initial state of the material into which the shock wave is propagating and is said to be centered on this initial state. If the Hugoniot curve centered at the state of rest under normal laboratory ambient conditions it is usually called the principal Hugoniot curve of the material.

Shock compression progresses at a rapid pace. The compression of a material element by a shock wave is completed in the time scale of the rise time of a shock front, which is usually a few nanoseconds or less. In this short time period, heat conduction between the elements being compressed and the external environment is impossible, so the shock compression process is said to be adiabatic.

Though both shock and isentropic compression processes are adiabatic, they are not the same thing. In an isentropic compression, it is possible to reach any state on the isentrope by following the actual isentropic curve as a thermodynamic path, in which the temperature will increase, but the process occurs at constant entropy with no heat flow. In the case of shock compression, a Hugoniot state, P_H , V_I is achieved via a thermodynamic path given by the straight line called Rayleigh line (see Fig. 2.2). Therefore, successive states along the Hugoniot curve can not be reached from one to another by a shock process. The Hugoniot curve itself just represents the locus of all possible final shocked state corresponding to a given initial state[14]. The difference between the Hugoniot and the isentrope indicates that shock compression is not an isentropic process. Nevertheless, it can be shown that if the initial state is at ambient condition, the entropy increase along the Hugoniot is of third order, and the isentrope and Hugoniot have the same first and second pressure-volume derivatives, which means that the zero-pressure shock velocity is the same as the ultrasonic sound velocity[12,17].

In order to relate the states on shock Hugoniot to the states off the Hugoniot, i.e., the states can be reached through some thermodynamic path such as the isentrope and isotherm, physics and thermodynamics based analytical EOS is needed.

There are many theoretical approaches addressing the formulation of EOS[18-24]. A thorough review of EOS of solids under strong compression was recently made by Holzapfel[25]. Based on the fundamental consideration of interactions between atoms, these theories formulate selected function (e.g., Internal energy, Helmholtz free energy, Gibbs free energy) in the terms of state variables (e.g., volume, pressure, temperature). One common assumption of those theories is that the state functions are additive in terms of contributions representing the effect of several independent mechanisms. Mostly, the state functions are expressed in three terms, which represent the behavior of the solid at absolute-zero temperature, thermal vibration of lattice atoms at temperature above absolute zero and effects of thermally excited electrons at high temperature[21]. Combining the state functions with thermodynamic laws, many different forms of EOS have been obtained. One of the most widely used EOS in the field of shock compression is the Mie-Gruneisen EOS,

$$P - P_{0K} = \frac{\gamma}{V}(E - E_{0K}), \tag{2.8}$$

where P and E are the pressure and internal energy of the state interested, and P_{0K}, E_{0K} are the pressure and the internal energy of the reference state, which can be the shock Hugoniot state or zero pressure isentrope state. γ is the Gruneisen constant defined as

$$\gamma = -\left(\frac{\partial \ln \nu}{\partial \ln V}\right)_T, \tag{2.9}$$

where ν is the vibrational frequency of atoms at some thermodynamic state. Gruneisen constant can also be expressed in the terms of thermodynamic state variables or thermodynamic parameters as

$$\gamma = V\left(\frac{\partial P}{\partial E}\right)_V = V\frac{\alpha}{C_V K}, \tag{2.9'}$$

where α, C_V, K are the thermal expansion coefficient, specific heat at constant volume and isothermal bulk modulus, respectively.

One important approximation in the model for calculating the Gruneisen constants is assuming that γ is only the function of volume and the ratio γ / V is a constant, i.e.,

$$\frac{\gamma}{V} = \frac{\gamma_0}{V_0} = const\,, \tag{2.10}$$

where γ_0 and V_0 are the Gruneisen constant and specific volume at zero pressure, respectively. And, furthermore, γ_0 can be approximated by

$$\gamma_0 = 2s - 1\,, \tag{2.11}$$

where s is the constant in equation (2.5) of the experimentally determined shock Hugoniot curve. Detailed discussion on the determination of Gruneisen constant can be found elsewhere[1,6,9,17,21].

2.3 Equation of State (EOS) for Mixture

Several approaches have been developed to predict the mechanical behavior of composite materials by using the known properties of their components[26-34]. Among them is the additive approximation to obtain the EOS of mixture developed by Dremin[33].

The basis of this mixture approach is that the rule of additivity is assumed to be sufficiently met. In the additive approximation, it is assumed that the volume of the shock-compressed mixture is equal to the sum of the volume of its components, obtained at the same pressure by separate shock compression in the form of homogeneous monolithic samples[33,37]. Thus, the volume-pressure form of equation of state of the shock-compressed composite is expressed by the following equation,

$$V_c(p) = \alpha_1 V_1(p) + \alpha_2 V_2(p)\,, \tag{2.12}$$

where p is the pressure or stress, V_c is the specific volume of the mixture, α_1, α_2 are the mass fraction of components 1 and 2 ($\alpha_1 + \alpha_2 = 1$), V_1, V_2 are the specific volumes of the components, which relates to the shock pressure on the Hugoniot through equation (2.6'). Some of the

theoretical basis of the mixture model have been considered by Nikolaevskii[35], and Duvall and Taylor[36]. Based on the experimental Hugoniot relations of two types of paraffin/tungsten composites, light and heavy mixtures with 8.4% and 19.8% volume fraction of tungsten, Alekseev and his coworkers[37] calculated the shock Hugoniot curve of paraffin using equation (2.12) and compared their computed results with experimental data, indicating that the predictions by additive mixture theory agree reasonably well with the experimental results. Al'tshuler and Sharipdzhanov[38] also used the additive approximation approach to calculate the equations of state of a large number of minerals and rocks on the basis of the oxide composition in the pressure range of 50 GPa to 150 GPa, and compared with experimental Hugoniot. They found out that the additivity principle works well.

Knowing the equation of state of the mixture above, i.e., equation (2.12), the relation of shock wave velocity and particle velocity can be deduced by combining with the mass conservation equation (2.1) and momentum conservation equation (2.2), which was rewritten with respect to initial state of zero particle velocity and zero pressure as follows:

$$V_c U_c = V_{c0}(U_c - u_c), \tag{2.13}$$

$$P = u_c U_c / V_{c0}, \tag{2.14}$$

where V_{c0} is the specific volume of mixture at initial state (i.e., zero pressure), U_c and u_c are the shock velocity and particle velocity of shock compressed mixture, respectively.

Also, using the bulk sound speed of each component, the bulk sound velocity of the mixture at a desired pressure can be formally calculated through the relation[34]

$$C^2 = V_c^2 / (\alpha_1 V_1 / C_1^2 + \alpha_2 V_2 / C_2^2), \tag{2.15}$$

where C, C_1, C_2 are respectively the bulk sound speed of mixture, component 1 and 2 at the shock pressure.

Meyers proposed a simple mixing approach to estimate the shock Hugoniot relation of mixture[32]

$$U_c = \alpha_1 C_{01} + \alpha_2 C_{02} + (\alpha_1 s_1 + \alpha_2 s_2) u_c , \qquad (2.16)$$

where U_c and u_c are the shock velocity and particle velocity of mixture, respectively, α_1, α_2 are the mass fraction of two components 1 and 2, C_{01}, C_{02} are the bulk sound speed of component 1 and 2 at zero pressure, and s_1, s_2 are the slope of U-u_1 curve of components. This approximation is also an additive method, but based on the assumption that the local particle velocity in components 1 and 2 are the same as the mean particle velocities in the mixture, rather than the assumption in the Dremin's model above where the local pressure in the components is the same as the mean pressure in the mixture.

2.4 Constitutive Models

Under high pressure shock wave loading, where the shear strength is small compared with the shock pressure, the hydrodynamic approximation is accurate enough to describe the shock response behavior of solids. At low and medium loading regimes, shear strength, heterogeneous structure, anisotropy, polymorphic phase transformations, rate effects, etc., properties of solids come into playing important roles, then, EOS alone can not properly describe the response of solids to shock loading. To address the significant features of solids, much effort has been made in constructing proper constitutive models. Many empirical or semi-empirical models[39-44], physically based models[45-47] and continuum theory of inelastic materials[48] have been developed to address different aspects of problems encountered in the study of shock compression solids, such as dynamic strain hardening, thermal softening, rate effects, material memory, etc.[11,49-52]

Among these models, perhaps the most popular used in numerical computations is the elastic-plastic-hydrodynamic model[53]. In this model, it is assumed that the stress response of a material can be decomposed into hydrodynamic pressure, which accounts for the uniform part of all normal stresses, and shear stress, which is associated with the resistance of the material to shear

distortion, and an increment in the total strain is the sum of the elastic and the plastic incremental strains. The shear stress and/or the elastic strain increment are calculated through Hooke's law. The yield condition is determined by the von Mises criterion. It is also assumed that plastic deformation, i.e., the deviatoric strain, causes no volume change. With these assumptions, for the one-dimensional deformation induced by plane shock waves, Wilkins derived the elastic-plastic-hydrodynamic constitutive relations[53]:

The normal stress σ_1 of shocked state in the direction of shock wave propagation is

$$\sigma_1 = -P_1 + s_x \,. \tag{2.17}$$

Normal deviatoric stress s_x in the direction of shock propagation and lateral deviatoric stress s_y are given by

$$\dot{s}_x = \frac{4\mu}{3}\frac{\dot{V}_1}{V_1}, \tag{2.18}$$

$$\dot{s}_y = -\frac{2\mu}{3}\frac{\dot{V}_1}{V_1}. \tag{2.19}$$

The yield condition can be expressed as

$$(s_x^2 + 2s_y^2) \le \frac{2}{3}Y^2, \tag{2.20}$$

where $Y = Y(W_p)$ is the yield stress in simple tension, and W_p is the plastic work defined in plane strain condition by

$$dW_p = s_x d\varepsilon_x^p \,. \tag{2.21}$$

No volume change due to plastic deformation requires

$$s_x + 2s_y = 0 \,. \tag{2.22}$$

The hydrodynamic pressure is calculated from EOS,

$$P_1 = P_1(V_1) = -K\ln(V_1), \qquad \text{for elastic regime} \tag{2.23}$$

$$P_1 = P_1(V_1) = A(V_0/V_1 - 1) + B(V_0/V_1 - 1)^2 + C(V_0/V_1 - 1)^3, \qquad \text{for plastic regime} \tag{2.23}$$

Here A, B, and C are constants such that $P_1(V_1) + 2Y/3$ reproduces the Hugoniot for shock above the elastic limit. The minimum pressure at which yield occurs under tension is

$$P_{1,\min} = -Y(0)/3 = -Y^0/3, \tag{2.24}$$

where Y^0 is the initial value of the yield stress. $d\varepsilon_x^p$ in equation (2.21) denote the plastic strain increment. If there is no work hardening Y in equation (2.20) will be a constant equal to Y^0.

2.5 Constitutive Models for Heterogeneous Composites

Viscoplasticity processes in macroscopically homogeneous media have generally been accepted as the underlying physics responsible for the dissipation and wave dispersion leading to observed structured shock waves, based on which many descriptive constitutive models have been developed[11, 43-49]. For the shock wave propagation in heterogeneous media, relatively little effort has been made, and only a few simplified models have been proposed to phenomenologically describe the response of heterogeneous solids to shock loading[29-31,34]. Due to the existence of internal interfaces inside heterogeneous media, the scattering of wave energy induced by microstructure during shock propagation could be an alternative to viscoplasticity as the physics underlying the formation of structured steady waves in heterogeneous composites[54]. Wave dispersion in heterogeneous solids due to scattering induced by microstructure has been examined and constitutive models based on the mechanism of acoustic scattering of wave energy for solids have proposed by Grady and his coworkers[54-56]. The theory and the formulation of a model for shock wave propagation in heterogeneous media is briefly described in this section.

As a finite amplitude shock wave passes through a heterogeneous solid, an incoherent acoustic wave motion due to scattering of the principal wave by the heterogeneous microstructure is induced (Fig. 2.3). The energy state of the matter behind the shock wave will include a component due to the lattice strain energy and a kinetic component corresponding to a field of

acoustic phonon energy caused by wave scattering within the heterogeneous microstructure[54], i.e.,

$$U = U_0(\varepsilon) + U_k, \tag{2.25}$$

where $U_0(\varepsilon)$ is the lattice strain energy at the current nominal axial state, and $U_k = \sum_i n_i h\nu_i$ is the acoustic phonon energy induced by the microstructure. n_i is the number of phonons with energy $h\nu_i$. ν_i and h are the normal mode frequency and Planck's constant, respectively.

The inducement of kinetic component of acoustic phonon energy during the dynamics of the shock compression process induces unique consequences. During passage of a structured shock, dispersion due to wave scattering leads to the production of phonon energy within a limited spectrum of normal mode coordinates in the shock front. Diffusion of this phonon energy to an equilibrium configuration throughout the acoustic normal modes is achieved as the final shock state is approached. Ultimately, continued diffusion throughout the full thermal spectrum occurs until complete thermoelastic equilibrium is achieved. These processes account for entropy production within the elastic shock process in the heterogeneous solid. Details of the steady shock wave profile structure are determined by characteristic relaxation times associated with specifics in the acoustic energy diffusion processes.

Since the real compression path of a material particle from its initial state to the final shocked state by a shock wave is along the Rayleigh line, the dynamic stress experienced by an element during the compression can be decomposed into equilibrium and nonequilibrium parts (see Fig. 2.4),

$$\dot{\sigma} = \dot{\sigma}_{cq} + \dot{\sigma}_n \,. \tag{2.26}$$

This decomposition is not an assumption. It is a recognition of the fact that the most fundamental level forces of interaction in the condensed matter are a composition of strain (lattice potential) and kinetic (momentum exchange) terms. The first term ($\dot{\sigma}_{eq}$) on the right hand side

of equation (2.26) will determine the equilibrium thermoelastic response of the heterogeneous solid. The second term ($\dot{\sigma}_n$) on the right hand side of equation (2.26) accounts for stress brought about by the nonequilibrium acoustic phonon energy induced in the heterogeneous microstructure by the transient wave. Equation (2.26) can be obtained through the strain and time derivative of equation (2.25) and the nonequilibrium term of the stress can be formally expressed as[54,55],

$$\dot{\sigma}_n = \sum_i s_i h\nu_i' - \sum_i \frac{1}{\tau_i}(n_i - n_{i0})h\nu_i' , \tag{2.27}$$

where s_i are phonon stimulation terms, τ_i are characteristic relaxation constants, n_{i0} are equilibrium phonon population numbers and ν_i' are strain derivatives of normal mode frequencies.

Single-mode Approximation

Under the assumption of a single relaxation time $\tau_i = \tau$, equation (2.27) reduces to,

$$\dot{\sigma}_n = S(.) - (\sigma - \sigma_{eq})/\tau , \tag{2.28}$$

or

$$\dot{\sigma}_n = S + R , \tag{2.29}$$

where $S = S(.)$ represents a phonon stimulation function dependent on the dynamics of the wave interaction with the heterogeneous microstructure and $R = (\sigma - \sigma_{eq})/\tau$ is the relaxation of nonequilibrium phonon energy. The modeling framework identified by equations (2.26) and (2.29) and the specific models to be considered presently, which fall within this framework, will be recognized as continuum inelastic representations of the stress versus strain response of heterogeneous solids.

Among the early models, a general nonlinear Maxwell model (viscoelastic) proposed by Barker[29] is of the form,

$$\dot{\sigma} - \varphi(\varepsilon)\dot{\varepsilon} = -\frac{1}{\tau}(\sigma - \sigma_{eq}), \tag{2.30}$$

and describes finite amplitude wave propagation in composite solids, where τ is the associated relaxation time constant. This model predictions compared favorably with both experimental data and numerical solutions of wave propagation in layered composites, and the stress decomposition of equations (2.26) and (2.29) is readily produced,

$$\dot{\sigma}_n = M(\varepsilon)\dot{\varepsilon} - \frac{1}{\tau}\sigma_n, \tag{2.31}$$

$$\dot{\sigma}_{eq} = \vartheta(\varepsilon)\dot{\varepsilon}. \tag{2.32}$$

Equation (2.31) explicitly displays the stimulation (*S*) and relaxation (*R*) terms in the model of Barker identified for the non-equilibrium stress in equation (2.30). Stimulation of nonequilibrium stress is accomplished through a modulus $M(\varepsilon) = \varphi(\varepsilon) - \vartheta(\varepsilon)$. A linear relation proportional to the non-equilibrium stress governs relaxation.

More recently Kanel *et al.*[34] have proposed an alternative continuum anelasticity model to describe wave propagation in solid composites. In the same framework the model can be written,

$$\dot{\sigma}_n = k\dot{\varepsilon}^m - \frac{1}{\tau}\sigma_n, \tag{2.33}$$

$$\dot{\sigma}_{eq} = \vartheta(\varepsilon)\dot{\varepsilon}. \tag{2.34}$$

Although quite similar to the Barker's model (the models differ only in the stimulation term, S) the physical implications in the stimulation term for $m > 1$ are profoundly different[55,56]. Rather than modeling a dichotomous (instantaneous and equilibrium) response of the material, the stimulation term implies a continuously increasing scattered energy (and hence nonequilibrium stress) with increasing strain rate within the shock wave.

Multimode Theory

The theory outlined at the beginning of this section can be expanded to model more complex substructure processes brought about by wave propagation in heterogeneous media. The evolution of nonequilibrium phonon population constitutive model as was done above in the single mode theory is not pursued here. In this multimode theory, the stress in the composite body is written as[56],

$$\dot{\sigma} = \dot{\sigma}_{eq} + \dot{\sigma}_{n1} + \dot{\sigma}_{n2}, \tag{2.35}$$

where the first term on the right hand side represents the stress rate supported by the lattice strain while the last two terms are transient stresses brought about by nonequilibrium acoustic energy within the lower frequency and higher frequency normal mode spectra, respectively.

As in the earlier single mode theory, the nonequilibrium phonon stresses, σ_{n1}, and σ_{n2}, are expected to be stimulated during the passage of shock wave and relax toward zero when stimulation is removed. Accordingly, it is reasonable to assume the following expression for the time dependence of the nonequilibrium phonon stress (due to acoustic scattering),

$$\frac{d}{dt}\begin{pmatrix}\sigma_{n1}\\ \sigma_{n2}\end{pmatrix}=\begin{pmatrix}s_1\\ s_2\end{pmatrix}+\begin{pmatrix}\alpha_{11} & \alpha_{12}\\ \alpha_{21} & \alpha_{22}\end{pmatrix}\begin{pmatrix}\sigma_{n1}\\ \sigma_{n2}\end{pmatrix}. \tag{2.36}$$

The physics described by equation (2.36) is readily apparent. The terms s_1 and s_2 determine stress wave stimulation of the lower frequency and higher frequency modes, respectively, while the matrix α_{ij} accounts for a coupling and transfer of energy between modes as well as relaxation of the nonequilibrium phonon (acoustic) energy to statistical mechanical equilibrium.

Equation (2.36), when stimulation functions and relaxation coefficients are specified, and when incorporated into equation (2.35), constitutes a viable constitutive relation for the transient stress versus strain behavior of the heterogeneous composite under the dynamic conditions of interest. When combined with the appropriate conservation laws, the system of equations is capable of describing nonlinear one-dimensional wave propagation in the media described. When combined with the appropriated conservation laws, general computational solutions could,

in principle, be pursued for modeling events such as hypervelocity impact of heterogeneous structures.

2.6 References

1. Asay, J.R. and Shahinpoor, M. *High-Pressure Shock Compression of Solids*, Springer-Verlag, New York (1993).
2. Davison, L., Grady, D.E., and Shahinpoor, M. *High-Pressure Shock Compression of Solids II: Dynamic Fracture and Fragmentation*, Springer, New York (1996).
3. Davison, L. and Shahinpoor, M. *High-Pressure Shock Compression of Solids III*, Springer, New York (1998).
4. Davison, L., Horie, Y., and Shahinpoor, M. *High-Pressure Shock Compression of Solids IV: Response of Highly Porous Solids to Shock Loading*, Springer, New York (1997).
5. Graham, R.A. *Solids under High-Pressure Shock Compression: Mechanics, Physics, and Chemistry*, Springer-Verlag, New York (1993).
6. Meyers, M.A. *Dynamic Behavior of Materials*, John Willey & Sons, Inc., New York (1994).
7. Cristescu, N. *Dynamic Plasticity*, North-Holland Publishing Company, Amsterdam (1967).
8. Chou, P.C. and Hopkins, A.K. *Dynamic Response of Materials to Intense Impulse Loading*, Air Force Materials Laboratory, Wright Patterson AFB, Ohio (1972).
9. Rice, M.H., Mcqueen, R.G., and Walsh, J.M. Compression of solids by strong shock waves, in *Solid State Physics*, edited by Seitz, F. and Turnbull, D., Academic Press Inc., Publishers, New York and London, Vol. **6**, 1 (1958).
10. Doran, D.G. and Linde, R.K. Shock effects in solids, in *Solid State Physics*, edited by Seitz, F. and Turnbull, D., Academic Press Inc., Publishers, New York and London, Vol. **6**, 230 (1966).
11. Murri, W.J., Curran, D.R., Peterson, C.F., and Crewdson, R.C. Response of solids to shock waves, in *Advances in High-Pressure Research*, edited by Wentorf, R.H., Jr., Academic Press, London and New York, Vol. **4**, 2 (1974).

12. Duvall, G.E. and Fowles, G.R. Shock waves, in *High Pressure Physics and Chemistry*, edited by Bradley, R.S., Academic Press, London and Now York, Vol. **2**, 209 (1963).

13. Meyers, M.A. in *reference 6*, chapter 4.

14. Ahrens, T.J. in *reference 1*, chapter 4.

15. Davson, L. and Graham, R.A. Shock compression of solids, *Phys. Rep.***55(4)**, 255 (1979).

16. Marsh, S.P. *LASL Shock Hugoniot Data*, University of California Press, Berkeley and Los Angeles (1980).

17. Mcqueen, R.G. Shock waves in condensed media: their properties and the equation of state of materials derived from them, in *Proceedings of the International School of Physics <<Enrico Fermi>>, Course CXIII: High-Pressure Equations of State: Theory and Apllications*, edited by Eliezer, S. and Ricci, R.A., North-Holland, Amsterdam, p101 (1991).

18. Slater, J.C. *Introduction to Chemical Physics*, McGraw-Hill, New York (1939).

19. Born, M. and Huang, K. *Dynamical Theory of Crystal Lattices*, Clarendon Press, Oxford (1954).

20. Torrens, I.M. *Interatomic Potentials*, Academic Press, New York (1972).

21. Anderson, O.L. *Equations of State for Solids in Geophysics and Ceramic Science*, Oxford University Press, New York (1995).

22. Vinet, P., Rose, J.H., Ferrante, J., and Smith, J.R. Universal Features of the Equation of State of Solids, *J Phys.: Condens. Matter* **1**, 1941 (1989).

23. Hama, J., Suito, K., and Kawakami, N. *Phys. Rev. B* **39**, 3351 (1989).

24. Kalitkin, N.N. and Kuz'mina, L.V. *Sov. Phys.-Solids State* **13**, 1938 (1972).

25. Holzapfel, W.B. Physics of Solids under Strong Compression, *Rep. Prog. Phys.* **59**, 29 (1996).

26. Sun, C.T., Achenbach, J.D., and Hermann, G., Continuum theory for a laminated medium, *J. Appl. Mech.* **35**, 467 (1968).

27. Ben-Amoz, M. On wave propagation in laminated composites-II. propagation normal to the laminates, *Int. J. Engng Sci.* **13**, 57 (1975).

28. Hashin, Z. Theory of mechanical behavior of heterogeneous media, *Appl. Mech. Rev.* **1**, (1964).

29. Barker, L. M. A model for stress-wave propagation, *J. Comp. Mat.* **5**, 140 (1971).

30. Chen, P. J. and Gurtin, M. E. On the propagation of one-dimensional acceleration waves in laminated composites, *J. Appl. Mech.* **40**, 1055 (1973).

31. Johnson, J.N., Hixson, R.S., and Gray, G,T.III Shock-wave compression and release of aluminum/ceramic composites, *J. Appl. Phys.* **76(10)**, 5706 (1994).

32. Meyers, M.A. *reference 6*, chapter 5.

33. Dremin, A.N. and Karpukhin, I.A. Method for determining the shock adiabatic curves for the disperse substances, *Zh. Prikl. Mekhan, i Teck. Fiz.* **1**, No. 3 (1960).

34. Kanel, G.I., Ivanov, M.F., and Parshikov, A.N. Computer simulation of the heterogeneous materials response to the impact loading, *Int. J. Impact Engng.* **17**, 455 (1995).

35. Kikolaevskii, V.N. Hydrodynamic analysis of shock adiabatic curves for heterogeneous mixtures of substances, *Zh. Prikl. Mekhan, i Teck. Fiz.* **10,** No. 3 (1969).

36. Duvall, G.E. and Taylor, S.M. Jr. Shock parameters in a two component mixture, *J. Comp.Mat.* **5**, 130 (1971).

37. Alekseev, Yu.F., Al'tshuler, L.V., and Krupnikova, V. P. Shock compression of two-component paraffin-tungsten mixture, *Zh. Prikl. Mekhan, i Teck. Fiz.* **12,** No. 4 (1971).

38. Al'tshuler, L.V. and Sharipdzhanov, I.I. Additive equations of state of silicates at high pressures, *Izv. Earth Physics* **3**, 11 (1971).

39. Ludwik, P. *Phys. Z.* **10**, 411 (1909).

40. Klopp, R.W., Clifton, R.J., and Shawki, T.G. *Mech. Mat.* **4**, 375 (1985).

41. Litonski, J. *Bull. Acad. Pol. Sci.* **25**, 7 (1977).

42. Vinh, T., Afzali, M., and Roche, A. in *Mechanical Behavior of Materials*, Proc. ICM, edited by Miller, K.J. and Smith, R.F., Pergamon Press, Oxford & New York, p633 (1977).

43. Johnson, G.R. and Cook, W.H. in *Proc. 7th Intern. Symp. on Ballistics*, Am. Def. Prep. Org.(ADPA), Netherlands, p541 (1983).

44. Campbell, J.D., Eleiche, A.M., and Tsao, M.C.C. in *Fundamental Aspects of Structural Alloy Design*, Plenum, New York, p545 (1977).

45. Zerilli, F.J. and Armstrong, R.W. *J. Appl. Phys.* **61**, 1816 (1987).

46. Follansbee, P.S. and Kocks, U.F. *Acta.Met.* **36**, 81 (1988).

47. Steinberg, D.J., Cochran, S., and Guinan, M. J. *Appl. Phys.* **51**, 1498 (1980).

48. Herrmann, W., *reference 1*, chapter 5.

49. Meyer, L.W. Constitutive equations at high strain rates, in *Shock-Wave and High-Strain-Rate phenomena in Materials*, edited by Meyers, M.A., Murr, L.E., and Staudhmmer, K.P., Marcel Dekker, Inc., New York & Basel & Hong Kong, p49 (1992).

50. Meyers, M.A., Murr, L.E., and Staudhmmer, K.P. *Shock-Wave and High-Strain-Rate phenomena in Materials*, Marcel Dekker, Inc., New York & Basel & Hong Kong (1992).

51. Burke, J.J. and Weiss, V. *Shock Waves and the Mechanical Properties of Solids*, Syracuse University Press, Syracuse & New York (1971).

52. Truesdell, C. and Noll, W. The non-linear field theories of mechanics, in *Encyclopedia of Physics*, Vol. **III/3**, edited by Flugge, S., Springer-Verlag & Berlin (1965).

53. Wilkins, M.L. Calculation of elastic-plastic flow, in *Methods in Computational Physics*, edited by Alder, B., Vol. **3**, p211 (1964).

54. Grady, D.E. Physics and modeling of shock wave dispersion in heterogeneous composites, *J. Phys. IV France* **7**, 669 (1997).

55. Grady, D.E Scattering as a mechanism for structured shock waves in metals, *J. Mech. Phys. Solids* **46**, 2017 (1998).

56. Grady, D.E., Ravichandran, G. and Zhuang, S. Continuum and subscale modeling of heterogeneous media in the dynamic environment, in *Proceedings of the AIRPAT Conference*, Honolulu, Hawaii, edited by. Manghani, M., Oxford University Press (1999).

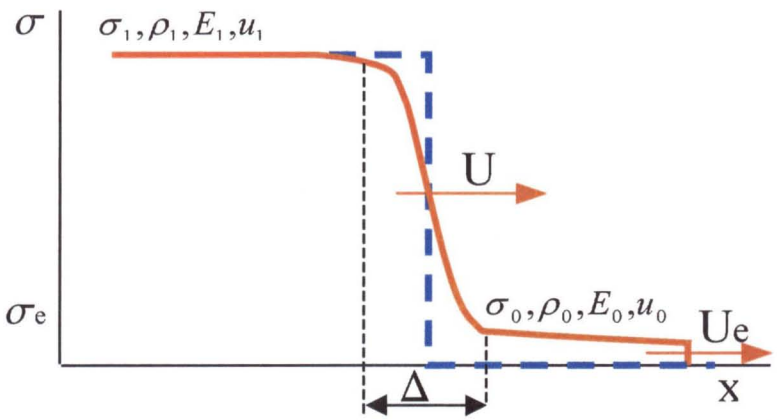

Figure 2.1 Schematic of a steady plane shock wave compresses a solid from the ambient state to a high pressure state. Solid and dashed lines represent real and ideal shock fronts, respectively.

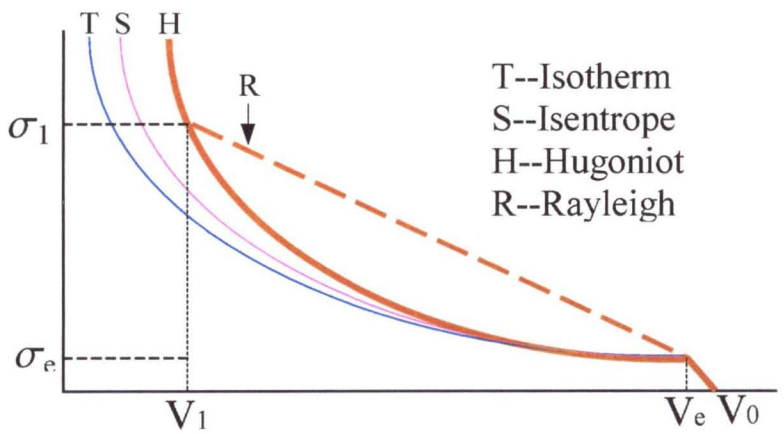

Figure 2.2 Illustration of the Hugoniot, isentrope, isotherm and Rayleigh lines.

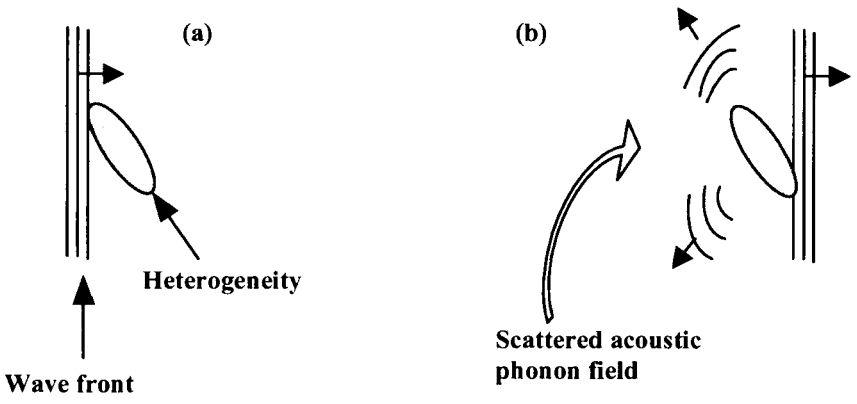

Figure 2.3 Illustration of acoustic phonon scattering of a shock wave front due to a heterogeneity, (a) before scattering and (b) showing the scattered acoustic field from the heterogeneity from the passage of the shock wave exciting internal degrees of freedom.

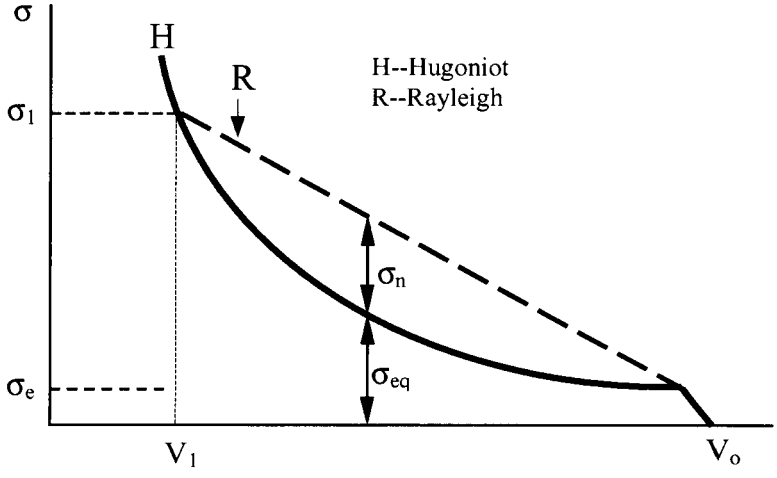

Figure 2.4 Schematic illustrating the decomposition of stress in to thermoelastic equilibrium (Hugoniot) and nonequilibrium (scattered acoustic phonon) components.

Chapter 3

Experimental Systems for Shock Compression of Solids

3.1 High Velocity Planar Impact Loading System

The loading system for shock compression of solids experiments is a powder gun which is housed in the Solid Mechanics Laboratories, GALCIT. The gun is 3 meters long (10 feet) and has a bore of about 36 mm (1.428"). The flyer velocity achieved by this gun ranges from 400 m/s to about 2,000 m/s. Upon the planar impact of a flyer onto a specimen, a shock wave is generated and propagates in the specimen.

The schematic of the powder gun loading system is shown in Fig. 3.1. When the circuit for powering the solenoid is closed, the solenoid shaft moves quickly and pushes against the trigger pin, which moves forward and penetrates into the primer. Upon the trigger pin's penetrating into the primer, the volume of the primer is reduced and the powder starts burning, thereby producing high-temperature, high-pressure gas, which is referred to as the "flame." The flame ignites the more powerful powder in the bullet case (more often called the "shell;" while some times it is also referred to as the "brass"). Then, an even hotter flame produced in the shell rushes into the flame "splitter," which is a hollow cylinder with 16 holes distributed evenly in a 45° spiral on the wall. The powder charge in the breech is ignited by the high-temperature, high-pressure flame from the flame splitter and produces very high-pressure gas in the breech. As this high-pressure gas exerts considerable transient force on the end of the sabot, the stop ring of the sabot is broken, and the sabot is continuously pushed forward and accelerated along the gun barrel. When it exits the muzzle of the barrel it has reached a very high velocity. The velocity of the sabot, i.e., the

flyer velocity, can be predetermined very accurately by controlling the mass of the powder in the breech.

The flyer velocity is measured by a light interruption system, which measures the time interval for the flyer passing two points along the gun barrel separated by a known distance. Near the gun muzzle, two pairs of fibers are mounted on the gun barrel and separated by 40.35 mm. The light beams are directed in and out of the vacuum chamber by two fiber optic cables. Before firing, both the receivers of the two cables are illuminated, and the photodiodes connected to them are in the "on" state. Once the light in the cable is blocked by the sabot, the photodiode immediately switches into "off" state. When the sabot passes the first fiber cable, the light in the fiber is blocked, and the timer starts. As soon as the timer receives the "off" signal due to the light in the second fiber being blocked, the timer stops and gives the time interval taken by the sabot to travel the distance between the fibers. More detailed information on the gun system and measurement of flyer velocity is available elsewhere[23].

The specimen, the fiber optic probe for VISAR system and the electrical pins (see next section) for triggering the oscilloscope and/or the tilt measurement of planar impact are assembled on a specimen holder. Then, the whole assembly is positioned in front of the gun muzzle. To ensure or increase the accuracy of planar impact, or in other words, to reduce the impact tilt, the specimen assembly in front of the gun muzzle is properly positioned such that when the flyer impacts the surface of the target, a small portion of the sabot is still inside the gun barrel. This reduces, or at least is well controlled, the impact tilt considerably. Also the possible disturbance to the specimen from the blow-off of the high pressure gas is reduced or avoided.

The sabot carries and supports the flyer. The sabot may be designed to be of different shapes to serve different experimental purposes. One of the versions that was used in shock compression experiments to carry the flat flyer plates is shown in Fig. 3.2. The specimen, as well as the backing plate of the specimen, if it is needed, is glued on the sabot and thoroughly dried before the experiment. The material used to make the sabot is an engineering plastic, Nylatron.

Nylatron is not the only material good for making the sabot; other polymer materials like polycarbonate (Lexan) are also good candidate materials.

The solenoid used in the firing system of the powder gun is a short stroke laminated solenoid with push style and intermittent duty, procured from the McMaster-Carr Supply Company. The solenoid is powered by 120 V AC power and can provide a force of up to 9.6 kg (336 oz). The trigger pin consists of a 4340 steel tapered cylindrical rod and a gauge steel pin. A circular hole of diameter 1.8 mm (0.070") is drilled 19 mm (3/4") deep at the center of the smaller end of the rod so that the gauge pin can be fitted into it (see schematic of gun system in Fig. 3.1). The proper length of the pin should be such that the end of the pin indents into the primer about 0.6 mm to 0.8 mm deep. If the penetration is not deep enough, the primer may not be triggered. Over-penetration will result in punching a hole in the primer, and the primer will fail to seal the high pressure gas, causing it to jet out backward. Both the primer and the brass used are those for the large rifle, which can be bought from any gun store. The hole for fitting the brass was machined by a special set of reamers (30-06 reamer set) which includes two pieces. One is a rough reamer, the other is a fine reamer. The powder used to charge the brass is the Hercules smokeless powder (3 grams). The flame splitter is made of Vascomax C-300 maraging steel which was machined first, and then heat treated.

The shock compression experiment is conducted under vacuum conditions. The vacuum chamber is evacuated to a reasonably high degree of vacuum condition ($\sim 10^{-2}$Torr) before the experiment.

3.2 Experimental Techniques: Diagnostic Systems

The diagnostic systems for shock compression experiments consist of an arrival time detector, a VISAR system, stress gages and oscilloscope recording instruments. The arrival time detector consists of charged electrical pins which are discharged by the arrival of a grounding surface[1,2].

The VISAR (the abbreviation of Velocity Interferometer System for Any Surface)[3] is used to measure the particle velocity time history of a free or internal surface of a specimen subjected to impact. Stress gages are used for measuring the stress history of shock compression and are made of either piezoresistive material (e.g., manganin, a copper alloy containing manganese and nickel) or piezoelectric materials (e.g., x-cut quartz and lithium-niobate crystals, polyvinylidene fluoride polymeric film-PVF_2). These are the common measurement techniques used in the field of shock compression of solids. There are many review papers available on shock wave diagnostic techniques[1,2,4-9].

3.2.1 Arrival Time Detector: Electric Shortening Pins

For the experiments of shock compression of solids it is necessary and important to measure the impactor velocity and the impact tilt of the flyer on the specimen. One of the earliest, and still the most popular technique, is charged electric pins or probes, which are sometimes called position transducers. The pin is a small coaxial probe that produces an electrical signal when impacted at its sensing end by a fast moving object, or by either an ionization or shock front.

Two types of pins are commonly used. One is the switch type, and the other is the piezoelectric type. The switch type pins can be divided into ionization and self-shorting type pins. The former is used in conjunction with conductive flyers such as metals, while the latter is used with non-metallic flyers. The advantage of using the pins is that they can be accurately positioned in space or within a material, thus providing a simple technique for measuring material and shock velocities, or impact planarity, or for use as a triggering source.

The arrangement of pins on the target is shown in Fig. 3.3. Pins # 1 and # 2 are used to measure the flyer velocity. They are installed such that the end of the pin # 1 is protruding at a known height, normally around several hundred micrometers to 1 millimeter, out of the impacted surface of the target, and pin # 2 is flush mounted. By measuring the difference in the discharged

time between the two pins, the velocity of the impactor or the flyer just prior to impact is obtained. Pins # 3, # 4 and # 5 are flush mounted and provide the impact times at specific locations on the specimen for measuring the impact tilt of the flyer with respect to the specimen. The pins used for PMMA specimens are the model CA-1038 self-shorting pins from Dynasen, Inc. The CA-1038 pins are the most immune to gas blow-by, which certainly exists when the sabot is accelerated using a powder gun.

In order to record the arrival time signals of the flyer impacting the specimen, a circuit to charge the pin and to turn the mechanical contact signal into an electrical signal is needed, which is called the "pin mixer" here. The circuit diagram of the pin mixer is shown in Fig. 3.4. The voltage of the power supply is E = 24 V DC. All cables used are 50 Ω impedance cables (i.e., RG58 type cables). In the circuit, R=50 Ω (W/4), C=0.001 μF (100 V, Mylar, 230B1B102K, Electro-cube), D is IN914B diode (PIV=75, I_f =75 mA, t_{rr}=4 ns), R1=200 Ω (5W), R2=400 Ω (5W), R3=500 Ω (8W), R4=750 Ω (1W), and R5=1.21K Ω (1W). This is a pre-charged open circuit when all pins are open to be shortened by the shock wave or impactor. The designed time resolution of the circuit is about 50 ns. As soon as a pin is closed, the sub-circuit, in which the pin is connected and the input terminal of the oscilloscope which is used as load of the circuit, forms a closed circuit, causing current flow through the sub-circuit, and the oscilloscope detects the corresponding voltage increase. Upon closing of each sub-circuit, there is an increment in the voltage at the input of the oscilloscope. For the parameters shown, the output of each sub-circuit designated to be about 4.80V, 2.70V, 2.20V, 1.50V and 1.0V, respectively, corresponding to pins # 1, # 2, # 3, # 4 and # 5. The power supply for the circuit is a 24 V DC linear power supply (International Series # HN24-3.6-A). The input of the power supply is 110 V AC with a current limit of 2 A.

3.2.2 Velocity Interferometry System for Any Reflector (VISAR)

3.2.2.1 Optical Principle of Velocity Interferometer

The basis of a velocity interferometer is the Michelson Interferometer (MI) and the Doppler effect. The setup and the principle of MI can be found in any optics text book[10]. Prior to a description of the optical principle of the VISAR system, it is useful to briefly introduce the Doppler shift effect.

The Doppler effect is the increase or decrease in the measured frequency of a wave depending on whether the source of light (or observer) is moving toward or away from the observer (or source). Let λ be the wavelength of laser light used in the interferometer and c be the velocity of light, then the frequency of the laser light is

$$\nu = \frac{c}{\lambda}. \tag{3.1}$$

If the laser light is impinged on an object moving with velocity u, the frequency of the reflected light, by Doppler effect, is

$$\nu' = \frac{\nu}{1 \pm u/c}, \tag{3.2}$$

where the minus (-) sign is for the case of the object moving towards the observer while the plus (+) sign is for the case of the object moving away from the observer.

The change in the wavelength of the reflected laser light is

$$\Delta\lambda = \lambda' - \lambda = \pm\frac{\lambda}{c}u. \tag{3.3}$$

Since the light transverses a round trip distance in the MI, the image velocity detected by the MI is twice that of the moving object[10], and the wavelength change from the MI should be

$$\Delta\lambda = \lambda' - \lambda = \pm\frac{2\lambda}{c}u. \tag{3.4}$$

The path of light in the MI shown in Fig. 3.5 is examined. A beam splitter, BS, is placed 45° with respect to the axis of the incident laser beam which contains the Doppler shift, such as the light reflected from the free surface or the internal interface of the specimen subjected to shock loading. The incident beam is split evenly into two beams. One beam is directed to mirror M1 and returned to BS, and the other (the transmitted part) goes to M2 and is reflected back to BS. The two returned beams are split again by BS. The transmitted part of the beam from M1 and the reflected part of the beam from M2 are recombined as they come out from the BS and interfere with each other forming interferometry fringes that can be observed at any point along the combined beam leaving BS.

Suppose the two beams from mirrors M1 and M2 have different frequencies, ν_1' and ν_2', respectively, the sum of the fields of these two beams at a given point can be written as

$$E_s = A_1 \cos(2\pi\nu_1' t + \phi_1) + A_2 \cos(2\pi\nu_2' t + \phi_2), \tag{3.5}$$

where E_s is the total electric vector, A_1 and A_2 are the amplitudes of the electric vector of the two beams, and ϕ_1 and ϕ_2 are the initial phase angles. The intensity of the light will be

$$\begin{aligned} I = |E_s|^2 &= A_1^2 \cos^2(2\pi\nu_1' t + \phi_1) + A_2^2 \cos^2(2\pi\nu_2' t + \phi_2) \\ &+ A_1 A_2 \cos[2\pi(\nu_1' + \nu_2')t + \phi_1 - \phi_2] + A_1 A_2 \cos[2\pi(\nu_1' - \nu_2')t + \phi_1 - \phi_2]. \end{aligned} \tag{3.6}$$

The first three terms are the intensity that oscillates at frequencies equal to or greater than frequency of laser light, which is normally on the order of 10^{14} to 10^{15} Hz. This is out of the response range of the recording instruments such as oscilloscopes and is very hard to detect, hence, only a time average intensity, which is essentially a constant, can be seen on an oscilloscope. The fourth term gives an output that is proportional to the so-called beat frequency, i.e., the difference between frequencies

$$\Delta\nu = \nu_1' - \nu_2'. \tag{3.7}$$

For $\Delta\nu = 0$, according to equation (3.6), the observed fringes are always static. If the two mirrors, M1 and M2, are equally positioned away from the beam splitter, BS, no matter how the frequency of the incident laser light changes with time, the frequency difference of the two beams reflected back from M1 and M2 are always zero, then the fringes will always be static. If M1 and M2 are positioned at different distances away from the BS (strictly, non-equal-length-legs configuration is not a setup in the classic MI, but hereafter it is still referred as MI for the sake of convenience), there exists a path length difference between two beams after they recombine. In case the object reflecting the laser light moves with a constant velocity, then, again, $\Delta\nu = 0$ though the incident laser light contains Doppler shift effects according to equation (3.2), the interferometry fringes are static. However, if the moving object is experiencing an acceleration or deceleration, the Doppler shift or the frequency change of the incident light of MI is a function of time. Due to the path length difference between the two legs of the MI, the light travelling in the longer leg takes more time to return to the BS, i.e., there exists a delay for the light traveling the long leg. In this case, $\Delta\nu \neq 0$, according to equation (3.6), we can observe the fringes moving with time. Therefore, in order for the velocity interferometer to be effective, the Doppler shift of incident light is a necessary condition, while the path length difference between two legs is a sufficient condition.

The delay leg is defined as the one with mirror M2, which is geometrically longer, then the other leg is known as the reference leg. Assume Δx is the length difference between the two legs, then, the delay time for the light to transverse the delay leg with respect to the reference leg is

$$\tau = \frac{2}{c}\Delta x \,. \tag{3.8}$$

Here the refraction index difference between the vacuum and the air is neglected. When the two beams recombine at some time instance, t, the frequency difference of the two light beams is $\Delta\nu = \nu_1'(t) - \nu_2'(t-\tau)$. Therefore, provided the moving object is experiencing a velocity change

(either acceleration or deceleration), one can always observe the change of the pattern of interferometry fringes with time at a fixed point in space.

For constant λ, if the path length difference satisfies the condition, $N\lambda = 2\Delta x$, where N is an integer, the delayed beam will arrive at BS with the same phase angle as that of the reference beam, thus the interferometry fringe pattern will be the same as that in the case where there is no path length difference between the two legs and thus reinforces the light at the observing point (bright fringe). If the length of the delay leg is held constant, i.e., Δx is fixed, but λ is changed slightly so that N increases (or decreases) by ½, the two beams arriving at BS are out of phase, and no light can be detected (extinction resulting in a dark fringe). By extension of this reasoning, one can conclude that if the delay is constant and the wavelength of reflected laser light is continuously changing due to the motion of the specimen under shock wave loading, the change of N will be continuous, then the light intensity detected will also vary continuously from bright to dark or vice versa, and as a result, the VISAR signals recorded on the oscilloscope will vary sinusoidally.

The length of the delay leg can be written in terms of the wavelength as follows:

$$N\lambda = c\tau . \tag{3.9}$$

Differentiating equation (3.9) results in

$$\Delta N(t) = -\frac{N}{\lambda}\Delta\lambda(t) = -\frac{c\tau}{\lambda^2}\Delta\lambda(t) . \tag{3.10}$$

Substituting for $\Delta\lambda$ in equation (3.9) from equation (3.4), and solving for the free (or internal) surface velocity,

$$u(t) = (\frac{\lambda}{2\tau})\Delta N(t) . \tag{3.11}$$

When a window is used behind the rear surface of the specimen to protect the reflecting surface from being damaged by the interaction between the arriving shock wave and the reflected release wave at the free surface, a correction for the refraction index of the window material is

necessary since its refraction index changes as a stress wave passes through it (see references [3,11,12] for details). Thus, the relation between the fringe count *F(t)* and the specimen velocity $u(t-\tau/2)$ can be written as

$$u(t-\tau/2)=\frac{\lambda F(t)}{2\tau(1+\delta)}, \tag{3.12}$$

where the velocity time instance is shifted by $\tau/2$ to be consistent with impact time; $\Delta N(t)$ has been replaced by *F(t)* since one can always choose the instance of the arrival of the shock wave at the surface as a reference for the starting point when the fringe starts to change; δ is an index-of-refraction correction factor for the window which is determined by experiment and equal to zero if no window is used in the experiment. Strictly speaking, λ in equation (3.12) should be the wavelength of laser light at time instance $(t-\tau/2)$, but, since the change in wavelength for the Doppler shifted laser light is very small ($\Delta\lambda/\lambda_0 \approx 10^{-6}$ for the particle velocity on the order of 1,000m/s), normally, the difference between the current $\lambda(t)$ and the original λ_0 is neglected.

3.2.2.2 Optical Principle of VISAR System

In both displacement interferometer[13] and velocity interferometer[12,14], a good mirror finish on the specimen surface is required so that spatial coherence of the laser beam can be maintained on reflection. Nevertheless, upon loading of a strong shock wave, the damage to the reflecting surface can not be avoided since the severe non-uniform deformation can always result in the generation of micro-jets on the shocked surface due to the interaction of defects in solids with a shock wave. The surface condition of a good mirror finish is hard, or even impossible, to be maintained in the whole process of shock compression. Therefore, in practice, a surface initially in good mirror finish may not remain a spectrally reflecting surface with the progress of shock

loading, thus the contrast of interferometry fringes will deteriorate, which will eventually make the shock velocity measurement ineffective.

Since the MI is not sensitive to the spatial incoherence of light, there is no problem for MI to give very good contrast fringes if the incident light is from a diffused reflecting surface, provided that the lengths of the two legs of the interferometer are nearly the same. But, as discussed in the last section, if the two legs of MI are of equal length, there is no time delay in one of the two legs, then, no fringe movement would be detected. If the lengths of the two legs are not strictly equal, there exists some difference. In principle, a good contrast fringe may still be generated, but the velocity resolution of the interferometer will be very low. If a long leg is used, high velocity resolution can be obtained, but fringe contrast may be lost.

Is there a way to obtain high velocity resolution without losing the fringe contrast? These seemingly contradictory requirements are met with a modification to the configuration of MI, the so-called wide-angle Michelson interferometer (WAMI)[3,15,16], shown in Fig. 3.6. The differences between the MI and the WAMI are the insertion of a piece of glass rod, the so-called etalon, between the mirror M2 and the splitter BS and the reposition of the mirror M2. M2 is placed so that its virtual image coincides with M1', the image of mirror M1 with respect to the beam splitter. In this way, when viewed by the detector, the apparent positions of the two mirrors are the same and the light beams from the two legs emerge collinearly; therefore, a good contrast of fringes can be obtained and at the same time the path lengths in the two legs are different, which satisfies the sufficient condition of the velocity interferometer. The optical principle of the WAMI and the detailed interpretation of VISAR system can be found elsewhere (see references 15, 16 and 3). Upon the insertion of the etalon (Fig. 3.6), the path length difference, half of the light path difference, of two legs is[16]

$$\Delta x = h(1 - \frac{1}{n}), \tag{3.13}$$

where h is the length of the etalon and n is the refractive index of the etalon. If the apparent position of mirror M2 is placed at the same distance from the beam splitter BS as mirror M1, then the spatial coherence of the light is not required, and very good fringe contrast can be obtained even with the light reflected from a diffuse surface. The light in the leg containing the etalon is delayed since it travels longer path. The time delayed in the delay leg is[16,3]

$$\tau = \frac{2h}{c}(n - \frac{1}{n}), \tag{3.14}$$

where c is the velocity of light in vacuum.

For a fixed set-up of VISAR system, the velocity-fringe equation (3.12) can be rewritten as

$$u(t - \tau/2) = CF(t), \tag{3.15}$$

where coefficient C is a constant, called the *fringe velocity constant*,

$$C = \frac{\lambda}{2\tau(1+\delta)(1+\alpha)}, \tag{3.16}$$

which is determined by the laser light wavelength, λ, delay time of light in the delay leg, τ, the correction due to the change of the refraction index of the window material with stress, δ, if window is used in the shock experiment, and a correction due to the wavelength dependence of the refraction index of the etalon material, α, if it is not negligible[17].

3.2.2.3 VISAR System

The arrangement of the VISAR diagnostic system is schematically shown in Fig. 3.7. The optical parts inside the dashed rectangle are part of the configuration of the WAMI (VISAR optical system). Through a laser-fiber coupler (8), the laser light from an Argon ion laser (9) (λ=514.5 nm) is coupled into an optical fiber of diameter 125 μm, which directs the laser light onto the mirror surface of the specimen. By an optical assembly called "optical fiber probe" (7), the reflected light is collected and coupled into an out-going fiber which has diameter of 300 μm.

The laser light from the out-going fiber, which contains the Doppler shift effect due to the motion of the surface under shock loading, is collimated through a collimator (1) before being directed into the VISAR Optical System to extract the interferometry information of particle velocity.

Mirror M3 guides the collimated laser beam into the VISAR optical system. In order to monitor any intensity change of the reflected laser beam resulting from self illumination due to shock compression, part of the light is sampled by a beam sampler S1 and directed through M4 to a photomultiplier tube (4), which converts the light signal into an electric signal to be recorded by the oscilloscope. The 50/50 beam splitter S2 evenly splits the light from the main beam into two; one is sent to mirror M1 of the interferometer which is 285.5 mm away from S2 in this setup, while the other passes through a 1/8 wave-plate (2), etalon (3) and then is returned by mirror M2, which is positioned at $285.5+\Delta x$ mm from S2 (Δx = 10.12, 32.32, 54.53, 76.73, 98.93, 121.14, 143.34, 165.55 mm, for etalon length of 0, 50, 100, 150, 200, 250, 300, 350 mm, respectively). The length of Δx is determined by the length of the etalon required to satisfy the apparent equal length of the two legs of the Wide Angle Michelson Interferometer. One half of the returned light from M1 passing through S2 is combined with the reflected part of the returned beam from M2 to form interference fringes. The interference fringes may be monitored through the bull's eye pattern after the laser beam exits from S2. S3 is a polarizing beam splitter separating the S and P components of the laser light, which have 90° phase angle difference due to the retardation of a 1/8 wave plate to the phase angle of the P component of the light. The S and P components of the interferometry fringes are separately directed into two photomultiplier tubes. The electrical signals from the photomultipliers are amplified by 1.2 GHz bandwidth amplifiers (5) before being sent to the 1 GHz 4 channel digital oscilloscope for recording.

All of the surfaces of the optical parts in the interferometer are flat to $\lambda/20$. Mirrors M1 and M2 are Stock Mirrors purchased from Newport Corporation. The 150 mm (6") diameter splitter S2 is a Broadband 50/50 dielectric beam splitter obtained from Newport Corporation. It is made of BK7 glass with a refractive index of 1.5205 at a wavelength of 514.5 nm. The thickness of S2

is 23.50 mm at the center. The reflecting surface is placed to face the incident laser beam from the collimator.

An etalon is actually a piece of glass rod or disc. The purpose for inserting the etalon into one of the legs of VISAR optic system is to delay the light in that leg while minimizing the difference of apparent path length in the two legs as much as possible. Therefore, glass with as large a refractive index possible is preferred. The glass used for the etalon in this system is SF11 glass, which is a product of Schott Glass Technologies, Inc. The etalon was specially ordered from Harold Johnson Optical Lab. According to the manufacturer of the etalon, the nominal refractive index of the SF11 glass is 1.7812. While, based on the index parameters of SF11 glass provided by Schott Glass Technologies, which was procured from Harold Johnson Optical Lab, the calculated value is 1.7988 at wavelength of 514.5 nm, which is exactly the value given in the catalog book of Melles Griot Company[24]. Therefore, the refractive index of SF11 glass used for calculating the fringe-velocity constant of this VISAR system was 1.7988. The diameter of the etalons used in the VISAR system is 30 mm. Totally, four pieces of etalons were ordered. One piece is 50 mm long along the axis, while the other three are 100 mm long. In order to eliminate fringe patterns and cavity feedback, a precise 30 arcmin wedge between optical faces was machined by tilting one surface 30 arcmin with respect to the other which is perpendicular to the axis of the glass rod.

The function of inserting a 1/8 wave plate into one of two legs of the interferometer is to retard the phase angle of the P component of the laser light by 90°. The 1/8 wave plate was from Valyn International. It is made of Quartz glass with a thickness of 3.556 mm (0.14 inch). According to the manufacturer, the refractive index is n_x=1.5473 along the x direction and n_y=1.5565 along the y direction at the wavelength of 525 nm. While the values are n_x=1.54787 and n_y=1.55711 at 514.5 nm. Barker suggested using the average of the two, so the refractive index used in the present calculation is 1.55249 at 514.5 nm, which is the average of the values given by Newport Corporation.

The laser used in this VISAR system is an Innova 304 water-cooled Argon ion laser, which is a product of Coherent Laser Group Company. The output power of this laser is 4.0 Watts on multiline visible mode, while the output is 1.7 W and 1.3 W at 514.5 nm and 488.0 nm single line mode, respectively. The beam diameter is 1.5 mm at the $1/e^2$ point. The divergence in full angle is 0.5 mrad. The beam pointing stability is less than 5.0 μrad[3]. The beam offset is less than 5.0 μm. For the long-term power stability, the maximum peak variation after a 15 minutes warm-up period is ± 0.5% in the operation mode of Light Regulation with PowerTrack, while it is ± 1.0% in the operation mode of Current Regulation with PowerTrack. The optical noise (rms) with PowerTrack operation mode is 0.2%. According to the manufacturer, the spatial coherence of the laser light (coherence length) is about 60 m. Normally, several hundred milliwatts output power is enough for a shock experiment.

Almost everything in the vacuum chamber will be damaged, or completely destroyed, during the shock compression experiments. The part of fibers inside the vacuum chamber are damaged during the experiment and can not be reused. Therefore, both the in-going fiber and the out-going fiber of the VISAR are split into two right before they enter the chamber. The portion of fibers outside the chamber can be repeatedly used, so it is called the permanent fiber, whose length is 15 m in this system; the other portion of the fibers extending inside the chamber are integrated with other optical parts to form a fiber optic probe, which directs laser light to the reflecting surface of specimen, collects the reflected light and then directs it out of the chamber. The connection between the fiber optic probe and the permanent fiber is through an optical coupler called the fiber optic splice board. Therefore, only the fiber optic probe needs to be replaced in each experiment.

The fiber optic probe assembly consists of an 1.5 m long ingoing fiber, a 1.5 m long outgoing fiber, a small lens for focusing the ingoing laser light onto the reflecting surface, a larger lens with a central hole (in which the small lens is incorporated) for collecting the reflected light from the reflecting surface and a holder for these parts. The probe should be mounted 30 mm away

from the reflecting surface if no window is used. In case a transparent window is used behind the reflecting surface, the distance from the probe to the reflecting surface should be approximately 30 + (1-1/n)*h* mm, where *h* is the window thickness in millimeter and the *n* is its index of refraction.

The photomultipliers used in this VISAR system are low-noise POD-4 Photomultiplier Units (PMU) produced by Valyn International Company. This PMU has a typical rise time of 1.0 ns. The photocathode response at 532 nm is 34 mA/W, and the maximum average anode current is 700 μA. The maximum required voltage and current of the power supply is 1,000 V DC and 10 mA, respectively. The electrical signal from the photomultiplier is amplified first, before being sent to the oscilloscope. The differential amplifier has a gain of 10 and bandwidth of 1.2 GHz to DC signal. The differential amplifier is powered by a ± 15 V DC power supplier. The input signal to the amplifier should be no more than 30 mV; otherwise, it may be damaged or ruined due to overload.

The laser-fiber coupler, fiber optic splice board, fiber optic probe and collimator are all the products of Valyn International Company. For the details on the function, configuration and use of these parts, one should refer to the corresponding product literature.

The oscilloscopes used to record the VISAR signals are a Tektronix TDS7104 digital phosphor oscilloscope with a bandwidth of 1 GHz, sampling rate up to 10 GS/s and recording length up to 2 Mb, or a Tektronix TDS3054 digital oscilloscope with a bandwidth of 500 MHz, maximum sampling rate on single channel mode of up to 5.0 GS/s and maximum record length of 10 K points.

3.2.2.4 Data Deduction of VISAR Signals

Fringe-Velocity Constant

For the current setup of the VISAR system, the Argon laser used is in continuous and single line mode with the wavelength $\lambda_0 = 514.5$ nm. The various combinations of the four pieces of optical SF11 glass rods, one 50 mm and three 100 mm long, makes up eight different lengths of etalons in the delay leg of the WAMI. Besides the glass rod etalon itself, any optical part in the delay leg, which has different refraction index from air and causes the delay of light, should be considered to be part of the etalon. Therefore, the 1/8 wave plate and the big splitter S2 are all treated as part of the etalon. For the 1/8 wave plate, the laser light is incident and transmitted through it in the direction of its surface normal, and the path length of light is determined by its thickness and the refraction index. While for the beam splitter the light is incident in the direction of 45° angle with respect to its surface normal, the path length of light is determined by the geometry, $h' = h/(1-(\sin 45^o / n)^2)^{1/2}$, where h and n are thickness and refraction index of the splitter, respectively. The length of the reference leg is nominally 285.5 mm. The length difference between the reference leg and the delay leg, the delay time of light in the longer leg and the fringe-velocity constants of the VISAR system for the different lengths of etalons are calculated using equations (3.13), (3.14) and (3.16) and listed in Table 3.1. The fringe-velocity constants given in Table 3.1 are obtained regardless of the corrections due to the change of the refractive index of the window, if it is used and the wavelength dependence of the refractive index of the etalon material, i.e., taking α=0 and δ=0 in equation (3.16). If in practice, for the given loading conditions, those effects are not negligible, then the corresponding corrections have to be made[12, 17].

Data Deduction of VISAR Signals

It is fairly straightforward to deduce the shock velocity particle history from the recorded VISAR signals. The VISAR signals are sinusoidal-like oscillating curves as a function of time. Two signals that are 90° out of phase can be obtained for each experiment; if one is sine, the other must be cosine. Fig. 3.8 shows typical VISAR signals recorded during an experiment of shock compression of solids. The sine and cosine curves, if necessary, are smoothed, then their amplitudes are scaled to be the same, and the tangent curve of the signal is determined by dividing the sine curve by the cosine. Finally, the fringe number is calculated as a function of time through the value of the tangent. By using the VISAR fringe velocity formula, equation (3.15), the shock particle velocity time history is obtained, which is also shown in Fig. 3.8. For the peak particle velocity of 100 m/s to 500 m/s, the measurement accuracy of this system should be better than 2%.

3.2.3 Stress Gages: Piezoresistive Manganin

Many materials have the property that their resistivity changes as a function of pressure, P, and temperature, T[1,8,17]. Generally, the resistivity is a decreasing function of pressure and increases with temperature, i.e.,

$$\rho = \rho_0(1 - \kappa P + \alpha T), \tag{3.17}$$

where ρ and ρ_0 are the current resistivity and the resistivity at room temperature and atmospheric pressure, and κ and α are the stress coefficient and the thermal expansion coefficient, respectively.

Manganin, a copper/manganese/nickel alloy (e.g., Cu-84/Mn-12/Ni-4), is a unique piezoresistive material. The change of its resistance is not sensitive to temperature, but increases with pressure. Therefore, its resistivity may be expressed as[18]

$$\rho = \rho_0(1+\kappa P). \tag{3.18}$$

Let l and A be the length and the cross-sectional area of a manganin wire, its resistance R is determined by resistance law,

$$R = \frac{\rho l}{A}. \tag{3.19}$$

Under the condition of one-dimensional plane strain shock wave loading, the change in the length of the shocked wire can be neglected; therefore, besides the change in the resistivity, there is change in its cross-sectional area. Hence,

$$\frac{A}{A_0} = \frac{V}{V_0}, \tag{3.20}$$

where V, V_0 and A_0 are the current volume of the shocked wire, initial volume and initial cross-sectional area of the wire.

Using equations (3.19) and (3.20),

$$\frac{\rho}{\rho_0} = \frac{RV}{R_0V_0} = \frac{V}{V_0}(1+\frac{\Delta R}{R}), \tag{3.21}$$

where $\Delta R = R - R_0$ is the change in resistance of the shocked wire. Combining equations (3.18) and (3.19),

$$\frac{\Delta R}{R} = \frac{(1+\kappa P)V}{V_0} - 1. \tag{3.22}$$

According to the shock Hugoniot curve of manganin, the ratio of volume of the shocked state to its initial volume is also just a function of stress (or pressure); therefore,

$$\frac{\Delta R}{R} = K(\sigma)\sigma. \tag{3.23}$$

In general, besides depending on stress[19], K is dependent on the composition of the material[6], and the gage shape, i.e., foil or wire[6,20]. Experimental results show that the manganin gage is useful up to 100 GPa and is the most widely used piezoresistive gage at high stresses (or pressure)[21], and the relation between the resistance change and stress can be approximated by a

linear function for the shock pressure higher than several GPa, say 4 or 5 GPa. At lower stress ranges a polynomial relation is more accurate. Fig. 3.9 shows the calibration curves of manganin gages used in this experimental study of the shock wave propagation in the heterogeneous composites, which is a product of Dynasen, Inc.

A power supply is needed to convert the resistance change signal from the manganin gage into an electric signal. This is analogous to the power supply used in a strain gage circuit (Wheatstone bridge). The difference is that a constant voltage power supply is used for the strain gage, while for the stress gage a pulse power supply is used since a very large current is needed to obtain a signal with high enough amplitude. The pulse supply used is Dynasen's Piezoresistive Pulse Power Supply Model CK2-50/0.05-300. It is a self-contained pulse bridge arrangement and can be used for the excitation of both 50 Ω and 0.050 Ω stress gages. It can provide a constant voltage from 30 V to 300 V with the pulse length adjustable from 5 μs to 1500 μs. The detailed specification, operation and data deduction of the pulse power supply can be found elsewhere[22].

3.3 References

1. Barker, L.M., Shahinpoor, M., and Chhabildas, L.C. Experimental and diagnostic techniques, in *High-Pressure Shock Compression of Solids*, edited by Asay, J.R. and Shahinpoor, M., Springer-Verlag, New York, p43 (1993).
2. Meyers, M.A. *Dynamic Behavior of Materials*, John Wiley & Sons, Inc., New York (1994).
3. Barker, L.M. and Hollenbach, R.E. Laser interferometer for measuring high velocities of any reflecting surface, *J. Appl. Phys.* **43**, 4699 (1972).
4. Fowles, G.R. Experimental technique and instrumentation, in *Dynamic Response of Materials to Intense Impulsive Loading*, edited by Chou, P.C. and Hopkins, A.K., Wright-Patterson AFB, Ohio, p405 (1973).
5. Grady, D.E. Processes occurring in shock wave compression of rocks and minerals, in *High Pressure Research Applications in Geophysics*, edited by Manghnani, M.H. and Akimoto, S., Academic, New York, p389 (1977).
6. Graham, R.A. and Asay, J.R. *High Temperature-High Pressures* **10**, 355 (1978).
7. Cagnoux, J., Chartagnac, P., Hereil, P., and Perez, M., *Ann. Phys.* **12**, 451 (1987).
8. Chhabildas, L.C. Survey of diagnostic tools used in hypervelocity impact studies, *Int. J. Impact Engng.* **5**, 205 (1987).
9. Graham, R.A. *Solids under High-Pressure Shock Compression--Mechanics, Physics, and Chemistry*, Springer-Verlag, New York (1993).
10. Cloud, G.L. *Optical Methods of Engineering Analysis*, Cambridge University Press, Cambridge (1998).
11. Barker, L.M. in *Behavior of Dense Media Under High Dynamic Pressures*, Gordon and Breach, New York, p483 (1968).
12. Barker, L.M. and Hollenbach, R.E *J. Appl. Phys.* **41**, 4208 (1970).

13. Barker, L.M. and Hollenbach, R.E. Interferometer technique for measuring the dynamic mechanical properties of materials, *Rev. Sci. Inst.* **36**, 1617 (1965).

14. Barker, L.M. Fine structure of compressive and release wave shapes in aluminum measured by the velocity interferometer technique, in *Behavior of Dense Media Under High Dynamic Pressure*, Gordon and Breach, New York, p483 (1968).

15. Hilliard, R.L. and Shepherd, G.G. Wide-Angle Michelson Interferometer for measuring Doppler line widths, *J. Opt. Soc. Amer.* **56**, 362 (1966).

16. Zwick, H.H. and Shepherd, G.G. Defocusing a Wide-Angle Michelson Interferometer, *Appl. Optics* **10**, 2569 (1971).

17. Chhabildas, L.C. and Graham, R.A. Development in measurement techniques for shock-loaded solids, in *Techniques and Theory of Stress Measurements for Shock Wave Applications*, edited by Stout, R.R., Norwood, E.R., and Fourney, M.E., American Society of Mechanical Engineers, New York, AMD-**83**, p1 (1987).

18. Bernstein, D and Keough, D.D. Piezoresistivity of Manganin, *J. Appl. Phys.* **35**, 1471 (1964).

19. Keough, D.D. and Wong, J.I. *J. Appl. Phys.* **41**, 3508 (1970).

20. Rosenberg, Z., Yaziv, D., and Partom,Y. *J. Appl. Phys.* **51**, 3702 (1980).

21. See references: 1, 8, and 17.

22. Instruction Manual, *Piezoresistive Pulse Power Supply Model CK2-50/0.05-300*, Dynasen, Inc. (2000)

23. Mutz, A.H. *Heterogeneous Shock Energy Deposition in Shock Wave Consolidation of Metal Powders*, Ph.D. Thesis, California Institute of Technology (1991).

24. Melles Groit Catalog (2001).

Table 3.1 The parameters of VISAR system

Item	material	*n*	*h(mm)*	*Δx(*mm)	*x*(mm)	τ (ns)	*C*(m/s)
1/8 wave plate	Quartz	1.5525	3.81	1.36			
Beam splitter	BK7 glass	1.5205	(h')25.60	8.76			
Etalon	**SF11 glass**	**1.7988**	**0.00**	**10.12**	**295.66**	**0.170**	**1508.9**
			50.00	**32.32**	**317.86**	**0.585**	**439.6**
			100.00	**54.53**	**340.07**	**0.999**	**257.3**
			150.00	**76.73**	**362.27**	**1.413**	**181.9**
			200.00	**98.93**	**384.47**	**1.827**	**140.6**
			250.00	**121.14**	**406.68**	**2.242**	**114.6**
			300.00	**143.34**	**428.89**	**2.656**	**96.8**
			350.00	**165.55**	**451.09**	**3.070**	**83.7**

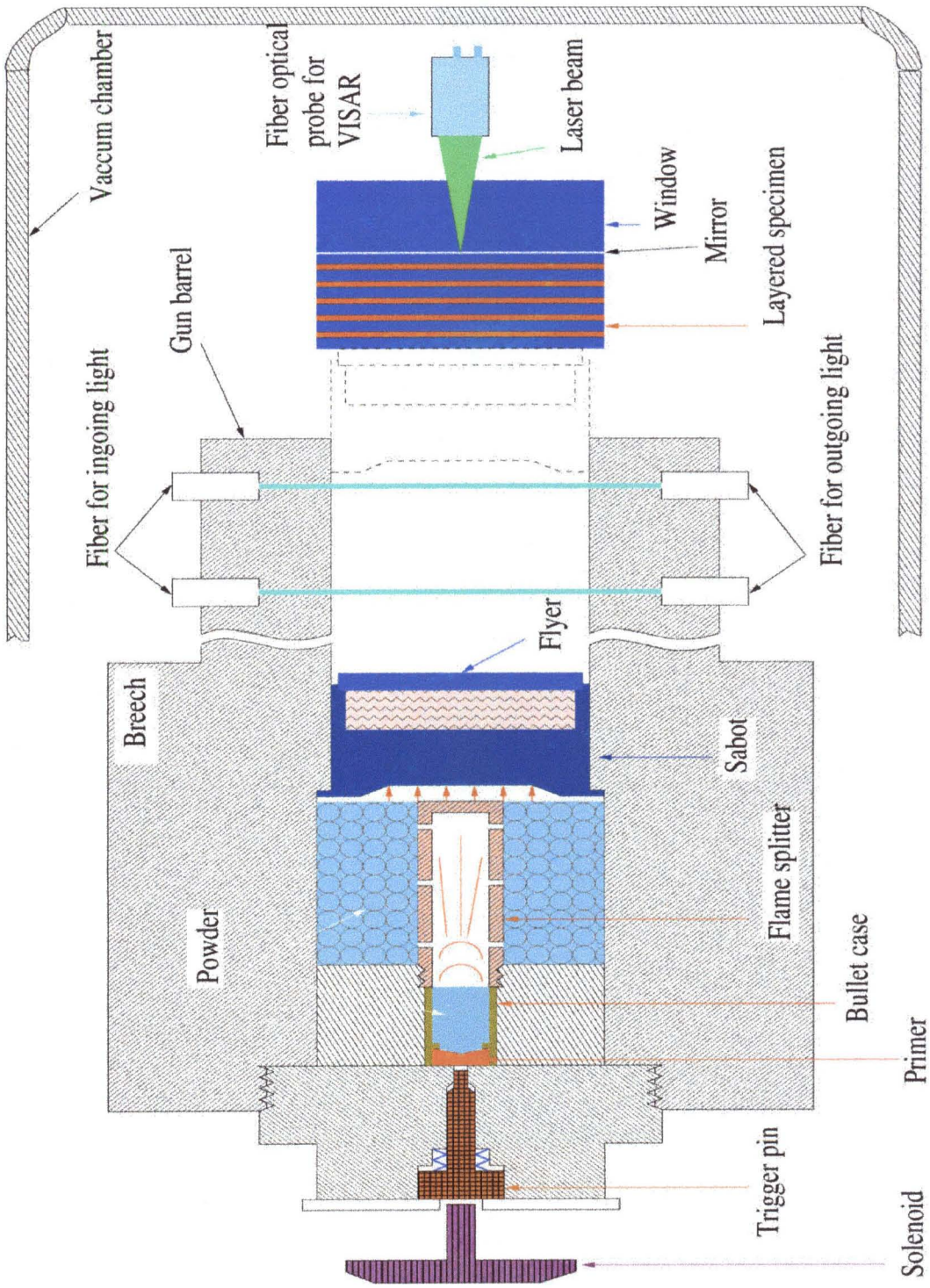

Figure 3.1 Powder gun system for shock wave compression experiment of solids.

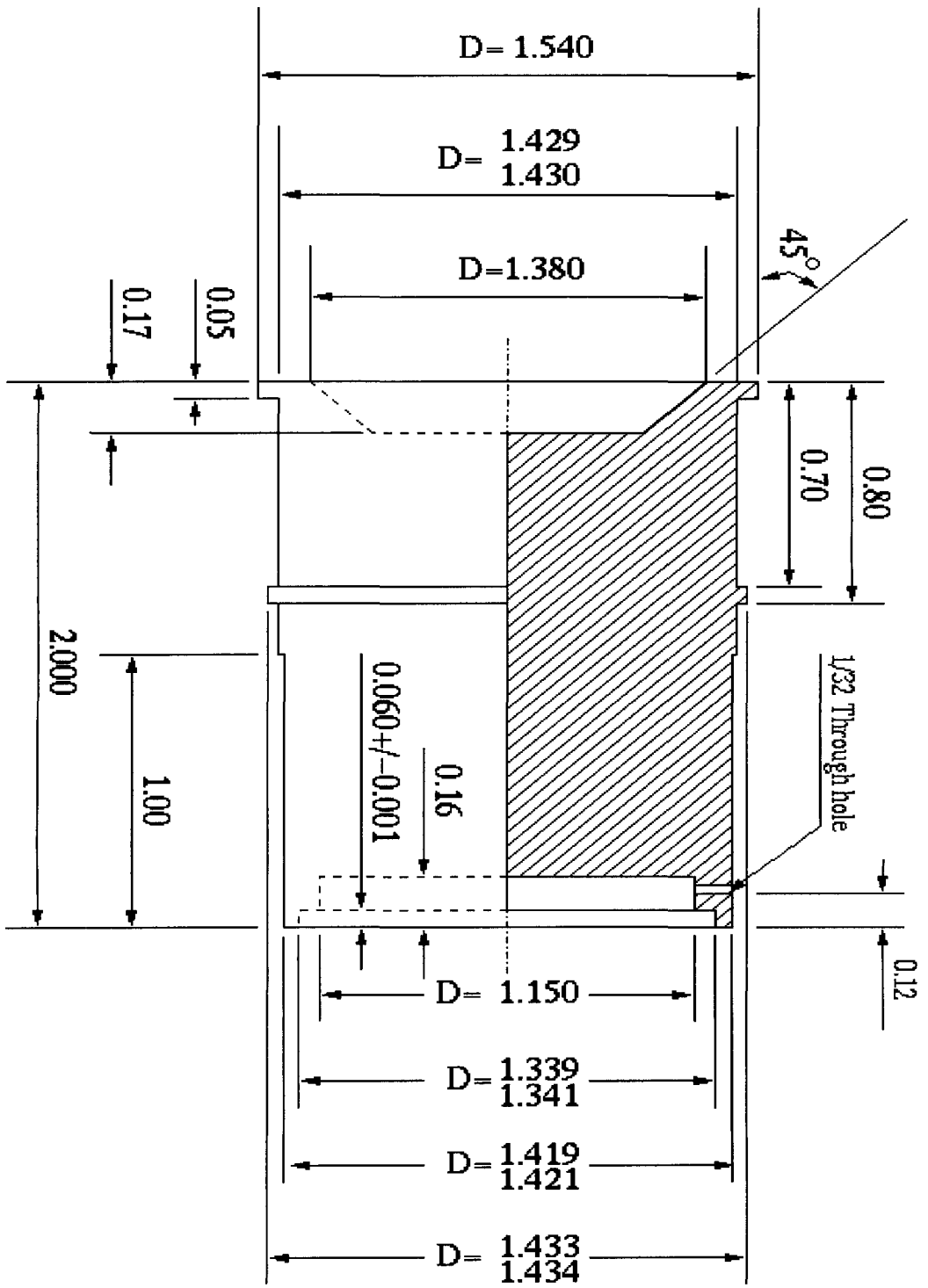

Figure 3.2 Dimensions of the sabot used to carry the flat flyer plate in shock wave compression experiment of solids.

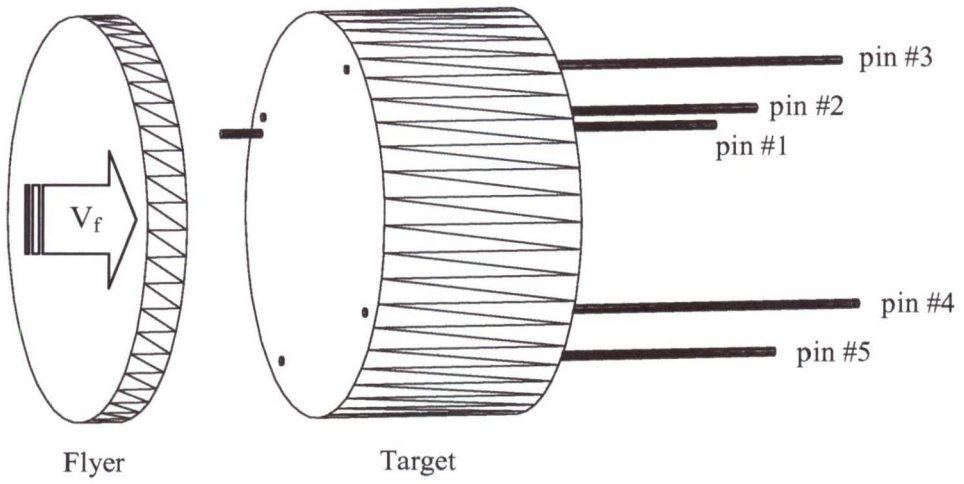

Figure 3.3 Arrangement of the electric shorting pins on the target.

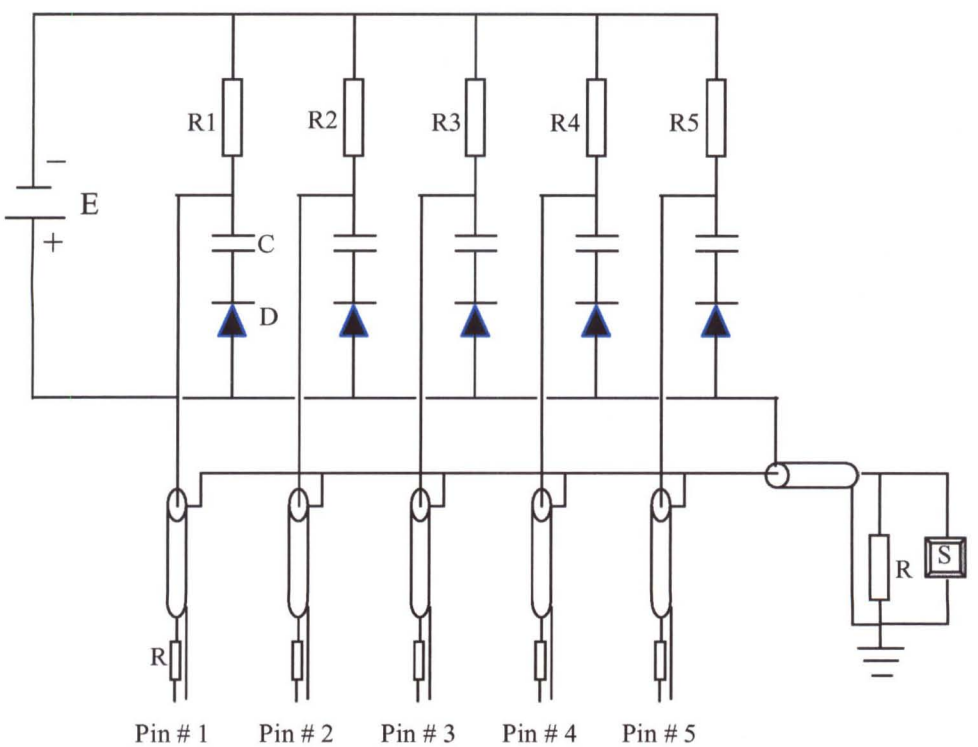

Figure 3.4 The schematic of the electric circuit for pin mixer. E is power supply, R, R_1, R_2, R_3, R_4 and R_5 are resistors, C is capacitor, D is diode and S is oscilloscope.

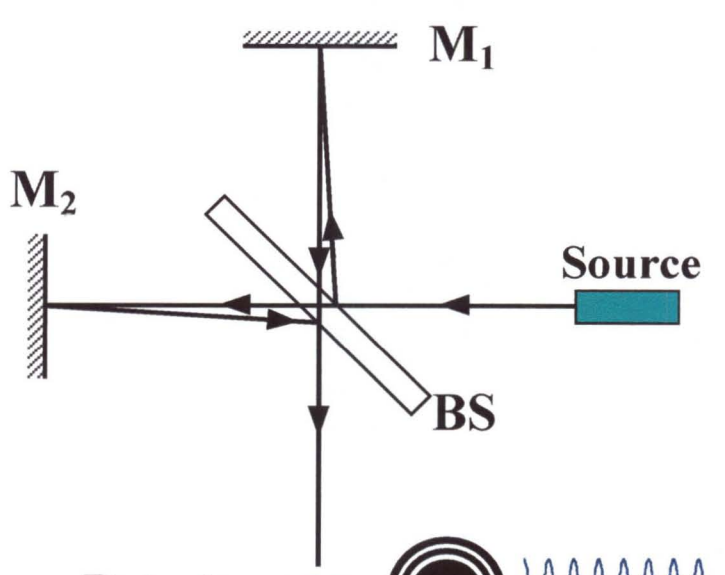

Figure 3.5 Schematic of Michelson Interferometer (MI). M_1 and M_2 are mirrors and BS is beam splitter.

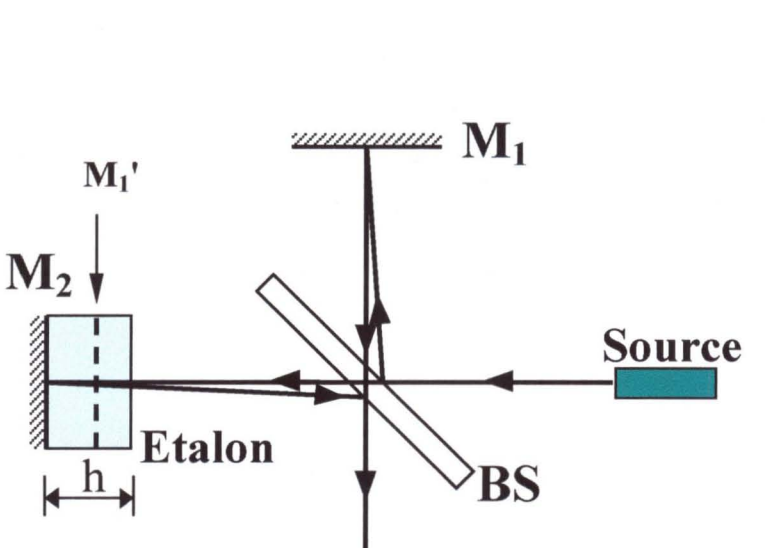

Figure 3.6 Schematic of Wide Angle Michelson Interferometer (WAMI). M_1 and M_2 are mirrors. BS is laser beam splitter, and M_1' is the image of M_1 with respect to the beam splitter.

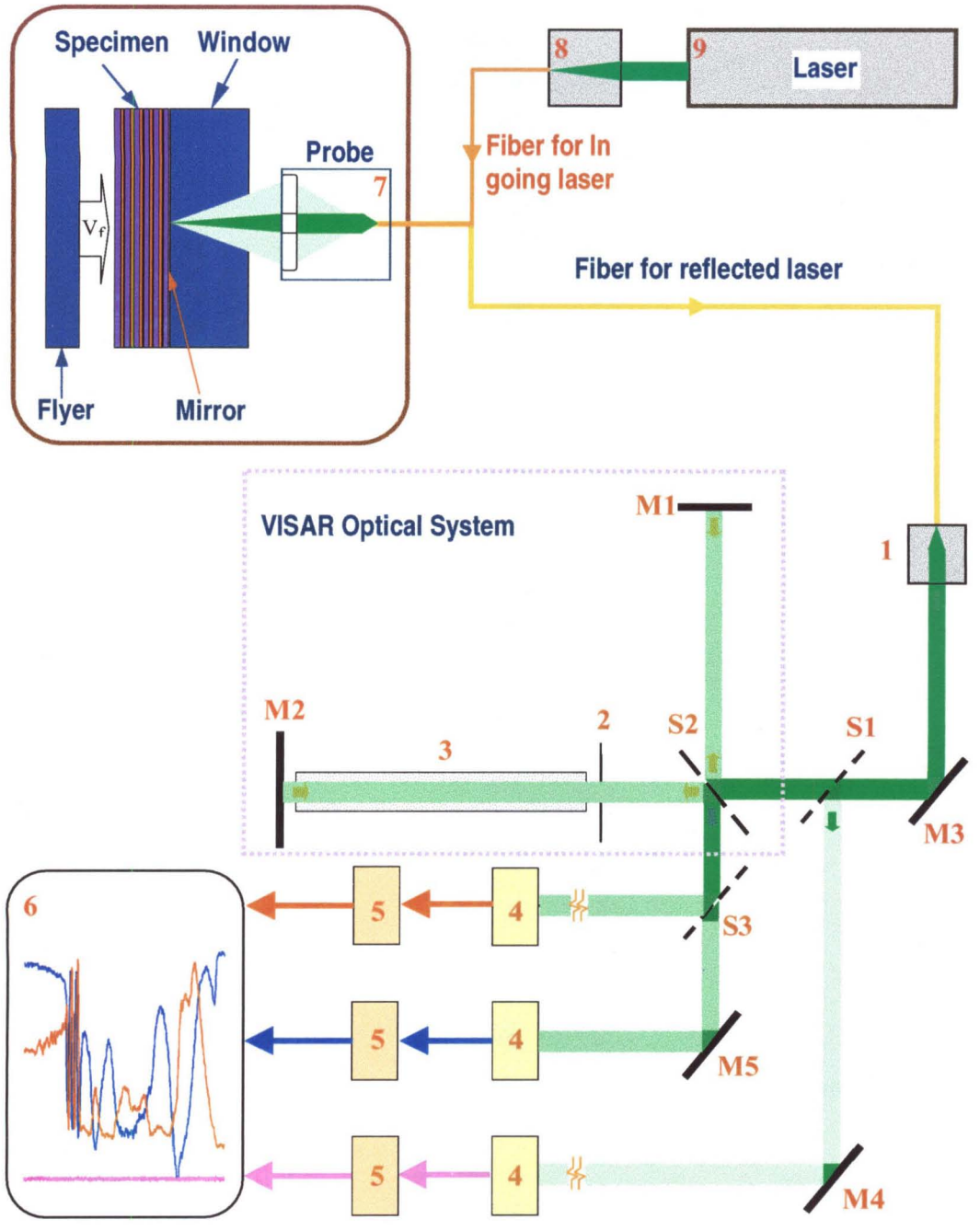

Figure 3.7 Schematic of VISAR diagnostic system.

1……..…....Collimator
2……1/8 wave plate
3…..……..Etalon
4……..…Photomultipliers
5…..……..…....Amplifiers
6..……..…..Oscilloscope
7……..Fiber optical probe
8……..Laser-fiber coupler
9…..……..Argon laser
M……..…...Mirrors
S……...Splitters

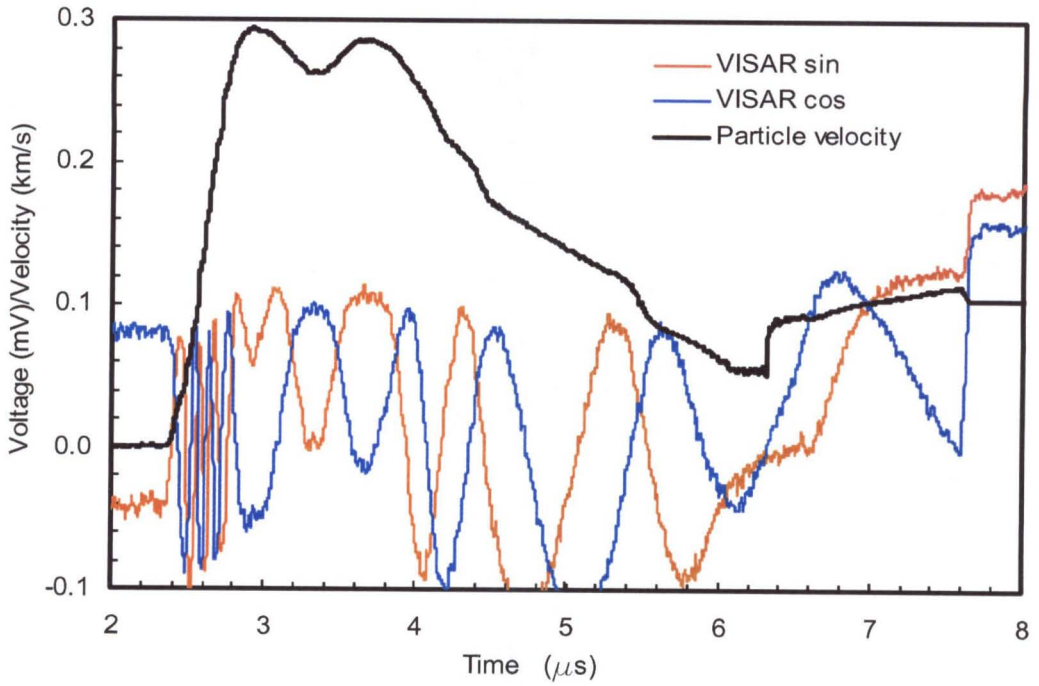

Figure 3.8 Typical VISAR signals and the deduced particle velocity profile of layered composites loaded by shock wave generated by planar impact. Here, the specimen is layered composite obtained by alternatively layering 5 pieces of 0.74mm polycarbonate and 0.37mm 6061 aluminum alloy; the velocity of polycarbonate flyer was 589m/s.

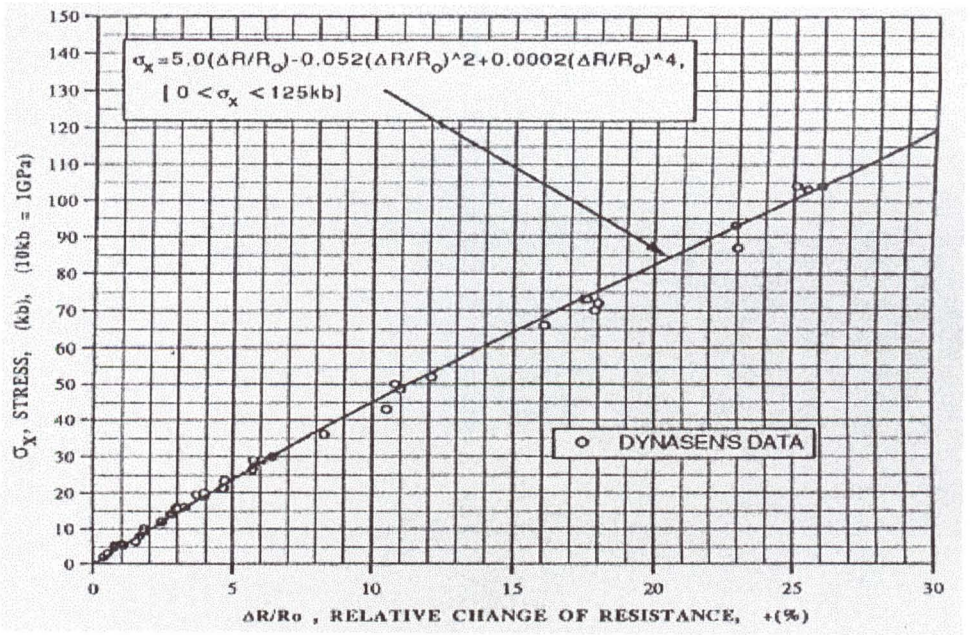

Figure 3.9 Calibration curve of the change in resistance as a function of shock stress for manganin (adapted from data sheet provided by Dynasen, Inc.).
(Provided by Dynasen, Inc.)

Chapter 4

Experiments on Shock Wave Propagation in Periodically Layered Composites

4.1 Specimen Configuration

The structure of a periodically layered composite specimen is shown in Fig. 4.1. It consists of two components in the form of thin disks that are alternatively stacked together. Hereafter, the component with larger mechanical impedance is called "hard" layer, while the other with lower mechanical impedance is called "soft" layer, and the combination of a soft layer and a hard layer will be referred to as a composite "unit" or a "unit cell." The layered composite specimen for the shock compression experiment is prepared by repeating the composite unit as many times as necessary to form a specimen with desired thickness. In this study, except when stated otherwise, the composite layers are ordered in such a way that the first layer is always soft layer in a unit cell, i.e., the soft layer will be the first to experience the planar impact loading. There is no special physical or mechanical consideration as to why the soft layer should be placed first, except that the specimens were consistently prepared this way. A buffer layer of the same material as the soft component of the specimen was used after the specimen. In order to prevent the free surface from serious damage due to unloading from shock wave reflection at the free surface, a window in contact with the buffer layer was used. The rear surface of the buffer layer or the front surface of the window was mirrorized to provide good reflectivity for VISAR optical measurements. The window behind the composite specimen thus insures a good reflectivity of the mirror surface during shock compression. The window is typically 12.7 mm (0.5") in

thickness and it is made of PMMA. The thickness of the buffer layer is typically 0.74 mm (0.03").

4.2 Materials

This investigation is not meant to be an exhaustive study of all possible homogeneous components of a typical composite system. Instead, attention is focused on understanding the role of different parameters that define heterogeneity (e.g., internal interfaces, impedance mismatch, length scale, etc.) of a composite on the evolution of a shock wave during its propagation in heterogeneous media. Therefore, the materials selected to form each individual layer of composites are those whose dynamic response to shock wave loading have been extensively studied and well described in the terms of their constitutive behavior. Four of these materials representing different types of dynamic mechanical response are used in this study to form layered heterogeneous composites of different properties in order to address various aspects of the influence of material heterogeneity on shock wave propagation in solids. The composite units used in the experiments consisted of a "soft" layer that was made of a polymeric material, polycarbonate (PC), and a "hard" layer that was made of one of the following materials: glass, stainless steel or aluminum. These materials provide a range of combinations of shock wave speeds, acoustic impedances and strength levels to develop a fundamental understanding of shock wave propagation through heterogeneous solids. The polymers serve as excellent model materials for matrices of composite solids of technological importance such as polymeric composites including continuously fiber-reinforced materials and have low shock wave speed, acoustic impedance and strength. The metallic materials (steel, aluminum) and glass serve as model materials for reinforcements (particle, fiber) of composite solids and have relatively high shock wave speed, acoustic impedance and strength.

Polycarbonate (PC) and polymethyl methacrylate (PMMA) are two representatives in the polymer family of viscoelastic materials. Both materials have many technological applications and have been extensively studied. Comparatively, PMMA is stronger, but much more brittle, and hence it is more difficult to manufacture it in the form of a very thin sheet. Initially, it was intended to use PMMA sheets as material for the soft layers of composites, but it is hard to obtain commercially available PMMA sheets with thickness less than 0.80 mm. Therefore, it was decided to use PC, instead of PMMA, as the soft layer of composites. The PC sheets used in this study were obtained from McMaster-Carr in two thicknesses, nominally, 0.37 mm (0.015") (shorted as PC37), and 0.74 mm (0.030") (PC74). The window material used was 12.7 mm (0.50") thick commercial PMMA plate.

Due to their excellent optical transparency and other special physical and mechanical properties, glass materials have been widely used in industry and scientific studies. The mechanical and shock response properties of glass have been studied thoroughly. For instance, according to the experimental studies conducted by Wackerle[1], Fraser[2], Barker [3], et al., fused silica glass behaves under dynamic compression as a nonlinear elastic solid up to its phase transformation at about 9.8 GPa. It has been found to be a very good window material for shock compression experiments. It has been determined that fused silica glass has the property of causing a shock front to become a ramp-wave front as a shock wave propagates through it. Therefore, it could be used as a ramp wave generator for studying the acceleration wave phenomena.

Two kinds of glass disk plates supplied by Erie Scientific Company were used in this study. One is 0.20 mm D-263 glass (GS20), and the other is 0.55 mm float glass (GS55). D-263 is a borosilicate glass, which is produced by melting the purest raw materials. Some of the relevant physical and mechanical properties of the two glasses are listed in Table 4.1.

For metal components that form the hard layer of the composite unit, 0.37 mm thick 6061-T6 aluminum sheet (Al37), 0.19 mm or 0.37 mm thick 304 stainless steel sheets (SS19 and SS37)

were used. The 6061-T6 aluminum alloy was a commercial grade material and the parameters listed in Table 4.1 were obtained from handbook[4]. The 304 stainless steel sheets are products of Allegheny Rodney Strip, the service center division of Allegheny Ludlum Corporation. The mechanical properties of all the five component materials of specimens and the PMMA window material are shown in Table 4.1.

4.3 Specimen Preparation

The as received piece of metal sheet was first cut into square plates of about 50 mm each side using sharp shear machine and several of these pieces were sandwiched between two thick (about 6.3 mm) aluminum plates. This sandwich was then clumped on a lathe and machined into 38.1 mm (1.50") diameter disks. In this way, the deformation or curvature of the disks could be well controlled and the flatness of disks can be satisfactorily guaranteed. The PC disks of 38.1 mm (1.5") diameter were machined in the same way from the as received sheets. As received PMMA plate of 12.7 mm thickness was machined into the window piece of 38.1 mm in diameter. Four holes of about 1 mm in diameter were drilled evenly on a circle of 30 mm diameter on the disks (except for the glass disks) in order to install electrical shorting pins used for triggering purpose.

In most applications of layered composites, especially where the tensile loading dominates the deformation processes of composites or structures, the main concern is the bonding strength between the layers. In order to achieve higher bonding strength of interface, it is customary to roughen the surfaces by sandblasting before they are bonded together.

The disk surfaces were not sandblasted during the preparation of specimens for shock compression experiments for the following two reasons: First, since the thickness of the disks is only in the range of 0.17 mm to 0.80 mm (0.008" to 0.030"), it very easy for such a thin disk to be deformed when they are subjected to the high speed impact sand particles used in sandblasting.

Even when the thin disk is backed with a flat plate on the other side, the blasted piece still could suffer permanent deformation. Second, in the present shock compression experiments, the compression response of composites is of primary interest, rather than the tensile deformation, which occurs much later when the shock wave is reflected back from the free surface or interface adjacent to a lower mechanical impedance medium. According to recent measurements[5], the strength of aluminum/PMMA (or steel/PMMA) interface is about 14-15 MPa if the surfaces were roughened by sandblasting, while the strength is 8-9 MPa if the surfaces were not sandblasted prior to bonding. Though roughening of mating surfaces helps increasing the tensile bonding strength, the surface finish between interfaces does not make much difference on wave propagation when compressive deformation is of primary concern. The important thing here is to bond the layers together avoiding an air gap between layers, which could affect the wave propagation significantly. Therefore, except for the first several specimens, the specimens used in this study were prepared by directly bonding layers together in the as received condition without any roughening treatment. The procedure of preparing a composite specimen is described next.

The machined disks were first washed with detergent and rinsed with tap water to remove the dirt and any oily residues. Then, the disks were put into a container of tap water and placed in an ultrasonic cleaner for 15 minutes. Next, they were ultrasonically cleaned with distilled water for 15 minutes. Finally, the metal and polymer disks were ultrasonically cleaned for 15 minutes in acetone and alcohol, respectively. Then, they were dried using compressed air or air duster. The surfaces of the PMMA window were cleaned with isopropyl alcohol and dried with compressed air. One of the window surfaces was aluminized to a mirror surface by sputtering aluminum in a vacuum chamber.

The cleaned disks were bonded together using epoxy adhesive to form periodically layered composite specimens. The epoxy adhesive used was Hysol 0151, clear two-component epoxy, manufactured by Dexter Corporation. The epoxy has 60 minutes pot-life and complete cure time

of three days at room temperature. The tensile lap shear strength of this epoxy, tested on etched aluminum per ASTM D 1002, is about 13 MPa after 3 days of cure at room temperature. The shock impedance of this adhesive is very similar to that of Polycarbonate (PC).

The bonding of polymer and metal/glass disks with epoxy was made in a specially designed and manufactured jig to maintain planarity. The procedure is as follows: First, one or two drops of the mixed epoxy are applied at the center of the first soft disk which is placed on a hard, optically flat metal plate at the bottom of the jig. Then a hard disk is placed on top with the four pin holes aligned with those of the soft disk, forming a unit of the composite specimen. This process is repeated as many times as necessary to form a specimen with the desired thickness. The composite specimen is then topped with a 0.74 mm buffer disk, which is made of the same polymeric material as that of the soft layer component. After the buffer layer a PMMA window was glued on the buffer with the mirror surface facing the buffer. Finally, four electrical shorting pins are carefully inserted into the holes making sure that the end of the pin is flush mounted with the impact surface of the specimen. In order to uniformly spread the epoxy and reduce the thickness of the glue layer as much as possible, a weight was placed on the assembled specimen to produce a stress of 50 MPa in the specimen. The applied stress guaranteed the composite specimen thus prepared has a very good planarity. The average thickness of the epoxy layer bond is about 20 μm. For the PC/Glass composites, the bonding layer can be as thin as 10 μm. In order to obtain a well-bonded specimen it is important to keep the environment clean during the whole process of preparing the specimens. Ideally, this specimen preparation should be performed in a clean room.

4.4 Experiments

The detail of the powder gun loading system, the arrival time detector, the VISAR system and the stress gage have been described in Chapter 3. For completeness, a brief introduction of the experimental system will be given first, followed by an outline of experiments to be conducted on the layered composites.

The experiments of shock compression of layered composites were conducted using a powder gun system located in the experimental Solid Mechanics facilities, Graduate Aeronautical Laboratories at Caltech (GALCIT). The bore of the gun is 36 mm, and flyer velocity achieved by this gun ranges from 400 m/s to about 2000 m/s. The flyer velocity is measured within 1% uncertainty by using a light interruption fiber optic system. More detailed information on the powder gun system is available elsewhere[27]. The tilt of the flyer with respect to the specimen during impact is measured by a method called "projectile's shorting of charged electrical probes" (or pins). Since most flyers used in this experiment were polymeric materials, it is not reliable, especially at relatively low impact velocities, to short the pins directly by the flyer plate upon its impacting the face of the target, i.e., composite specimen. Therefore, instead of using ionization type pins, self-shorting electric pins were flush mounted on the impacted surface of the specimen, so that the arrival times of flyer at four positions where pins are installed can be accurately detected. Upon impact and due to shock compression, the pin is shortened, which causes the circuit in a "Pin Mixer" to close and generate an electric signal recorded by an oscilloscope. Four pins provide arrival (or impacting) time of shock wave at four positions on the impacted surface, by which the tilt of the flyer with respect to the specimen can be deduced. The average tilt divided by the impact velocity in this study was generally much less than 0.005 rad/mm/μs.

The particle velocity history on the interface between the window and the buffer layer (Fig. 4.2) was measured by the so called VISAR system[6]. As shock wave propagates in the layered

composites, due to the multiple reflections from internal interfaces, it is expected that the resonant oscillation wavelets will appear in the shock pulse. In order to understand the process of how the shock wave energy is transported, dissipated or dispersed, and evaluate the role of interface in shock compression process, it is of paramount importance to capture the fine details of shock velocity profile, to the extent possible. To meet this need, a VISAR system with very high velocity resolution was constructed. The velocity fringe constant of this VISAR system is adjustable from 85 m/s/fringe up to 1,500 m/s/fringe (for the details, see Chapter 3). The interferometer fringes from VISAR are sensed by fast response photomultipliers with bandwidth of 1 GHz. The electric signals from photomultipliers were amplified through amplifiers with a bandwidth of 1.2 GHz and gain of 10 and then recorded using an oscilloscope. The oscilloscope used is a Tektronix TDS 7104 digital phosphor oscilloscope with bandwidth of 1GHz, sampling rate up to 10 GS/s and recording length up to 2 Mb.

Typical VISAR signals recorded by the oscilloscope for a shock compression experiment on a layered composite are shown in Fig. 4.2. The two sinusoidal signals with phase angle difference of 90° are from the VISAR for the same experiment, which makes it easy to deduce whether the observed interface is experiencing acceleration or deceleration. Based on the measured VISAR fringe signals, the particle velocity history of an element on the buffer/window interface can be reduced through the VISAR velocity-fringe formula. Let *F(t)* be the fringe count as a function of time *t*, then the normal particle velocity $u(t-\tau/2)$ can be calculated by

$$u(t-\tau/2)=(\frac{\lambda}{2\tau})\frac{F(t)}{(1+\Delta\upsilon/\upsilon_0)}, \tag{4.1}$$

where λ is the wavelength of the laser light, τ is the delay time of light making a round trip in the delay leg of the VISAR, and $\Delta\upsilon/\upsilon_0$ is an experimentally determined function which accounts for the change of index of refraction of the window material due to the compression of shock wave when it propagates in the window. The laser used in this VISAR system is an Argon laser with a wavelength λ=514.5 nm. The length of etalon, the glass rod added into the delay leg

of VISAR, is adjustable, which results in the delay time, τ, of the delay leg ranging from 0.577 to 3.016 ns. The corresponding velocity fringe constant ranges from 85.3 m/s/fringe to 1500 m/s/fringe. For most experiments in this study the velocity fringe constant was set at 85.3 m/s/fringe.

For the PMMA window, according to experimental results from Barker[3], the refraction index parameter $\Delta\upsilon/\upsilon_0$ decreases at first, reaching its minimum value of -0.0117 for particle velocity of around 300 m/s, and then increases; and for the particle velocity of about 550 m/s, the correction is zero. For the maximum particle velocity of about 800 m/s in the experiments, it is estimated that index refraction correction, $\Delta\upsilon/\upsilon_0$, is about 0.01. Therefore, the maximum velocity correction due to the change of the refraction index of the window material (PMMA) will be at most 1%. The correction due to the wavelength dependence of the refraction index of the etalon material, α, in equation (3.16), is ignored since the refraction index of etalon used to calculate the delay time is the value at the wavelength of 514.5 nm.

The typical particle velocity profile of shock pulse reduced from the measured VISAR signals is also shown in Fig. 4.2, which is the shock compression experimental results on a layered composite specimen with 5 units of PC37 (0.37 mm thick polycarbonate)/SS19 (0.19 mm thick 304 stainless steel) impacted by a 2.78 mm PC flyer at a velocity of 548 m/s. The resonant oscillations induced by the multiple reflection at interfaces to the shock wave is clearly observed, which is made possible by the high velocity resolution (low velocity fringe constant) of the VISAR system.

In order to extract as much information as possible during experiments, besides the measurements of particle velocity profiles by the VISAR system, manganin gages were also embedded between layers of some specimens to measure the stress history at selected internal points as shown in Fig. 4.1. Since the shock stress level in experiments is expected to be in the range of 1 to 10 GPa, manganin gages with a resistance of 50 Ohms were used. Some of the

gages were produced by Dynasen, Inc., and others by Micro Measurements (MM) Group. The pulse power supply for the manganin gages is model CK2-50/0.050-300 from Dynasen, Inc., which can provide power pulses up to several milliseconds in duration and voltages up to 300 V. The signals from the manganin gages were recorded using a Tektronix TDS3054 digital phosphor oscilloscope with bandwidth of 500 MHz, sampling rate up to 5 GS/s and recording length of 10 kb.

In order to investigate the attenuation and dispersion of shock waves in periodic layered heterogeneous solids as well as the length scales associated with the heterogeneity and material properties, various specimen configurations were chosen. In particular, three types of specimens with five different thicknesses were prepared following the procedure described in the previous section. The first type is a periodically layered polycarbonate (PC)/6061-T6 aluminum alloy (Al) composite. The thickness of PC and Al are 0.74 mm and 0.37 mm, respectively, and the composite of this type is referred to as PC74/Al37. For the sake of convenience, the two numbers following the abbreviation of the material name of a composite component are the individual layer thickness in hundredths of a millimeter. For instance, 0.74 mm polycarbonate layer is abbreviated as PC74. The second type of composite is formed by Polycarbonate (PC) and 304 stainless steel (SS). Two thicknesses of each component were used, forming two kinds of structures of this type, PC74/SS37 and PC37/SS19. The third type composite is made of polycarbonate (PC) and glass (GS) layers. Again, specimens with two different thickness combinations were prepared, PC74/GS55 and PC37/GS20. The different specimen thickness and the corresponding loading conditions for the three types of composites are summarized in Table 4.2. Note that the specimen thickness shown in the table is the total thickness of the composite and the 0.74 mm buffer. From now on, unless otherwise stated, the specimen thickness refers to the total thickness of the layered composite and the 0.74 mm thick buffer, and the flyer is always a PC plate of thickness 2.87 mm. The diameters of specimen and flyer are 38.1 mm (1.5") and 34 mm (1.335"), respectively.

4.5 Results

4.5.1 Influence of Loading on Shock Profile

The influence of shock loading on the dynamic response of composites was investigated by impacting specimens with flyers at different velocities. Fig. 4.3 shows the measured VISAR particle velocity profiles at the buffer/window interface of PC74/Al37, PC74/SS37, PC37/SS19, PC74/GS55 and PC37/GS20 composites. V_f and V_p in the legend of plots are the flyer velocity and shock particle velocity, respectively; h is specimen thickness and w is the flyer thickness. All flyers used in the experiments are 2.78 mm thick PC. For the purpose of comparison, the particle velocity V_p in the plots is normalized by a dimensional factor, $V_f/2$, one half of the flyer velocity of the corresponding experiment. Some composites were impacted at three different flyer velocities, while some were impacted only at two different flyer velocities. It was found out that when a flyer is accelerated to a velocity higher than about 1200 m/s, the sealing of the sabot to the high-pressure gas (powder explosion products) is not very good. The blow-off of high pressure gas before the flyer impacts on the specimen could lead to erroneous results. In other words, there exists a possibility that the specimen may be disturbed by the high pressure gas as it blows off from gun muzzle before the flyer impacts on the specimen, since the high pressure gas moves faster than the sabot if leakage happens. Operating the gun at lower flyer velocity is a way to avoid the possible disturbance from the blow-off of high pressure gas. Therefore, in order to achieve higher shock pressure while operating the gun at relatively low flyer velocities, the flyer was changed from 2.87 mm PC plate to 5.55 mm 6061-T6 aluminum alloy flyer plate which produces about the same shock pulse length as the former. The aluminum flyer at a velocity of about 1100 m/s generates the same pressure as a PC flyer at a velocity of about 1600 m/s.

For PC74/Al37, PC74/GS55 and PC37/GS20 composites, specimens with only one thickness were used. The nominal thicknesses (including buffer layer) of the three composites are 6.60

mm, 9.95 mm and 10.45 mm, respectively. The corresponding shock particle velocity profiles measured by VISAR at different flyer velocities for each of the composites are shown in (a), (g) and (h) of Fig. 4.3, respectively. For PC74/SS37 composite, specimens of two different thickness, nominally 6.45 mm and 9.90 mm, were impacted at flyer velocities of about 570 m/s and 1060 m/s, and the results are shown in (b) and (c) of Fig. 4.3, respectively. While for PC37/SS19 type composite, specimens with three different thicknesses, 3.77 mm, 7.00 mm and 10.40 mm, were impacted at flyer velocities of about 550 m/s, 1040 m/s and/or 1590 m/s. The corresponding measured VISAR particle velocity profiles are shown in (d), (e) and (f) of Fig. 4.3, respectively.

It can be observed that for all composites investigated in this work, a common feature of those shock velocity profiles is that the rise time of the shock front decreases with increasing flyer velocity, or in other words, the shock front steepens with the increase of shock loading strength. This indicates that the shock viscosity of the composites decreases with shock strength, which is similar to observations of shock wave propagation in homogeneous materials[7].

When a single phase homogeneous material is compressed by a shock wave, the particle velocity profile typically reaches a plateau following the initial jump, i.e., the shock front, indicating the attainment of equilibrium, and is later followed by release wave which decompresses the shocked high pressure state into a low pressure state. The length of shock pulse (the plateau) is determined by the boundary conditions (flyer thickness and velocity) of the shock loading. However, when a layered heterogeneous composite is compressed by a shock wave, due to the interaction of the multiple reflections between the hard and soft layers, a level plateau on the wave profile is generally not observable. Instead, oscillations superposed on the top of a nominal plateau is typically observed. The duration and magnitude of the oscillations depend on the geometrical length scale and the mechanical properties of each component layer, as well as the loading strength of the shock wave. It is noticed that for all kinds of composites studied here, the magnitude of oscillation of the shock profile, especially that of the first peak, increases as the

shock strength increases, while at the same time, the period of oscillation becomes shorter. Furthermore, the effect of multiple reflections of internal interfaces is not only affecting the shock compression process, but also affecting the unloading process, which can be easily observed from the shock velocity profile of decompression process in which release progresses by multiple step-like unloading.

The influence of multiple reflections of internal interfaces on shock wave propagation in the layered composites is more clearly illustrated by the shock stress time history profiles measured by manganin gages. The manganin gages are embedded between the soft and hard layers where the stress profiles are to be measured. Fig. 4.4 shows the comparison of shock stress profiles for PC74/SS37, PC37/SS19, PC74/GS55 and PC37/GS20 composites loaded by planar impact at different flyer velocities. The parameter x shown in the legend of the plots is the distance of the manganin gage from the impact surface of the specimen. Since manganin gages are very thin, only about 20-30 μm thick, they can be embedded anywhere inside the composite without seriously disturbing the propagation of the shock wave in the composite. The shock stress profile measured by the manganin gage is the actual shock compression process, while the particle velocity time history measured by VISAR at buffer/window interface includes the decompression effect of the release wave from the interface due to the impedance mismatch between composite and window (PMMA) materials. Comparing the stress profiles measured using manganin gages inside the composite (e.g., Fig. 4.4 (d)) with the particle velocity profiles measured by VISAR at the buffer/window interface (e.g., Fig. 4.3 (h)), it is evident that the magnitude of oscillation at the particle velocity profiles has been largely reduced due to the partial release at the buffer/window interface. Again, from the stress profiles in Fig. 4.4, it is observed that the shock profile is affected significantly by the shock loading strength, as well as the geometrical length scale and mechanical properties of each component layer, which will be discussed in more detail in the later sections.

One more thing worth noticing is that for a given loading strength the shock front rise time of a layered composite is much longer than that of either homogeneous component material of which the composite is made. For instance, according to Fig. 4.3, for particle velocity about 300 m/s, the rise time of the shock front in PC74/Al37 composite is about 0.80 μs, while at similar loading condition, the shock front rise time of 6061-T6 aluminum alloy, estimated based on the experimental results by Johnson and Barker[8], is about 20 to 30 ns if only the time of plastic wave front is considered. For PMMA, the major (initial) portion of shock front rises very rapidly and is followed by a slower compression process[3,9]. It appears reasonable to take the rise time in PMMA to be 0.3 μs at particle velocity of 300 m/s. Since the shock compression behavior of PC should not be too different from that of PMMA, it is reasonable to believe that the corresponding rise time in PC should not be longer than 0.4 μs. The much longer rise time of shock front observed in the composite indicates that the presence of the internal interfaces in heterogeneous materials enhances the dispersion effects, which affects the shock response of the composite in a way similar to the viscosity effects in viscoelastic materials.

4.5.2 Effects of Interface Impedance Mismatch

When a plane elastic wave propagating in a homogenous material meets an interface or boundary, it will be partially reflected and partially transmitted. The ratios of reflected wave and transmitted wave to the incident wave depend on the mechanical impedance mismatch between the materials on either side of the interface. Generally, the larger the impedance mismatch, the larger the portion of the wave that will be reflected back into the first medium, and the smaller the portion that will be transmitted into the second medium.

In order to study the influence of impedance mismatch of interface on shock wave propagation in heterogeneous media, layered composite specimens having the same geometrical

structure, but different combinations of layer component materials, were prepared using the procedure described in the previous section and were subjected to planar impact loading at different flyer velocities. The corresponding of experimental results are shown in Fig. 4.5 and Fig. 4.6. Plots (a) and (b) in Fig. 4.5 show the shock particle velocity profiles for 6.5 mm PC74/Al37 and PC74/SS37 composites impacted by flyers at nominal velocities of 588 m/s and 1060 m/s, respectively. Similarly, plots (c) and (d) in Fig. 4.5 show the experimental results for 9.9 mm PC74/SS37 and PC74/GS55 specimens subjected to impact loading of flyers at velocities of 560 m/s and 1060 m/s. The plots (e) and (f) of Fig. 4.5 show the results of 10.3 mm PC37/SS19 and PC37/GS20 composites impacted by PC flyers at velocity of 560 m/s and Al flyers at velocity of 1160 m/s. For PC37/SS19 and PC37/GS20 composites, besides the particle velocity profiles at buffer/window interface measured using VISAR, the stress time histories of shock wave at internal interfaces were also measured by manganin gages, which are shown in the Fig. 4.6 (again, x in the legend of the plots is the distance of manganin gage from the impact surface of the specimen).

The ratios of mechanical impedance of the "hard" layer to the "soft" layer in PC/SS, PC/Al and PC/GS are approximately 23/1, 7.5/1 and 8/1, respectively, which are estimated based on one-dimensional elastic compression wave speed and initial density of the materials. From Fig. 4.5 and Fig. 4.6, it is apparent that the interface impedance mismatch has very large effect on the structure of the shock front. For the PC74/SS37 composite, subjected to impact loading by a PC flyer at a velocity of 588 m/s, the rise time of the shock wave after propagating 6.45 mm distance away from the impact surface is about 0.88 μs, while for the PC74/AL37 composite, which has less interface mechanical impedance mismatch, under similar loading condition, the shock front rise time is about 0.47 μs (see Fig. 4.5 (a)). When the flyer velocity is increased to about 1050 m/s, the shock front rise times for PC74/SS37 and PC74/AL37 are 0.38 μs and 0.16 μs, respectively (see Fig. 4.5 (b)). Therefore, the larger the impedance mismatch between the components of layered composite, the longer the time that is needed for a shock front to reach its

final shocked steady state. Besides affecting the shock front rise time, plots (a) and (b) in Fig. 4.6 show that impedance mismatch also affects the magnitude and duration of the resonant oscillations of the shock profiles, and the degree of influence depends on the shock loading strength. When the flyer velocity is about 560 m/s, the larger the impedance mismatch, the larger the magnitude and duration of oscillations on the stress profiles. As the flyer velocity increases to 1050 m/s, the amplitudes of oscillations of the stress profiles for both PC37/SS19 and PC37/GS20 are about the same, though the oscillation duration in the former is still larger than that in the later. The interface impedance mismatch also affects the unloading process from the shocked state, which can be seen from the release processes of the shock particle velocity profiles in Fig. 4.5. The PC/SS composite has larger interface impedance mismatch, its unloading process is slower than that of PC/Al or PC/GS composite and the final released state also has a higher residual particle velocity.

4.5.3 Influence of Interface Number on Shock Profile

In the previous two sections the influence of shock loading strength and interface impedance mismatch on shock profiles have been presented. In this section the experimental results illustrating the influence of interface number density on shock profiles will be presented. To investigate the effect of interface number on shock profile, specimens of PC/SS and PC/GS composites were prepared in two types of geometrical structures. For PC/SS type composite, PC37/SS19 specimens with two different thickness, 7 mm and 10.4 mm, and PC74/SS37 specimens with two thicknesses, 6.45 mm and 9.90 mm, were prepared. For PC/GS type composite, only nominally 10 mm thick PC74/GS55 and PC37/GS20 specimens were prepared and manganin gages were embedded in them to measure the shock stress history.

The comparison of shock particle velocity profiles and the stress profiles for composite specimens with different interface number density is shown in Fig. 4.7 and Fig. 4.8, respectively. It can be observed that for both PC/SS and PC/GS composites the shock front steepens as the number of interfaces (density) doubles, which implies that the nonlinearity of composite increases with increasing number of interfaces. At first glance, this change in property very much resembles that of the effect of reduction in interface impedance mismatch on the shock profile, since in both cases the shock front rise time and the duration of resonant oscillations superposed on the shock profiles are decreased. But, in more detail, some differences can be easily seen by comparing the shock velocity profiles in Fig. 4.7 with those in Fig. 4.5. In the case where the shock front steepens due to reduction of interface impedance mismatch between components, the magnitude of the shock particle velocity profile remains the same or increases. For almost all the experiments shown in Fig. 4.5, the final released state of composites with lesser impedance mismatch has lower particle velocity. But, in the case where the interface numbers is doubled, the magnitude of the wave profiles tends to decrease and the particle velocity in the final released state is not significantly different from the previous two cases. Furthermore, by comparing plot (a) with plot (b), and plot (c) with plot (d) in Fig. 4.7, it can also be observed that the peak of the shock profile of composites with smaller density of interfaces attenuates faster with the propagation distance at lower flyer velocity than that at higher flyer velocity. This indicates that the dispersion of shock energy due to the interface has a more dominant effect than the material nonlinearity at low shock pressures. With increasing shock pressure, the nonlinearity of the material increases. It is expected that the difference between the shock profiles of two composites, which contain different densities of interfaces, will become smaller at higher impact velocities. This is confirmed by the experimental results shown in Figs. 4.7 (c) and (d).

Figures 4.7 (e) and (f) illustrate the effect of interface number density on shock profiles in PC/GS type composites at two different loading conditions. One is due to a PC flyer impacting at a velocity of 565 m/s, the other is by an Al flyer impacting at velocity of about 1,100 m/s. Again,

increasing the interface density steepens the shock front, or in other words, the nonlinearity of composites is an increasing function of the interface density. Therefore, both the shock loading strength and the interface density influence the nonlinearity response of composites, but these effects become less important as the shock loading increases to sufficiently high level where the intrinsic material nonlinearity becomes more dominant.

Figures 4.8 (a), (b) and (c) show the comparisons of shock stress profiles of PC/GS composites, which clearly indicate that besides the influence on the shock compression process (rise time of the shock front), the interface density of composites also affects the dynamic steady shocked state, i.e., details of the structure of the shock profile. When the interface density doubles, the frequency of resonant oscillations due to the multiple reflections between interfaces is also doubled. It is also noted that as the shock loading strength increases, the magnitude also increases. Hence, it may be concluded that the duration of oscillation in the shock profile is determined by interface density, while the amplitude is dominated by the shock strength. It is interesting to note that for the PC flyer impacting at a velocity of about 560 m/s, the ratio of amplitude of oscillations of the stress profile for PC74/GS55 to that of PC37/GS55 is about 1. However, this ratio is apparently less than 1 as the flyer velocity is increased to 1060 m/s, but, when the loading pressure increasing further, achieved by the impact of Al flyer at the velocity of 1,100 m/s, this ratio becomes larger than one.

4.5.4 Evolution of Shock Profile with Propagation Distance

Figure 4.9 shows the evolution of shock particle velocity profiles with propagation distance of shock wave in the different types of composites. For the purpose of comparison, the profiles measured at different distances away from the impact surface, corresponding to different initial wave arrival times, are shifted along the time axis to the same starting point. Figs. 4.9(a) and (b)

show the comparison of measured shock particle velocity profiles at buffer/window interface of 6.45 mm and 9.9 mm thick PC74/SS37 specimens loaded by 2.87 mm PC flyers at velocities of 550 m/s and 1060 m/s, respectively. Figs. 4.9(c), (d) and (e) show the comparison of velocity profiles for the 3.7 mm, 7.1 mm and 10.5 mm thick PC37/SS19 composite specimens loaded by the 2.87 mm PC flyers at velocities of 550 m/s and 1040 m/s and by a 5.63 mm PC flyer at a velocity of 1060 m/s, respectively.

Figures 4.10(a) and (b) are the shock stress profiles at interfaces at 3.44 mm and 6.5 mm away from impact surface of 10.2 mm and 10.6 mm thick PC37/SS19 specimens impacted by 2.87 mm flyers at velocities of 564 m/s and 1043 m/s, respectively. Shown in Fig. 4.10(c) is the comparison of shock stress profiles at 3.44 mm and 9.88 mm away from the impacted surface for a 10.61 mm thick PC37/SS19 composite, impacted at 1045 m/s. In this case, the initial shock fronts and the first oscillation resemble each other. However, there are substantial differences in the rest of the shock profile. This is because the stress state at the interface, which is the last internal interface surface formed by the last hard (SS) layer of composite and the buffer layer (PC), is affected by the release wave originating from the interface between the buffer and the window. The evolution of shock stress profiles inside the PC37/GS20 and PC74/GS55 composites, impacted by 2.87 mm PC flyers at velocities of 560 m/s and 1,070 m/s, is shown in Figs. 4.10(d), (e), (f) and (g), respectively.

From the comparisons of shock profiles discussed above, a common feature emerges. The initial compression process of shock waves (or the shock front) is independent of the propagation distance in the composites. This indicates that a structured steady wave, or a quasi-steady wave if not strictly steady, can be achieved and propagated in layered composites. For all cases considered here, the difference between the shock profiles becomes important only after the initial compression. Two mechanisms may be responsible for this difference. One is due to the dispersion resulting from the multiple reflections of interface to the shock wave, or the scattering of the shock wave by the internal interface (e.g., Figs. 10(f) and (g)). The other is due to the

release wave originating from the rear (free) surface of the flyer (see Figs. 4.10(a), (b), (d) and (e)) and its interaction with the propagating shock wave in the composite.

Comparing the shock particle velocity profiles in Fig. 4.8 (which includes the partial decompression influence from the window) with the shock stress profiles in Fig. 4.10 (which is essentially structured steady wave propagating inside the composites without being disturbed by any release wave except the unloading), it may be concluded that the effect of the scattering of interface to the decompression (release) wave is even more pronounced since the difference between particle velocity profiles for different thickness of specimens at same loading condition is apparent (see Fig. 4.9). By comparing plots (d) and (e) with (f) and (g) in Fig. 4.10, as well as plots (a) and (b) with (c) and (d) in Fig. 4.9, it is worth noting that the dispersion due to interface scattering is more pronounced in the composite with smaller density of interfaces than in the composite with higher interface density, since the peak attenuation of shock profiles in the former (Figs 4.9(a), (b), 4.10(f) and (g)) is larger than those in the latter (Figs. 4.9(c) and (d), 4.10(d) and (e)).

4.5.5 Influence of Pulse Duration on Propagation of Shock Waves

To investigate how the pulse duration affects the shock wave propagation in layered composites, shock compression experiments were carried out by impacting flyers of different thickness, at the same velocity, onto specimens of the same thickness. The shock profiles were either measured by the VISAR at buffer/window interface or sensed by manganin gages embedded inside the composites. Fig. 4.11 shows the shock particle velocity profiles for 3.7 mm, 7.0 mm and 10.6 mm thick PC37/SS19 specimens loaded by flyers of thickness 2.87 mm and 5.63 mm at velocity of about 1,050 m/s. The corresponding shock stress profiles for the 10.6 mm thick PC37/SS19 composites are shown in Fig. 4.12. The initial pulse duration generated by the 5.63 mm and 2.87

mm PC flyers at velocity of 1,050 m/s is about 3.6 μs and 1.8 μs, respectively. To obtain shorter pulse duration, say 0.5 μs, in principle, it can be achieved by reducing the thickness of the PC flyer to about 0.8 mm. But, in practice, if the polymeric flyer is thinner than 1.0 mm, it will most likely bow out backwards when it is accelerated in the barrel of the powder gun. The impact of a specimen by a curved flyer will result in a non-planar shock front in the specimen. To obtain a shorter shock pulse and avoid the problem of bowing out, a 1.20 mm aluminum flyer is accelerated to a velocity of 657 m/s impacting a PC37/SS19 specimen. The shock pulse duration generated by this Al flyer is about 0.4 μs and the shock pressure is about the same as that achieved by impacting of a PC flyer at velocity of 1,050 m/s. The corresponding shock particle velocity at buffer/window interface is compared with others in Fig. 4.11(c).

It can be seen from Fig. 4.12 (also in Fig. 4.11) that as a shock wave propagates in the layered PC37/SS19 composites, the structure of the shock front does not depend on its pulse duration. Even in the case of a specimen loaded by a very short pulse (0.4 μs duration), when its front is overtaken by the release wave from the rear (free) surface of the flyer, it affects the attenuation of the shock amplitude, but not the slope of the front (Fig. 4.11(c)). This indicates that the layered composite does indeed support steady shock waves.

4.5.6 Influence of Release Wave from Window on Shock Profile

It is possible to measure the particle velocity history by VISAR at an internal interface of PC/GS type composite without using a window since both the components, PC and GS, are transparent. A PC74/GS55 specimen of total thickness 20.54 mm (15 units plus a buffer layer) was prepared in the same way as described in the section on specimen preparation. Before bonding the layers, one surface of a 0.55 mm glass plate was aluminized to a mirror surface in the same way as aluminizing the PMMA windows. This mirror surface was located 9.92 mm away from the

impact surface, which is the exact position of the buffer/window interface of a PC74/GS55 specimen with window. The VISAR laser beam was focused on the internal mirror surface. The specimen was loaded by a 2.87 mm thick PC flyer at a velocity of 568 m/s. In this case, the measured particle velocity time history is the shock profile at an interior location of specimen without being affected by the release wave from the buffer/window interface. The shock profile obtained in this experiment is compared with that obtained for the specimen with the window under nominally the same conditions in Fig. 4.13.

It can be seen that the release wave from buffer/window interface does affect the shock profile. The influence is evident not only on the oscillatory portion of the shock profile, but also in the slope of the shock front. When a shock wave is partially released by a tensile wave traveling in the opposite direction, the shock front rises faster since the tensile wave accelerates a particle in the direction opposite to its own travelling direction. Therefore, the front of the shock wave in the specimen with window is steeper than in the transparent specimen with internal mirror. This is due to the release wave that originated from the buffer/window interface because of the mechanical impedance mismatch. Also, this release wave from the window tends to subdue the oscillations resulting from the scattering of the shock wave by internal interfaces. The magnitude of the oscillation in the shock profile of the specimen with window is much smaller than that of the specimen without window. It is expected that the shock particle velocity profile at the internal interface should resemble the shock stress profile measured by manganin gages at the interface. This is verified by plotting the stress profile and velocity profile together (Fig. 4.14). The stress and velocity profiles are normalized by their own maxima for comparison. The difference in the slope of the shock front between the stress and velocity profiles is attributed to the phase shift between the shock velocity profile and shock stress profile, which is caused by the interaction of multiple reflected waves with the shock wave and will be discussed in more detail in relation to the numerical simulation analysis in the next chapter.

4.6 Discussion and Conclusions

By the experimental results shown in the previous sections, it can be seen that the layered polymer/metal composites do support structured steady shock wave propagation. The interface density (i.e., measure of the length scale associated with heterogeneity), component material properties (dominating the mechanical properties of interface) and loading strength have pronounced effects on the dissipation and dispersion processes of shock wave propagation in heterogeneous media. The apparent effect on the shock front by increasing shock loading pressure, increasing the interface number density, or decreasing the interface impedance mismatch are similar since all of them lead to steepening of the shock front. However, the underlying physics of each case may be very different. In fact, at medium loading stress range, even the dynamic behavior of homogeneous media is very complicated. The scattering effects due to heterogeneity add the complex in analysis of the mechanisms of dynamic response of composite materials. Analogous to the analysis of shock compression homogeneous solids, the response behavior of composites can be separated into two parts, bulk and deviatoric. The propagation or transport property, i.e., the speed of the shock wave in the composites, is dominated by the bulk properties, while the deviatoric properties are responsible for the structure of the shock wave.

4.6.1 Influence of Interface Scattering on Bulk Response of Composites and Shock Hugoniot

The determination of the bulk response behavior of a material to shock compression relies on the experimental measurement of the relation between shock velocity and particle velocity, the so-called Hugoniot curve. The particle velocity history of a free surface or an internal interface, as well as the shock wave velocity, can be measured using the VISAR system[6] and wave arrival

time detectors such as electronic charged pins and flash gaps[10-13]. In the present experimental study, electric charged pins, manganin stress gages and VISAR system were used to determine the shock velocity and particle velocity. The measured shock and particle velocity data for PC/GS and PC/SS composites are shown in the Fig. 4.15 and Fig. 4.16, respectively.

One may expect that the shock velocity of a mixture (composite) should fall in the range bounded by the Hugoniots of its two components. The experimental results show, however, that the shock velocity of composites could be between the shock Hugoniots of its two components (e.g., PC/GS composites shown in Fig. 4.15), or be lower than the Hugoniot curves of both components (e.g., PC/SS composite shown in Fig. 4.16). The physical mechanism for the slowing down of a shock wave in the composites is due to the interaction of multiple reflected waves from the internal interface with the shock wave, i.e., the scattering effects of internal interface on the shock wave. The details of the processes of interaction of reflected waves with incident shock wave will be found in next chapter on numerical analysis of shock wave propagation in layered composites.

Theoretical models have also been developed to predict the bulk response behavior of the composite in terms of the properties of its components, which are called mixture models. One of the mixture models, developed by Dremin and Karpukhin [14], hereafter referred to as Dremin's model, is an additive approach, in which the volume of the shock-compressed mixture is assumed equal to the sum of volumes of its components, obtained at the same pressure by separate shock compression in the form of homogeneous monolithic samples. The details of Dremin's model were described in Chapter 2.

The shock wave velocities, predicted by the Dremin's additive approach of mixture, as a function of volume (or mass) fraction of hard layer component for three layered composites, PC/GS, PC/SS and PC/W, are shown in Fig. 4.17. The unit length of the composite considered here is 1.12 mm. It can be seen that the shock velocity of the mixture depends on both the bulk volume ratio and bulk response behavior of the components. If the ratio of mechanical

impedance of the two components is small, the shock velocity of the mixture will most likely be between those of the two components. With the increase in volume ratio of the "hard" (heavy) component, the shock velocity of the mixture will eventually become less than the velocity of either component. The shock velocity varies with the change of the volume ratio of two components (see Fig. 4.17). The upward concave shape of the shock velocity-volume fraction curve implies that there is a minimum shock velocity for some value of the volume ratio. The value of this minimum volume ratio depends on the mechanical and physical properties of component materials. The shock velocity of the mixture as a function of the mass fraction of the "hard" component is also shown in Fig. 4.17. Knowing that the mass or the density of a material is an important parameter that enters all of the governing equations of conservation laws, and noticing the difference between the shapes of the shock velocity-volume fraction (D-α_1) and shock velocity-mass fraction (D-β_1) curves, it is concluded that the geometric structure (volume ratio) of the mixture does affect its dynamic behavior, but in a different way from the mass of a components.

Figure 4.18 shows the mixture model predictions for the shock velocity of PC/SS composite under different equilibrium pressures as a function of volume fraction of steel. This illustrates the dependence of the shock velocity of mixture on the bulk geometric structure since the value of the minimum velocity of the shock wave in the composite at a constant shock pressure varies with the change of shock pressure. Similar dependence of the bulk sound speed, on the mixture volume fraction, calculated using equation (2.15), as well as the pressure of shocked state, is also shown in Fig. 4.18.

The shock velocity of the mixture predicted by Meyers' model[15] is also compared with that predicted by the Dremin's model in Fig. 4.18. Meyers' model is also based on the additive approximation, but it is assumed that the local particle velocity in each component is the same as the mean particle velocity in the mixture, rather than Dremin's model where the local pressure in each component is assumed to be the same as the mean pressure in the mixture (see Chapter 2).

The shock velocity of mixture predicted by Meyers' model could be higher than that of either or both components and always higher than that predicted by Dremin's model. The Meyers' model overpredicts the shock velocity of the mixture because it neglects the scattering effects of interface to the shock wave propagation.

The shock-particle velocity relations of PC/GS and PC/SS composites predicted by additive methods of Dremin and Meyers are compared with the experimental data, as well as the shock Hugoniots of their components, in Figs. 4.15 and 4.16, respectively. For the PC/GS composites, the shock velocities predicted by both models fall into the range bounded by the Hugoniot curves of its components, and the difference between the curves predicted by the two models becomes smaller with the increase of the shock pressure. But, for the PC/SS composite which has larger interface mechanical impedance difference, the Hugoniot curve predicted by Meyers' model falls within the range bounded by the Hugoniots of the two components, while the curve calculated using Dremin's model falls out of the range bounded by the Hugoniots of the two components for the loading conditions of the experiments. It can be seen that Dremin's model agrees better with experimental data, which means that the constant pressure assumption is more valid. It will be shown in the next chapter, however, that by numerical simulations the constant pressure assumption is not strictly satisfied.

There are two groups of data shown in Figs. 4.15 and 4.16. One set is represented as hollow symbols (square or triangle) captioned "experimental," which are the shock Hugoniot data obtained experimentally. The shock velocity was obtained through the measurement of the arrival time of the shock wave by manganin gages embedded in the specimen at positions separated by a known distance. The corresponding particle velocity was determined from the particle velocity profile detected using VISAR. The second set is denoted by the solid symbols, which are the calculated Hugoniot of the homogenized mixture using Dremin's model. The shock velocities of the homogenized mixture are those obtained experimentally by stress gages, while the corresponding particle velocities were calculated through pressure and velocity continuity

conditions at the impacting interface of homogeneous plates. The layered composites are treated the same as mixture with the same volume ratio, neglecting any possible difference of bulk response between the layered composite and the mixture. The initial density of the homogenized mixture is calculated by the additive approach as in Dremin's mixture model. The computed results are compared with experimental data in Figs. 4.15 and 4.16. The calculated data are more consistent with Dremin's model than the experimental data. It is noted that the experimental Hugoniot curve is generally lower by up to 10 percent in comparison to the prediction of Dremin's model and the corrected experimental curve (the solid data points). The reason for the difference between the experimental data and the model prediction may be due to the fact that the scattering effect considered in Dremin's model is based on the geometrical volumetric average, while for layered composites the scattering is due to only the normal scattering.

In fact, for any given pair of components, the additive approximation of Dremin's model is more predictive at lower shock pressures and becomes less accurate at large amplitudes when shock compression depends considerably on the entropy[16]. Using Dremin's additive method, based on the experimentally measured Hugoniot adiabatic curves of paraffin, tungsten and their mixtures, Alekseev et al.[16] calculated the Hugoniot curve of paraffin. Their results show that over the entire experimentally investigated region of pressures up to 200 GPa, the calculated Hugoniot curve for paraffin coincides very well with the experimental data. The pressure range of the present experimental investigation is much lower than that of the experiments performed by Alekseev, et al. The predictions using the additive method here should not have any larger error than their study since the thermal effects in this range are very small. Therefore, by comparing the shock adiabatic Hugoniot curves of the calculated, which only partially accounts for the interface scattering effects, and experimentally measured curve, it is clear that the influence of geometric scattering of interface on the bulk response of composite can not be neglected and is more important at lower shock loading pressures.

4.6.2 Influence of Interface Scattering on Deviatoric Response of Composites and Shock Viscosity

From the particle velocity profile measured by VISAR, the mean value (amplitude of the coherent part) of the particle velocity profile and the slope of the fastest rising portion of the shock front can be determined. By combining the additive equation of the specific volume of composite (Dremin's mixture model) with the conservation laws of continuity and momentum, the corresponding shock velocity and the stress (or pressure) at the shocked state can be calculated. The calculated shock velocity is generally slightly higher than the experimentally measured (see Figs 4.15 and 4.16), while the calculated stress value falls in the region between the maximum and the minimum of the oscillations in the stress profile measured by the manganin gages. The strain rate was obtained by dividing the slope of the shock front by the calculated shock velocity. The plot of shock stress against the strain rate at the shock front is shown in Fig. 4.19. In the calculation of the shock front strain rate, the error due to the slightly overestimated shock wave velocity by the mixture theory is canceled by the small amount of steepening of the shock front due to the release wave reflected back into the composite at buffer/window interface. The steepening of shock front occurs due to the mechanical impedance mismatch between the window material (PMMA) and the buffer, and can be observed from the comparison of velocity profiles for specimens with and without window (Fig. 4.13). The estimated error of calculated data in Fig. 4.19 is within 4%.

The shock stress (σ)-strain rate ($\dot{\varepsilon}$) data can be fitted by a linear relation when plotted on logarithmic scale. The slope of segment for each composite is slightly different from the other, but on the whole, the strain rate increases roughly as a square of the shock stress, or may be expressed as $\dot{\varepsilon} \sim \sigma^n$, where $n \approx 1.8$-2.4. While for many common metals such as Al, Fe, Be, Bi, Cu and U, $n \approx 4$, even for fused silica and MgO $n \approx 4$ seems also true[7], in the stress range of one to tens of GPa (Fig. 4.20). For polymeric materials (PC, PMMA) under the shock loading range

of interest in this study, their response to shock loading may be best described by a nonlinear viscoelastic model. Based on the available shock particle velocity profiles of PMMA[3,9], the stress-strain rate relation of PMMA, or Polycarbonate, which are considered to be homogeneous materials under shock compression, appears to be similar to the one for the metals, i.e., $n \approx 4$.

Based on the empirical description of the Hugoniot stress-strain rate relation for metals, Swegle and Grady[7] developed a constitutive model for the shock viscosity process during large-amplitude compressive steady stress wave propagation in solids. They successfully reproduced the experimentally observed structure of shock fronts for steady shock waves in metals. The model was developed under the assumption that there is no bulk viscosity and the viscous stress is a purely deviatoric. Regardless of how close this assumption is to reality, the success of the model in reproducing the structure of shock front shows us that, at least, a phenomenological description of shock deformation process is possible, if for some reason, the underlying physics of the process or the phenomenon has not been understood yet, or the physical mechanisms are clear but too complicated to be accurately modeled. According to this model, the larger the viscous stress, the longer the time the shock front takes to reach its maximum (steady state) amplitude, which means that the deformation process is slower, and the strain rate of the shock front is smaller.

Roughly, each homogeneous component of the layered composites studied here has an exponent of about 4 (n) (see Fig. 4.20) in the relation of shock stress-strain rate, $\dot{\varepsilon} \sim \sigma^n$. While for the composites, as discussed above and shown in Fig. 4.19, the exponent is only about 2. This means the shock front in the composite will take much longer time to reach its maximum stress under the same loading strength. The interpretation of this observation may be associated with the microscopic processes of shock wave propagation in the solids.

In metals, the underlying physics responsible for the observed structured shock front is the time-dependent plasticity processes due to the energy dissipation and wave dispersion induced by

the dislocation multiplication and motion, twinning, vacancy production, precipitate alternation, etc., based on which many constitutive models have been developed[7,17-19]. In composite materials, besides the above viscoplastic processes existing in each homogeneous component, the microstructure induced scattering during shock compression could be also an important wave dispersion mechanism. Based on the physics of acoustic wave scattering, Grady[20,21] proposed a continuum constitutive model to address shock viscosity in metals, in which he attributed the viscous stress to the generation and redistribution of nonequilibrium acoustic phonons induced by the scattering of microstructures to the shock wave. Later, the theory was generalized to address the finite-amplitude nonlinear wave propagation in heterogeneous media[22].

In composites, especially the layered composites used in this investigation, which consist of homogeneous components, due to the existence of internal interfaces, acoustic scattering could be also a dominant physical mechanism responsible for structured shock waves besides the dissipation and dispersion due to viscoplasticity or viscoelasticity, which dominates the deformation processes of the component materials. This provides a reasonable explanation of why strain rate associated with the shock front in a composite is smaller than that of its homogeneous component materials.

4.6.3 Summary and Conclusions

In this experimental investigation of shock wave propagation in the periodically layered composites, three types of composite specimens with five geometric configurations were prepared and subjected to shock loading generated by planar impact of a flyer. The composites that were studied include PC74/Al37, PC74/SS37, PC37/SS19, PC74/GS55 and PC37/GS20. The specimen thickness is nominally 3.7 mm, 7 mm and 10 mm. Most flyers are made of PC with 2.87 mm in thickness, and the typical flyer velocities are about 600 m/s and 1,060 m/s. Several

5.63 mm thick flyers were also used to generate shock waves with longer pulse duration. To generate higher shock loading Al flyers were also used.

In each of the experiments conducted, the VISAR system was used to obtain the shock particle velocity profiles at the buffer/window interface. In addition, in some of specimens manganin stress gages were also embedded at selected interfaces where the shock stress history and shock arrival times were of interest.

The results of this systematic experimental investigation lead to the following conclusions:

1) Periodically layered composites such as the ones used in this investigation can support steady structured shock waves.
2) The influence of internal interface on the shock wave propagation is through scattering mechanism. The interface scattering affects both bulk and deviatoric response of the composites to shock compression loading. The influence of scattering on the bulk response is to reduce the propagation velocity of shock wave, while the influence of the deviatoric response is in structuring the shock front, or in the other words, increasing the shock viscosity, which increases the shock front rise time similar to the effect of viscous material behavior in homogenous solids. In homogeneous media such as metals, the strain rate of the shock front increases by the fourth power of the shock stress, while the results of this investigation show that for layered composites, the strain rate at the shock front increases by about the square power of the shock stress, indicating much larger shock viscosity than the former.
3) With the increase of shock loading strength, the slope of the shock front increases very rapidly. At the same time the amplitude of oscillations in the wave profile also increases, which could be considered to be one of the dissipation mechanisms of the shock wave.
4) Keeping the total mass of each component unchanged, an increase in the number of interfaces (or the density of interfaces) results in (a) steepening of the shock front slope, which indicates that the nonlinearity of the composite increases, and (b) an increase in the amplitude of

oscillations in the shock profile, which implies that more of the kinetic energy has been transformed to internal energy and the dissipation of shock energy increases. From Fig. 4.15 it is seen that the shock Hugoniot curve of the composite is not sensitive to the density of interfaces, so it can be postulated that interface density plays a dominant role for the structuring of the shock front.

5) Impedance mismatch between constituents at the interface also contributes to the dissipation and dispersion of the shock energy during propagation. The larger the impedance mismatch between the components, the smaller the slope of the shock front, which means the larger the dispersion. From Fig. 4.17 it is seen that the impedance mismatch has very strong influence on the shock wave velocity of the composite. Therefore, it may be postulated that the interface mechanical impedance mismatch contributes to both the bulk and the deviatoric responses of the composite to shock compression.

6) The existing mixture theories can reasonably predict the bulk response behavior of the mixtures to shock compression, but, not the deviatoric response, or the shock viscosity. In order to properly describe the shock wave propagation in heterogeneous media, a physically based constitutive model which takes into account the scattering effects of internal interfaces to shock compression must be formulated.

4.7 References

1. Wackerle, J. *J Appl. Phys.* **33**, 922 (1962).
2. Fraser, D.B. *J. Appl. Phys.* **39**, 5868 (1968).
3 Barker, L.M. and Hollenbach, R.E. Shock-wave studies of PMMA, fused silica, and Sapphire, *J. Appl. Phys.* **41**, 4208 (1970).
4 Marsh, S.P. *LASL shock Hugoniot data*, University of California Press, California (1980).
5 Samudrala, O. private communication (2000).
6 Barker, L.M. and Hollenbach, R.E. Laser interferometer for measuring high velocities of any reflecting surface, *J. Appl. Phys.* **43**, 4669 (1972).
7 Swegle, J.W. and Grady, D.E. Shock viscosity and the prediction of shock wave rise times, *J.Appl. Phys.* **58**, 692 (1985).
8 Johnson, J.N. and Barker, L.M. Dislocation dynamics and steady plastic wave profiles in 6061-T6 aluminum, *J. Appl. Phys.* **40**, 4321 (1969).
9 Schuler, K.W. and Nunziato, J.W. The dynamic mechanical behavior of polymethyl methacrylate, *Rheol. Acta* **13**, 265 (1974).
10 Goranson, R.W., Bancroft, D., Burton, B.L., Belchar, T., Houston, E.E., Gittings, E.F., and Landeen, S.A. *J. Appl. Phys.* **26**, 1472 (1955).
11 Minshall, S. *J. Appl. Phys.* **26**, 463 (1955).
12 Mallory, H.D. *J. Appl. Phys.* **26**, 555 (1955).
13 Walsh, J.M. and Christian, R.H. *Phys. Rev.* **97**, 1544 (1955).
14 Dremin, A.N. and Karpukhin, I.A. Method for determining the shock adiabatic curves for the disperse substances, *Zh. Prikl. Mekhan. i Teck. Fiz.* **1**, No. 3 (1960).
15 Meyers, M.A. *Dynamic behavior of materials*, John Wiley & Sons, Inc., New York (1994).

16 Alekseev, Yu.F., Al'tshuler, L.V., and Krupnikova, V. P. Shock compression of two-component paraffin-tungsten mixture, *Zh. Prikl. Mekhan, i Teck. Fiz.* **12**, No. 4 (1971).

17 Rubin, M.B. Analysis of weak shocks in 6061-T6 aluminum, in *Shock Waves in Condensed Matter-1989*, edited by Schmidt, S.C., Johnson, J.N., and Davison, L.W., American Institute of Physics, New York, p321 (1990).

18 Partom, Y. Understanding the Swegle-Grady fourth power relation, in *Shock Waves in Condensed Matter-1989*, edited by Schmidt, S.C., Johnson, J.N., and Davison, L.W., American Institute of Physics, New York, p317 (1990).

19 Johnson, J.N. Calculation of path-dependent wave shock hardening, *J. Appl. Phys.* **72**, 797 (1992).

20 Grady, D.E. Shock-wave compression of brittle solids, *Mech. Mater.* **29**, 181 (1998).

21 Grady, D.E. Scattering as a mechanism for structured shock waves in metals, *J. Mech. Phys. Solids* **46**, 2017 (1998).

22 Grady, D.E., Ravichandran, G., and Zhuang, S. Continuum and subscale modeling of heterogeneous media in the dynamic environment," in *Proceedings of the AIRPAT Conference*, Honolulu, Hawaii, edited by Manghani, M., Oxford University Press (1999).

23 Sun, C.T., Achenbach, J. D., and Hermann, G. Continuum theory for a laminated medium, *J. Appl. Mech.* **35**, 467 (1968).

24 Nayfeh, A.H. *Wave propagation in layered anisotropic media: with applications to composites*, Elsevier (1995).

25 Kikolaevskii, V.N. Hydrodynamic analysis of shock adiabatic curves for heterogeneous mixtures of substances, *Zh. Prikl. Mekhan, I Teck. Fiz.* **10**, No. 3 (1969).

26 Duvall, G.E. and Taylor, S.M., Jr. Shock parameters in a two component mixture, *J. Composite Materials* **5**, 130 (1971).

27 Mutz, A.H. *Heterogeneous Shock Energy Deposition in Shock Wave Consolidation of Metal Powders*, Ph.D. Thesis, California Institute of Technology (1991).

Table 4.1 Mechanical properties of components of layered composites and window materials

Material	$\rho(g/cm^3)$	G (GPa)	σ_y (GPa)	E_p (GPa)	υ
PC	1.19	0.94	0.00	1.60	0.37
PMMA	1.18	1.20	0.00	1.60	0.34
6061Al	2.71	30.0	0.32	0.69	0.33
304 SS	7.89	77.0	0.33	1.70	0.29
D 263	2.51	30.1			0.208
Float	2.50	28.2			0.24

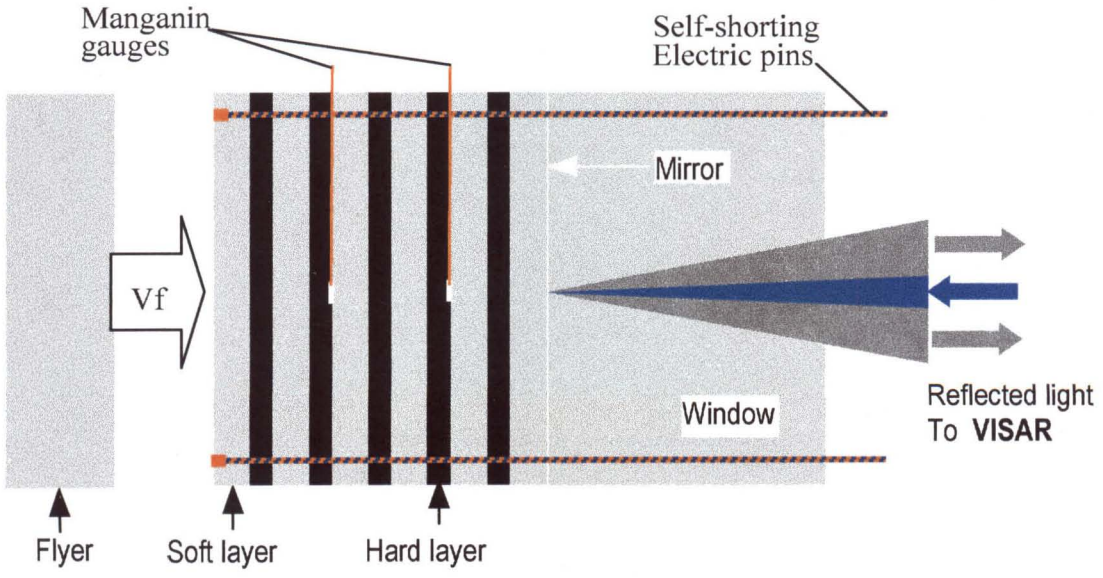

Figure 4.1 Specimen configuration and schematic of shock compression experiment for periodically layered composite.

Table 4.2 Specimen parameters and the corresponding loading conditions

Experiment number	Specimen[1] soft/hard	Units	Thickness[2] mm	Flyer velocity m/s	Flyer thickness[3] mm	Gage 1[4] mm	Gage2[4] mm
072701	PC74/Al37	5	6.59	1060	2.87 (PC)	/	/
072702	PC74/Al37	5	6.62	589	2.87 (PC)	/	/
112902	PC74/Al37	5	6.54	1826	2.87 (PC)	/	/
080301	PC74/SS37	5	6.45	588	2.87 (PC)	/	/
080302	PC74/SS37	5	6.46	1056	2.87 (PC)	/	/
112501	PC74/SS37	8	9.84	561	2.87 (PC)	0.76	/
112502	PC74/SS37	8	9.97	1062	2.87 (PC)	0.76	/
111601	PC37/SS19	16	10.20	564	2.87 (PC)	3.44	6.50
110501	PC37/SS19	16	10.60	1043	2.87 (PC)	3.44	6.50
082201	PC37/SS19	10	6.91	542	2.87 (PC)	/	/
082202	PC37/SS19	10	7.10	1035	2.87 (PC)	/	/
091001	PC37/SS19	5	3.72	548	2.87 (PC)	/	/
091002	PC37/SS19	5	3.70	1043	2.87 (PC)	/	/
103002	PC37/SS19	5	3.77	1589	2.87 (PC)	/	/
102502	PC37/SS19	5	3.70	1065	5.63 (PC)	/	/
102501	PC37/SS19	10	6.94	1076	5.63 (PC)	/	/
110502	PC37/SS19	16	10.61	1045	5.63 (PC)	3.44	9.88
120702	PC37/SS19	16	10.23	657	1.20 (Al)	/	/
111901	PC37/GS20	16	10.43	567	2.87 (PC)	3.41	6.44
112302	PC37/GS20	16	10.50	1160	5.59 (Al)	3.55	3.55
112301	PC37/GS20	16	10.62	1079	2.87 (PC)	3.41	6.44
120201	PC74/GS55	7	9.95	563	2.87 (PC)	3.37	6.07
120202	PC74/GS55	7	9.88	1056	2.87 (PC)	3.35	5.97
120701	PC74/GS55	7	10.07	1070	5.55(Al)	3.41	6.07
121001	PC74/GS55	7	9.92	568	2.87 (PC)	0.74	/

Note 1: PC--polycarbonate, Al--6061-T6 aluminum alloy, SS--304 stainless steel; the number following abbreviation of component material represents the layer thickness in hundredths of a millimeter.

Note 2: Specimen thickness includes the 0.74mm PC buffer; the mirror for reflecting laser light to VISAR is located at back surface of the buffer.

Note 3: Material in parentheses is the flyer material.

Note 4: The distance of manganin stress gage away from the impact surface.

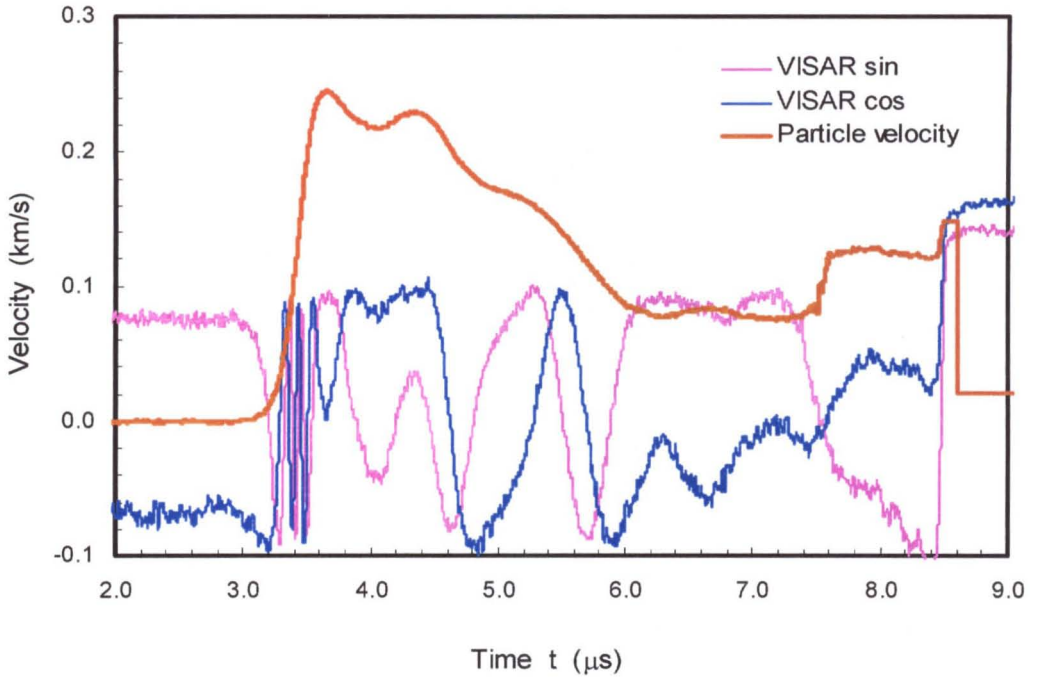

Figure 4.2 Typical oscillograms of VISAR signals and the deduced particle velocity profile at buffer/window interface obtained in a shock compression experiment. The specimen is 7 mm thick PC37/SS19 layered composite specimen and was impacted by 2.87 mm thick PC flyer at a velocity of 542 m/s.

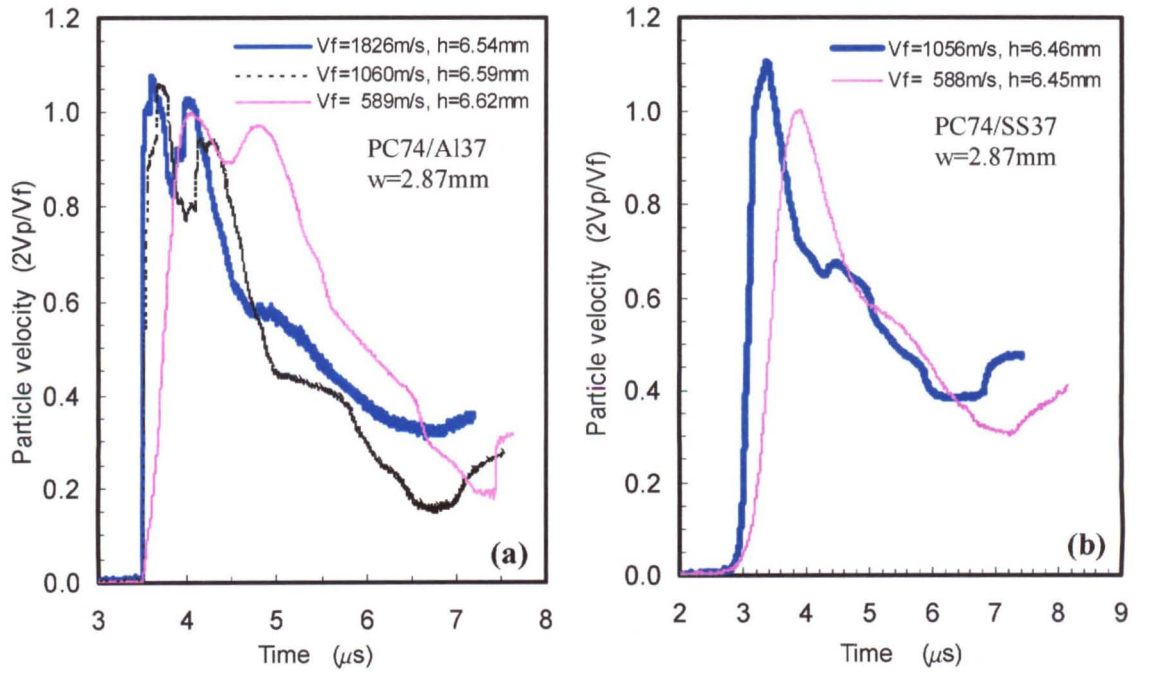

Figure 4.3 Influence of loading strength on the shock particle velocity profile for the PC74/Al37 (a) and PC74/SS37 (b) composites. h and w are specimen and flyer thickness, respectively; v_f is the flyer velocity.

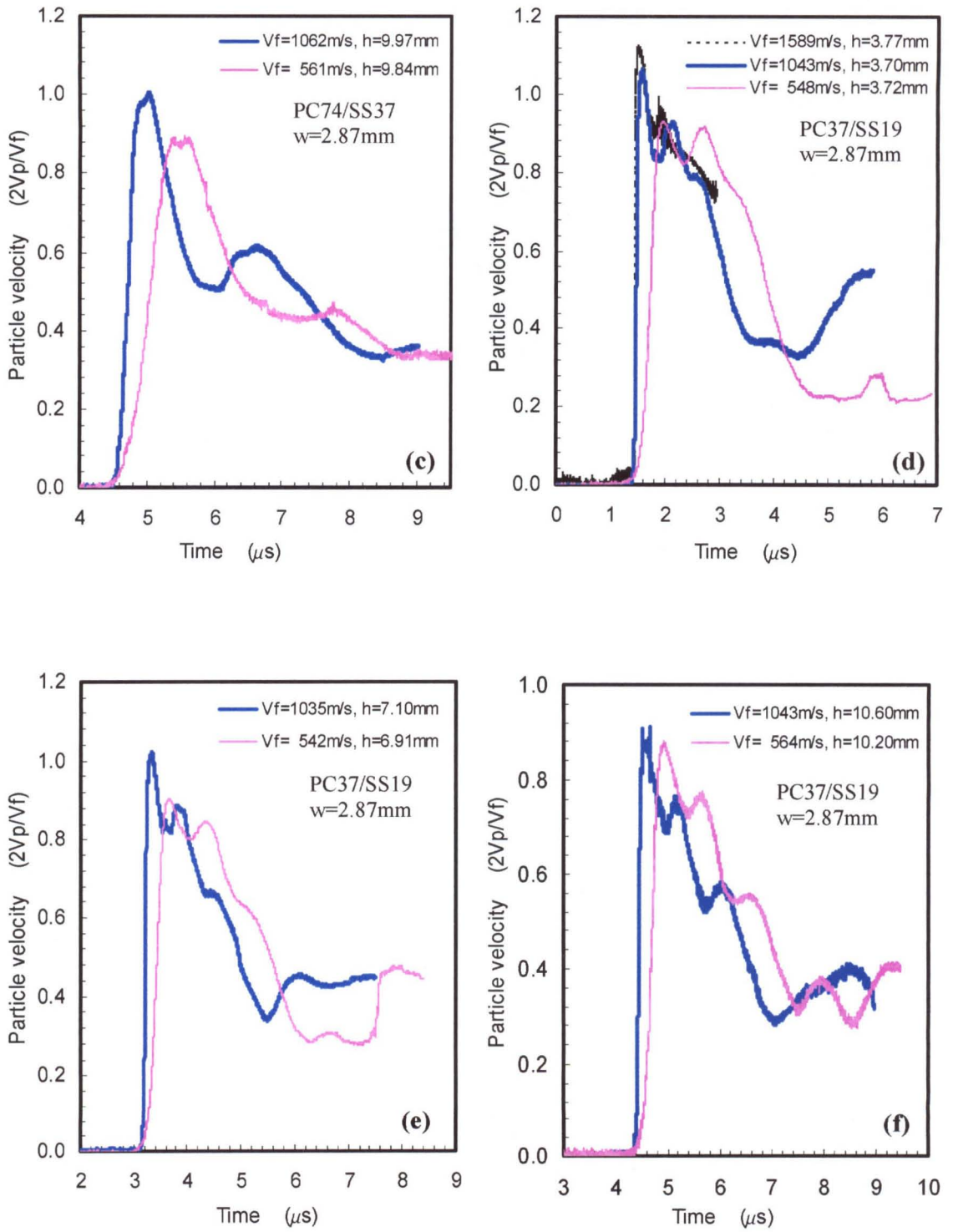

Figure 4.3 Influence of loading strength on the shock particle velocity profile for the PC74/SS37 (c) and PC37/SS19 (d, e, f) composites. h and w are specimen and flyer thickness, respectively; v_f is the flyer velocity.

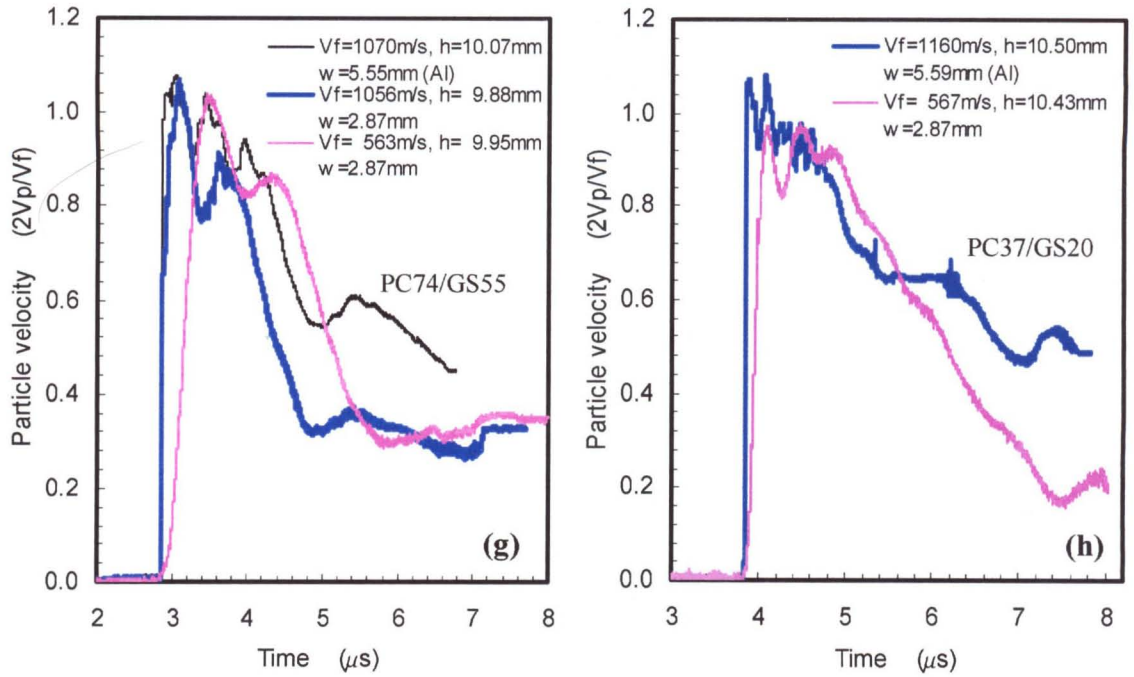

Figure 4.3 Influence of loading strength on the shock particle velocity profile for the PC74/GS55 (g) and PC37/SS19 (h) composites. h and w are specimen and flyer thickness, respectively; v_f is the flyer velocity.

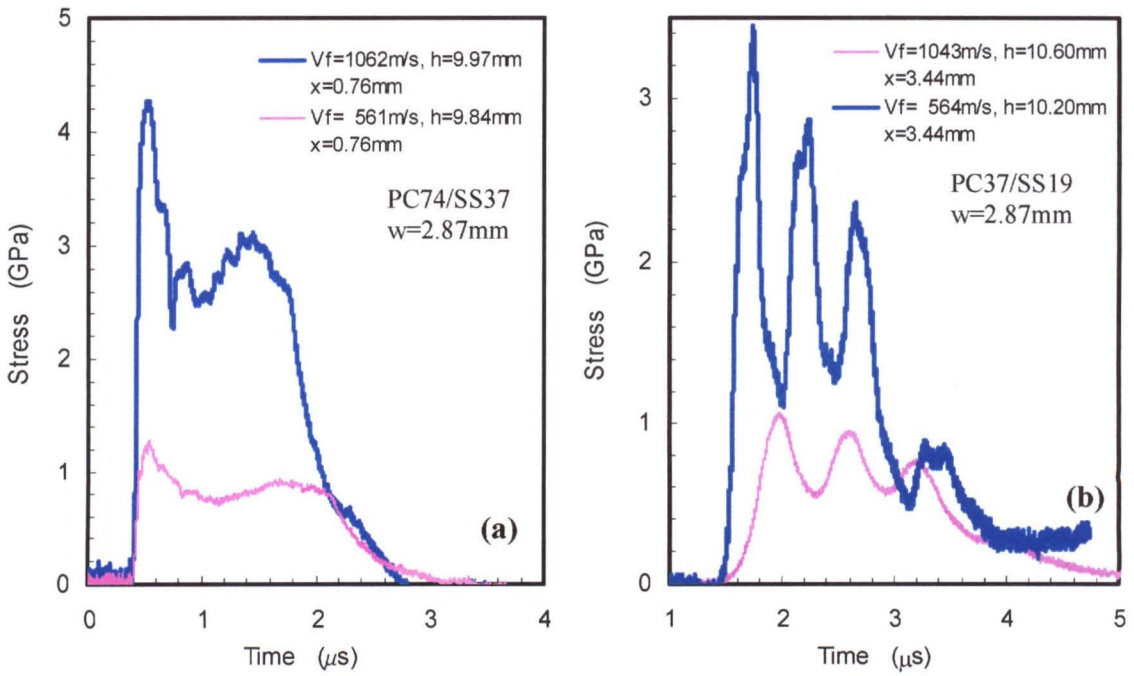

Figure 4.4 Influence of loading strength on the shock stress profile for the PC74/SS37 (a) and PC37/SS19 (b) composites. h and w are specimen and flyer thickness, respectively; v_f is the flyer velocity and x is the distance from the impact face.

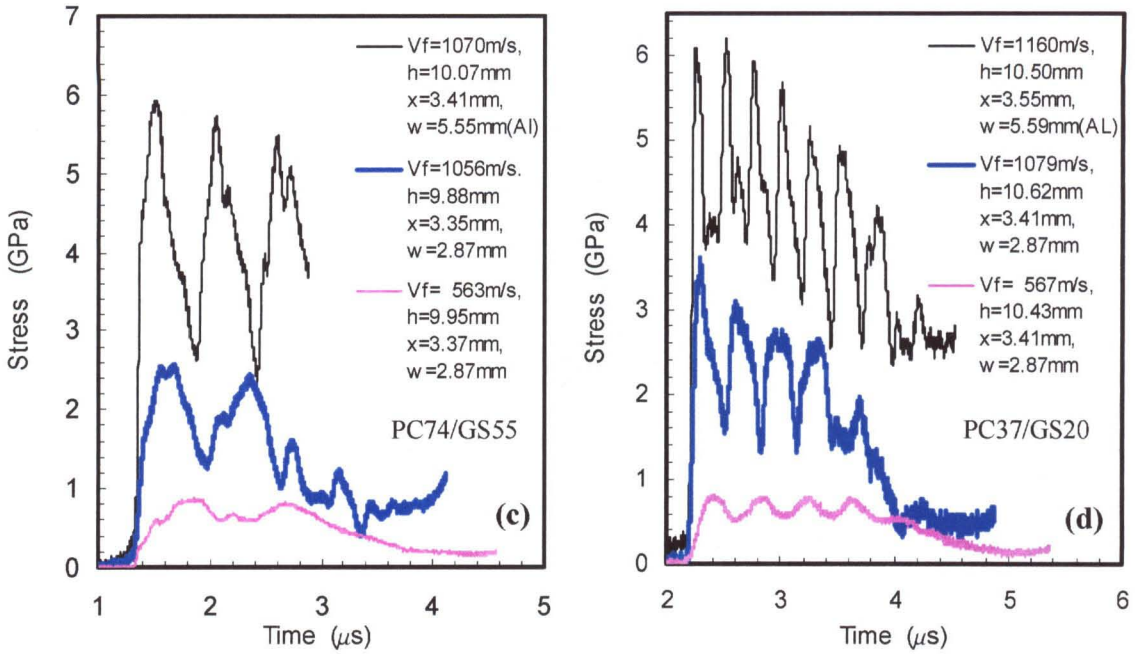

Figure 4.4 Influence of loading strength on shock stress profile for the PC74/GS55 (c) and PC37/GS20 (d) composites. h and w are specimen and flyer thickness, respectively; v_f is the flyer velocity and x is the distance from the impact face.

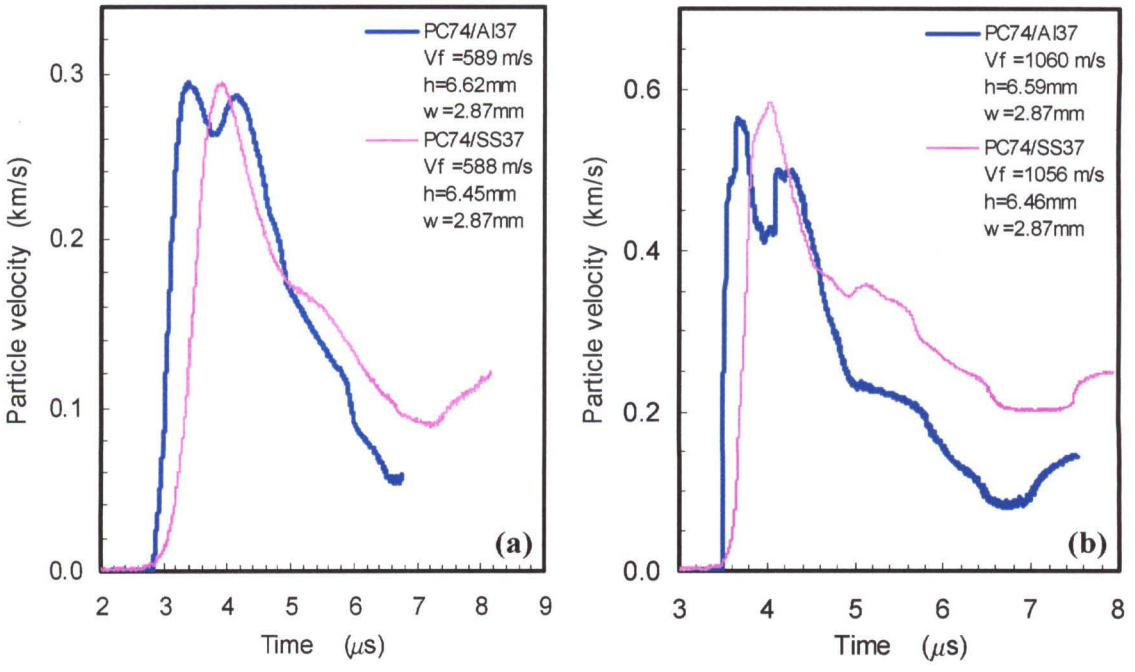

Figure 4.5 Influence of interface mechanical impedance mismatch on shock particle velocity profile for the composites. h and w are specimen and flyer thickness, respectively; v_f is the flyer velocity.

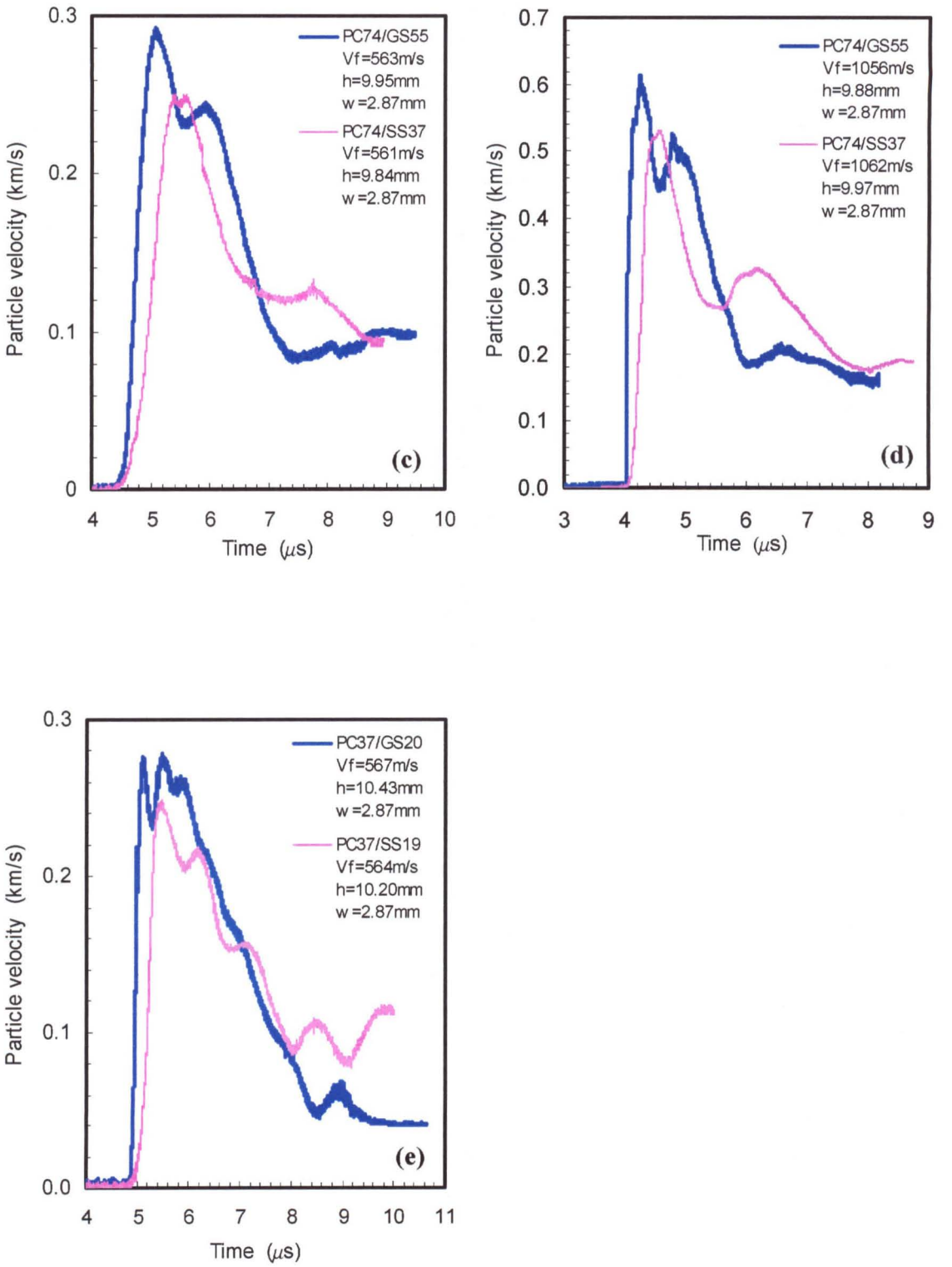

Figure 4.5 Influence of interface mechanical impedance mismatch on shock particle velocity profile for the composites. h and w are specimen and flyer thickness, respectively; v_f is the flyer velocity.

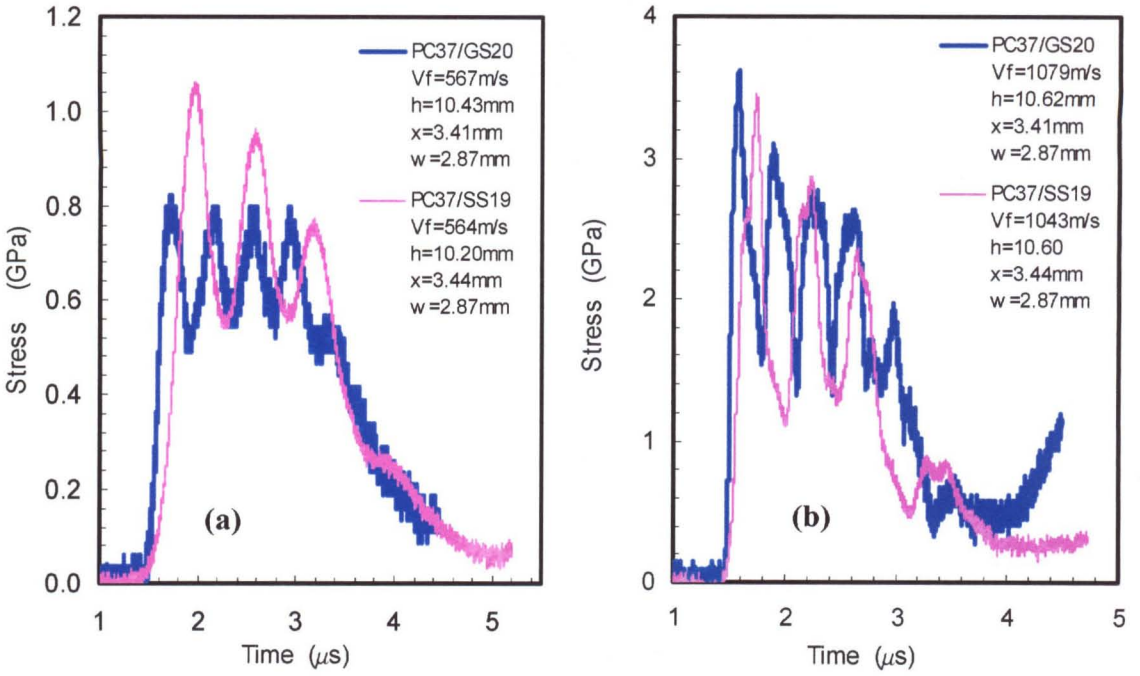

Figure 4.6 Influence of interface mechanical impedance mismatch on shock stress profile for the composites. h and w are specimen and flyer thickness, respectively; v_f is the flyer velocity and x is the distance from impact face.

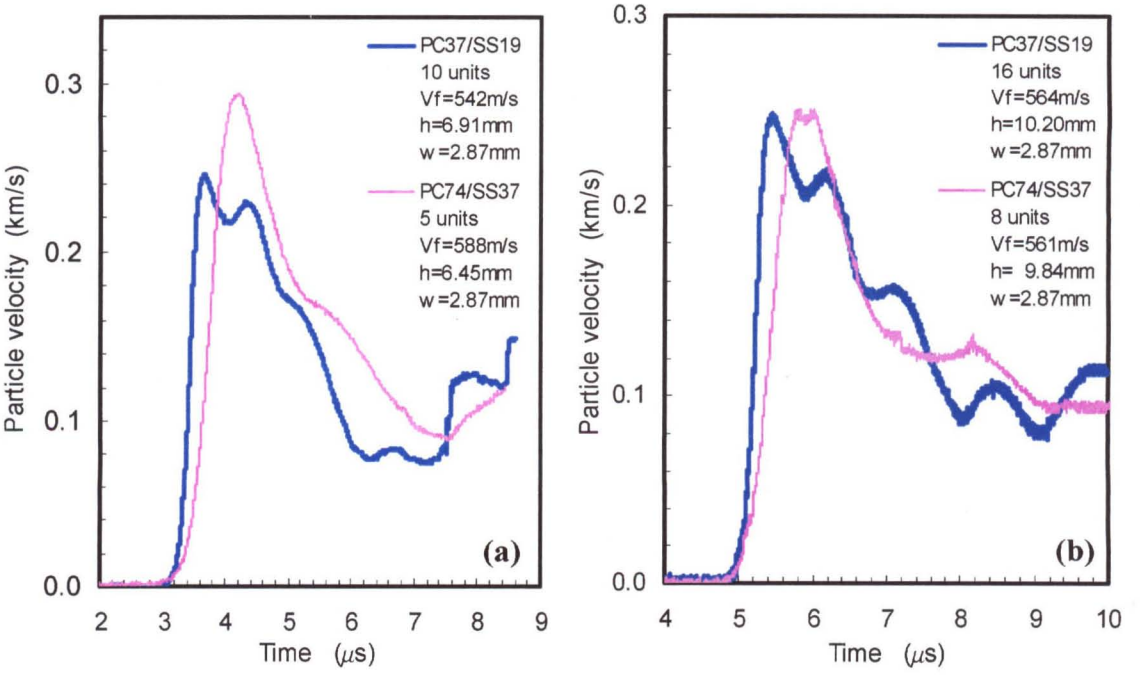

Figure 4.7 Influence of interface number on shock particle velocity profile for the PC/SS composites. h and w are specimen and flyer thickness, respectively; v_f is the flyer velocity.

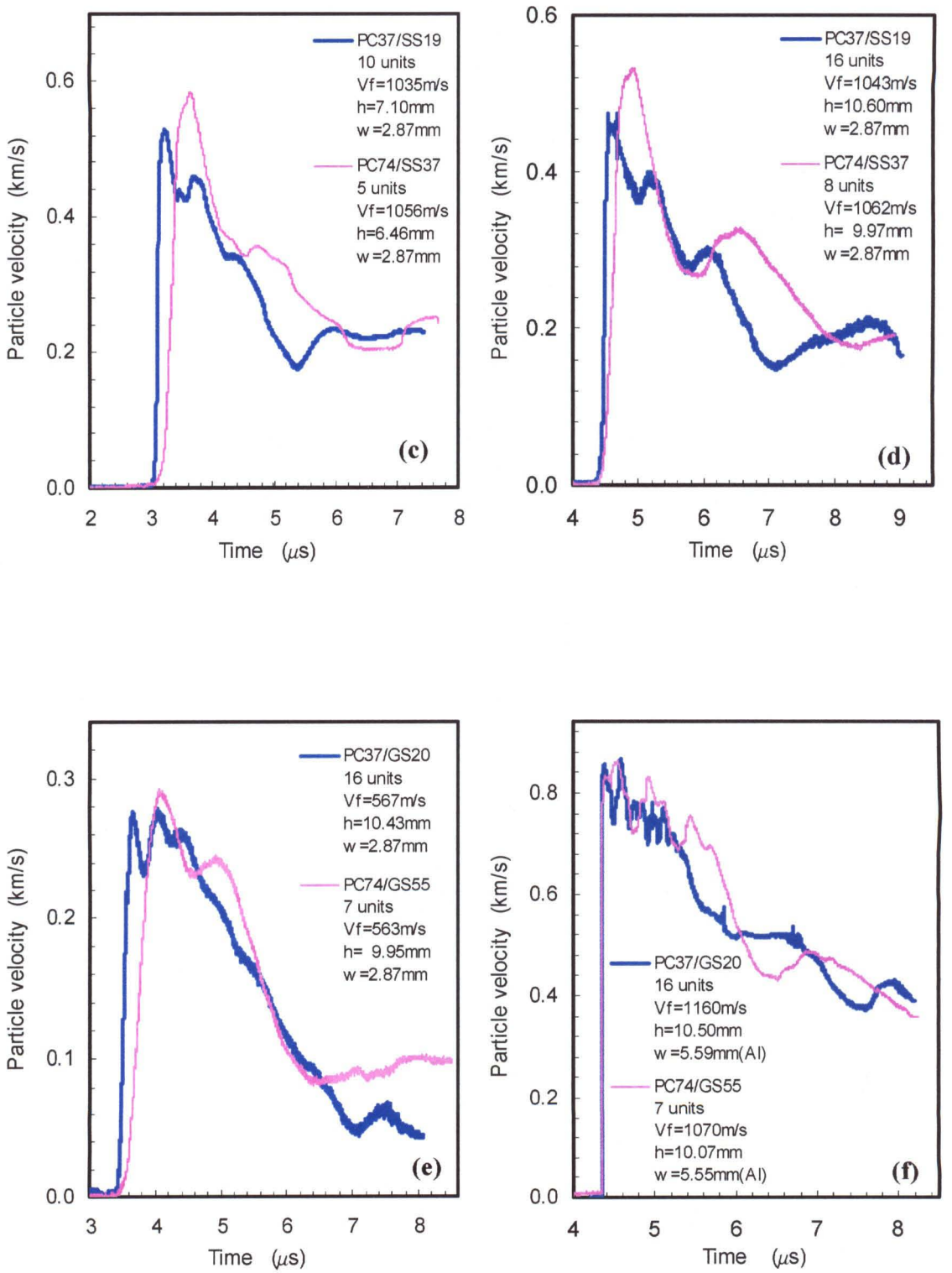

Figure 4.7 Influence of interface number on shock particle velocity profile for the PC/SS and PC/GS composites. h and w are specimen and flyer thickness, respectively; v_f *is the flyer* velocity.

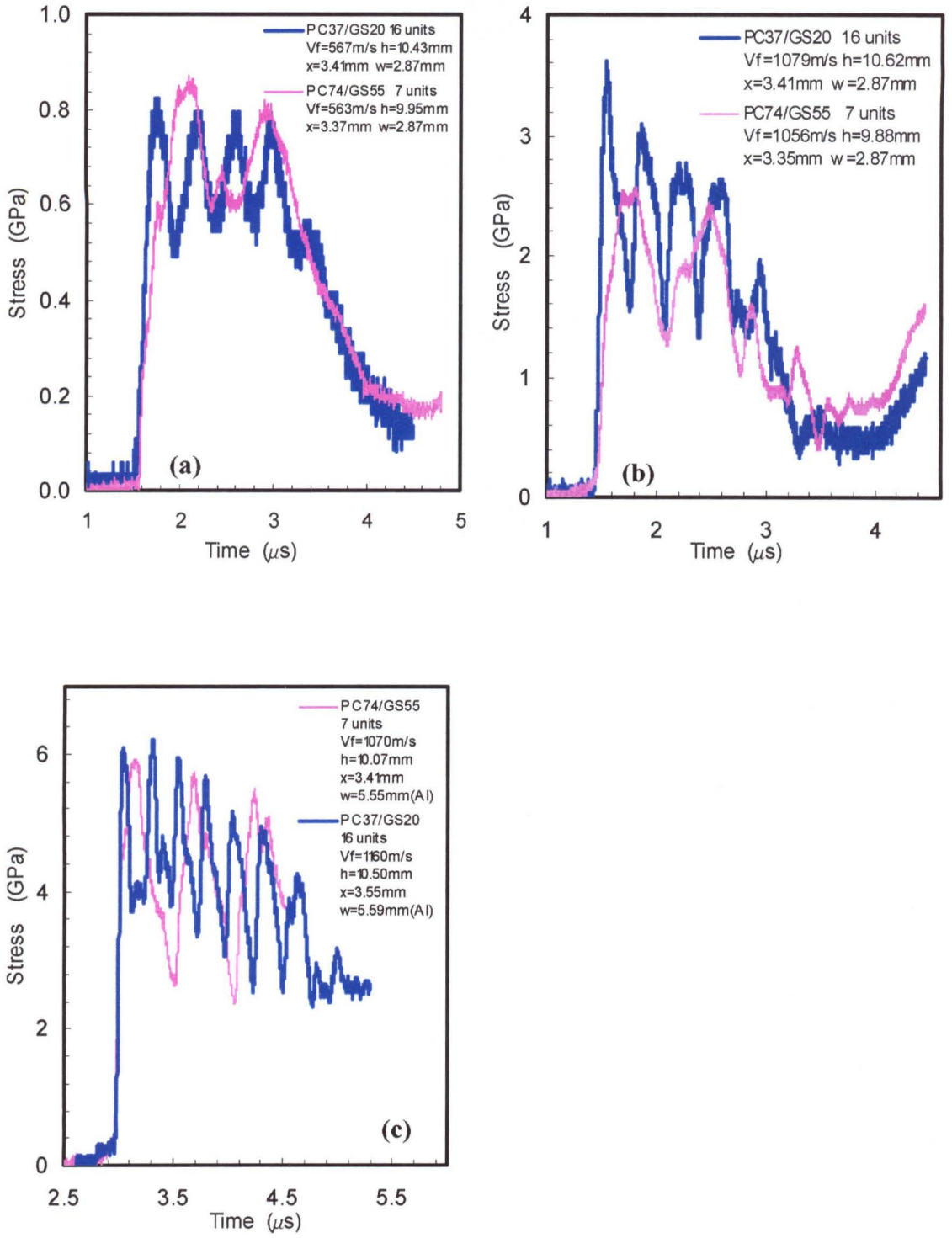

Figure 4.8 Influence of interface number on shock stress profile for the PC/GS composites. h and w are specimen and flyer thickness, respectively; v_f is the flyer velocity and x is the distance from impact face.

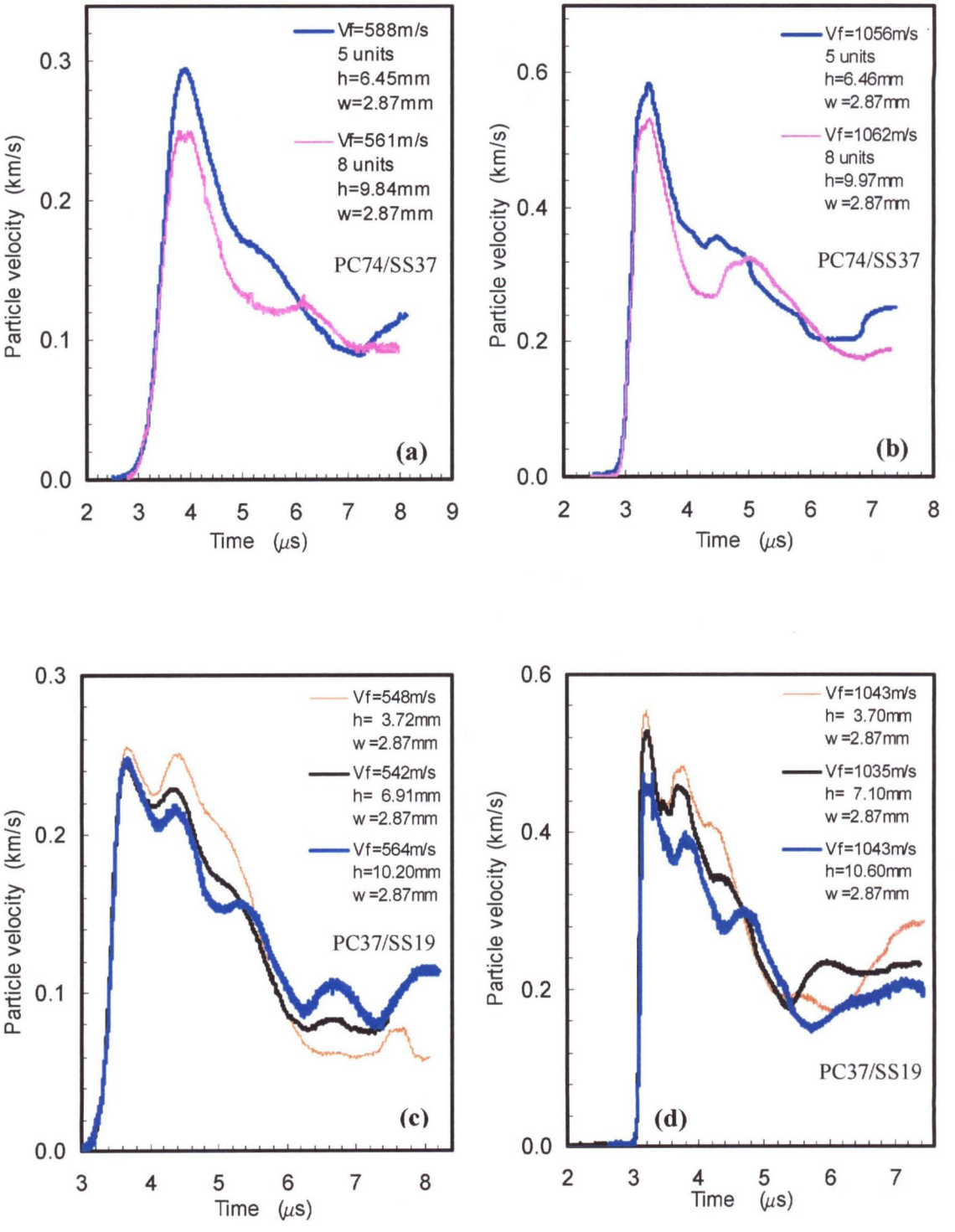

Figure 4.9 Evolution of shock particle velocity profile with wave propagation distance in the PC/SS composites. h and w are specimen and flyer thickness, respectively; v_f is the flyer velocity.

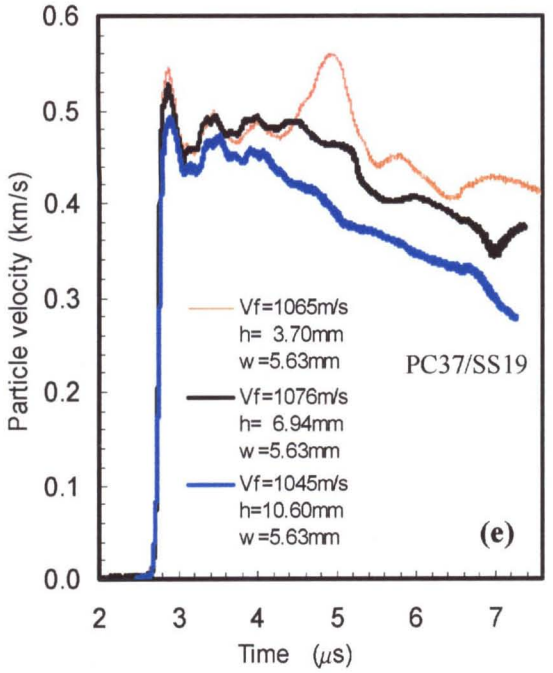

Figure 4.9 Evolution of particle velocity profile with wave propagation distance in composites.

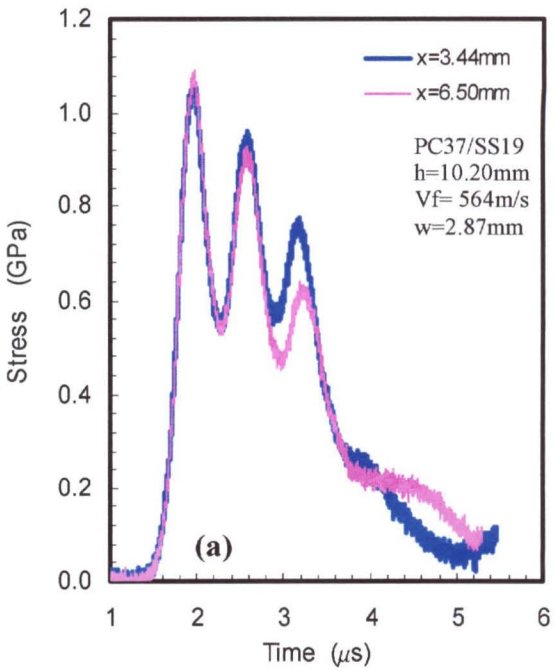

Figure 4.10 Evolution of stress profile with wave propagation distance in composites.

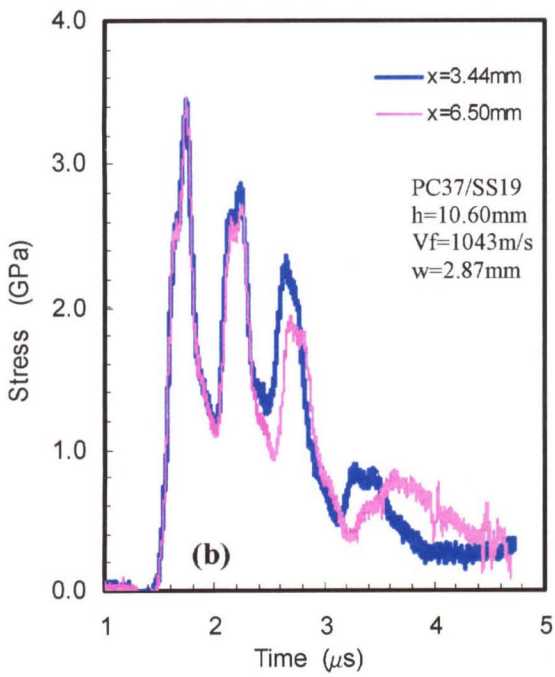

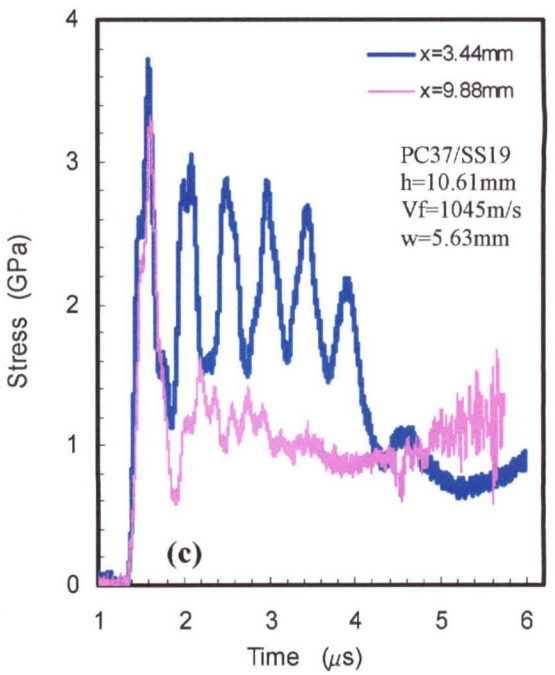

Figure 4.10 Evolution of shock stress profile with wave propagation distance in composites. h and w are specimen and flyer thickness, respectively; v_f is the flyer velocity and x is the distance from impact face.

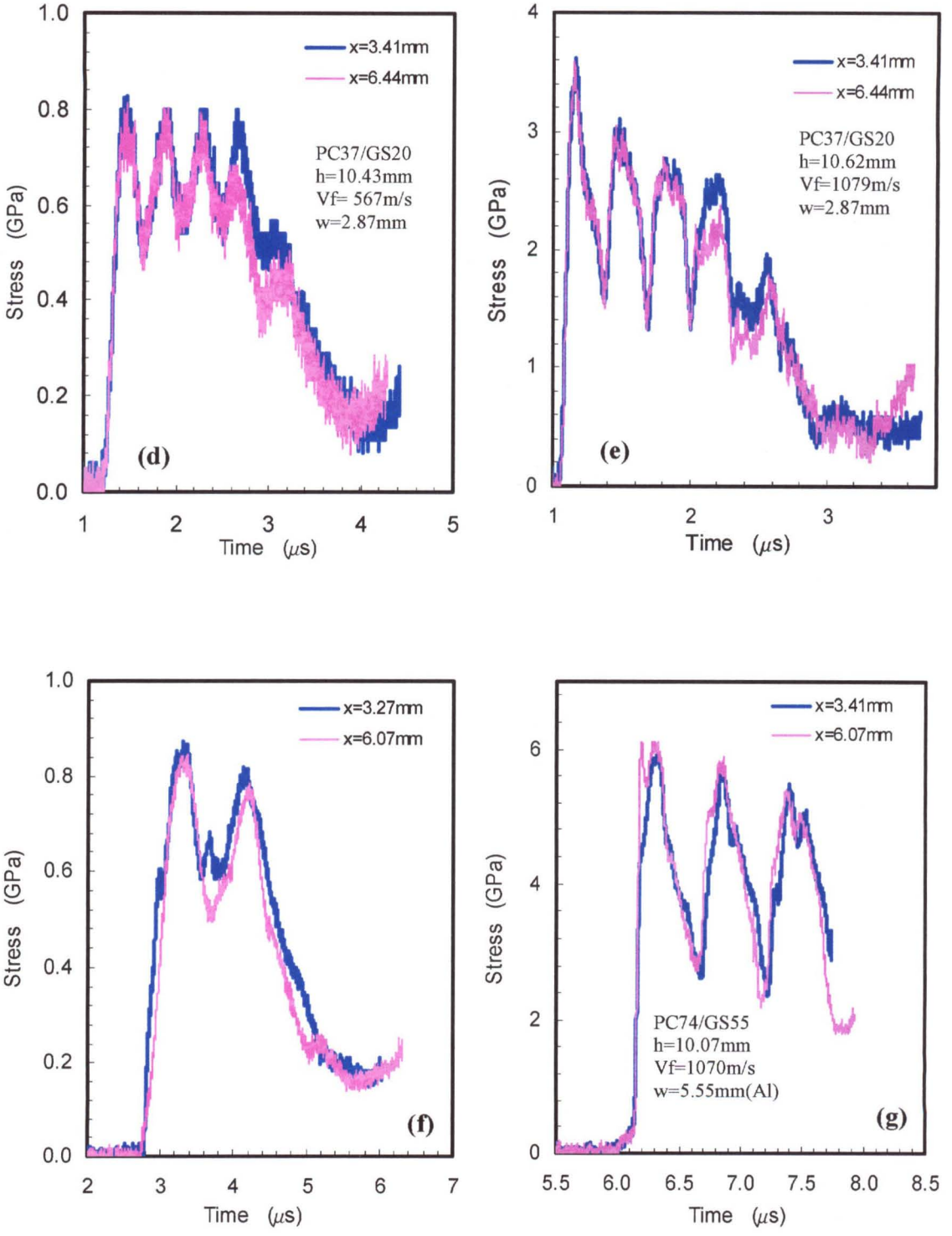

Figure 4.10 Evolution of shock stress profile with wave propagation distance in composites. h and w are specimen and flyer thickness, respectively; v_f is the flyer velocity and x is the distance from impact face.

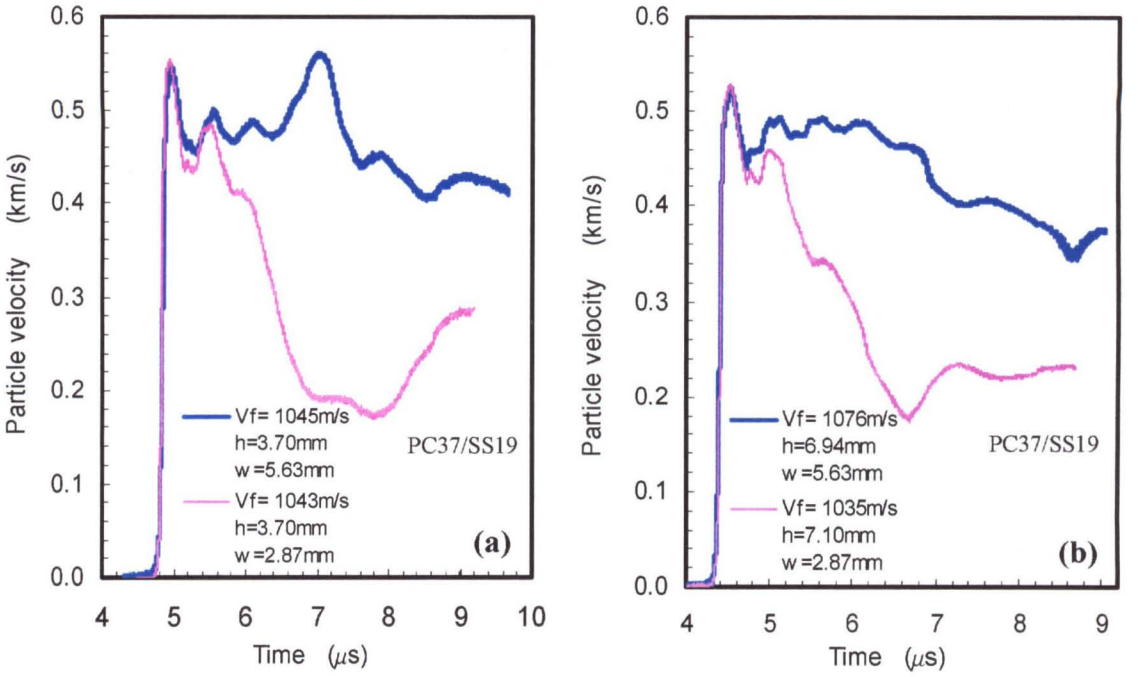

Figure 4.11 Influence of loading pulse duration on the propagation of shock wave in composites (velocity profile). h and w are specimen and flyer thickness, respectively; v_f is the flyer velocity.

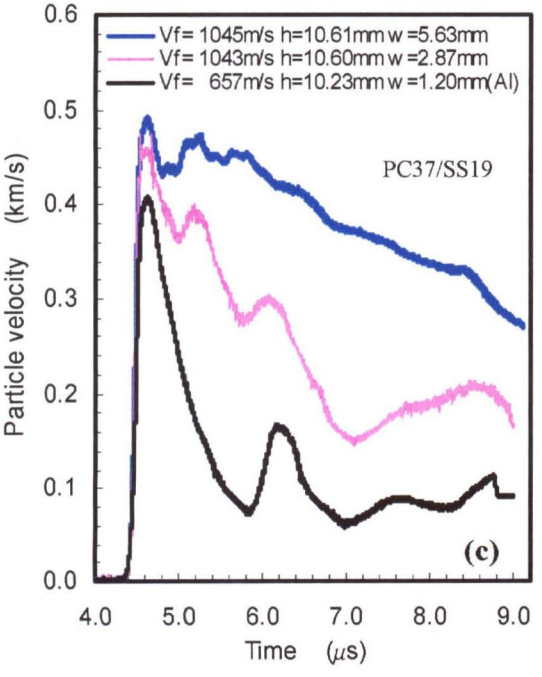

Figure 4.11 Influence of loading pulse duration on the propagation of shock wave (particle velocity profile).

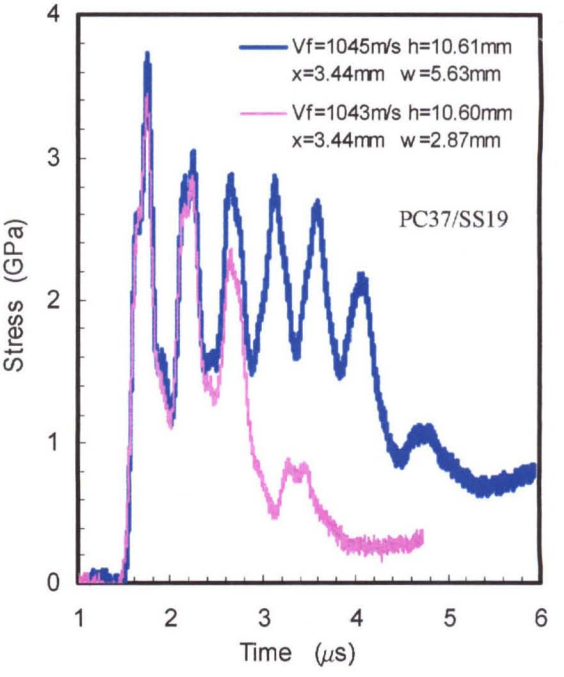

Figure 4.12 Influence of loading pulse duration on the propagation of shock wave (stress profile).

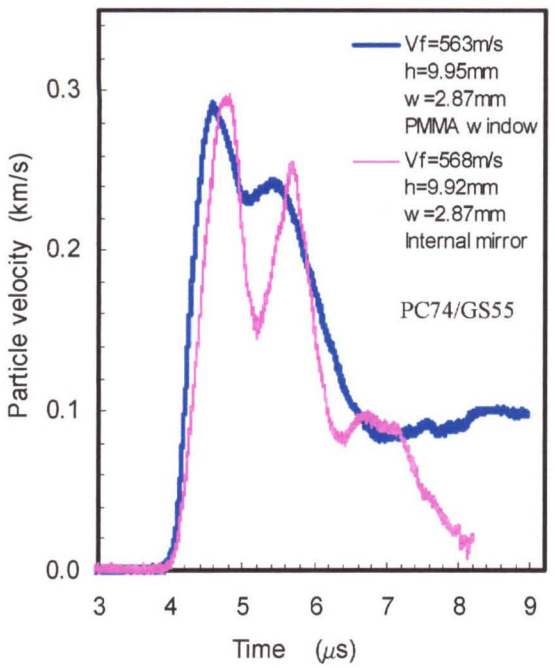

Figure 4.13 Influence of release wave on shock particle velocity profile.

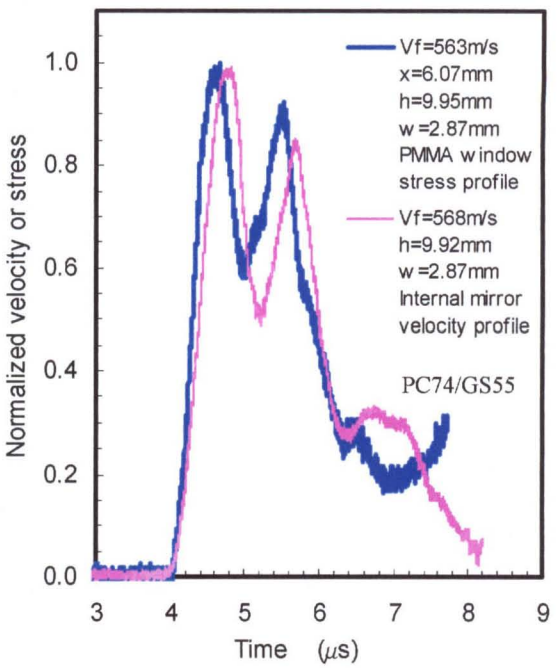

Figure 4.14 Comparison of stress profile with velocity profile at an internal interface.

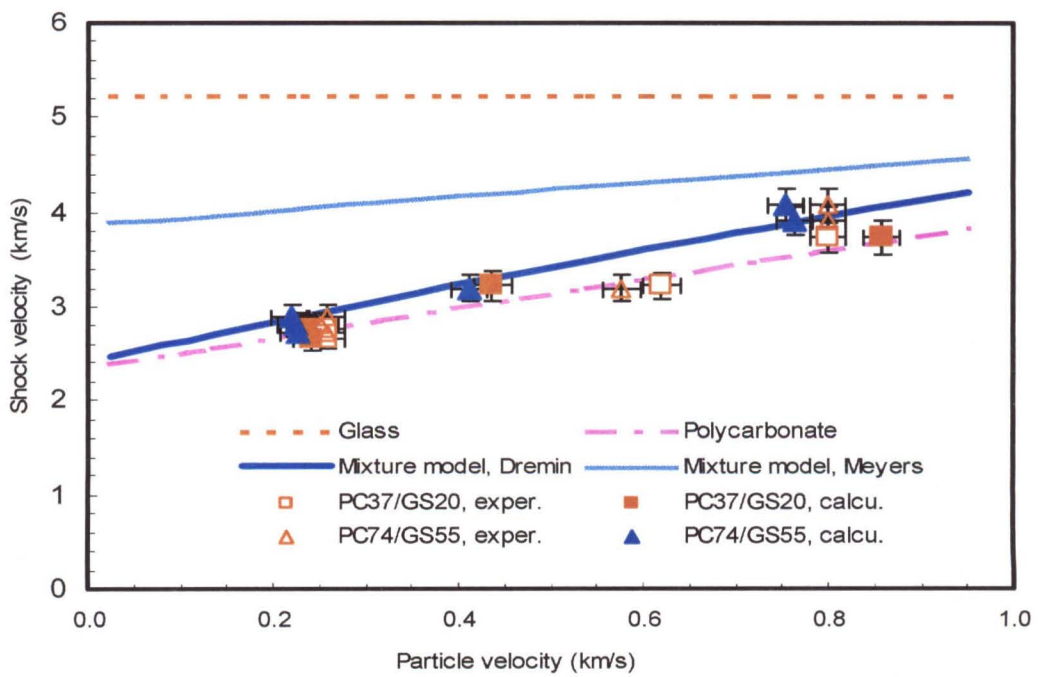

Figure 4.15 Comparison of PC/GS composite Hugoniots between experiments and predictions of mixture models, and the Hugoniots of their homogeneous components.

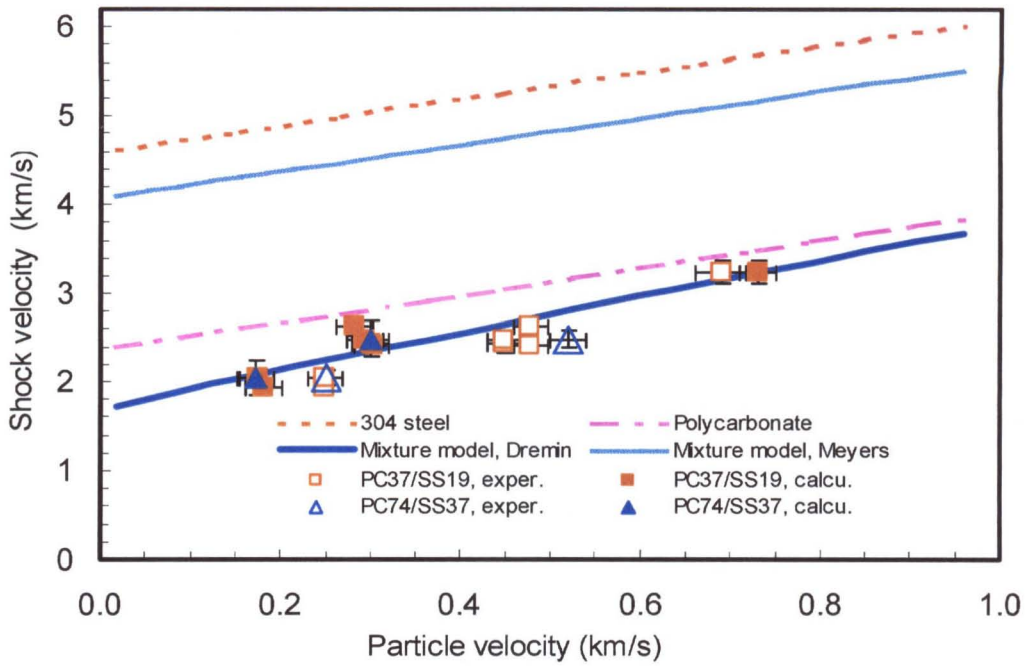

Figure 4.16 Comparison of PC/SS composite Hugoniots between experiments and predictions of mixture models, and the Hugoniots of their homogeneous components.

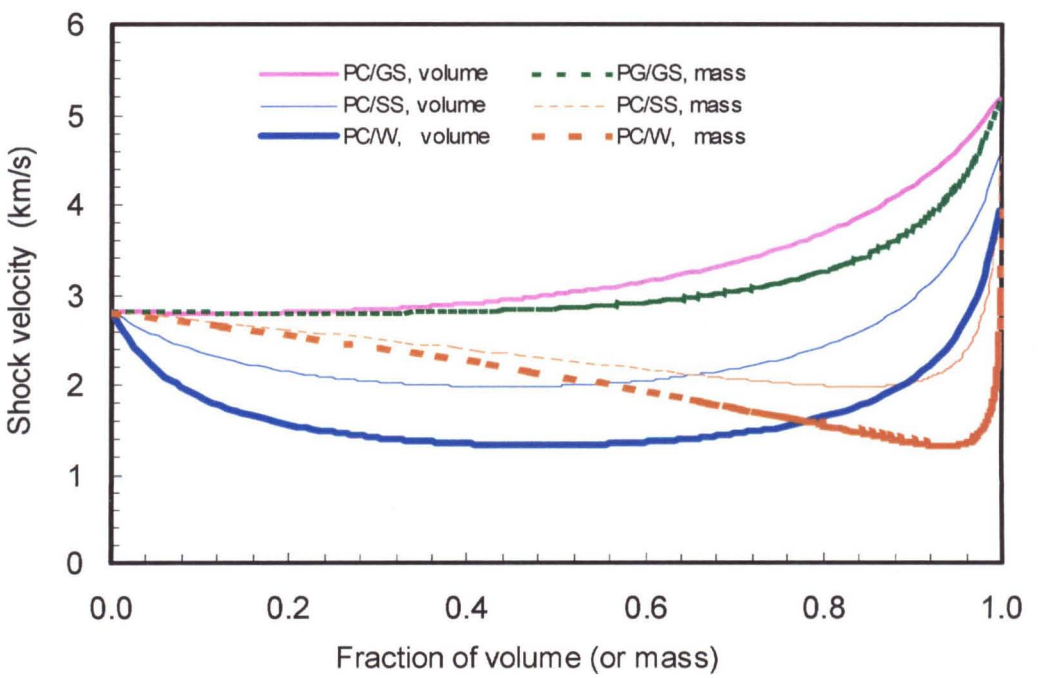

Figure 4.17 Shock velocity of layered composites as a function of volume (or mass) fraction of their hard layer at a constant shock pressure of 1.0 GPa for unit length of 1.12 mm.

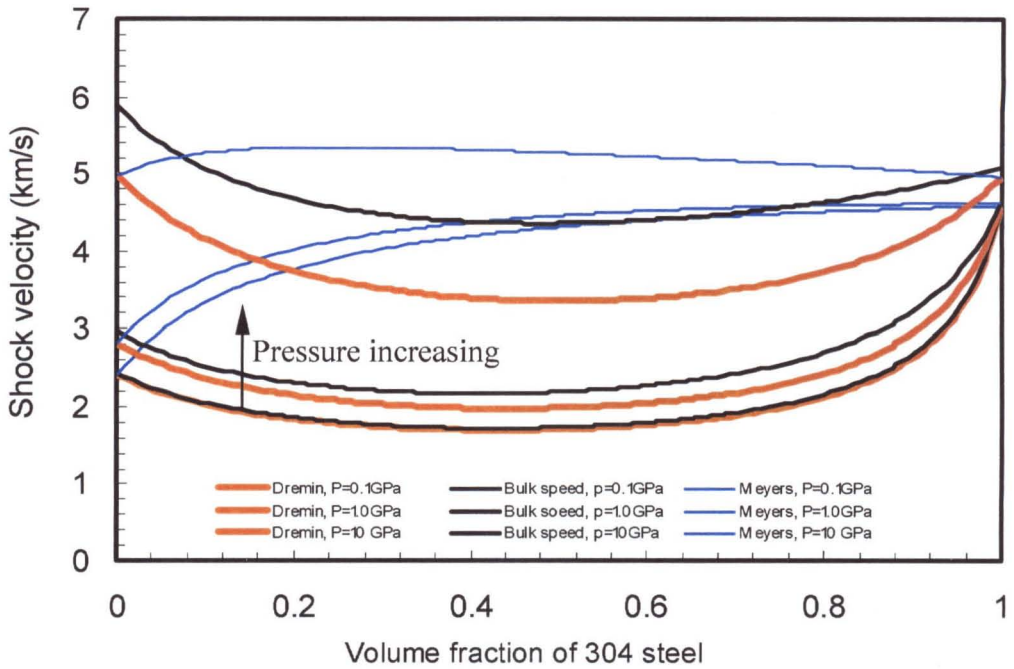

Figure 4.18 Shock velocity and bulk wave speed predicted by mixture models as a function of volume fraction of steel for PC/SS composites at different shock pressures.

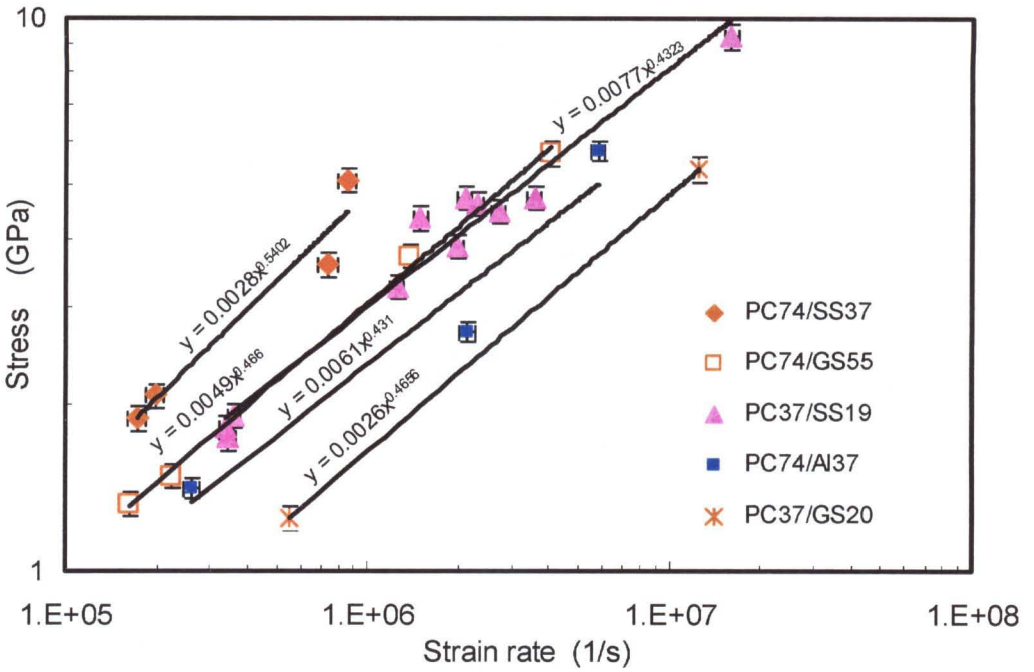

Figure 4.19 Shock stress vs. strain rate for the layered composites.

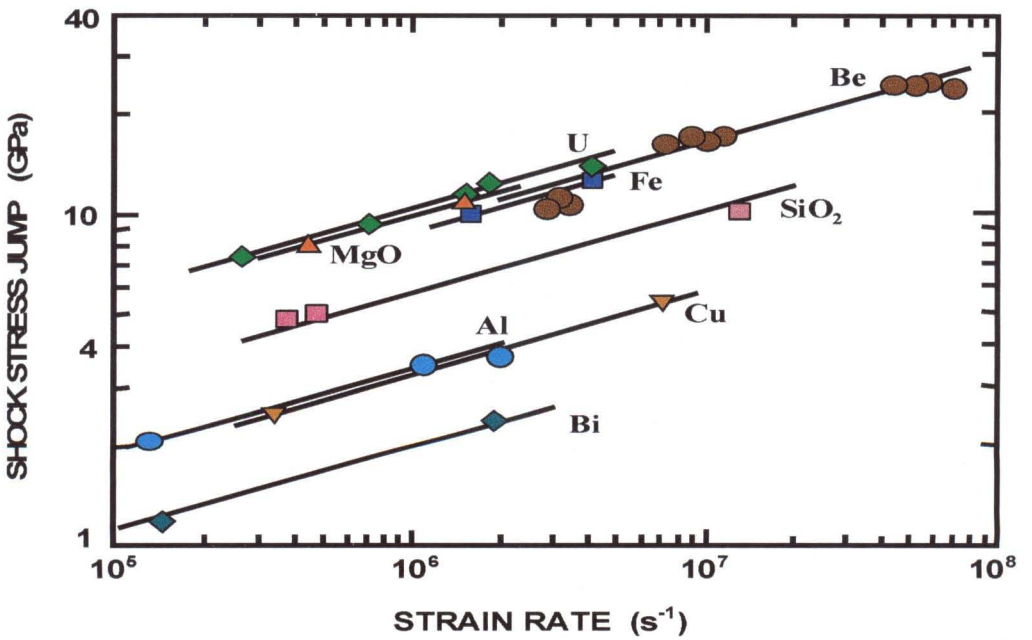

Figure 4.20 Shock stress vs. strain rate for the homogeneous media (adapted from reference 7).

Chapter 5

Numerical Analysis on Shock Wave Propagation in Periodically Layered Composites

5.1 Constitutive Models

In principle, stress wave propagation can be predicted by solving the equations of conservation of mass, momentum and energy subject to the appropriate initial and boundary conditions. However, the conservation equations are the general laws describing the motion of matter. They are not sufficient in themselves and must be supplemented by another equation that contains the information of the specific material behavior[1]. This equation is the so called constitutive relation or constitutive model, which specifies the relationship between stress, strain, particle velocity (or strain rate) and time. Since most of the constitutive models are phenomenological in nature, their specific form may be very different for materials with different physical and mechanical properties, or even for the same material under different loading conditions, e.g., stress state, loading rate, ambient temperature, etc.

For the purpose of simulating the shock compression process in periodically layered composite specimens with geometric structure described in Section 4.1, the constitutive description of the composites can be formulated in two ways. The first is to treat each component layer individually as a homogeneous material. The geometric structure of the simulated specimen reflects the difference between the components. The constitutive model of each component is exactly the same as the one used in modeling the dynamic response of the component material when it alone is subjected to shock loading. The simulations performed based on this model will

be referred to as the Full Structure (FS) Simulations. An alternative approach is to homogenize the mechanical properties of the composite over its entire geometrical structure using the mixture theory described in Chapter 2 and treat the composite as a homogeneous body. The simulations of the composite response to shock loading through homogenization of its properties are referred to as Composite Homogenization (CH) Simulations. The models for each of the homogeneous components and homogenized mixture used in this numerical simulation analysis are briefly described below.

5.1.1 Models for Homogeneous Components

The component materials of layered composites are polycarbonate (PC), 6061-T6 aluminum alloy (Al), 304 stainless steel (SS), D 263 glass and float glass (GS). The window material used in the shock compression experiments was polymethyl methacrylate (PMMA). The physical and mechanical properties of these materials are summarized in Table 5.1. For the purpose of simplification, the difference in the properties of two types of glasses was neglected and D 263 glass and float glass were treated in the same manner in this study.

5.1.1.1 Elastic Model for Glass (GS)

Glasses are typically brittle at room temperature. According to experimental studies conducted by Wackerle[2], and Barker and Hollembach[3], fused silica glass behaves as a nonlinear elastic solid up to the phase transformation at about 9.8 GPa. Its behavior is well approximated by treating it as a linear solid as seen in Fig. 5.1. Considering that the shock loading level in this study is in the range of 1 to 10 GPa, the D 263 and float glasses will be treated as linear elastic solids and their constitutive property is described by the Hooke's law[4].

5.1.1.2 Isotropic-Elastic-Plastic-Hydrodynamic (IEPH) Model

Metals are typically elastic-plastic materials. When they are subjected to a plane shock wave loading, the deformation occurs only in the direction of wave propagation, while the lateral motion is confined, i.e., state of uniaxial strain. Therefore, there is a stress exerted laterally on the material during the shock compression process as a shock wave propagates through it. If one invokes the Tresca yield criterion, the material yields only when the difference of stress in the wave direction from that in the lateral direction is equal to or larger than the yield stress.

In the simulation of shock compression in solids, it is customary to decompose the stress state into two parts: the average stress, which is associated with a uniform hydrodynamic pressure, and the deviatoric stress, which is associated with the resistance of the material to shear distortion[5]. The hydrodynamic pressure is responsible for the volumetric or bulk deformation, while the deviatoric stress responsible for the shear deformation or plastic flow.

In describing yielding and plastic flow, only the stress contribution from the shear distortion is considered. The deviatoric deformation is decomposed into elastic and plastic components. The deviatoric stress is calculated using the elastic strain and Hooke's law, and the yield surface is determined by the von Mises yield criterion (J_2 plasticity). Isotropic hardening is considered in the model and the influence of the hydrodynamic pressure on the hardening is also taken into account. The flow strength of a metal takes the form[4]

$$\sigma_y = \sigma_0 + E_h \bar{\varepsilon}^p , \tag{5.1}$$

where σ_0 is the initial yield strength, E_h is the plastic hardening modulus and $\bar{\varepsilon}^p$ is effective plastic strain.

The bulk behavior of the material is described by the Gruneisen equation of state (EOS). In order to use this EOS to calculate the pressure, an experimentally determined Hugoniot equation

must be provided, which is normally expressed in terms of shock wave velocity as a function of particle velocity. For most metals, a linear function is good enough, while for polymeric materials, higher order terms of the function need to be included to more accurately describe the response behavior. A particular form of the third order Hugoniot equation is

$$U_S = C_0 + SU_p + S_1U_p^2 + S_2U_p^3, \tag{5.2}$$

where U_s, U_p are shock velocity and particle velocity, respectively, C_0 is the bulk sound speed and S, S_1 and S_2 are experimentally determined coefficients. For most metals, S_1 and S_2 are taken to be zero.

Considering the fact that the shock pressure range achieved in this study of shock compression of solids is not extremely high, but much higher than the yield strength of each component, the constitutive behaviors of Al, SS and PC are all described by this IEPH model. The elastic parameters of each material are listed in Table 5.1, and the EOS parameters are listed in Table 5.2. Some of the mechanical properties were provided by the suppliers[6] and the rest are from other sources. The parameters for EOS were either taken from or obtained by fitting the data from the handbooks edited by Marsh[7] and Steinberg[8].

5.1.2 Model for Homogenized Mixtures

For the same reasons mentioned in the section above, the homogenized mixture of periodically layered composites needs to be modeled by an equivalent IEPH constitutive relation when it is subjected to a loading of plane shock wave generated by impact.

The bulk response of the homogenized composites to shock compression is described by the EOS of the mixture, which is obtained by a so called volume additive approach as described in Chapter 2. The description of this approach is not repeated here. The EOS parameters of PC/SS and PC/GS mixtures are listed in Table 5.2. The difference between the two types of geometric

structures (stacking) of PC/SS composites is neglected in this homogenization treatment, and only the homogenization of PC74/G55 composite will be discussed later.

To describe the distortion response of the mixture to shock compression by the IEPH model, three basic quantities, the shear strength, yield stress and plastic modulus, need to be specified. Again, the additive approximation method is employed here to determine these parameters for the elastic-plastic model of mixtures. Under the plane strain deformation induced by one-dimensional shock wave loading, it is assumed that (1) the strain in the direction of wave propagation is additive, (2) the force or stress in the lateral direction is additive, and (3) in the wave propagation direction, the local stresses in each component are equal to the mean stress of the mixture[9,10]. It will be seen later, based on the results of FS simulation analysis, that the assumption (3) may not be strictly true. However, by no means is it necessary for us to pursue a precise homogenization since some of the physical processes and their effects on the constitutive behavior of the composite, e.g., the role of scattering of the interface on viscosity, are still not clearly understood. The study of physical mechanisms of dissipation and dispersion due to scattering induced by microstructure and how to formulate a model taking into account its effects needs to be pursued further both experimentally and theoretically. The purpose of the present analysis is to approximately model the response of the composite through a homogenization approach and thus verify and validate the usefulness of existing models.

For plane strain deformation, the stress σ and strain ε in the wave propagation direction are related through Hooke's law,

$$\varepsilon_i = \frac{(1-2\nu_i)}{2\mu_i(1-\nu_i)}\sigma_i \qquad i = m,1,2\,, \tag{5.3}$$

and the lateral stress σ^l can be determined by

$$\sigma_i^l = \frac{\nu_i}{1-\nu_i}\sigma_i \qquad i = m,1,2\,, \tag{5.4}$$

where ν is Poisson's ratio, and subscripts *m*, *1* and *2* represent the corresponding variables in the mixture, and component 1 and 2 of the composite, respectively.

By additive approximation of strain in the wave propagation direction, and the assumptions (1) and (3) above,

$$\frac{1-2\nu_m}{\mu_m(1-\nu_m)} = \frac{1-2\nu_1}{\mu_1(1-\nu_1)}\alpha_1 + \frac{1-2\nu_2}{\mu_2(1-\nu_2)}\alpha_2 . \tag{5.5}$$

By additive approximation of lateral stress,

$$\frac{\nu_m}{1-\nu_m} = \frac{\nu_1}{1-\nu_1}\alpha_1 + \frac{\nu_2}{1-\nu_2}\alpha_2 , \tag{5.6}$$

where α_1, α_2 in equations (5.5) and (5.6) are the volume friction of components 1 and 2, respectively.

Similarly, the yield strength σ_y and the plastic hardening modulus, E_h, of the mixture are also estimated by the additive approximation as follows:

$$\sigma_y^m = \sigma_y^1\alpha_1 + \sigma_y^2\alpha_2 , \tag{5.7}$$

and

$$E_h^m = E_h^1\alpha_1 + E_h^2\alpha_2 , \tag{5.8}$$

where the superscripts *m*, *1* and *2* have the same meaning as the subscripts in the previous equations.

The parameters of the IEPH constitutive model, initial density and the parameters of EOS for the mixtures calculated by the additive approximation described above are listed in Tables 5.1 and 5.2, respectively.

5.2 Computational Tools

5.2.1 DYNA2D Code

The finite element code used in the numerical simulation of shock compression on layered composites is DYNA2D, which is a nonlinear, explicit, Lagrangian code, developed by Lawrence Livermore National Laboratory, for analyzing the transient dynamic response of two-dimensional solids[4]. This code features 4-noded isoparametric elements with several types of viscous and stiffness hourglass control. It incorporates many constitutive models that are available for simulating a wide range of material behavior including elasticity, plasticity, thermal effects, rate-dependence, and different types of EOS for accurate modeling of the hydrodynamic response of materials. In addition, it is capable of modeling contact interfaces including frictionless sliding, frictional sliding, tied interface and single interface contact. The options of rezoning and remeshing allow for analyzing problems which involve very large distortion and shape change.

The initial mesh of the DYNA2D is generated by MAZE, a preprocessor of DYNA2D[11], and the binary plot files output by DYNA2D are processed by ORION, a postprocessor of DYNA2D[12].

5.2.2 Geometry Definition and Initial Conditions

The DYNA2D code is used to carry out axisymmetric two-dimensional analysis of the shock compression of periodically layered composites impacted by a planar flyer. The specimen configuration is shown in Fig. 4.1 (Chapter 4). The soft and hard layers of the layered composite are repeated as many times as necessary to form a composite specimen with the desired thickness. Three different thicknesses, nominally 3.70 mm, 6.70 mm and 10.0 mm, of specimens were prepared and investigated experimentally to study the evolution of shock propagation in the

layered heterogeneous composites. For all specimens studied, the soft layer is PC of thickness 0.74 mm or 0.37 mm; the hard layer is one of the following: 0.37 mm Al, 0.37 mm SS, 0.19 mm SS, 0.55 mm GS and 0.20mm GS disks. By using a different hard layer material, a different type of composite is generated, and by varying the thickness of component layers, a specimen with different geometrical structure is obtained. In this study, three different types of composites with five geometrical structures were prepared, experimentally investigated and were numerically analyzed using DYNA2D. From the experimental results shown in the Chapter 4, and the numerical analysis results to be shown later, it is evident that both the mechanical properties and geometrical structure (or configuration) of the composite affect its response to the shock wave. The detailed configuration and dimensions of each composite specimen tested, which is to be numerically analyzed, were listed in Table 4.2. Again, following the convention used in Chapter 4, in naming the composites, the number following the abbreviation of the component material represents the component thickness in hundredths of a millimeter. For example, PC74/SS37 means that a 0.74 mm PC layer and a 0.37 mm SS layer forms a unit of the composite specimen (which is 38.1 mm in diameter).

In most experiments the flyer is a 2.87 mm thick and 32 mm in diameter PC disk. Since shock compression induced by the planar plate impact is uniaxial strain, the quantities of interest are mainly along the axis of the specimen, while the state of deformation near the periphery of the specimen, where it is affected by lateral release waves, is relatively not important. In order to save time involved in rezoning and/or remeshing due to the severe distortion of the mesh resulting from the interaction between the release wave at the corner of the flyer's lateral surface and the specimen's outer edge, the diameter of the specimen for simulation is taken to be the same as that of the flyer, i.e., 32 mm. The reduction of the specimen diameter does not result in any loss of generality and will not affect the results or conclusions of numerical analysis since the part of the specimen that is ignored is in the outer edge where it is dominated by the release wave

phenomena. PC flyer of thickness 5.63 mm was also used to achieve longer pulse of shock loading, and an Al flyer with thickness of 1.2 mm was used to produce a shorter loading pulse.

For most specimens, the shock compression experiment was performed with different flyer velocities, nominally, 600 m/s and 1,060 m/s. A few of specimens were loaded by a higher velocity PC flyer or the Al flyer at a velocity of about 1,100 m/s.

For the purposes of comparison, numerical simulations were also carried out for shock wave propagation in 9.97 mm thick homogeneous PC, SS and GS component materials. The flyer was a 2.87 mm PC disk and its velocity was 1,062m/s. These three specimens have exactly the same geometrical configuration as that in the experiment of 9.97 mm PC74/SS37 specimen; a 0.74 mm thick PC buffer layer and a 12.70 mm thick PMMA window plate are included.

The size of the 4-node elements in the direction of wave propagation is about 130 μm and the aspect ratio of the elements was chosen to be as close to 1 as possible. In some cases where the distortion may be much larger, the size of the elements was doubled. The interface between layers was treated as a frictionless slide line. In the numerical simulations, the increase in thickness of the specimen due to the adhesive bonding between layers was treated as increasing the thickness of the PC layer to include the bond thickness since the physical and mechanical properties of the epoxy adhesive are very close to those of PC.

In simulating the process of shock compression solids, it is necessary to introduce artificial viscosity. In the present simulation, the standard DYNA2D artificial viscosity was used for all materials except in one case where the 2.87 mm PC flyer impacts the 9.97 mm GS specimen, in which the linear shock viscosity coefficient was taken to be 10 times larger than the standard value and the quadratic shock viscosity coefficient about twice the standard value in order to reduce the initial overshoot of the shock profiles. The increase in artificial viscosity results in a much slower rise in the shock front for elements far away from the impacting surface (see Fig. 5.4).

5.3 Two-Dimensional Simulations

In this section, the numerical results of shock wave propagation in homogeneous component materials and heterogeneous composites are presented first. The deformation process of composites under impact loading is presented next and is followed by a critical comparison of the shock particle velocity and stress profiles between numerical simulations and experimental measurements. Finally, the results of the numerically predicted shock Hugoniot are compared with the mixture model. All numerical results presented here are the quantities on the symmetry axis, i.e., along the central axis of the disk. In all the simulations, the x-axis denotes the direction of the shock wave propagation and the y and z axes correspond to the lateral (transverse) directions. In some figures, y and z are also used to denote the time and pressure or velocity. With regard to the comparison of shock stresses between simulations and experiments, theoretically, the shock pressure and the shock stress in the direction of wave propagation are different and can be distinguished. Nevertheless, the measurement of shock stress in the wave direction obtained using the manganin stress gage is only an assumption. It is difficult to tell whether the stress gage measures the real shock stress in the wave direction or the shock pressure. Fortunately, the difference between the two becomes smaller as shock strength increases. For the shock loading level of interest in this investigation, shear strength of materials may not be ignored, but it is not a large quantity in most cases; therefore, in use of the terms, stress and pressure will not be strictly distinguished in the rest sections of this chapter.

5.3.1 Shock Wave Propagation

5.3.1.1 Homogeneous Solids

The shock particle velocity and stress time histories of all axial elements for the PC, SS and GS planar specimens impacted by a PC flyer at a velocity of 1062 m/s are shown in Figs. 5.2, 5.3 and 5.4, respectively. The thickness of the specimen and the flyer are 9.97 mm and 2.87 mm, respectively. It can be seen that upon the impact of flyer on the specimen, two shock waves originate at the impact surface, one propagates into the specimen and the other propagates into the flyer. When the shock wave in the flyer, which travels in the negative x direction, meets the free surface, it is reflected and a release wave is formed, which eventually propagates into specimen. The release wave is partially reflected and partially transmitted at the impact surface. The release wave propagates supersonically in the specimen, so it will eventually overtake the shock wave ahead provided the specimen is thick enough. The particle velocity and stress histories of the buffer and window elements are also shown in the plots.

For symmetric impact of a PC flyer on a PC specimen (Fig. 5.2), the particle velocity in the shocked state is one half of the flyer's velocity, and, as expected, both stress and particle velocity of shocked state are brought back to zero by the release wave. In the case of PC impacting onto SS or GS, the particle velocity in the equilibrium shocked state is less than half of the flyer's velocity, and the elements are in a tensile state of loading after the passage of the release wave. For the case of PC impacting SS (Fig. 5.3), due to the elastic-plastic behavior of steel, the wave front is two-wave structured during both shock loading and unloading processes. An elastic loading or unloading wave (precursor) propagates ahead and is followed by a plastic loading or unloading (shock) wave. When the waves reach the SS/buffer interface, and the buffer/PMMA interface, both waves are reflected and transmitted partially. The unloading waves reflected from the interfaces of SS/buffer interact with those coming from the free surface of the flyer, and a

tensile state is built up at the region where they meet. The elastic-plastic loading and unloading waves, as well as their interactions, can be clearly seen in Fig. 5.3. In the case of PC impacting GS, since GS is treated as an ideally elastic material, no two-wave structure is observed. Other features of wave propagation and interaction are similar to the case of PC impacting SS.

The initial overshoots on both particle velocity and stress profiles of SS and GS specimens are due to the inertial effect of sudden boundary loading by planar impact, which, in principle, can be reduced or eliminated by increasing artificial viscosity during simulation. However, in doing so, the slope of the shock front will also be reduced dramatically. The effects of increasing artificial viscosity on the wave profile can be seen in the plots in Fig. 5.4, where the linear artificial viscosity coefficient is 10 times larger than that of the standard value used in DYNA2D, while the standard DYNA2D viscosity were used in all other cases. If the artificial viscosity coefficients are increased in order to eliminate the initial overshoot of the shock profiles, the shock front at locations far away from impact will be unreasonably smoothed down.

According to the experimental observations in Chapter 4, and the work by Barker[13], Oved *et al.*[14], Lundergan and Drumheller[15], and Kanel *et al.*[16], the influence of scattering effects of interfaces (or dispersion) on the shock wave propagation in the composites is similar to that of the viscous effects of the material on the shock front structure. Since the nonlinear functional dependence of dispersion, or viscosity, on the heterogeneity properties and shock loading strength have not been systematically understood yet, detailed numerical investigation of the influence of 'shock viscosity' (due to dispersion or interface scattering) on the structure of the shock front will not be pursued here. Without loss of generality, as will be seen in the following sections, the use of standard DYNA2D artificial viscosity still makes it possible for us to qualitatively study the influence of viscosity on the structure of shock front when comparing the numerical results with experimental observations presented in Chapter 4 and also to shed light on the influence of interface scattering on apparent viscosity of the composite.

5.3.1.2 Periodically Layered Heterogeneous Composites

Numerical simulations were carried for the shock compression of PC/Al, PC/SS and PC/GS composite specimens under planar plate impact. Figs. 5.5 and 5.6 show the plots of shock particle velocity and stress time histories of all axial elements of a 9.97 mm thick PC74/SS37 specimen and a 9.95 mm thick PC74/GS55 specimen impacted by a 2.87 mm thick PC flyer at a velocity of 1,062 m/s and 563 m/s, respectively. One of the notable features is that the stress in the soft layer is generally higher than that in the hard layer, while the particle velocity distribution has the opposite sense, i.e., the velocity is higher in the hard layer in comparison to the soft layer, which indicates that the hard layer material contains relatively larger kinetic energy while the soft layer material experiences larger hydrodynamic compression during the shock compression process of composites. In the sense of geometric distribution average, the composite does not, and may possibly never, reach an equilibrium state in the conventional sense, though a steady state does exist since the shock time histories of corresponding elements in each unit, which is located several units away from the impact surface, correspond very well.

From Figs. 5.5 and 5.6, it is seen that the difference in stress and/or particle velocity between hard and soft layers is determined by the difference in mechanical properties between them. Generally, the larger the mechanical impedance mismatch between the layers, the larger the difference in stress and particle velocity between the layers. Also, notice from Fig. 5.6a that for the PC/GS composite, there exists a large stress gradient at the interface, but it is not the case for the PC/SS composite. It will be seen later (Figs. 5.26 and 5.27) that for PC/SS composites, the time average of stress profiles is the same for the elements at both sides of the interface though their oscillation amplitudes are quite different, while for PC/GS composites, both the oscillation amplitude and the average of the stress profile are different for the two materials across an interface.

The spatial profiles of a shock wave in PC/SS composite are shown in Figs. 5.7 and 5.8 for different time instants after impact loading. The results are the same as shown in Fig. 5.5, but plotted in a different way. Fig. 5.7 shows the profiles in the early stage of impact loading, and Fig. 5.8 shows the steady state profiles when the shock is about to be reflected by the PMMA window. The time interval between the curves is 30 ns. It can be seen that the stress in the soft (PC) layer is much more uniformly distributed within each layer during the whole process of shock compression. But, in the hard (SS) layer there exists a very large spatial stress gradient during most of the period of shock compression. As far as the spatial distribution of particle velocity is concerned, the behavior in the hard and soft layers is interchanged, i.e., the velocity in the hard layer is uniformly distributed and monotonically increases with time, while a very large velocity gradient exists in the soft layer.

These features of wave propagation in layered composites are attributed to the interactions of multiple reflections of the incident wave. The incident waves in both hard and soft layers are compression waves. But the reflected wave in the hard layer is different from the one in the soft layer. Reflected waves in the soft layer are compressive, while in the hard layer they are tensile. The reflected tensile wave decreases the stress or pressure in the hard layer, but increases particle velocity in the initial shock direction. Conversely, reflected compressive wave in the soft layer increases the stress or pressure and decreases the particle velocity in the direction of propagation of the initial shock.

Briefly going through the process of propagation and interaction of waves in the first two units of the composite may be helpful in understanding many of the features illustrated through the simulations. For the case of a PC flyer impacting the PC/SS composite, the surface layer is PC, labeled as PC1 in Fig. 5.5 and unlabeled in Figs. 5.7 and 5.8. Note, in this section, the one number following the name of layer material represents unit number of the layer component, rather than the thickness of the layer. Due to the symmetric nature of impact, a steady shock wave with particle velocity equal to half of the flyer velocity is generated and propagates into

PC1. Upon reaching the interface of PC1/SS1, the shock wave is partially reflected and partially transmitted. Both the reflected wave and the transmitted wave are compressive. Due to further compression of the reflected wave, the pressure in the PC1 layer increases, while, at the same time, the motion of the particle in the initial shocked direction is slowed down, since the reflected wave in PC1 moves backward with respect to the initial shock wave. When the transmitted shock wave from PC1/SS1 interface propagates in the SS1 layer and meets the interface SS1/PC2, it is again partially reflected and partially transmitted. This transmitted wave is still a compressive wave, but, the reflected wave at this interface is not compressive any more. Instead, it is a rarefaction wave, which speeds up the motion of the particles in the initial shock wave direction and relieves the compression of the particles inside the layer (SS1). The interaction of the incident compressive wave and the reflected rarefaction wave, as well as the multiple reflection of waves at later time, results in a large stress gradient and an almost uniform particle velocity distribution in the SS layer. In the PC2 layer, both the incident wave from the SS1/PC2 interface and the reflected wave from PC2/SS2 are compressive; the resultant state is that of almost uniform stress and a large velocity gradient during most of the period of shock compression. This pattern of pressure and particle velocity distribution and the evolution with time repeat in the later units of the composite. From Figs. 5.7 and 5.8, it can also be seen that due to the interaction between the shock wave and multiple reflection of waves, the phases of velocity and stress of the resultant wave are not synchronous, as they were for a shock wave propagating in a homogeneous medium.

For a shock wave with particle velocity of 500 m/s propagating through a 2.22 mm thick homogeneous PC layer and then a 1.11 mm thick homogeneous SS layer, it takes about 0.95 μs. But, according to the results of numerical simulations shown in Figs. 5.7 and 5.8, it takes about 1.5 μs for a shock wave with equivalent strength to propagate through three units of PC74/SS37 composite with an equivalent thickness of 3.33 mm. Besides, it can also be observed that the maximum stress of the shock front is far from being reached in the third SS layer at 1.5 μs after

impact, and though the maximum stress is reached in the third PC layer, the maximum velocity has not yet been achieved.

Based on the numerical simulation results, as well as experimental measurements presented in Chapter 4, and the analysis above, it can be concluded that *it is due to the interaction of multiple reflection (compressive and/or rarefaction) waves with the incident shock wave, that the effective propagation velocity of shock wave in the layered composites is slowed.*

Figure 5.9 shows the maximum stress and maximum velocity experienced by each of the axial elements during the propagation of a shock wave in a PC74/SS37 specimen impacted by a PC flyer at a velocity of 1,062 m/s. On one hand, it is seen that the maximum stress in the PC layer increases with the propagation distance and reaches a steady state around the end of the fifth unit, i.e., about 5.55 mm away from the impact surface. The maximum stress is almost unchanged in all SS layers, though there is a small drop observed at the third and fourth layers. On the other hand, the maximum velocity in the SS layer increases with propagation distance, while in PC layers it is almost a constant except in the first layer.

It is generally expected that the transient distance for a shock wave to reach a steady state after being generated by impact varies with the loading level. For shock wave propagation in the PC74/SS37 and PC74/GS55 composites, the transient distances (number of units) as a function of loading strength, i.e., the velocity of a PC flyer, are numerically obtained and listed in Table 5.3. Also, shown in the Table 5.3 are the average maximum pressure experienced by the hard layer, the upper and the lower limits of the maximum pressure experienced by the PC layers, and the ratios between them. It is seen that for PC74/SS37 composites, the longest transient distance for a shock wave to reach steady state corresponds to the loading condition of lowest flyer velocity. However, the lowest ratio between the maximum pressures experienced by the SS and PC layer does not correspond to the lowest loading strength. The lowest flyer velocity simulated is 140 m/s, while the longest shock transient distance and the lowest P_h / P_u occur at a flyer velocity between 280 m/s and 560 m/s. For flyer velocities beyond this point, the transient distance to

reach a steady shocked state decreases and the ratio of the maximum pressures increases with increasing flyer velocity. For the PC74/GS55 composites, the shock transient distance decreases with increasing loading, but the ratio of the maximum pressure seems not to be sensitive to the change of loading strength. The reason for the tendency of the change in transient distance with shock loading for the PC/SS composite may be intimately related to the properties of the components, the interaction between waves and the length scale associated with the heterogeneity. It may also be postulated from the results listed in Table 5.3 that the dependence of transient distance of shock wave on loading level in layered composites becomes stronger for flyer velocities higher than about 1,000 m/s for PC/SS composites and 800 m/s for PC/GS composites, respectively.

5.3.2 Deformation of Layered Composite Under Planar Impact

Figure 5.10 illustrates the deformation process of a 9.97 mm thick PC74/SS37 layered composite impacted by a 2.87 mm thick PC flyer at a velocity of 1,062 m/s at 0, 2, 4 and 6 μs after impact. The plots consist of two parts: the left half is the distortion of the finite element mesh, and the right half is the vector field of particle velocity. The largest distortion occurs in the area around the corner of the lateral surface crossing the impact surface where the edge release wave originates. The lateral release wave propagates radically inwards. Due to this release wave, the particles in its affected area gain lateral velocity. With shock propagation, the distortion area becomes larger, while at the same time, the area dominated by uniaxial strain becomes smaller. This occurs even though the shock state in the area around the axis of the disk is still in one-dimensional plane strain compression even at 6 μs after impact, as can be seen from the velocity vector field. It takes more than 4 μs for the shock wave to propagate through the PC74/SS37 composite of thickness 10 mm (with buffer), indicating that the shock velocity in the composite is

slow in comparison with homogeneous solids. Indeed, it is even slower than shock speed in either of its components. The reasons for this were discussed in the previous section.

Numerical simulation results shown in Fig. 5.10 indicate that the PC layers have much larger lateral deformation (extrusion) than SS layers. It may be interpreted that, as shown in the last section, the pressure in the PC layers is larger than that in the SS layers, and hence larger lateral release waves are developed in the PC layers. Therefore, the lateral outward motion of the PC elements is faster. On the other hand, the SS particles are heavier (higher density), so even when they are subjected to the same force, they will move slower than the PC particles. As a result, the lateral displacement of PC is much larger. In this numerical simulation, the interface between PC and SS layers was treated as a frictionless slide line. Considering the large difference in strength between the two materials and the high level of loading, this is not a bad approximation.

5.3.3 Comparison of Shock Particle Velocity Profiles Between Simulations and Experiments

In this section, the shock particle velocity profiles obtained from the numerical simulations will be compared with those measured experimentally by VISAR (see Chapter 4). Since the mirror reflecting laser light back to the VISAR was located at the interface between the PC buffer layer and PMMA window, the numerical particle velocity profile to be compared is taken from the velocity time history of the element located at the window side of the buffer/window interface. Due to the delay of the response of the capped electric shorting pins or possibly the earlier trigger due to the blowoff of high pressure gas from the gun muzzle, the trigger time of the oscilloscope in the experiments may not be exactly the instant when the flyer arrives at the specimen surface. Therefore, the recorded arrival time of the shock particle velocity profile by VISAR is not a good measure of propagation time of the shock wave in the specimen. Similarly, the starting time of shock profiles shown in the plots does not represent the exact propagation time of the shock

wave. It is obtained by randomly shifting either experimental profiles or simulated profiles for the purpose of comparison. The shock wave speeds predicted by numerical simulation are obtained by checking the time difference of shock propagation though two points inside the specimen. The numerical results are compared with experimental measurements for three types and five geometric structures of layered composites in the following sections.

5.3.3.1 PC74/Al37 Composite

Three 6.60 mm thick PC74/Al37 specimens that were studied experimentally were simulated under planar impact loading conditions. The PC flyer thickness is 2.87 mm and flyer velocity is, nominally, 600 m/s, 1,060 m/s and 1,800m/s for each of the three specimens, respectively. The numerical results are compared with experimentally measured shock velocity profiles in Fig. 5.11. On the whole, the computed profiles are consistent with the experimental results, but the differences in the detail of the profiles are obvious. In the case of lowest flyer velocity (600 m/s), the shock fronts of experimental and computed profiles happen to be coincident with each other when the standard artificial viscosity of DYNA2D is used in the simulation. With the increasing flyer velocity, the difference of shock front slope between the two becomes larger. For the resonant oscillations on the top of the shock profiles, which is attributed to the interaction of shock wave with multiple reflections within the layers, the predicted amplitude decreases with the increase in flyer velocity, while in experimentally measured profiles, the amplitude increases with increasing flyer velocity. The duration of oscillation in the experimental profiles is slightly shorter than that predicted by computation. Furthermore, as a whole, the measured shock pulse length is shorter than the numerically predicted one, which implies that the actual sound velocity in the shocked state of the composite is larger than that predicted by simulation. Another difference between experiments and simulations is the decompression process, especially in the

later stages. The simulation predicts a much lower residual particle velocity state than the experimental observation shown for the lowest released state. This will be more clearly seen in the cases of other composites in the subsequent sections.

5.3.3.2 PC74/GS55 Composite

Figure 5.12 shows the comparisons between experiments and simulations for the nominal 10 mm thick PC74/GS55 composites impacted by PC flyers at velocities of nominally 600 m/s, and 1,060 m/s, and Al flyers at velocities of 1,070 m/s. The analysis techniques in the section above for studying the shock compression of PC74/Al37 composites are also applied here. Shown in Fig. 5.12d is the case where the velocity profile has reached the steady state inside the composite without disturbance from the release process originating from the buffer/window interface as in all other experiments. For this experiment, as described in Chapter 4, the specimen was prepared in the same way as others, but, instead of bonding a buffer and a window after the seventh unit, eight more composite units were used. Since both PC and GS layers are transparent, the function of the later eight units is the same as the PMMA window. The first seven units made up the specimen. The front surface (facing the arriving shock wave) of the eighth unit was a mirror surface. In the specimen prepared in this way, the shock wave would not be disturbed by the release wave originating from the buffer/window interface. Comparing plot *d* with *a* in Fig. 5.12, it is seen that the oscillation amplitude is larger for the profile of the corresponding internal point, which implies that the disturbance in the shock profile due to the release process reduces the effects of interface scattering on wave propagation. Apart from this, the differences between the computation and experiment are similar to those discussed in the previous section.

5.3.3.3 PC37/GS20 Composite

Two specimens of 10.50 mm thickness were studied experimentally and simulated numerically. One was loaded by a 2.87 mm thick PC flyer at a velocity of 567 m/s, and the other was impacted by a 5.59 mm thick Al flyer at a velocity of 1,160 m/s. The Al flyer produces a shock pulse length equivalent to that produced by a 2.87 mm thick PC flyer under the same loading condition. In this type of specimen, since the thickness of layers was reduced to about half of the thickness of layers used in the PC74/GS55 type composite, the interface density (interface area per unit volume) increased, while the volume ratio of two components is about the same as that of PC74/GS55. The simulation results are compared with the experimental results in Fig. 5.13. For the case where the specimen was loaded by a 2.87 mm thick PC flyer at a velocity of 567 m/s, it appears that the only difference between experiment and simulation is the resonant oscillation part of the profile, while the mean amplitude of the oscillations are in good agreement. At the higher loading level achieved by the Al flyer, the differences are large in both loading and unloading processes. In principle, the slower rising slope of the simulated shock front can be fixed by reducing the artificial viscosity and the size of the elements, but it was not pursued here.

The detailed study of the structure of the shock front requires the formulation of new types of constitutive models, which can take into account not only the dissipation processes (e.g., dislocation, twinning, defects, etc.) in the homogeneous components, but also dispersion and dissipation due to microstructure (e.g., the grain boundaries, particle/matrix interfaces, fiber/matrix, etc.) scattering effects to the waves.

5.3.3.4 PC74/SS37 Composite

The comparisons of numerical results with the experiments are shown in Fig. 5.14 for PC74/SS37 layered composites. Two types of specimens, with thickness nominally 6.50 mm and 10.0 mm,

were shock loaded by planar impact at two different flyer velocities, nominally, 600 m/s and 1,060 m/s, respectively. In general, the simulation results agree well with the experimental measurements except at the later unloading stage. At this stage, the numerical analysis predicts a much faster unloading process and indicates that the specimen can be unloaded to a tensile state, which has not been observed in any of the experimental measurements. Comparing Figs. 5.14a with 5.14b, and 5.14c with 5.14d, it is seen that the attenuation of shock peak predicted by the numerical simulation is smaller than that measured experimentally, which may be due to the interface scattering effects that are not taken into account in the models used in the present simulations.

5.3.3.5 PC37/SS19 Composite

For this type of composite, three different thicknesses of specimens, nominally 3.70 mm, 7.00 mm and 10.20 mm, were studied experimentally and analyzed numerically. Figs. 5.15a and 5.15b show the experimental and computational results for the 3.70 mm thick specimens impacted by 2.87 mm PC flyers at velocities of about 600 m/s and 1,060 m/s, respectively. Figs. 5.15c and 5.15d are the results for the 7.00 mm thick specimens under similar loading conditions. Figs. 5.15e and 5.15f are the results for 10.20 mm thick specimens. The general pattern of the profiles is similar to those discussed in the previous sections. At the low flyer velocity, the simulated shock fronts agree reasonably well with experimental measurements for all three thicknesses, while the differences become evident for the loading at flyer velocity of 1,060 m/s. Again, the unloading at later stages predicted by numerical simulations is much faster than that observed experimentally. The attenuation of the shock peak observed experimentally is faster than the numerical prediction. Since the duration of the experimentally measured shock pulses are generally shorter than numerical predictions, it is postulated that the actual sound speed of

shocked state is larger than the numerical prediction. Comparing Fig. 5.15a with 5.15c and 5.15e, as well as Fig. 5.15b with 5.15d and 5.15f, it is seen that the amplitude of resonant oscillation predicted by simulation increases with the propagation distance. However, the experimental results show that the amplitude of oscillations decreases with propagation distance, which may be attributed to neglecting the interface viscosity in the numerical model.

The influence of loading duration on the shock profiles was also investigated both experimentally and numerically. For the shorter pulse case, a 1.2 mm Al flyer was accelerated to a velocity of 660 m/s and impacted a 10.20 mm thick specimen. The loading strength generated by this is equivalent to that of a PC flyer at a velocity of 1,060 m/s. The experimental and numerical results are compared in Fig. 5.15g. For the longer pulse loading, a 5.63 mm thick PC flyer was used at a velocity of 1,060 m/s. The corresponding results are shown in Figs. 5.15h, 5.15i and 5.15j for the specimens of thickness 10.60 mm, 7.0 mm and 3.70 mm, respectively. It appears that the longer the shock pulse, the larger the difference of the unloading process between the experiments and simulations.

5.3.4 Comparison of Shock Stress (Pressure) Profiles Between Simulations and Experiments

As described in Chapter 4, stress gages were embedded in some specimens to measure the stress histories at internal points in order to extract more information and get a better understanding of the compression processes. The stress gages were embedded between soft and hard layers where the stress profile was to be measured.

The full structure (FS) simulations of experiments were also carried out. Considering that the matrix of the stress gage is a polymer, it is natural to think that the stress history of the element at the side of PC layer of the interface will be closer to the environment of the stress gage during the

shock compression. Therefore, the stress profile compared with experimental measurement is the stress history of the interface element of the corresponding PC layer in the numerical simulations.

5.3.4.1 PC/SS Type Composite

For two types of geometrical structure specimens, PC74/SS37 and PC37/SS19, the stress profiles of simulation are compared with experimental measurements in Figs. 5.16 and 5.17, respectively. In each 10 mm thick PC74/SS37 specimen, only one gage was embedded 0.76 mm (one PC layer) from the impact surface. The experiments and simulations were performed with a 2.78 mm thick flyer impacting at velocities of 560 m/s and 1,062 m/s. From Figs.5.16 and 5.17 it can be seen that the difference between the experiment and simulation is large at low loading strength (flyer velocity of 561 m/s), while with the increase of loading, the difference becomes smaller.

This phenomenon may be interpreted if the scattering effects, i.e., the dispersion, of the interface on the shock wave are taken into account, since the scattering or dispersion is important only when the material strength is important (at low strength of loading). At higher loading levels, the hydrodynamic pressure is high and dominates the shock process and the effect of material strength becomes less important or even negligible. Therefore, the models, which neglect the scattering effects, become more accurate and predict better results under strong loading conditions.

In each of the PC37/SS19 specimens, two gages were embedded at interfaces, which are 3.4 mm and 6.50 mm from the impact surface, respectively. The results of experiments and simulations are shown in Fig. 5.17. Again, the difference of stress profiles between experiment and simulation is large at lower loading strength and becomes smaller with the increase in loading strength. For a flyer velocity of 1,043 m/s, the comparison between experiment and simulation here is not as good as that in the case of PC74/SS37 composite loaded at the same condition. The

only difference between the two experiments is that the interface number in PC37/SS19 composite is doubled. It appears that the larger the interface density, the higher the loading that is needed to reduce the discrepancy between experiments and predictions using homogeneous material properties. In other words, the interface scattering effects existing in composites has to be taken into account if a more accurate constitutive model is to be formulated.

The difference in the duration and amplitude of resonant oscillations, as well as the difference in the unloading processes, discussed in Section 5.3.3 are also observed here and the corresponding discussion is not repeated.

Figure 5.18 is the comparison between experiment and simulation for a 10.60 mm thick PC37/SS19 specimen impacted by a 5.63 mm flyer at a velocity of 1,045 m/s. The profiles look similar to those in Fig. 5.17. One thing worth noting is the difference in stress profiles between experiment and simulation for the gage located at 9.88 mm away from the impact surface. At this position, the stress state is affected by the release wave from the window. The simulation predicts much larger amplitude of the resonant oscillation than that observed experimentally.

5.3.4.2 PC/GS Type Composite

Figures. 5.19 and 5.20 show the comparison of stress profiles between experiments and simulations for nominally 10 mm thick PC37/GS20 and PC74/GS37 composites, respectively. The number of gages and the positions where the gages are embedded in each specimen, as well as the material, thickness and velocity of flyer, are indicated in the legend of the plots. The same analysis for the PC/SS type composites in the last section is not repeated here for PC/GS type composites. For each kind of composite, the experiments were conducted at three different loading levels. The results show that, in general, at low loading level, the difference between the experiments and simulations is large and the difference becomes smaller with the increase of the

loading strength. For all loading conditions, the duration of oscillations predicted numerically is larger than that of the experimental measurements, and the predicted amplitude is larger, too.

5.3.5 Numerical Predictions Using Mixture Model

The mixture model outlined at the beginning of this chapter was used in this numerical analysis to model the response of layered composites by treating them as homogenized solids. The method and procedures of simulation were exactly the same as used in the full structure (FS) simulations. Everything, including element size, element number, input parameters, etc., was the same as the ones used in the FS simulation. The only difference was that both PC and SS (PC/SS specimen) and GS (PC/GS specimen) layers of the composite were replaced by the corresponding equivalent homogenized solids. The PC buffer layer and PMMA window were treated in the same manner as before. The elements for which the stress or particle velocity profiles were plotted and compared with others were also the same as those used in the FS simulations. The predictions obtained using the mixture model are compared with both experimental results and the FS simulation predictions.

Figure 5.21 shows the comparison of numerical results using mixture model with the results of experiments and FS simulations for PC74/SS37 composites under PC flyer impact at velocities of 561 m/s and 1,062 m/s. The thickness of specimen and flyer are nominally 10 mm and 2.87 mm, respectively. Fig. 5.22 shows the same kind of results for PC37/SS19 composites under similar loading conditions. In general, the prediction of the mixture model is approximately the mean of the resonant oscillations for the shock profile predicted from the FS simulation. For the PC37/GS20 composite loaded at a flyer velocity of 1,062 m/s, where the FS simulation agrees best with the experiment, the prediction of mixture model is at the upper limit of stress on the profile. The high frequency oscillations in profiles obtained using mixture model (Figs. 5.21,

5.22 and 5.23) were due to the slide lines representing the PC/SS interfaces. The slide lines used in the FS simulations were not removed since the simulation meshes for the homogenized mixtures were kept the same as those for the corresponding layered composites. These slide lines should be removed during the computations using the mixture model, but they were kept for two reasons: (1) they would not produce any apparent effect on the simulation results, and (2) for convenience in forming the mesh based on the previous FS simulation.

Since the mixture model does not take into account the dispersion due to scattering effects, it is not surprising that when the loading level is low, the mixture model overpredicts the response of the composite and when loading level is increased, the agreement between the predictions and experiments becomes better (see Figs. 5.21 and 5.22). Furthermore, it can be observed from Fig. 5.22 that for flyer velocity of 563 m/s, the shock velocity predicted using FS simulation agrees very well with the experiment, but the mixture model overpredicts the shock velocity since the predicted arrival time at the location of the second gage comes earlier than in the experiment. As the flyer velocity is increased up to 1,043 m/s, the mixture model prediction agrees well with experiment, while the FS simulation underpredicts the shock velocity. It should be noted that though the reference or the origin of the time axis may be not accurately defined for comparison purposes, the time interval between any two points is accurate.

One thing worth noting is the slope variation of the shock profiles. At a flyer velocity of about 1,060 m/s, for both PC74/SS37 and PC37/SS19 composites, the slopes of both the velocity and stress profiles predicted by both the FS model and mixture model agree reasonably well with the experimental measurements. However, it is not the case for the lower flyer velocities. At a flyer velocity of 560 m/s, for the PC74/SS37 composite, the slopes of the stress profiles agree with each other, while the slope of the velocity profile predicted by the mixture model is steeper than the others. For the PC37/SS19 composite, the slopes of the velocity profiles agree reasonably well, but the slope of the stress profile predicted by the mixture model is steeper than

the other two. This phenomenon is intimately related to the number density of interfaces and is due to the influence of interface scattering on wave propagation.

Figure 5.23 shows the comparison of the profiles between numerical analysis and experiment for the PC74/GS55 composite impacted by a 2.87 mm thick PC flyer at a velocity of 563 m/s. For the particle velocity profile, the prediction of the mixture model is the mean of the oscillations on the profiles of the FS simulation and the experimental measurement. But, for the stress profile, the prediction of the mixture model is between the FS simulation and the experimental result. It can also be observed that the mixture model over predicts the shock speed of the composite in comparison to the experiment.

5.4 Results from One-Dimensional Simulations

For the purpose of comparison, one-dimensional (1D) simulations were also carried out using DYNA2D. The 1D simulations also provide validation of the uniaxial strain assumption used in interpreting the experimental results. The simulations were carried out for two experiments, # 111901 and # 110501 in Table 4.2. One-dimensional plane strain analysis of shock compression using a two-dimensional finite element code can be realized in the following way. The number of finite elements of the specimen discretized in the wave propagation direction is the same as that in the FS simulation, while there is only one element in the lateral direction. The motion of nodal points in the lateral direction is constrained, i.e., the displacement of nodal points is always zero in the lateral direction. The aspect ratio of elements is taken as close to one as possible. All other procedures are the same as in the FS simulation. In this way the one-dimensional plane strain problem is solved using a two-dimensional (2D) finite element code.

The comparisons between the 1D and 2D simulations are shown in Figs. 5.24 and 5.25. Fig. 5.24 is for the 10.43 mm thick PC37/GS20 composite specimen impacted by a 2.87 mm thick PC

flyer with a velocity of 567 m/s. It can be seen that profiles of 1D and 2D simulations are almost identical except the shock speed predicted by 1D is larger than that by 2D. In Fig. 5.24 the stress and particle velocity profiles of 1D were shifted 0.08 μs and 0.12 μs, respectively, along the time axis. The reason for the faster shock velocity predicted by 1D simulation is because the lateral relaxation of motion was completely constrained, even for the Poisson's effects in the elastic region. The conclusion remains the same for the higher shock loading level for a flyer velocity of 1,079 m/s.

Figure 5.25 shows the results for the 10.60 mm thick PC37/SS19 composite under compression of the shock wave generated by the PC flyer. Again, the 1D stress profiles and the 1D particle velocity profile have been shifted along the time axis by 0.06 μs and 0.16 μs, respectively. Here, not only was there the difference of shock speeds between the 1D and 2D simulations, but also in the structure of the profiles, especially at the later stage of the unloading process. At the longer propagation distances, the difference between the two increases. This implies that the influence of lateral constraint on the shock wave propagation in the layered composite is also related to the compatibility of mechanical properties of components and the propagation distance. The difference in the unloading part can be attributed to the influence of release wave from the boundary in 2D simulations.

It can be concluded that in general the 1D approximation of plane strain problem is a very good approximation of the 2D simulation. The accuracy of 1D approximation depends on both the geometric size and the mechanical properties of the components of the composite. If the detailed structure of the shock profile and accuracy of the simulation are desired, then 2D simulations are preferred.

5.5 Discussion and Conclusions

In the section on shock wave propagation of periodically layered heterogeneous composite (see Figs. 5.5 to 5.9), the numerical simulations indicate that when a layered composite is compressed by a shock wave, due to the interactions between the multiple reflection waves within the individual layers and the shock wave, the stress in soft layer is higher than that in the hard layer, while the particle velocity in the hard layer is higher than that in the soft layer. The resonant oscillations are formed and observed on the shock profiles. Physically, the stresses and the particle velocities across any interface should continue. It should not make any difference whether the shock profile at the interface is taken from element in the soft layer or the hard layer. But, according to the simulation results presented in the previous sections, it seems there are some differences between the shock profiles of elements at each side of an interface.

It is constructive to look in more detail at the shock profiles of the elements at both sides of the interfaces. Figs. 5.26 and 5.27 show the shock stress and particle velocity profiles of interface elements at three interfaces inside the PC74/GS37 (experiment # 120201, see Table 4.2) and PC37/SS19 (experiment # 110501, see Table 4.2) composites, respectively. It is seen that for the PC/GS composites the stress histories experienced by the elements on either side of an internal interface are not the same, not even close to each other (Figs. 5.26a and 5.26c). There exists a very large stress gradient, or even being considered to be discontinuity, at the internal interface. The stress of GS elements is much lower than that of PC elements. But, strangely enough, the particle velocity histories experienced by the interface elements are almost the same the difference is negligible (Figs. 5.26b and 5.26d). The third pair of curves shown is the stress or particle velocity profiles of the elements bordering the buffer/window (PC/PMMA) interface, which are identical to each other even as loading conditions change.

For PC/SS composites (Fig. 5.27), the amplitudes of resonant oscillations on stress profiles of interface elements are different, but the mean of the oscillations are the same. Therefore, in the

sense of mean stress, the stress is continuous at the internal interfaces of PC/SS composites, which is different from that in the PC/GS composites. The particle velocity histories are almost the same for the elements on either side of the interfaces. Both the stress and particle velocity profiles are continuous at the buffer/window interface.

Based on the numerical analysis, it is clear that these features of stress and particle velocity field and history are controlled by the length scale of heterogeneity and the mechanical properties of the components in the composite. From the point of view of experimental investigation, it is hard to properly interpret the results of stress gage measurements. Physically, there should not exist a stress discontinuity at interface though the stresses in the soft layers and hard layers may be very different. But, if the difference of material properties at each side of interface is large, then, the stress gradient around the interface could be very large. If so, the question arises as to whether the stress gage measured stress profile should be compared with the simulated stress histories of an element in the soft layer or in the hard layer? Comparing Fig. 5.26a with 5.20b, and Fig. 5.26c with 5.20c, it appears that the experimental measurement is closer to the predicted stress profiles in GS (hard layer) for flyer velocity at 563 m/s. But, at flyer velocity of 1,056 m/s, the experimental results is closer to the average of the stress profiles of the two adjacent interface elements. Up to this point, it seems that the physical and mechanical processes of shock wave interaction with the interface is still not clearly understood, and need further experimental investigations, as well as numerical simulation analysis, on the stress distribution and evolution inside composite during shock compression process. It is suggested that the stress distribution inside the layers, or at least the stress history at the central point, be experimentally measured. In numerical analysis, more accurate constitutive models for the homogeneous components are needed to take into account material viscosity, the interface viscosity, etc., and much finer element size should be used to address the structuring of the shock front.

The influence of element size on the accuracy of numerical simulation was checked by increasing the element size from 130 μm to 390 μm for the experiment # 112501. The results

show that with the increase of the element size, the peak value of the shock profile decreases and the pulse width (of bottom) increases by about 3 or 4%.

The influence of the yield stress of the elastic-plastic material on the shock profile was also investigated for the experiment # 080301. The yield stress of annealed 304 stainless steel used in this analysis is 0.34GPa[8]. The Hugoniot elastic limit (about one and one-half times the yield stress) of 304 stainless steel used by Lundergan is 0.83GPa[15]. This analysis was carried out using the 1D simulation described in the Section 5.4. The results show that the profiles obtained by varying yield stress from 0.34 GPa to 0.83 GPa are almost identical except that the shock wave speed decreases by about 3% for the larger yield stress, which implies that the shock profile of layered composites may not be sensitive to the yield stress of its components, but the shock speed may be affected.

In the experimental study of shock compression of composites as described in Chapter 4, besides the shock stress and particle velocity profiles that were obtained, the shock Hugoniots of the composites were also calculated. Similarly, based on results of this numerical simulation analysis, the shock wave velocity were also calculated for each specimen in which manganin stress gages were embedded and the shock velocities were experimentally measured. The results of numerical predictions and the experimental measurements are compared in Figs. 5.28 and 5.29 for PC/SS and PC/GS composites, respectively. It is seen that the predictions of shock speed from simulations are consistent and agree reasonably well with experimental results. The predictions of Dremin's mixture model, which somewhat overpredicts the bulk response of mixtures, are also compared. The Hugoniot curves of mixture predicted by Meyers' model are much higher than experiment results since it corresponds to an ideal situation that the mechanical impedance of each component is perfectly matched with the other, and hence there is no wave reflection at any interface; or in other words, the Meyers' model does not take account for the scattering effects of interface to shock wave propagation in the composites.

In Dremin's model it is assumed that the pressure in each component, the local pressure, is equal to the pressure of the mixture, i.e., the mean pressure, and the volumes of components are additive. But, from the numerical analysis of shock wave propagation in the layered composites presented in this chapter, it is clear that these assumptions are not satisfied, or at least not well satisfied. It may not be possible to know how close the assumption is to the real situation, or how much deviation from the real process exists, if the assumption breaks down. The difference between the prediction of Dremin's model and the results of numerical simulation and experimental data is most likely due to the fact that the model neglects the effects of dynamic process of interface scattering the waves.

The influence of interface scattering on the bulk behavior is to slow down the propagation velocity of waves. This fact is generally assumed though it is hard to precisely formulate the physic and mechanics of the associated phenomena. Based on the experimental observation, it is obvious, but comparatively less known, that the interface scattering also contributes to the structuring of shock profile. In this numerical analysis, the quantitative study of the influence of geometric dispersion was not carried out, which needs further investigation. Should the quantitative study on the structure of wave profile be pursued later on, a new constitutive model will need to be formulated to account for the effect of interface, or microstructure, scattering on the dissipation and dispersion processes during shock compression of heterogeneous solids. Grady recently addressed the issue by proposing scattering as a mechanism for structured steady shock waves in metals, as well as in heterogeneous composite materials[17,18], and presented a physics-based approach to model the finite-amplitude nonlinear wave propagation in the heterogeneous media. It was based on nonequilibrium phonon energy induced within the media substructure by microstructure scattering[19]. The study of shock structuring in homogeneous solids like metals have been investigated by Swegle and Grady[20], Johnson and Barker[21].

Through this numerical analysis on shock wave propagation in periodically layered composites, several conclusions can be made and summarized as follows:

1) Numerical analysis reveals that due to the interaction of multiple reflection of waves within the layers and the incident shock wave, or the scattering of interface to the shock wave, the pressure and particle velocity in the layered composites during the shock compression are not uniformly distributed even if the steady shocked state is achieved. The pressure in hard layer is lower, while the particle velocity is higher, in comparison to their corresponding values in the adjacent soft layer. The difference of pressures and particle velocities between the hard and soft layers and the amplitude of the resonant oscillations on the shock profiles, and as well as the oscillation duration, are influenced by both the mismatch of their mechanical impedance and the geometric structure of the composite. Furthermore, the phases of velocity and pressure profiles of steady wave are not synchronous as they are in the homogeneous media.

2) The influence of interface scattering effects on the bulk response of composites is to slow down the propagation velocity of the shock wave. The two-dimensional numerical simulation analyses carried out by using DYNA2D finite element code show that computations can predict the shock speed very well, but not the structure of the shock profiles.

3) At low loading level, where the strength of material is still playing an important role, the full structure (FS) numerical simulation is mostly over predicting the response of the composites, such as larger duration and amplitude of resonant oscillations than those in the experimental observations, higher mean of the stress profiles, etc. With the increase in the level of loading, the difference between the numerical predictions and experiments becomes smaller. This indicates that the dispersion induced by microstructure scattering and the dissipation related to the viscous processes due to the interactions between interface and waves is not negligible when the loading is comparable with the strength of component materials. In order to precisely model the response of composite, it is necessary to take wave scattering effects into account in the constitutive model of heterogeneous media.

4) The existing mixture constitutive models, such as Dremin's, are proposed mostly based on the volumetric average under certain assumptions, which can predict the response of composites reasonably under strong loading conditions. With the decrease in loading, i.e., the role of the strength of material becomes important, the error in the models' prediction increases. This is because of the fact that the scattering effects of interface is neglected in those mixture models.

5) The simulation of the structure of shock front relies on the accurate modeling of the constitutive relation. In order to obtain an accurate physics-based constitutive relation for the modeling of shock compression processes in heterogeneous media, the interface scattering induced by the heterogeneous microstructure has to be taken into account.

5.6 References

1. Murri, W.J., Curran, D.R., Peterson, C.F., and Crewdson, R.C. Response of solids to shock waves, in *Advances in High-Pressure Research*, edited by Wentorf, R.H., Jr., Academic Press, vol. **4**, p1 (1974).
2. Wackerle, J. *J.Appl. Phys.* **33**, 922 (1962).
3. Barker, L.M. and Hollenbach, R.E. Shock-wave studies of PMMA, fused silica and sapphire, *J. Appl. Phys.* **41**, 4208 (1970).
4. Whirley, R.G., Engelman, B.E., and Hallquist, J.O. *DYNA2D, A Nonlinear, Explicit, Two-Dimensional Finite Element Code For Solid Mechanics, User Manual,* University of California (1992).
5. Wilkins, M.L. Calculation of elastic-plastic flow, in *Methods in Computational Physics--Advances in Research and Applications*, edited by Alder, B., Academic Press, vol.**3**, p211 (1964).
6. Erie Scientific Company, and Allegheny Rodney Strip, service center division of Allegheny Ludlum Corporation (2000).
7. Marsh, S.P. *LASL Shock Hugoniot Data*, University of California Press, Berkeley (1980).
8. Steinberg, D.J. *Equation of State and Strength Properties of Selected Materials*, Lawrence Livermore National Laboratory, UCRL-MA-106439 (1996).
9. Dremin, A.N. and Karpukhin, I.A. Method for determining the shock adiabatic curves for the disperse substances, *Zh. Prikl. Mekhan, i Teck. Fiz.* **1**, No. 3 (1960).
10. Duvall, G.E. and Taylor, S.M. Jr. Shock parameters in a two component mixture, J. *Composite Materials* **5**, 130 (1971).
11. Hallquist, J.O. *MAZE-An Input Generator for DYNA2D and NIKE2D*, Lawrence Livermore National Laboratory (1985).

12. Hallquist, J.O. and Levatin, J.L. *ORION: An Interactive Color Post-processor for Two-Dimensional Finite Element Codes*, Lawrence Livermore National Laboratory, UCID-19310 (1985).

13. Barker, L.M. A model for stress wave propagation in composite materials, *J. Composite Materials* **5**, 140 (1970).

14. Oved, Y., Luttwak, G.E., and Rosenberg, Z. Shock wave propagation in layered composites, *J. Composite Materials* **12**, 84 (1978).

15. Lundergan, C.D. and Drumheller, D.S. Dispersion of shock waves in composite materials, in *Shock Waves and Mechanical Properties of Solids*, edited by Burke, J. and Weiss, V., Syracuse University Press, New York, p141 (1971).

16. Kanel, G.I., Ivanov, M.F., and Parshikov, A.N. Computer simulation of the heterogeneous materials response to the impact loading, *Int. J. Impact Engng.* **17**, 455 (1995).

17. Grady, D.E. Scattering as a mechanism for structured shock waves in metals, *J. Mech. Phys. Solids* **46**, 2017 (1998).

18. Grady, D.E. Physics and modeling of shock-wave dispersion in heterogeneous composites, *J.Phys. IV France* **7**, C3-669 (1997).

19. Grady, D.E., Ravichandran, G., and Zhuang, S. Continuum and subscale modeling of heterogeneous media in the dynamic environment, in *Proceedings of the AIRPAT Conference*, Honolulu, Hawaii, edited by Manghani, M., Oxford University Press (1999).

20. Swegle, J.W. and Grady, D.E. Shock viscosity and the prediction of shock wave rise times, *J.Appl. Phys.* **58**, 692 (1985).

21. Johnson, J.N. and Barker, L.M. Dislocation dynamics and steady plastic wave profiles in 6061-T6 aluminum, *J. Appl. Phys.* **40**, 4321 (1969).

22. Barker, L.M. and Hollenbach, R.E. Shock-wave studies of PMMA, fused silica, and sapphire, *J. Appl. Phys.* **41**, 4208 (1970).

Table 5.1 Mechanical properties of Polycarbonate, PMMA, 6061-T6 Aluminum alloy, 304 Stainless steel, D263 glass and Float glass

Material	ρ (g/cm^3)	G (Gpa)	σ_y (GPa)	E_h (Gpa)	υ
PC	1.192	0.94	0.00	1.60	0.34
PMMA	1.18	1.20	0.00	1.60	0.35
6061Al	2.71	30.0	0.32	0.69	0.33
304 SS	7.89	77.0	0.33	1.70	0.29
D 263	2.51	30.1	/	/	0.208
Float	2.50	28.2	/	/	0.24
PC/SS	3.343	3.358	0.109	0.546	0.325
PC/GS	1.754	4.147	0.80	0.00	0.29

Table 5.2 Parameters of EOS for Polycarbonate, PMMA, 6061 Aluminum alloy, 304 Stainless steel

Material	C_0 (km/s)	S	S_1	S_2	γ
PC	2.042	2.195	-0.335	0.047	0.61
PMMA	2.815	1.973	-2.280	1.527	0.85
6061Al	5.24	1.40	0.00	0.00	1.97
304 SS	4.58	1.49	0.00	0.00	1.93
PC/SS	1.722	2.047	0.00	0.00	1.16
PC/GS	2.473	1.853	0.00	0.00	1.00

Table 5.3 The transient distance D_f of shock wave before steady state is reaching; the maximum pressure experienced by hard layer element (P_h), upper limit (P_u), lower limit (P_l) of maximum pressure experienced by soft layer element during shock compression

Specimen	V_f (m/s)	D_t (units)	P_u (GPa)	P_l (GPa)	P_h (GPa)	P_h/P_u	P_l/P_u
PC74/SS37	140	5~6	0.33	0.30	0.19	0.55	0.91
	280	6	0.79	0.67	0.28	0.35	0.85
	560	6~7	2.08	1.60	0.90	0.43	0.77
	1060	6	5.00	3.70	3.00	0.60	0.74
	1500	3	7.00	6.05	4.70	0.67	0.86
PC74/GS55	140	5~6	0.30	0.28	0.15	0.50	0.93
	280	5~6	0.69	0.62	0.32	0.46	0.90
	560	5	1.70	1.40	0.75	0.44	0.82
	1060	4	4.00	3.60	1.60	0.40	0.90

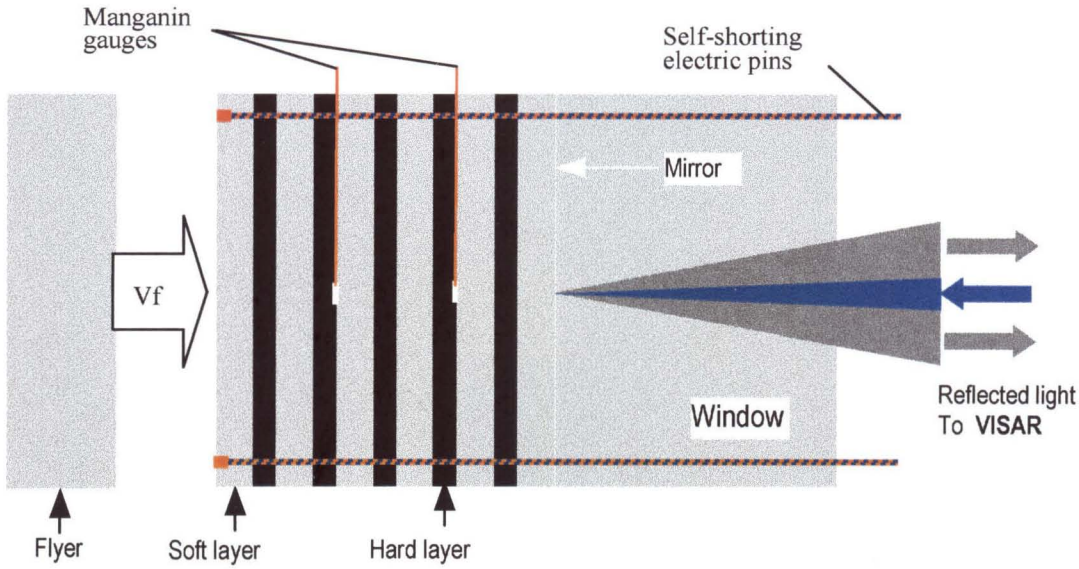

Figure 4.1 Configuration of a periodically layered composite and the schematic of shock compression experiment (for the sake of convenience, the figure is repeated here).

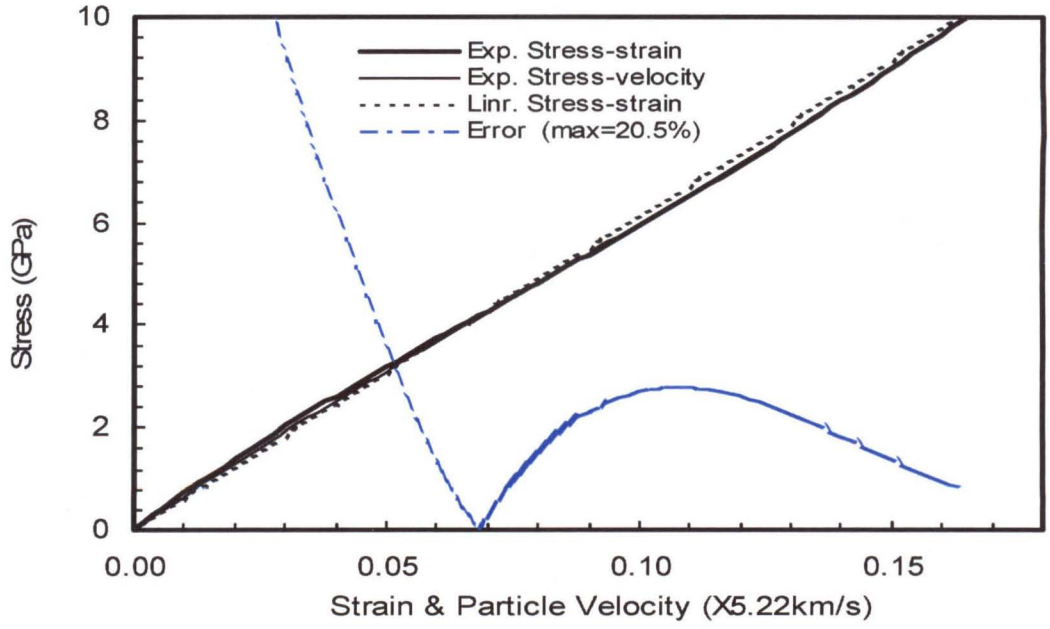

Figure 5.1 Experimental stress-strain relation, stress-particle velocity relation and the linear elastic approximation for fused silica [22].

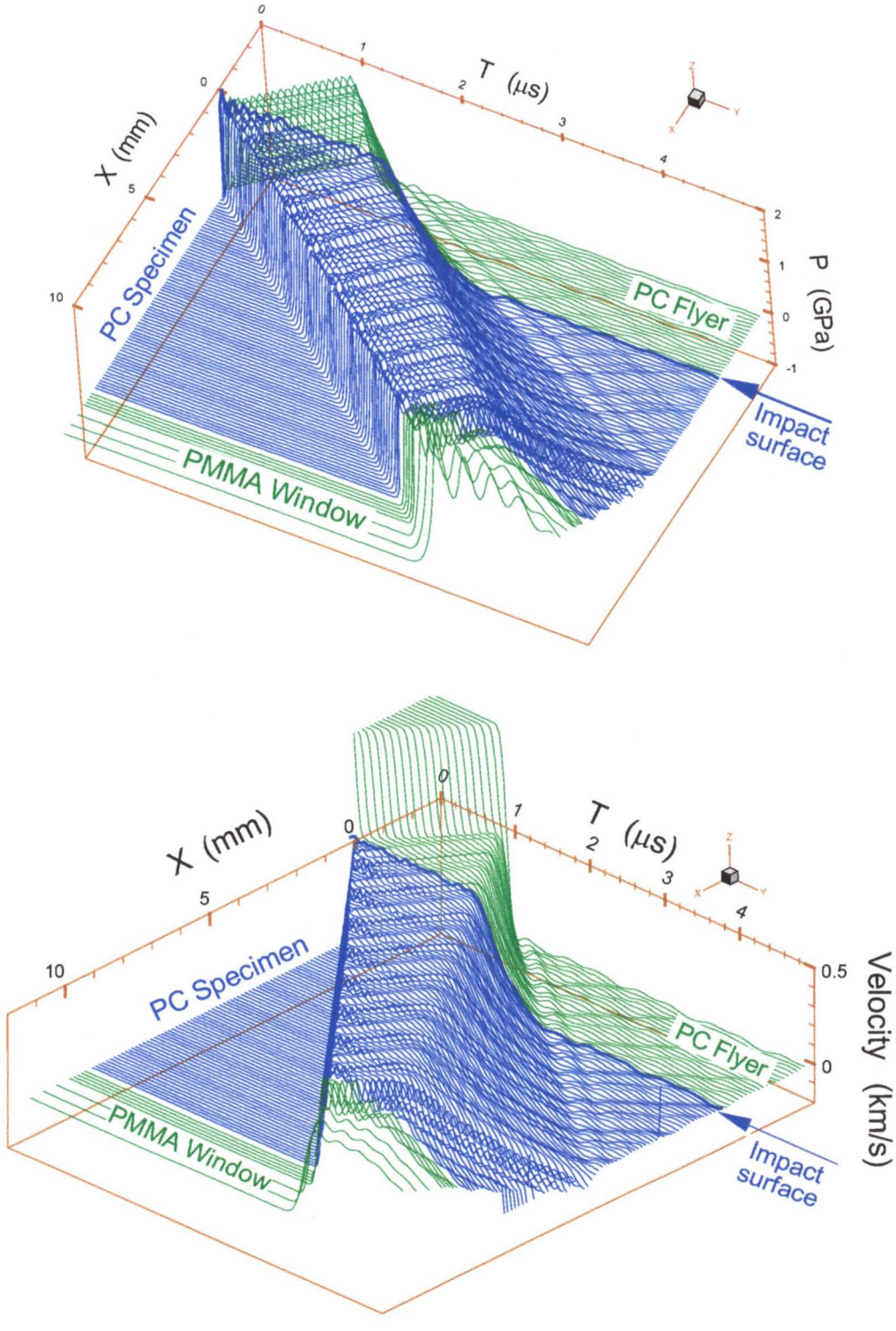

Figure 5.2 Numerically obtained pressure (top) and particle velocity (bottom) time histories of axial elements for 9.97 mm thick PC specimen impacted by 2.87 mm thick PC flyer at a velocity of 1,062 m/s.

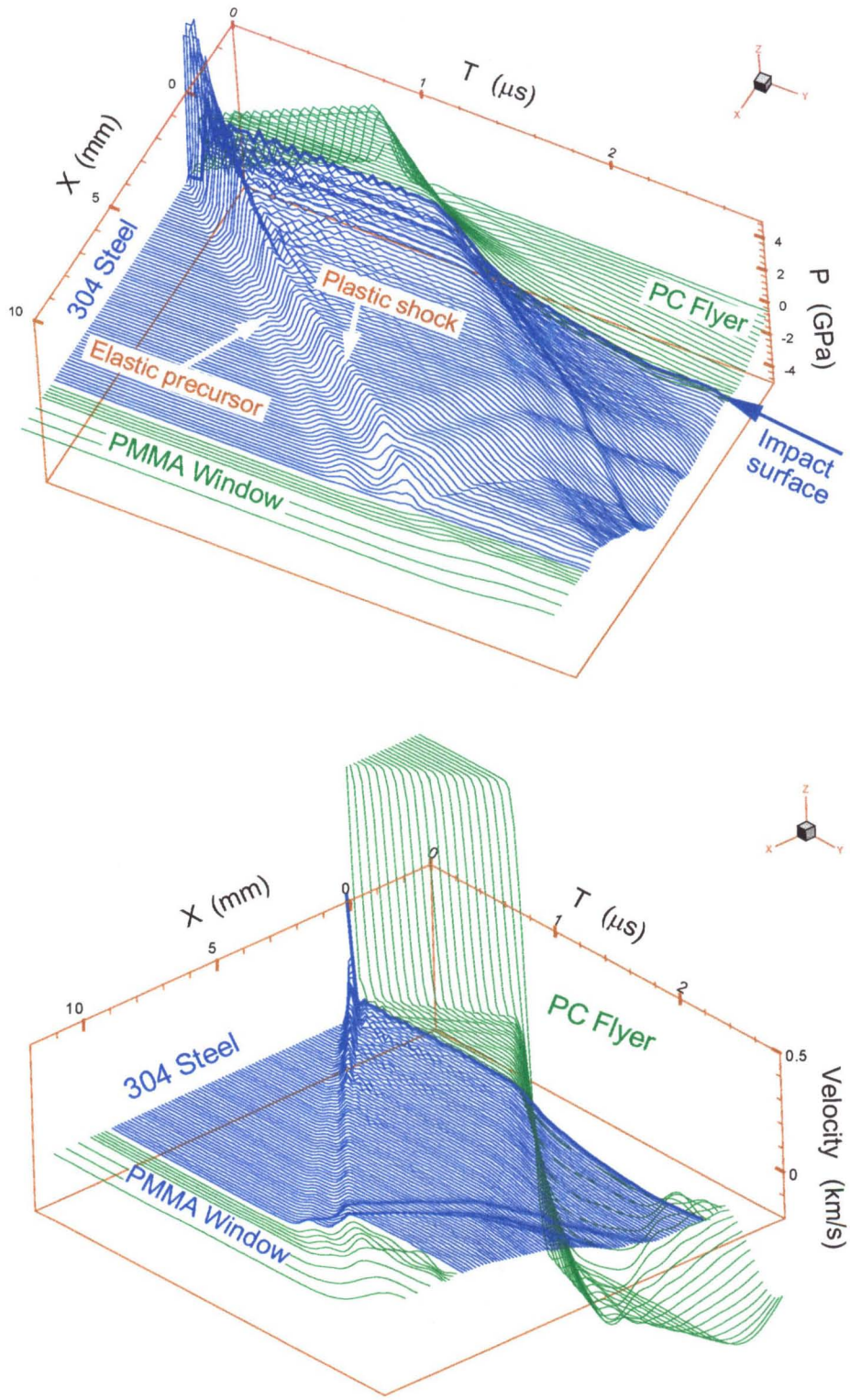

Figure 5.3 Numerically obtained pressure (top) and particle velocity (bottom) time histories of axial elements for 9.97 mm thick 304 steel specimen impacted by 2.87 mm thick PC flyer at a velocity of 1,062 m/s.

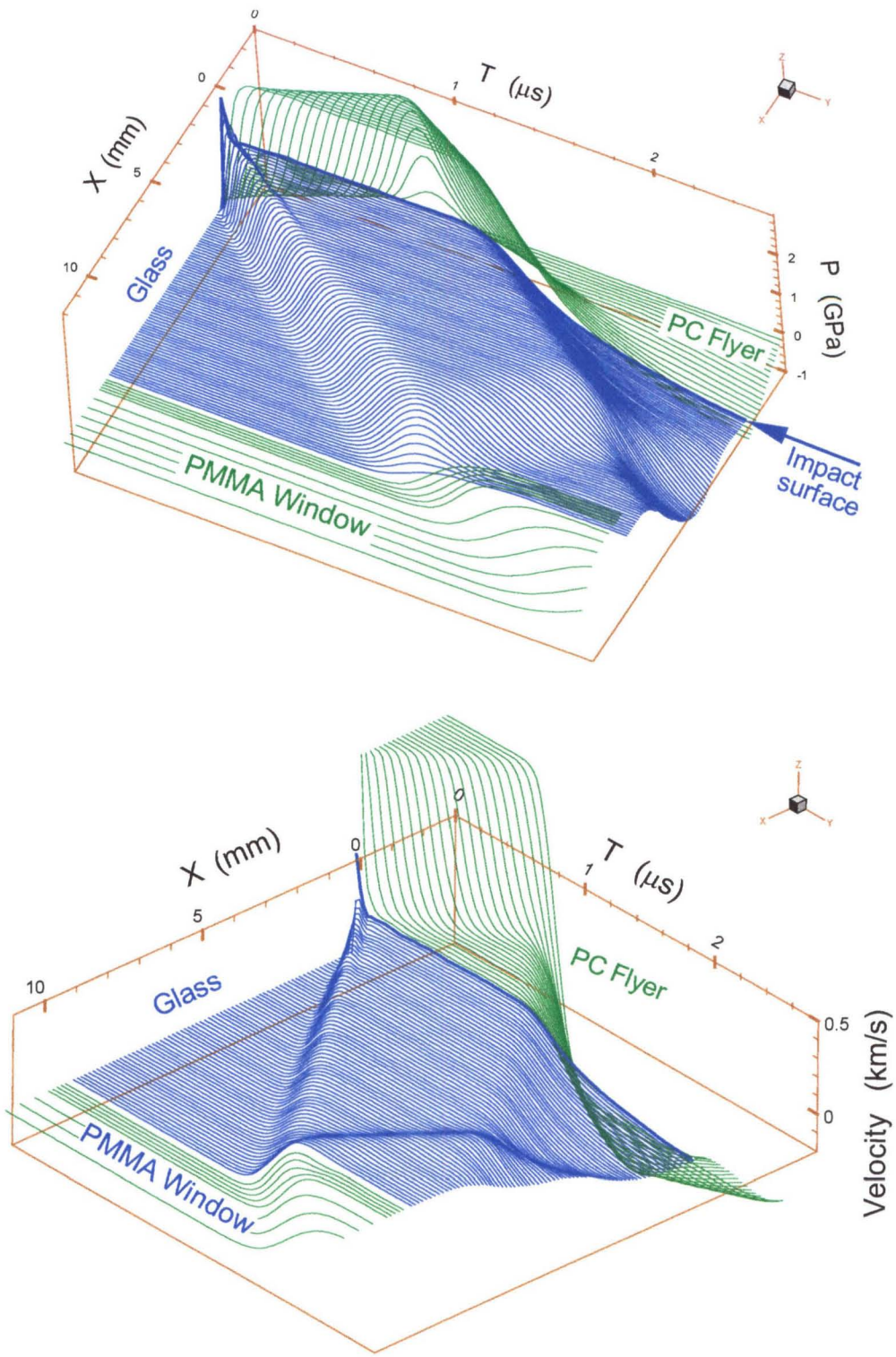

Figure 5.4 Numerically obtained pressure (top) and particle velocity (bottom) time histories of axial elements for 9.97 mm thick glass specimen impacted by 2.87 mm thick PC flyer at a velocity of 1,062 m/s.

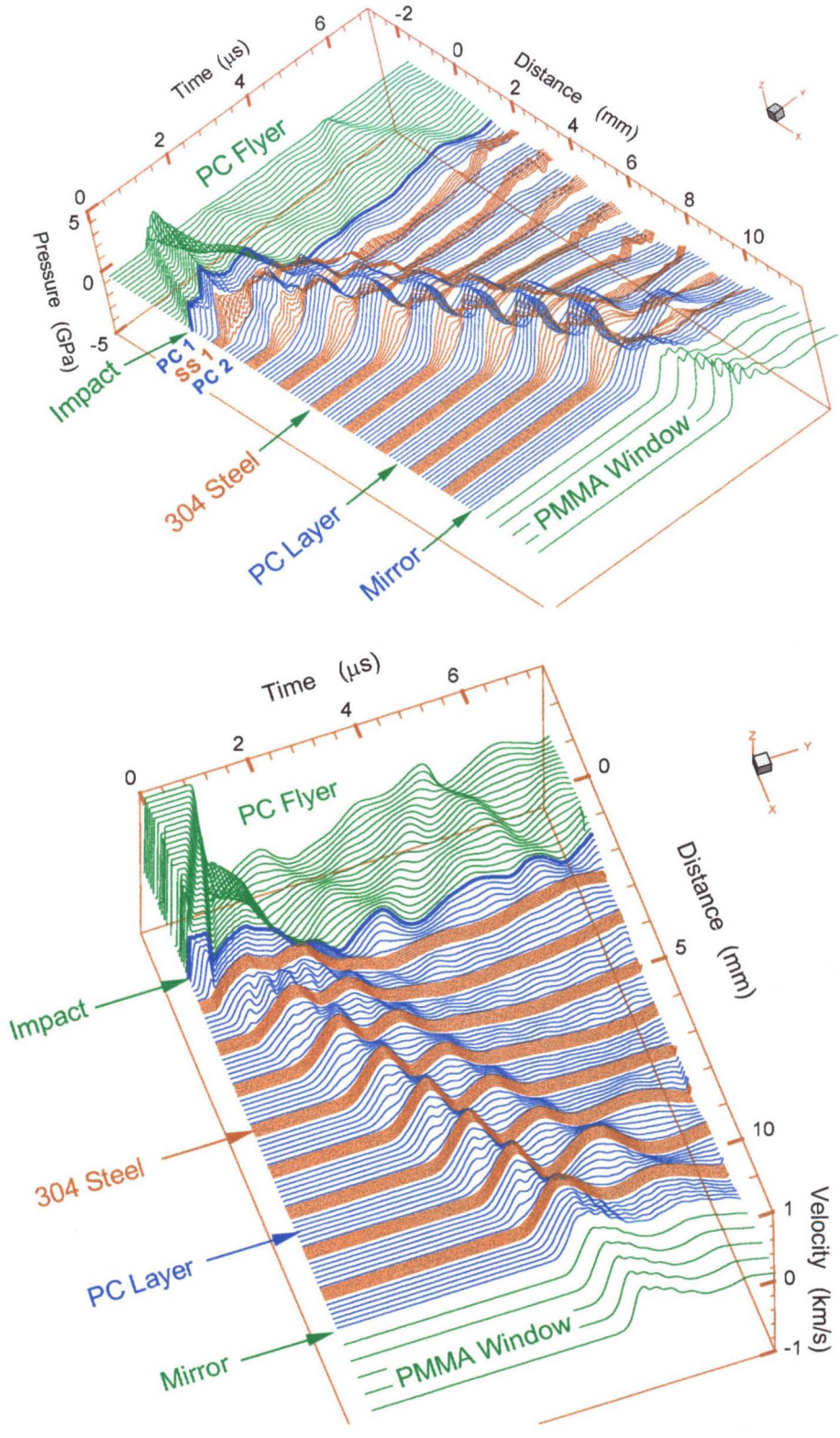

Figure 5.5 Numerically obtained pressure (top) and particle velocity (bottom) time histories of axial elements for 9.97 mm PC74/SS37 specimen impacted by 2.87 mm thick PC flyer at a velocity of 1,062 m/s.

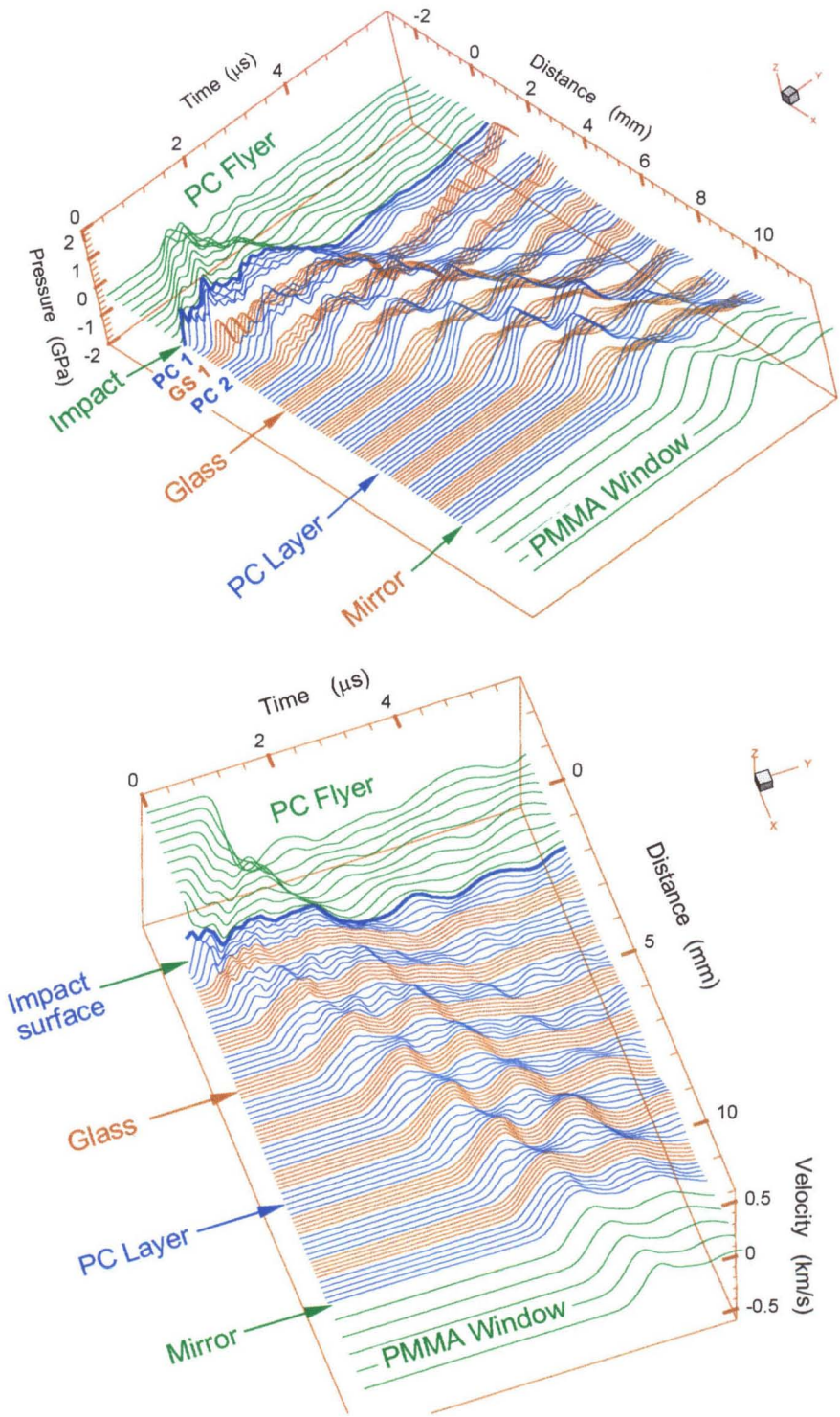

Figure 5.6 Numerically obtained pressure (top) and particle velocity (bottom) time histories of axial elements for 9.95 mm thick PC74/GS55 composite specimen impacted by 2.87 mm thick PC flyer at a velocity of 563 m/s.

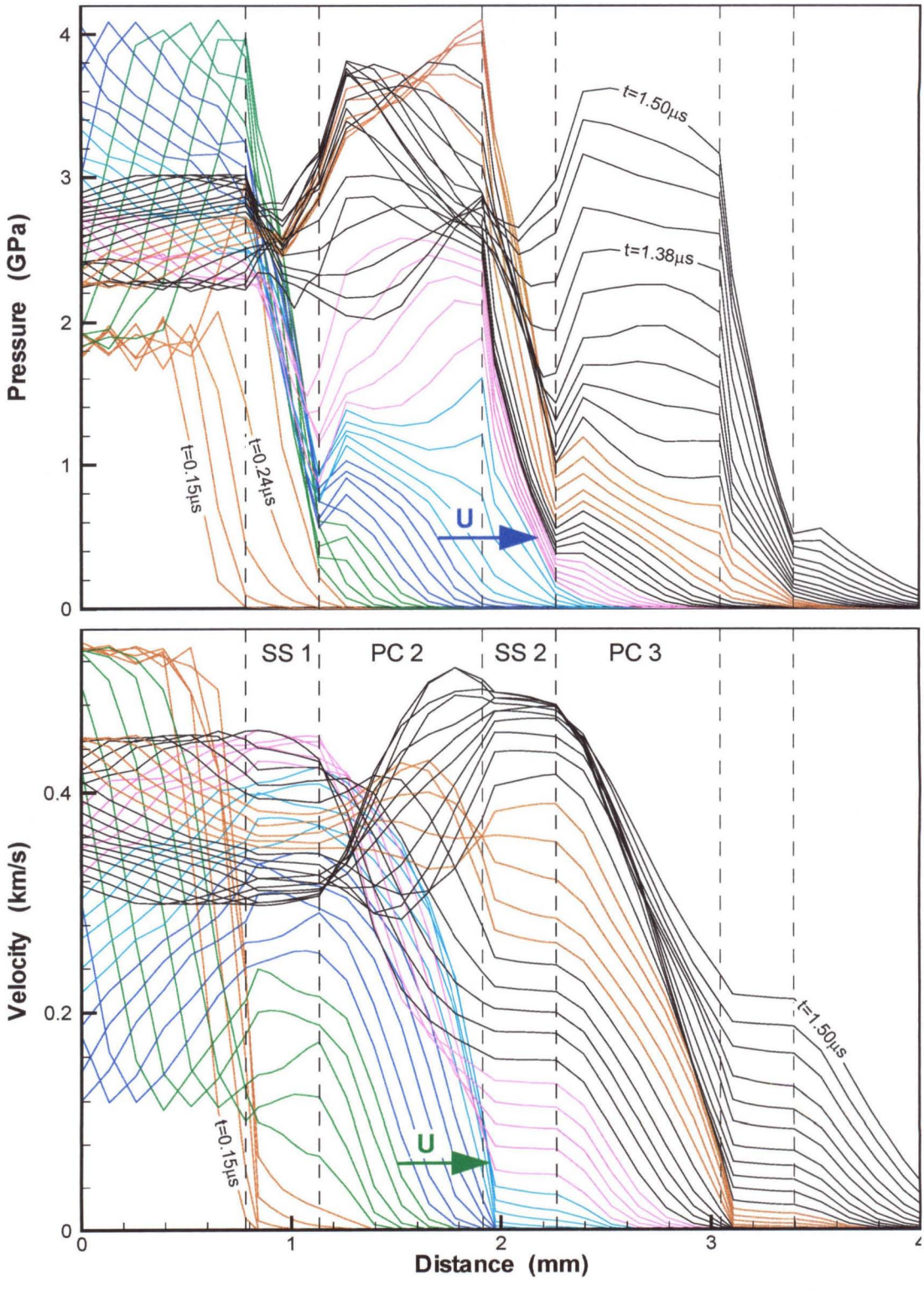

Figure 5.7 Numerically obtained evolution of pressure (top) and particle velocity (bottom) spatial profiles of shock wave propagation for 9.97 mm thick PC74/SS37 composite specimen impacted by a 2.87 mm thick PC flyer at a velocity of 1,062 m/s.

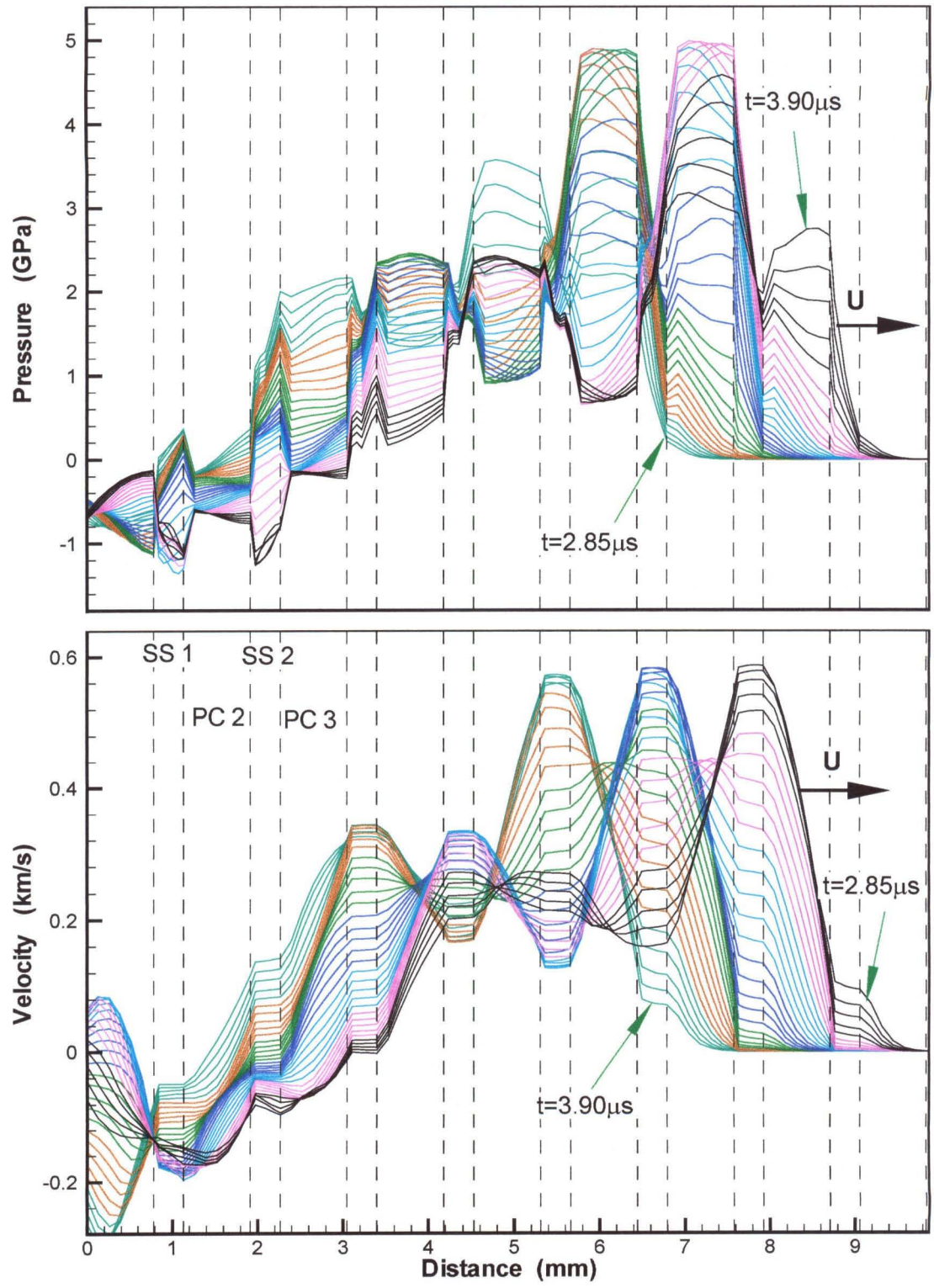

Figure 5.8 Numerically obtained evolution of pressure (top) and particle velocity (bottom) spatial profiles of shock wave propagation for 9.97 mm thick PC74/SS37 composite specimen impacted by 2.87 mm PC flyer at a velocity of 1,062 m/s.

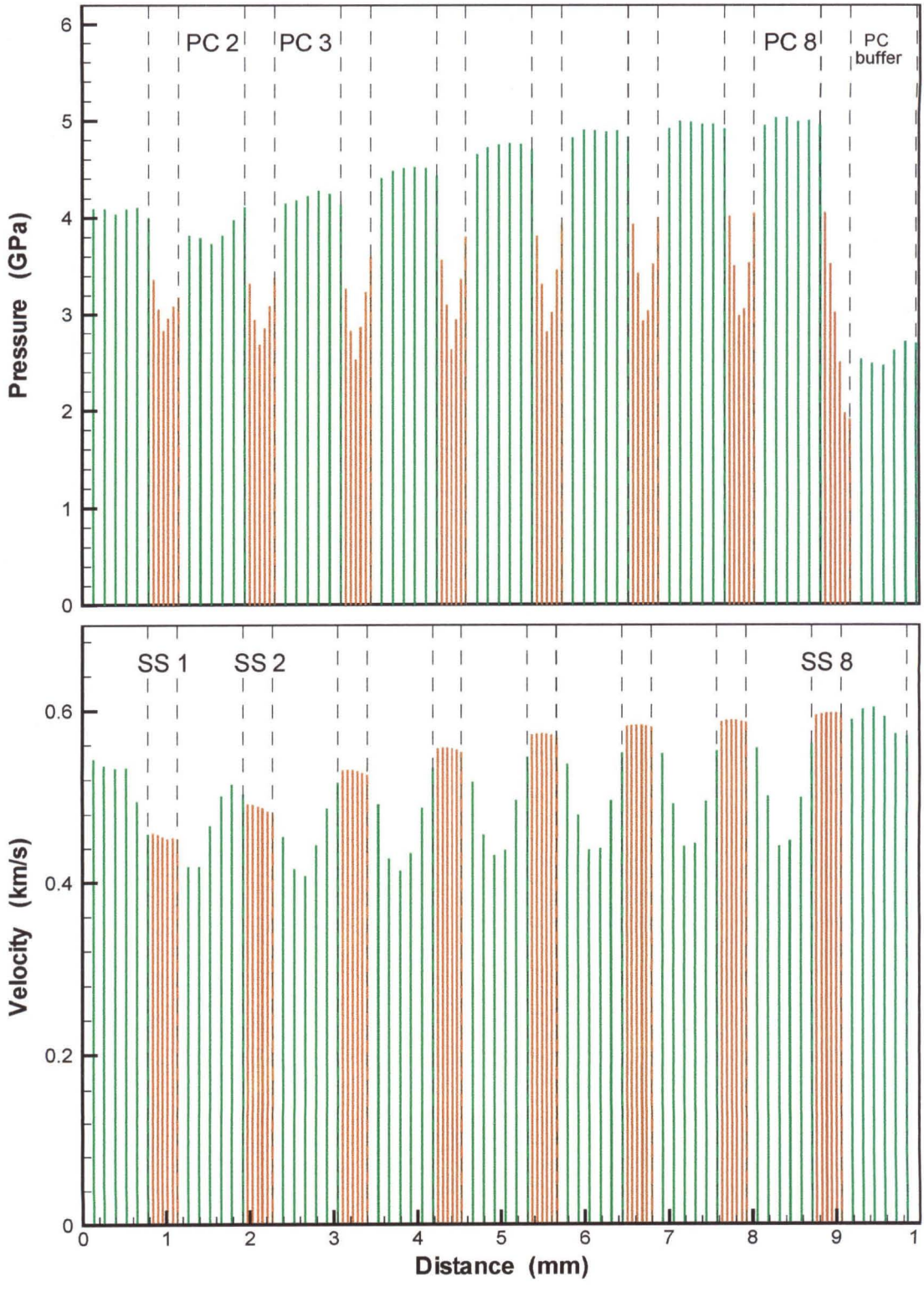

Figure 5.9 The maximum pressure (top) and maximum particle velocity (bottom) experienced by axial elements under shock compression for 9.97 mm thick PC74/SS37 composite specimen impacted by 2.87 mm thick PC flyer at a velocity of 1,062 m/s.

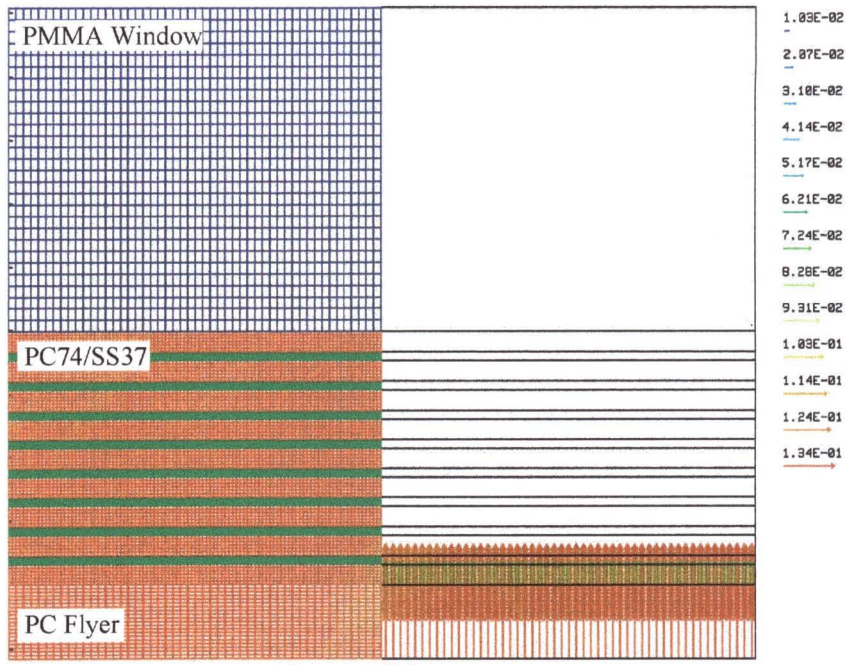

(a) t=0.0μs

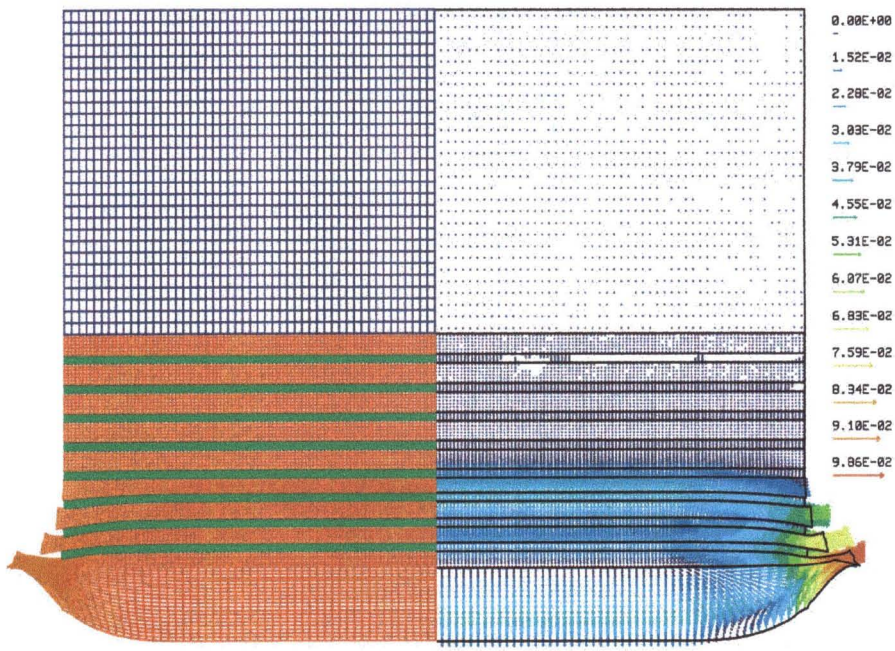

(b) t=2.0μs

Figure 5.10 Material distortion (left half) and velocity vector field (right half) at (a) t=0.0 μs, (b) t=2.0 μs after impact during deformation of 8 units of PC (0.74 mm)/SS (0.37 mm) layered composite under planar impact of 2.87 mm thick PC flyer at a velocity of 1,062 m/s.

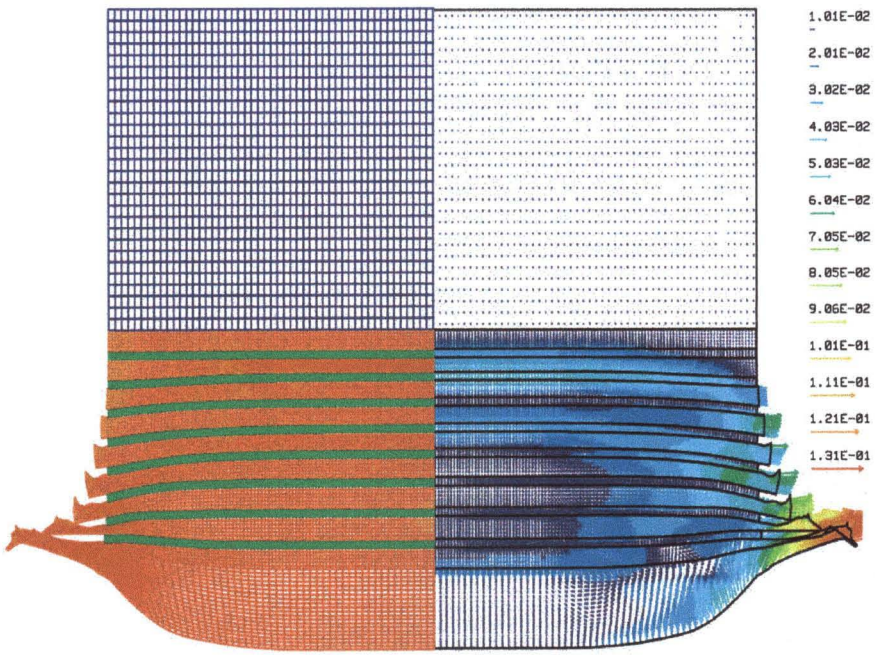

(c) t=4.0μs

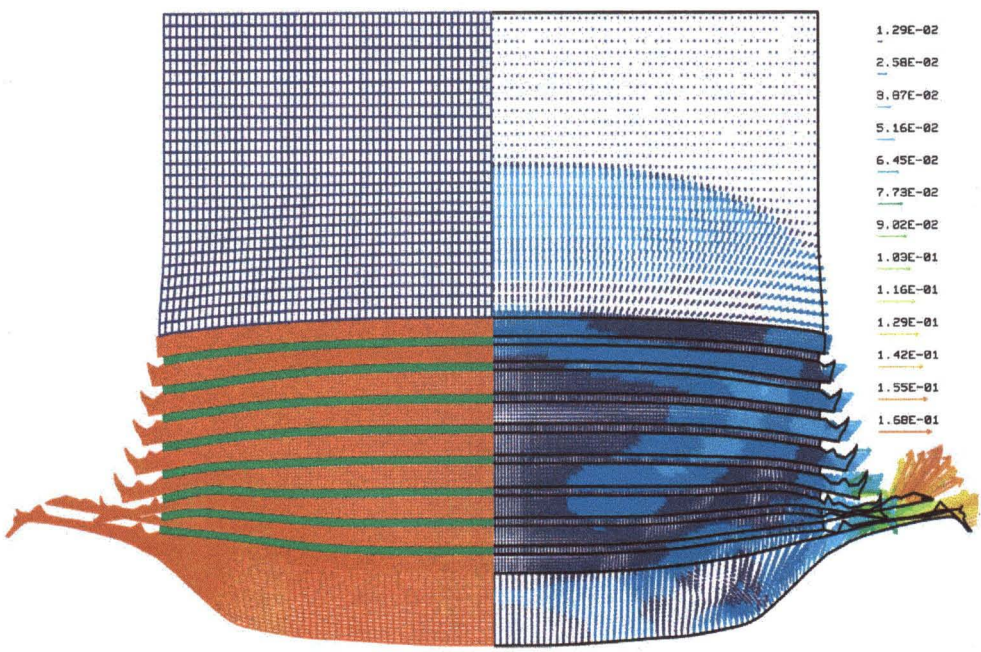

(d) t=6.0μs

Figure 5.10 Material distortion (left half) and velocity vector field (right half) at (c) t=4.0 μs and (d) t=6.0 μs after impact during deformation of 8 units of PC (0.74 mm)/SS (0.37 mm) layered composite under planar impact of 2.87 mm thick PC flyer at a velocity of 1,062 m/s.

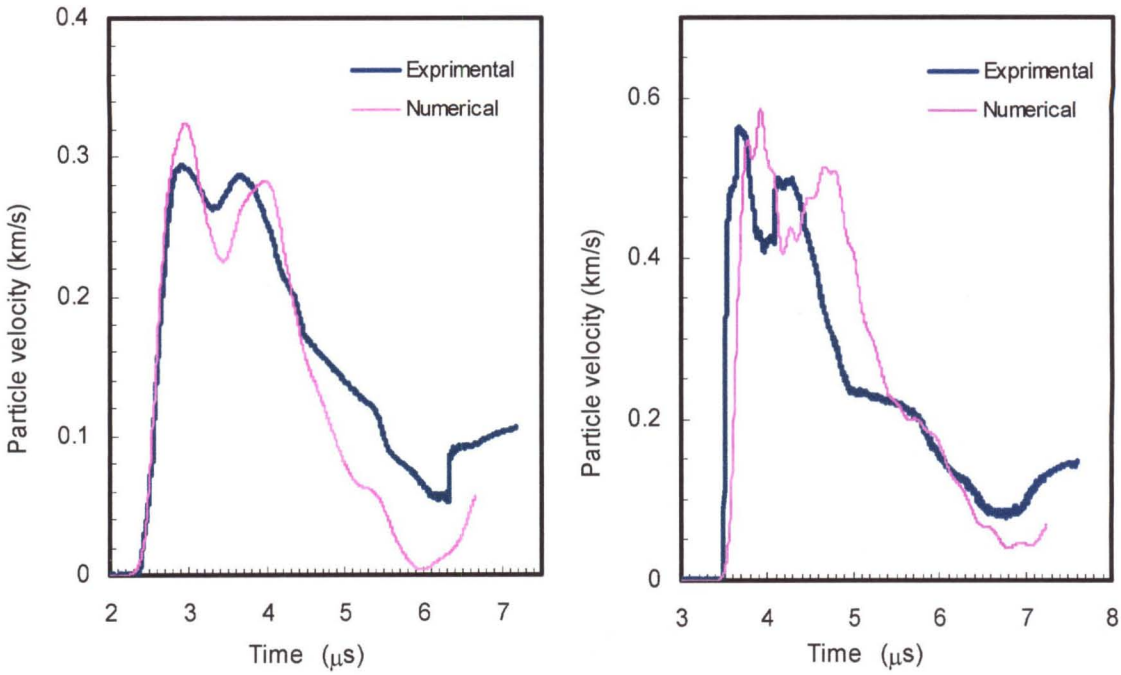

(a) h=6.62mm, w=2.87mm, v_f=589m/s

(b) h=6.59mm, w=2.87mm, v_f=1060m/s

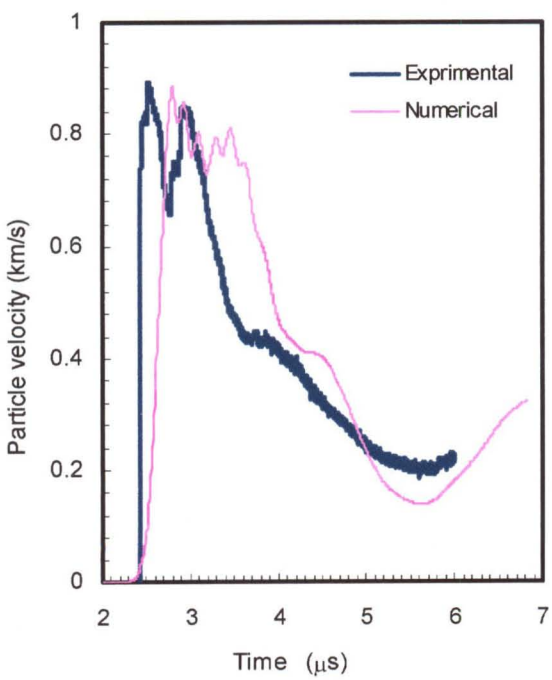

(c) h=6.54mm, w=2.87mm, v_f=1826m/s

Figure 5.11 Comparison of shock particle velocity profiles between numerical simulations and experimental measurements for the PC74/Al37 layered composites impacted by PC flyers; h and w are specimen and flyer thickness, respectively; v_f is the flyer velocity.

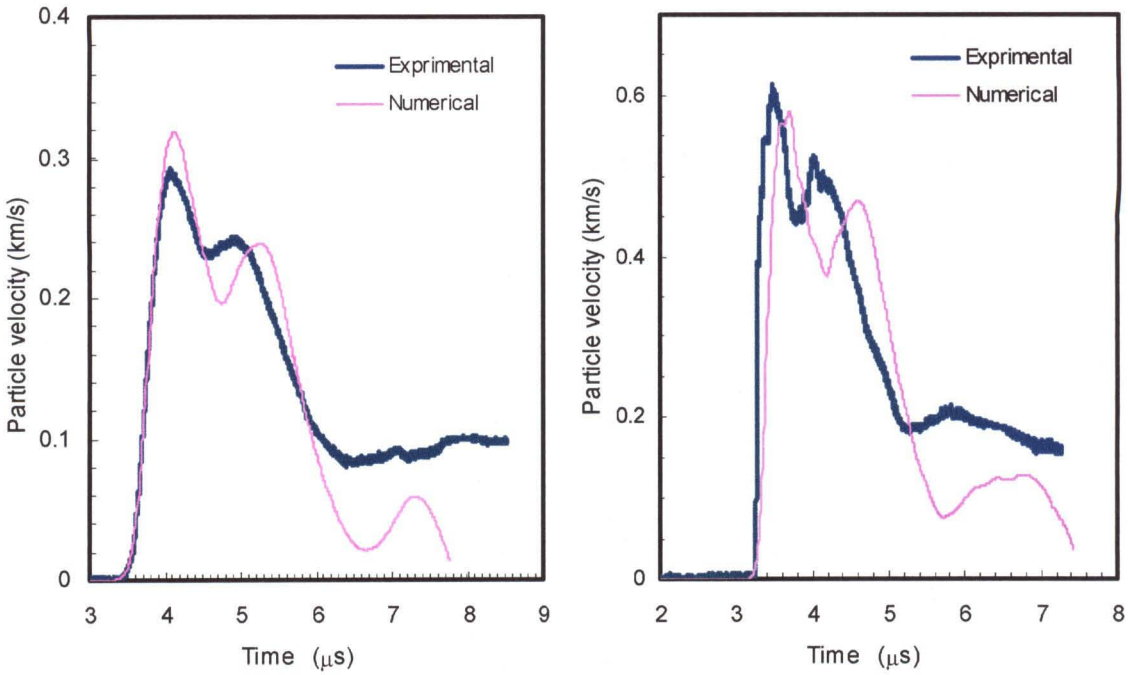

(a) h=9.95mm, w=2.87mm, v_f=563m/s

(b) h=9.88mm, w=2.87mm, v_f=1056m/s

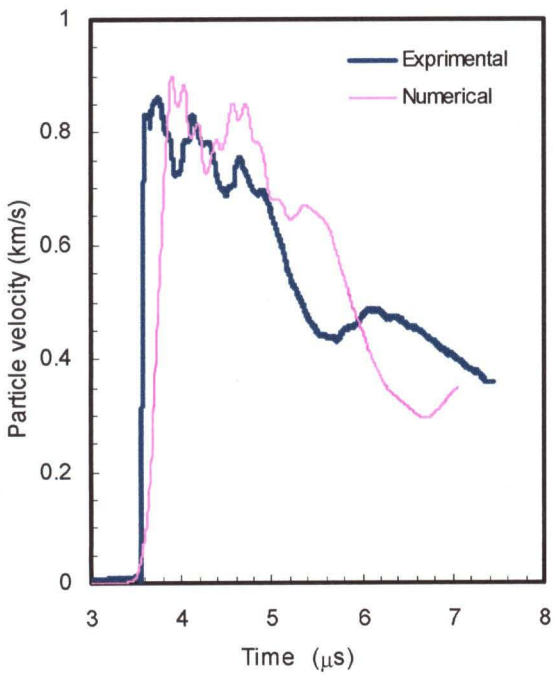

(c) h=10.07mm, w=5.55mm(Al), v_f=1070m/s

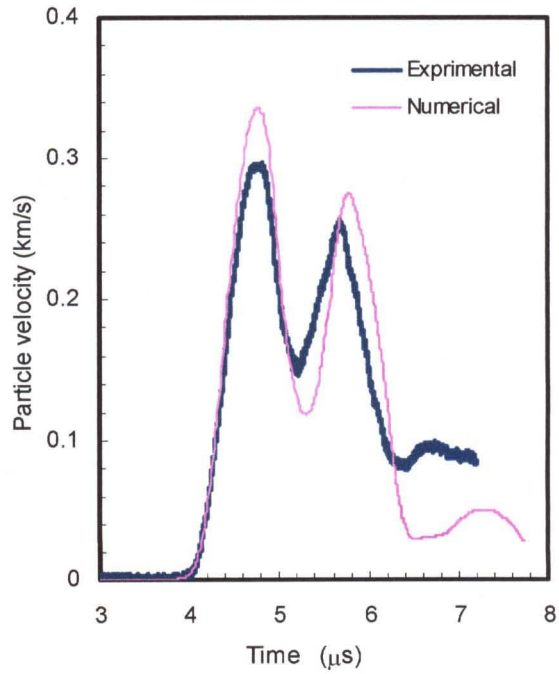

(d) h=9.92mm, w=2.87mm, v_f=568m/s

Figure 5.12 Comparisons of shock particle velocity profiles between numerical simulations and experimental measurements for the PC74/GS55 layered composites impacted by PC (Al) flyers; h and w are specimen and flyer thickness, respectively; v_f is the flyer velocity.

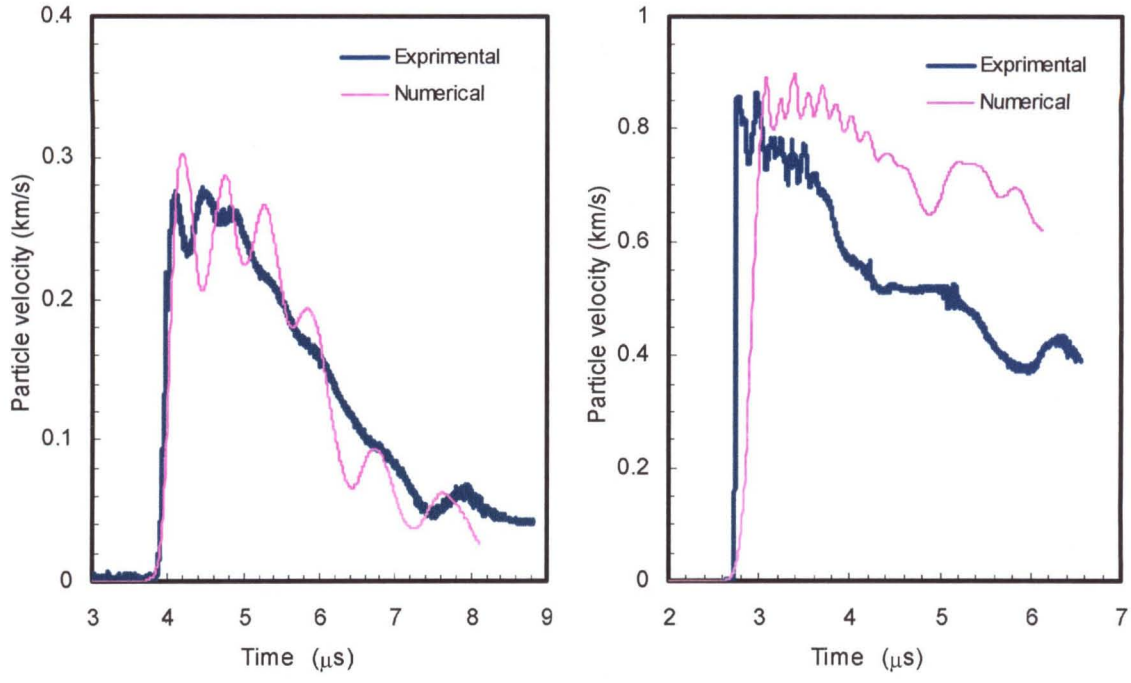

(a) h=10.43mm, w=2.87mm, v_f=567m/s (b) h=10.50mm, w=5.59mm(Al), vf=1160m/s

Figure 5.13 Comparisons of shock particle velocity profiles between numerical simulations and experimental measurements for the PC37/GS20 layered composites impacted by PC (Al) flyers; h and w are specimen and flyer thickness, respectively; v_f is the flyer velocity.

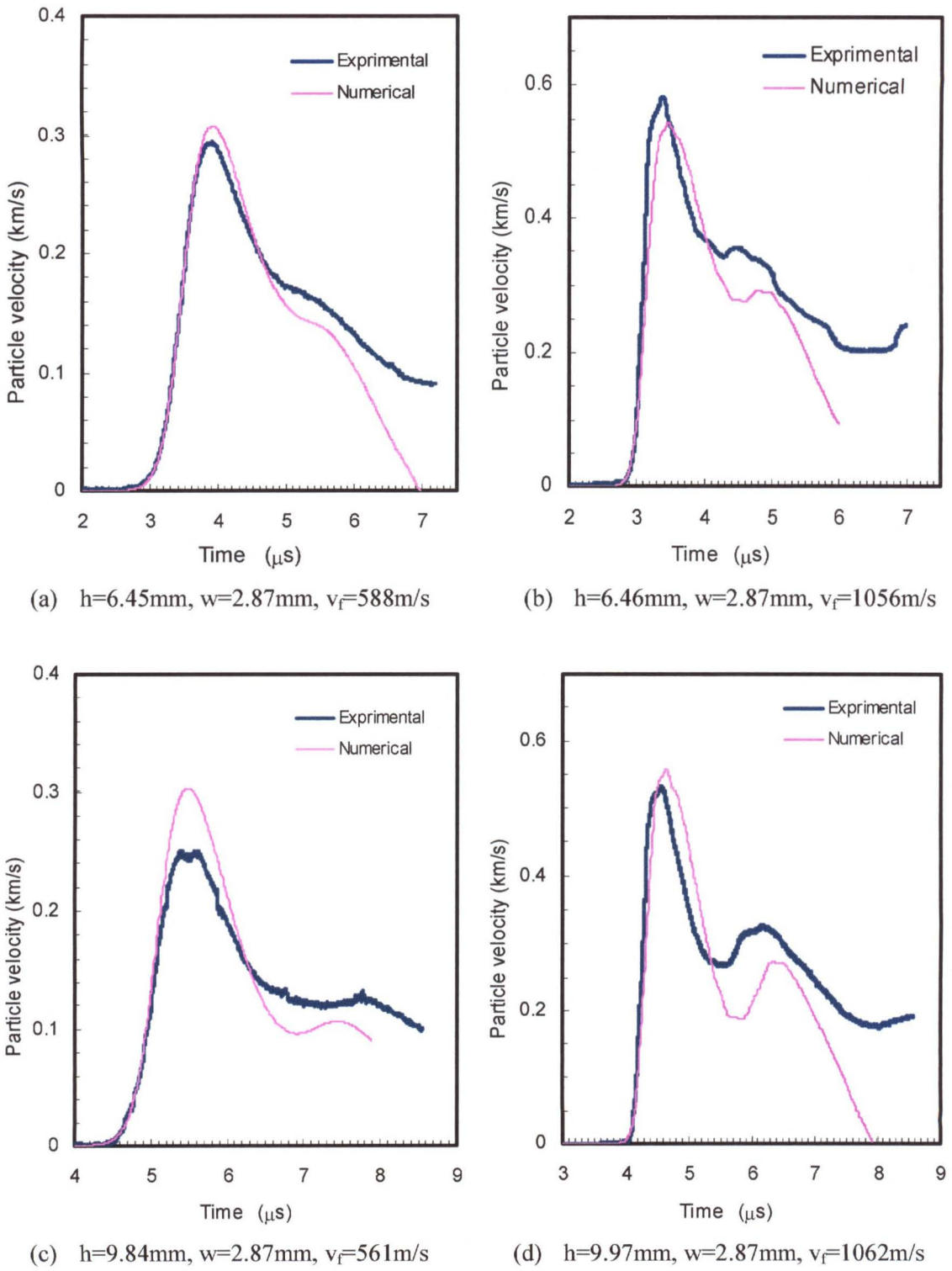

(a) h=6.45mm, w=2.87mm, v_f=588m/s

(b) h=6.46mm, w=2.87mm, v_f=1056m/s

(c) h=9.84mm, w=2.87mm, v_f=561m/s

(d) h=9.97mm, w=2.87mm, v_f=1062m/s

Figure 5.14 Comparisons of shock particle velocity profiles between numerical simulations and experimental measurements for the PC74/SS37 layered composites impacted by PC flyers; h and w are specimen and flyer thickness respectively; v_f is the flyer velocity.

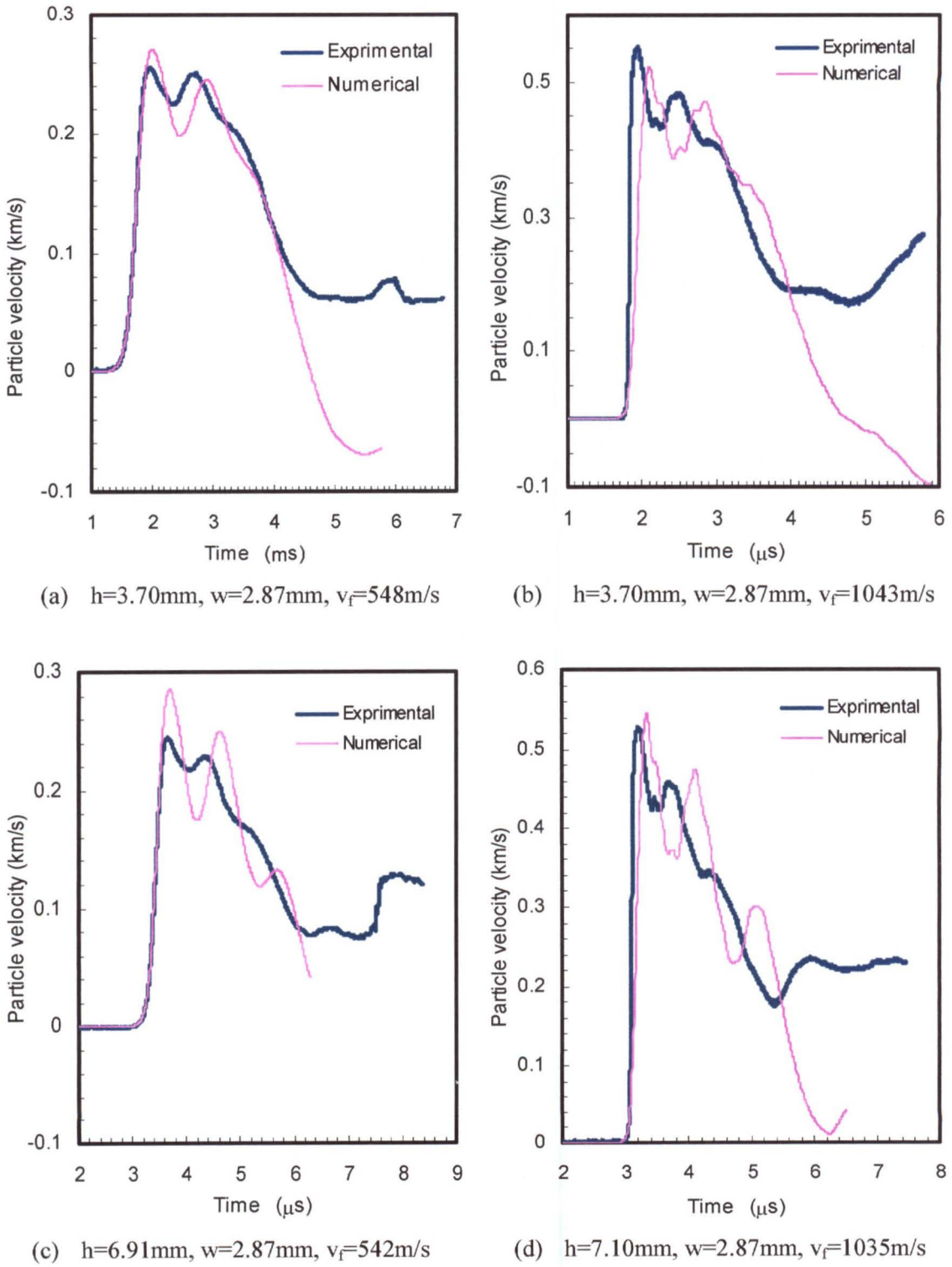

(a) h=3.70mm, w=2.87mm, v_f=548m/s

(b) h=3.70mm, w=2.87mm, v_f=1043m/s

(c) h=6.91mm, w=2.87mm, v_f=542m/s

(d) h=7.10mm, w=2.87mm, v_f=1035m/s

Figure 5.15 Comparisons of shock particle velocity profiles between numerical simulations and experimental measurements for the PC37/SS19 layered composites impacted by PC (Al) flyers; h and w are specimen and flyer thickness respectively; v_f is the flyer velocity.

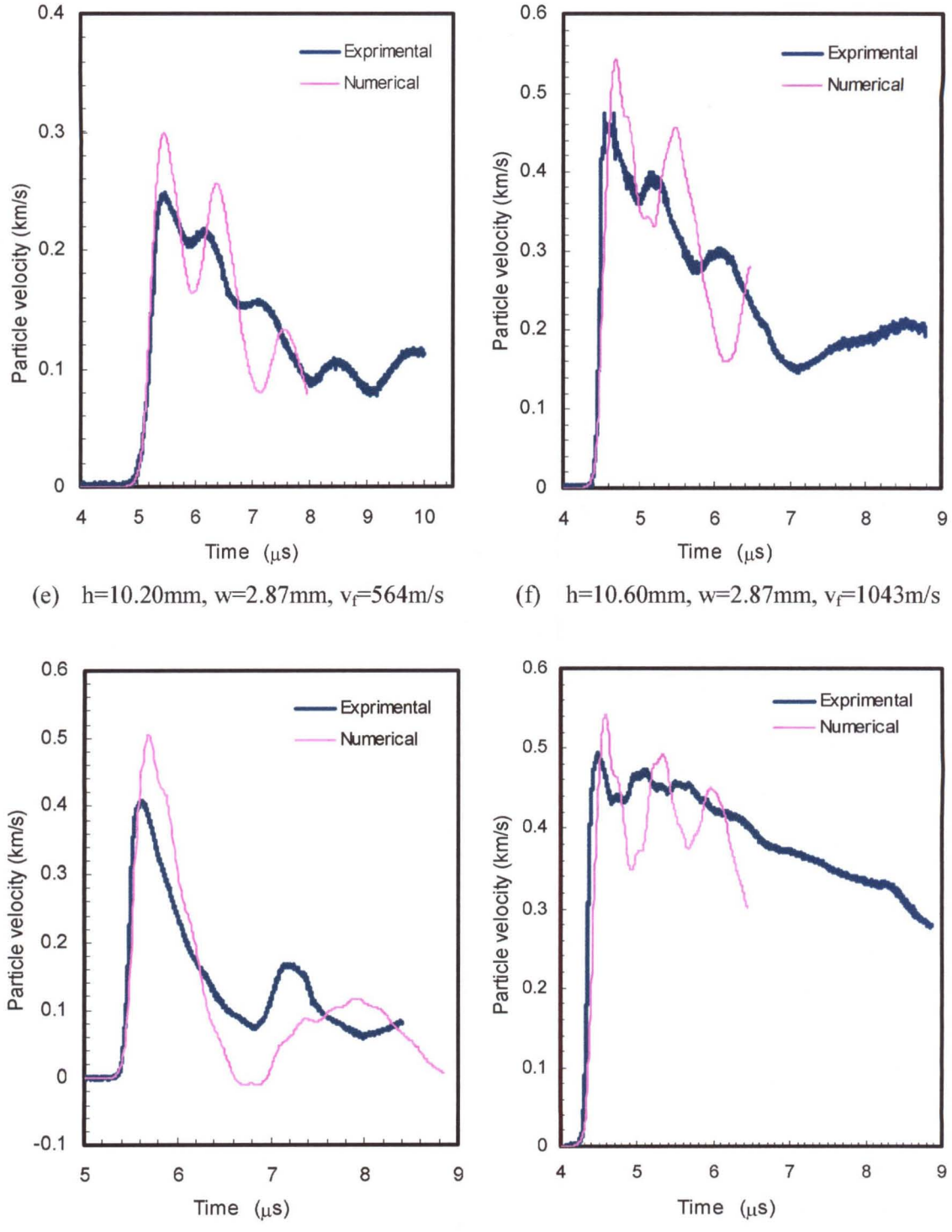

(e) h=10.20mm, w=2.87mm, v_f=564m/s (f) h=10.60mm, w=2.87mm, v_f=1043m/s

(g) h=10.23mm, w=1.20mm(Al), v_f=1045m/s (h) h=10.61mm, w=5.63mm, vf=657m/s

Figure 5.15 Comparisons of shock particle velocity profiles between numerical simulations and experimental measurements for the PC37/SS19 layered composites impacted by PC (Al) flyers; h and w are specimen and flyer thickness, respectively; v_f is the flyer velocity.

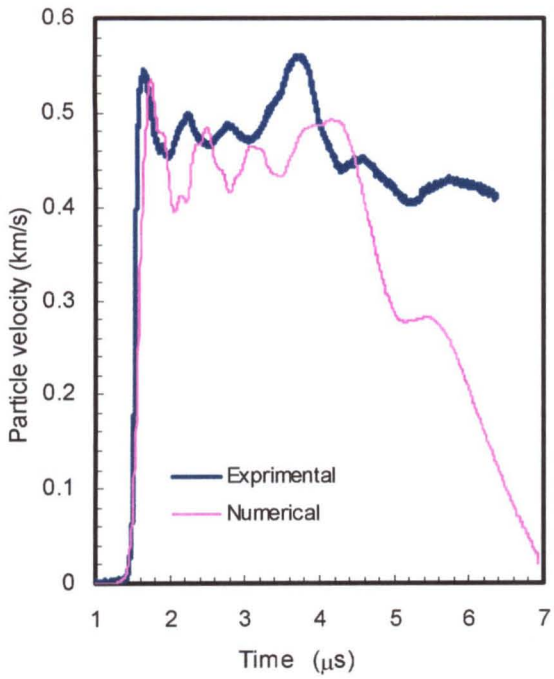

(i) h=3.70mm, w=5.63mm, v_f=1065m/s

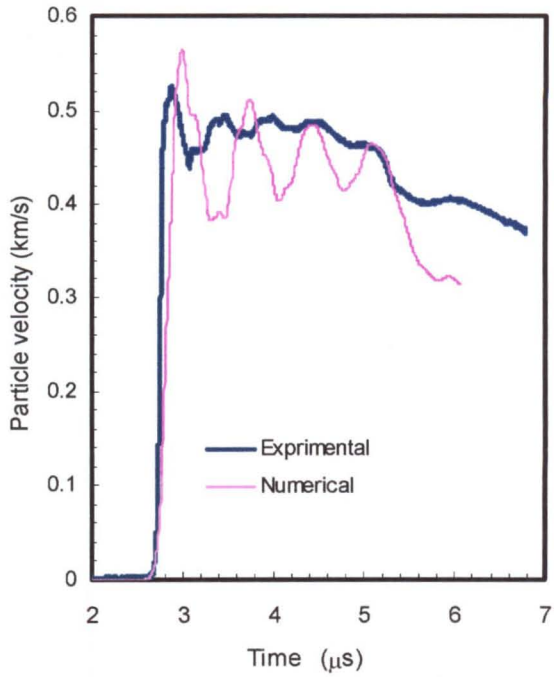

(j) h=6.94mm, w=5.63mm, v_f=1076m/s

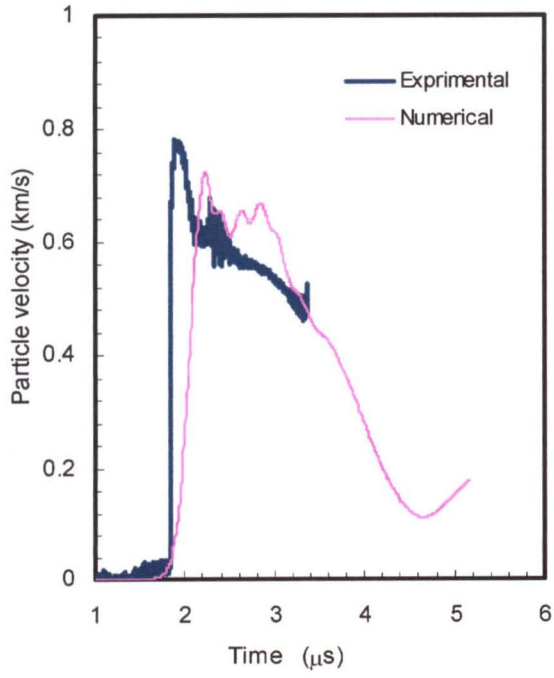

(k) h=3.77mm, w=2.87mm, v_f=1589m/s

Figure 5.15 Comparisons of shock particle velocity profiles between numerical simulations and experimental measurements for the PC37/SS19 layered composites impacted by PC (Al) flyers; h and w are specimen and flyer thickness, respectively; v_f is flyer velocity.

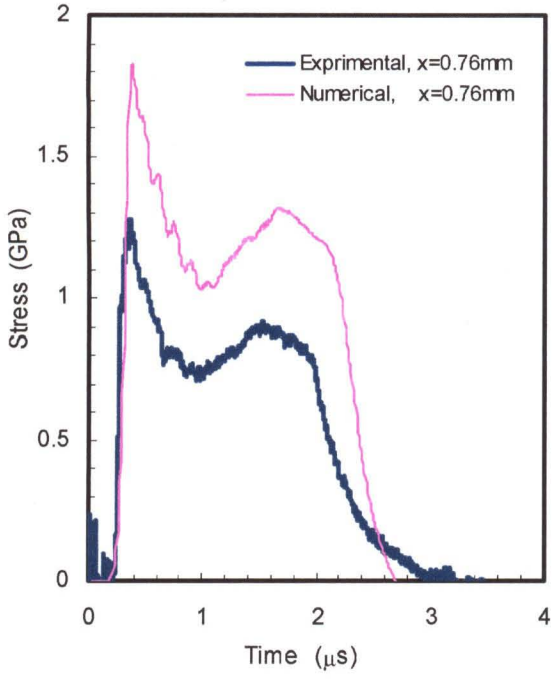

Figure 5.16 (a) PC74/SS37, PC flyer
h=9.84 mm, w=2.87 mm, v_f=561 m/s

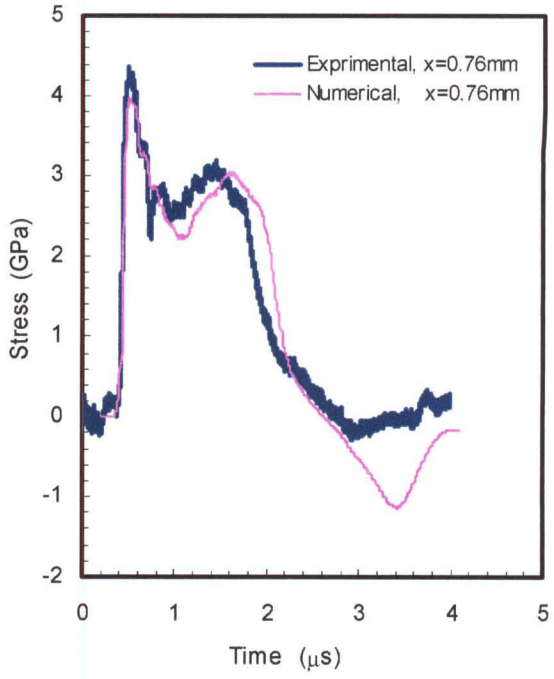

Figure 5.16 (b) PC74/SS37, PC flyer
h=9.97 mm, w=2.87 mm, v_f=1,062 m/s

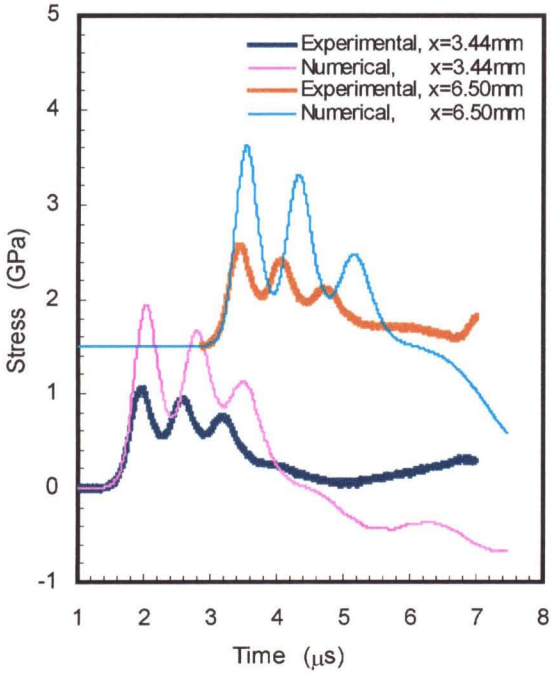

Figure 5.17 (a) PC37/SS19, PC flyer
h=10.20 mm, w=2.87 mm, v_f=564 m/s

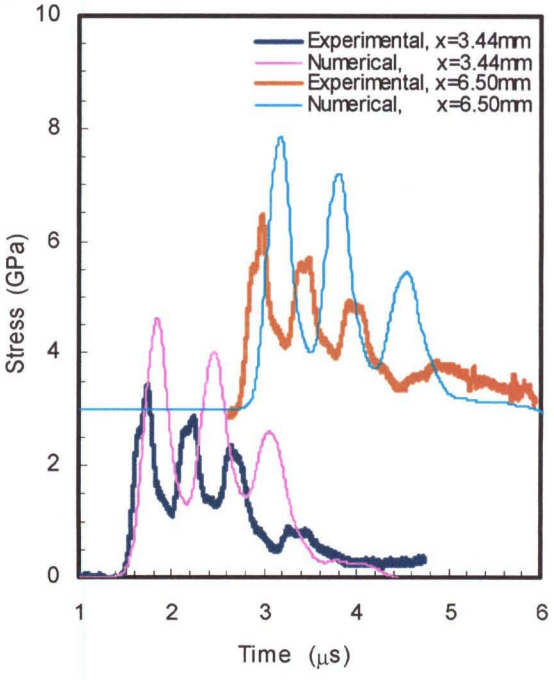

Figure 5.17 (b) PC37/SS19, PC flyer
h=10.60 mm, w=2.87 mm, v_f=1,043 m/s

Comparisons of shock stress profiles between simulations and experiments; h and w are specimen and flyer thickness, respectively; v_f is the flyer velocity and x is the distance from the impact face.

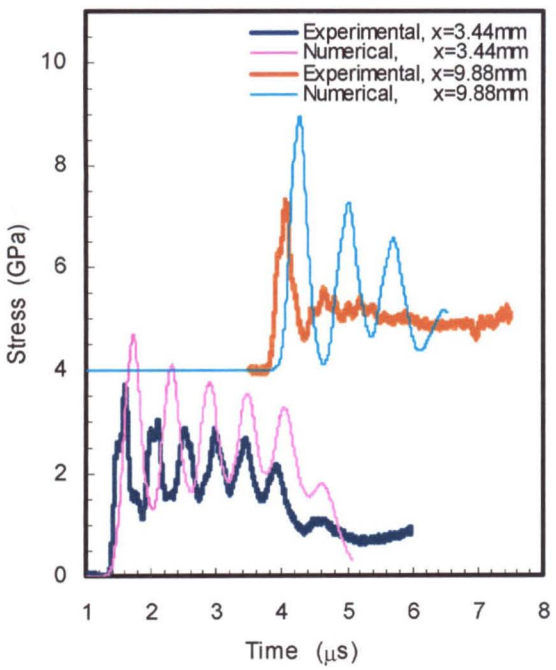

Figure 5.18 PC37/SS19, PC flyer
h=10.61 mm, w=5.63 mm, v_f=1,045 m/s

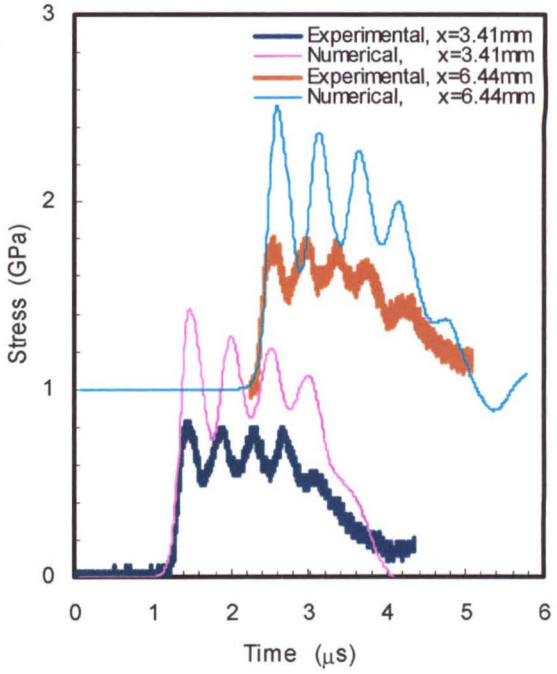

Figure 5.19 (a) PC37/GS20, PC flyer
h=10.43 mm,w=2.87 mm, v_f=567 m/s

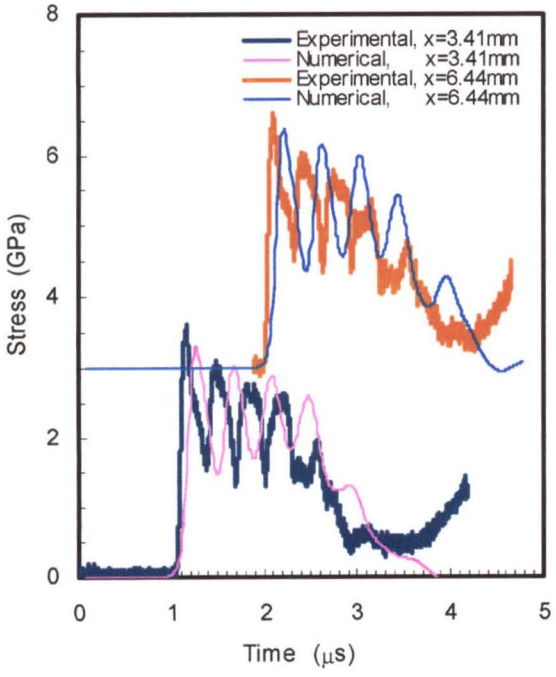

Figure 5.19 (b) PC37/GS20, PC flyer
h=10.62 mm,w=2.97 mm, v_f=1,079 m/s

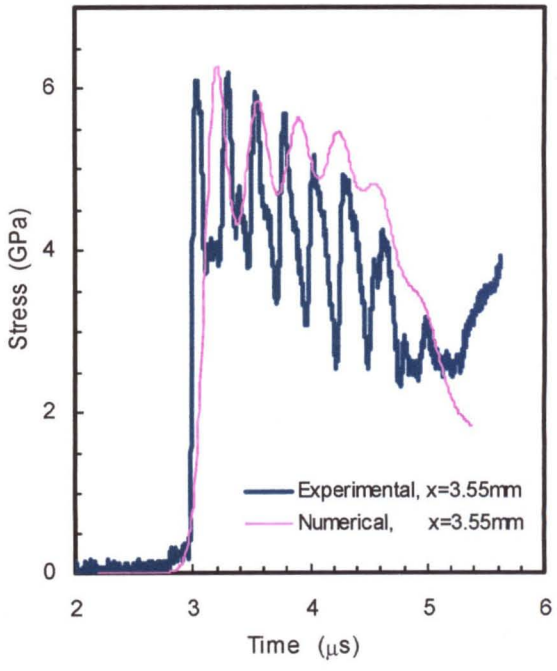

Figure 5.19 (c) PC37/GS20, Al flyer
h=10.50 mm,w=5.59 mm(Al), v_f=1,160 m/s

Comparisons of shock stress profiles between simulations and experiments; h and w are specimen and flyer thickness, respectively; v_f is the flyer velocity and x is the distance from the impact face.

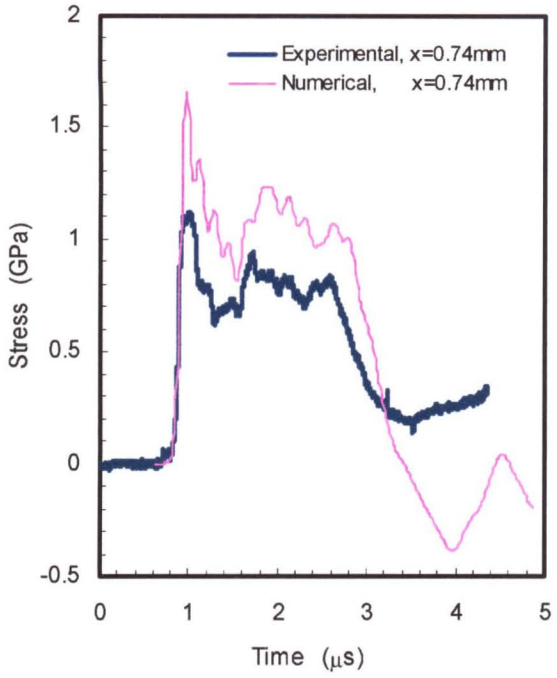

(a) h=9.92mm, w=2.87mm, v_f=568m/s

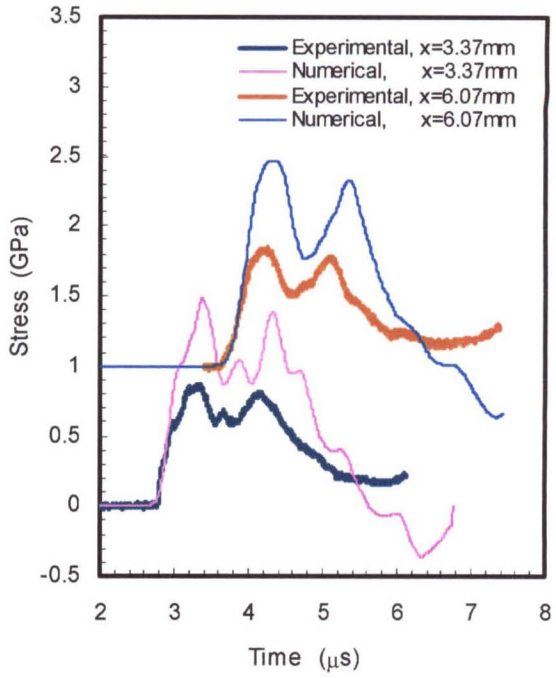

(b) h=9.95mm, w=2.87mm, v_f=563m/s

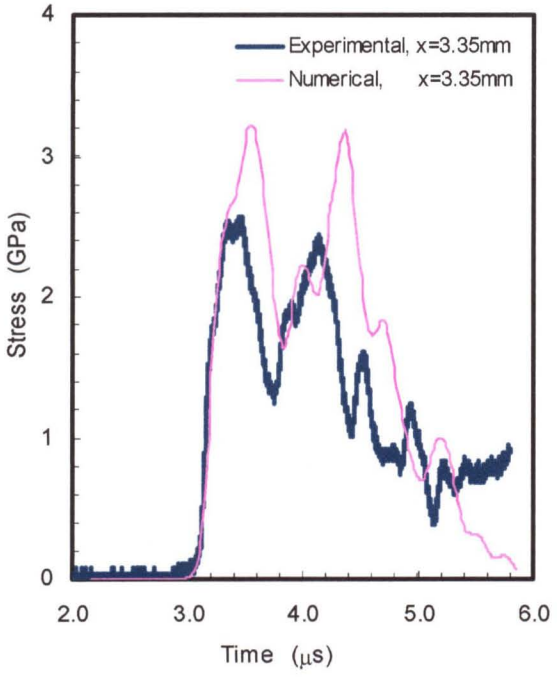

(c) h=9.88mm, w=2.87mm, v_f=1056m/s

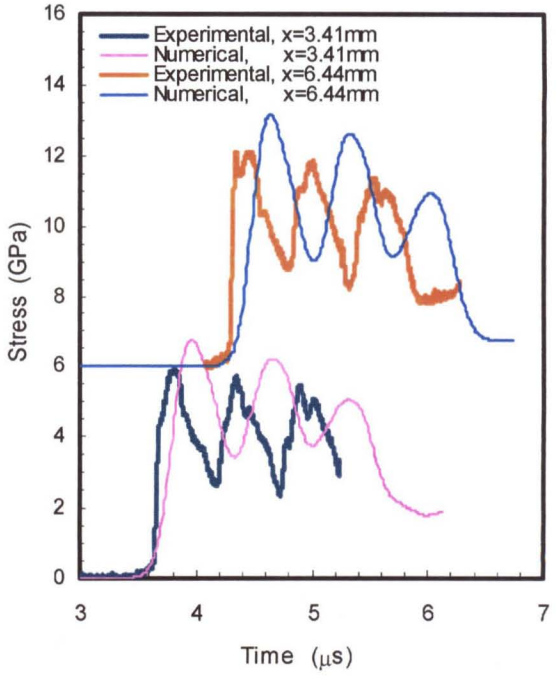

h=10.07mm, w=5.55mm(Al), v_f=1070m/s

Figure 5.20 Comparisons of shock stress profiles between numerical simulations and experimental measurements for the PC74/GS55 composites impacted by PC (Al) flyers; h and w are specimen and flyer thickness respectively; v_f is the flyer velocity and x is the distance from the impact face.

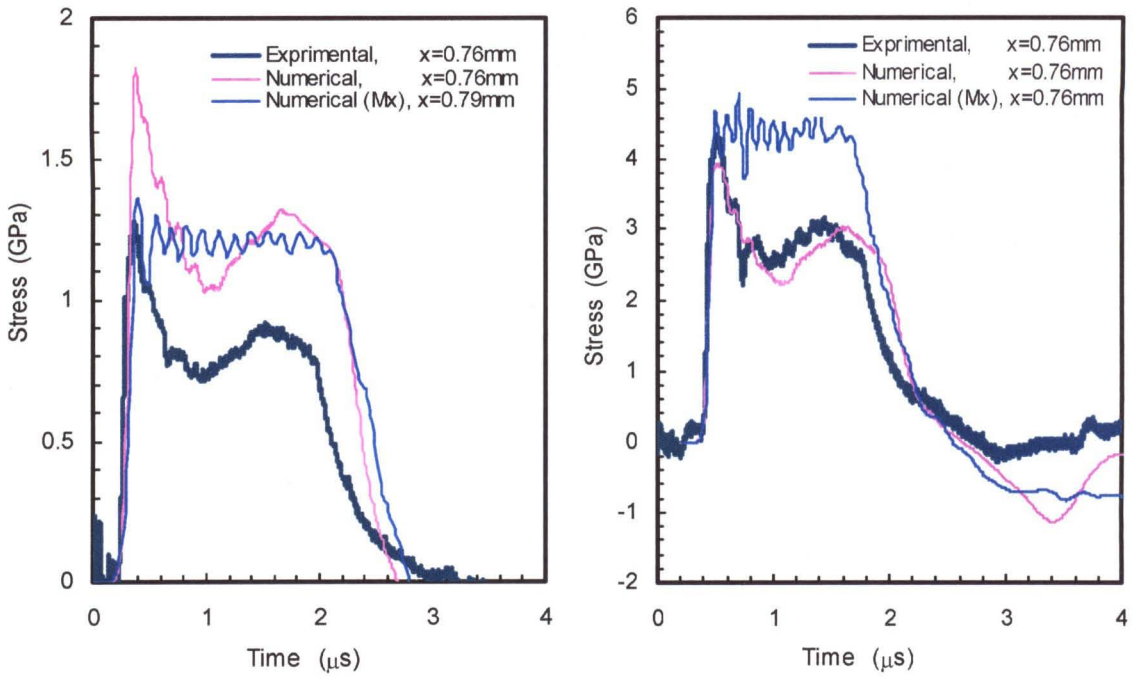

(a) h=9.84mm, w=2.87mm, v_f=561m/s (b) h=9.97mm, w=2.87mm, v_f=1062m/s

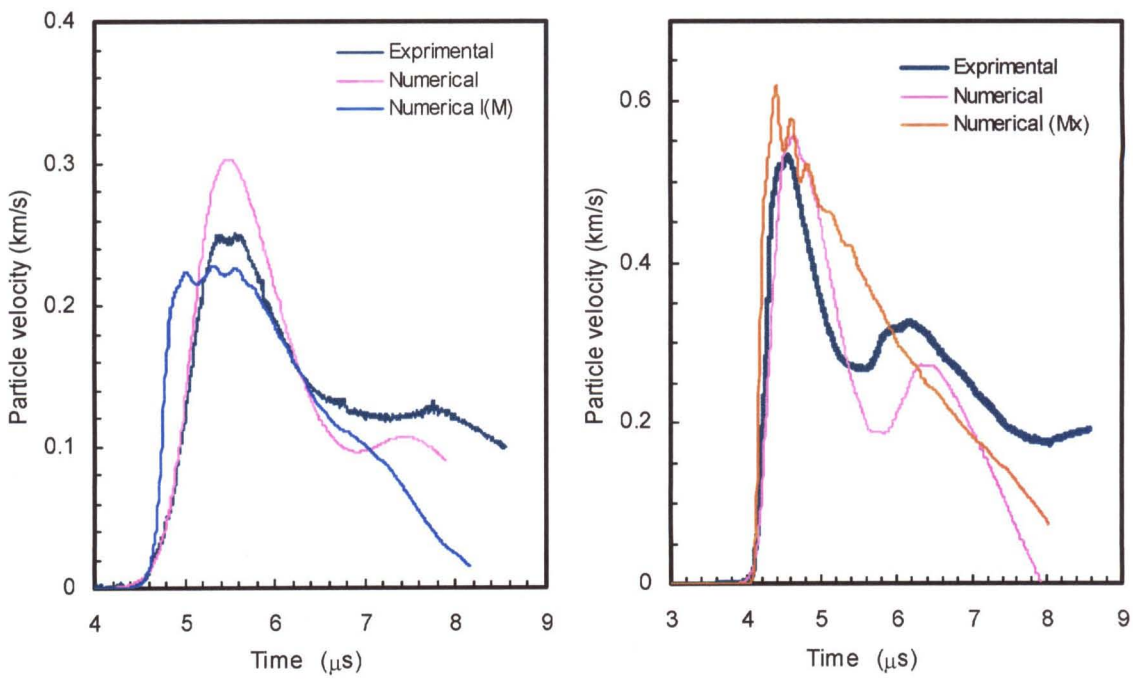

(c) h=9.84mm, w=2.87mm, v_f=561m/s (d) h=9.97mm, w=2.87mm, v_f=1062m/s

Figure 5.21 Comparisons of predictions from the mixture model with full structure simulations and experimental measurements for PC74/SS37 composites impacted by PC flyers; h and w are specimen and flyer thickness, respectively; v_f is the flyer velocity and x is the distance from the impact face.

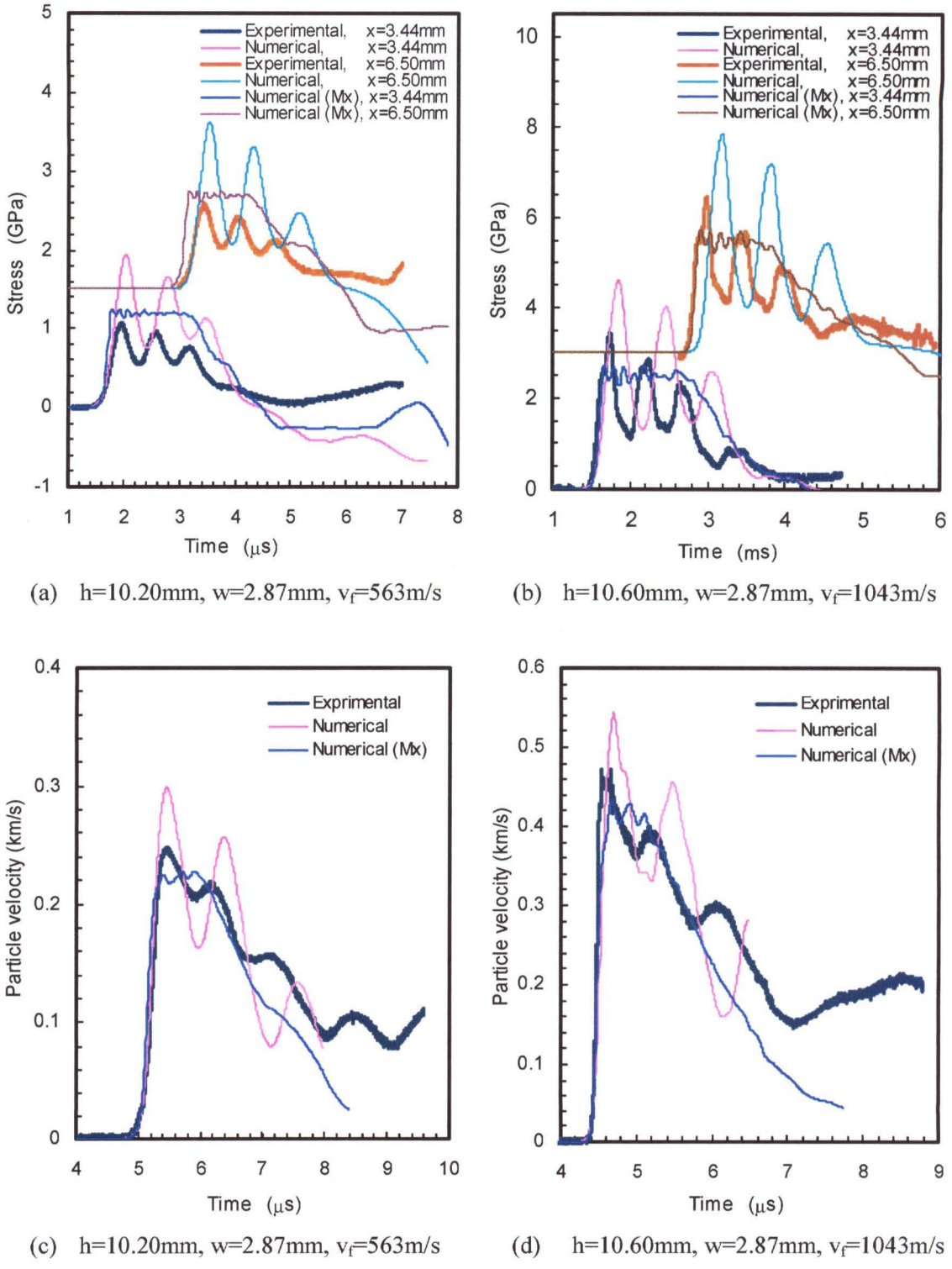

(a) h=10.20mm, w=2.87mm, v_f=563m/s

(b) h=10.60mm, w=2.87mm, v_f=1043m/s

(c) h=10.20mm, w=2.87mm, v_f=563m/s

(d) h=10.60mm, w=2.87mm, v_f=1043m/s

Figure 5.22 Comparisons of predictions from the mixture model with full structure simulations and experimental measurements for PC37/SS19 composites impacted by PC flyers; h and w are specimen and flyer thickness, respectively; v_f is the flyer velocity and x is the distance from the impact face.

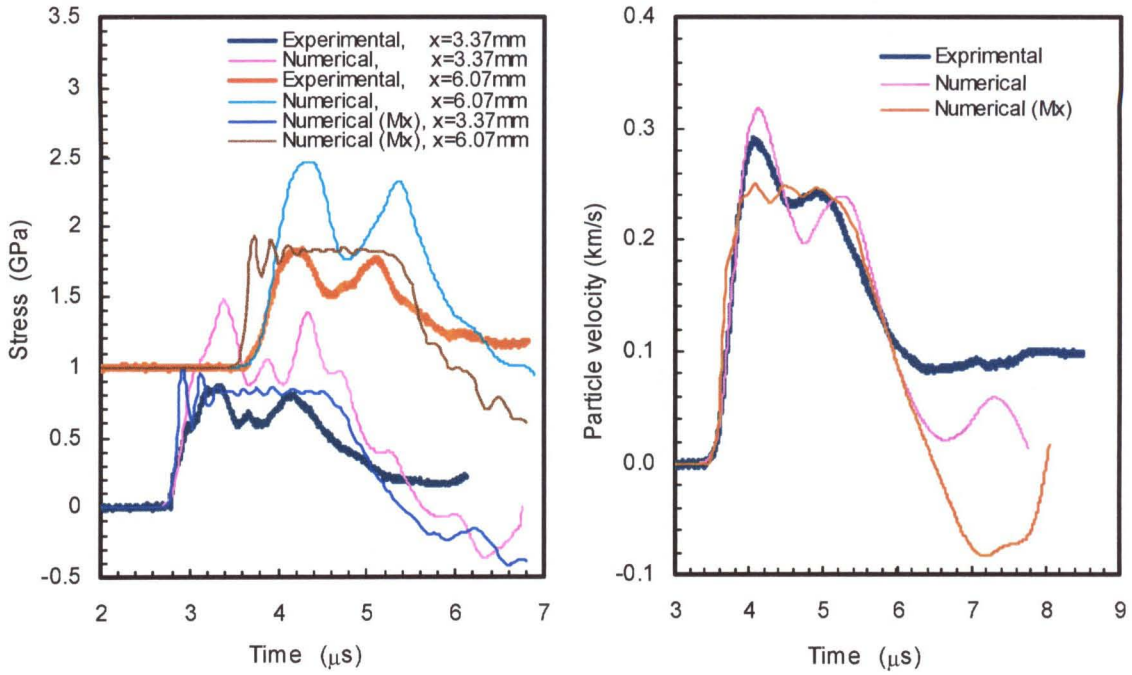

(a) h=9.95mm, w=2.87mm, v_f=563m/s (b) h=9.95mm, w=2.87mm, v_f=563m/s

Figure 5.23 Comparisons of predictions from mixture model with full structure simulations and experimental measurements for PC74/GS37 composites impacted by PC flyers; h and w are specimen and flyer thickness, respectively; v_f is the flyer velocity and x is the distance from impact face.

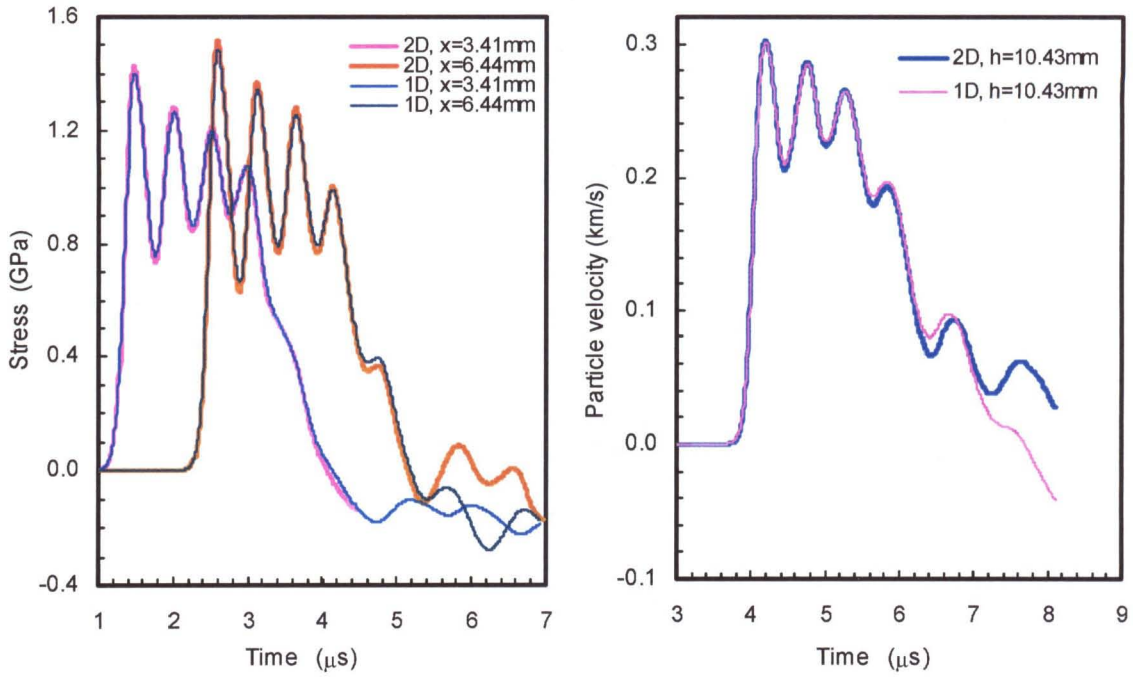

Figure 5.24 Comparisons of shock profiles between 1D and 2D simulations for 10.43 mm (h) thick PC37/GS20 specimen impacted by 2.87 mm thick flyer at a velocity of 567 m/s; x is the distance from the impact face.

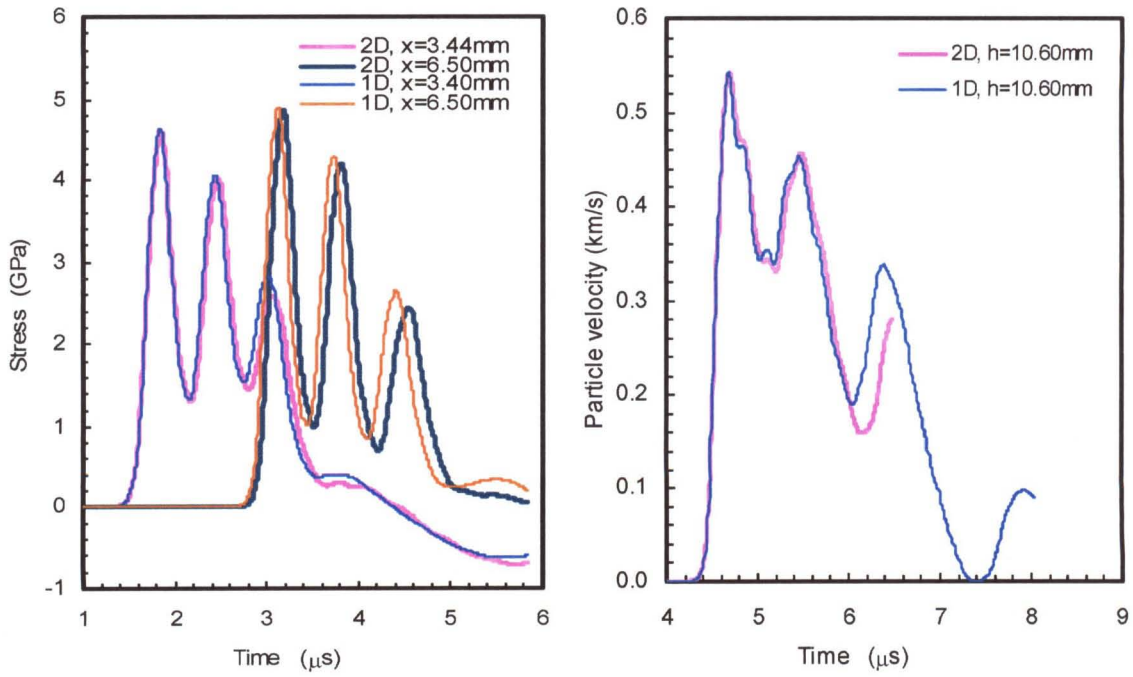

Figure 5.25 Comparisons of shock profiles between 1D and 2D simulations for 10.60 mm (h) thick PC37/SS19 specimen impacted by 2.87 mm thick flyer at a velocity of 1,043 m/s; x is the distance from the impact face.

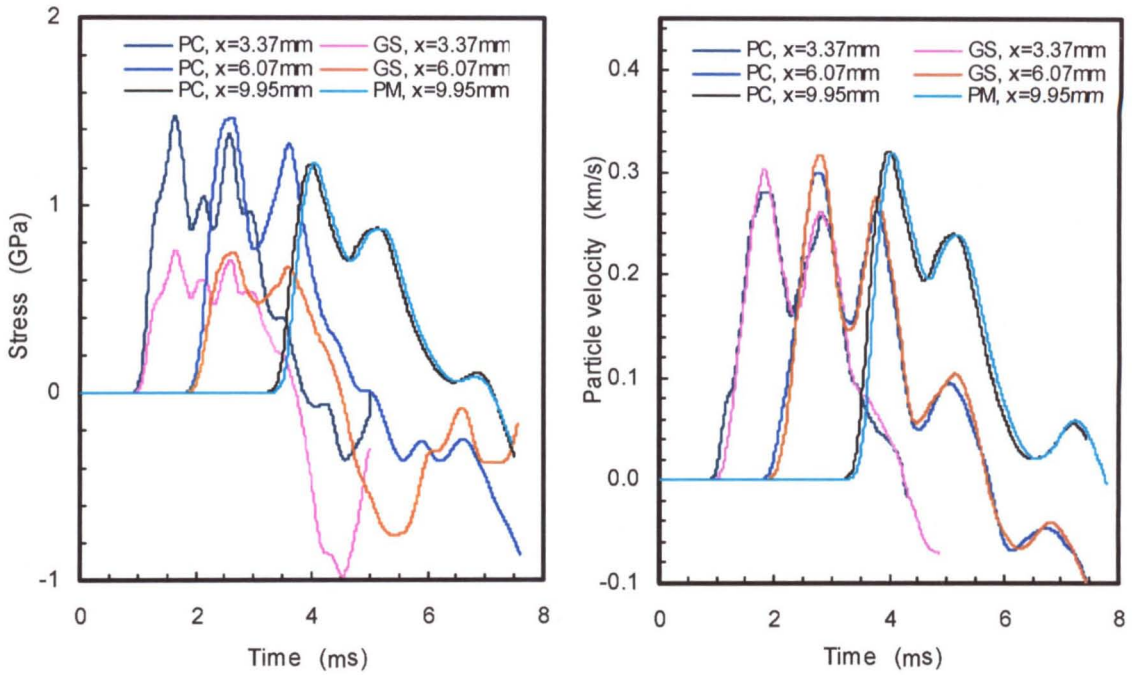

(a) h=9.95mm, w=2.87mm, v_f=563m/s (b) h=9.95mm, w=2.87mm, v_f=563m/s

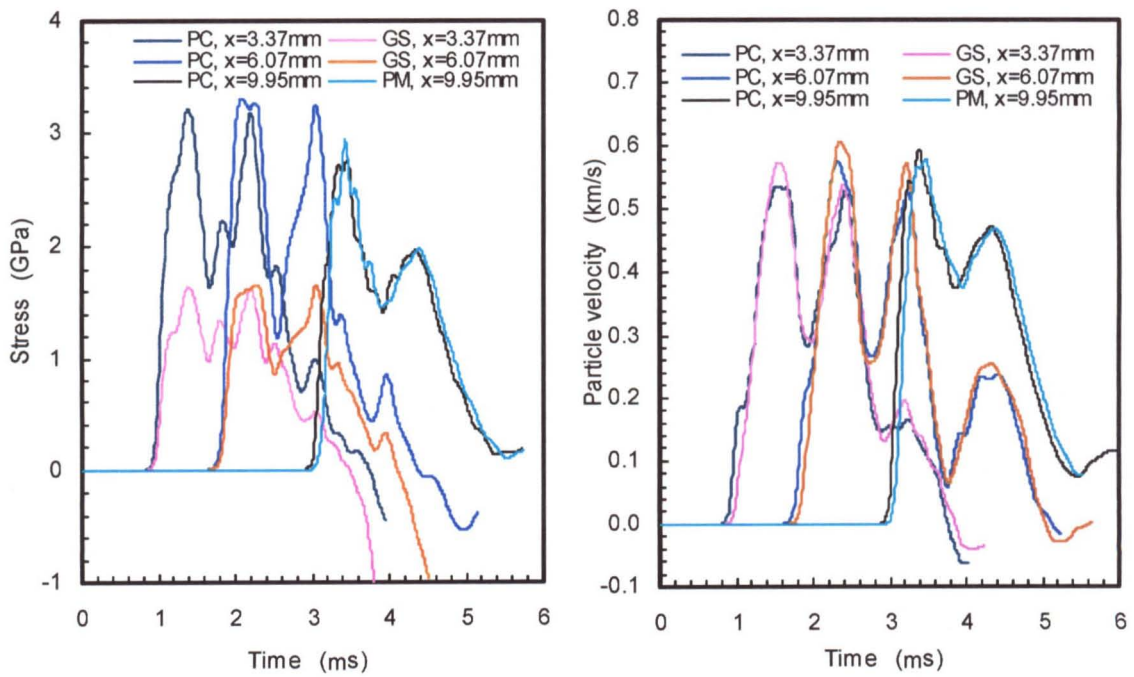

(c) h=9.88mm, w=2.87mm, v_f=1056m/s (b) h=9.88mm, w=2.87mm, v_f=1056m/s

Figure 5.26 Comparisons of shock compression time histories experienced by the elements on either side of interfaces in the PC74/GS55 composites impacted by PC flyers; h and w are specimen and flyer thickness, respectively; v_f is the flyer velocity and x is the distance from the impact face.

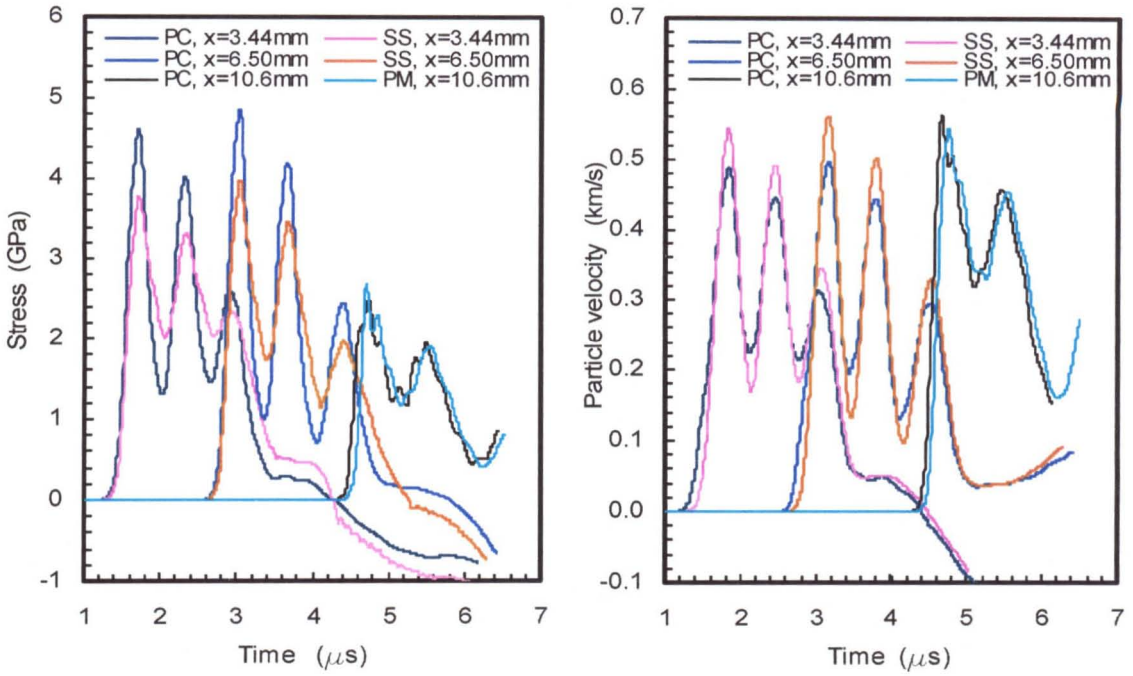

(a) h=10.60mm, w=2.87mm, v_f=1043m/s (b) h=10.60mm, w=2.87mm, v_f=1043m/s

Figure 5.27 Comparisons of shock compression time histories experienced by the elements on either side of interfaces in the PC37/SS19 composite impacted by PC flyer; h and w are the specimen and flyer thickness, respectively; vf is the flyer velocity and x is the distance from the impact face.

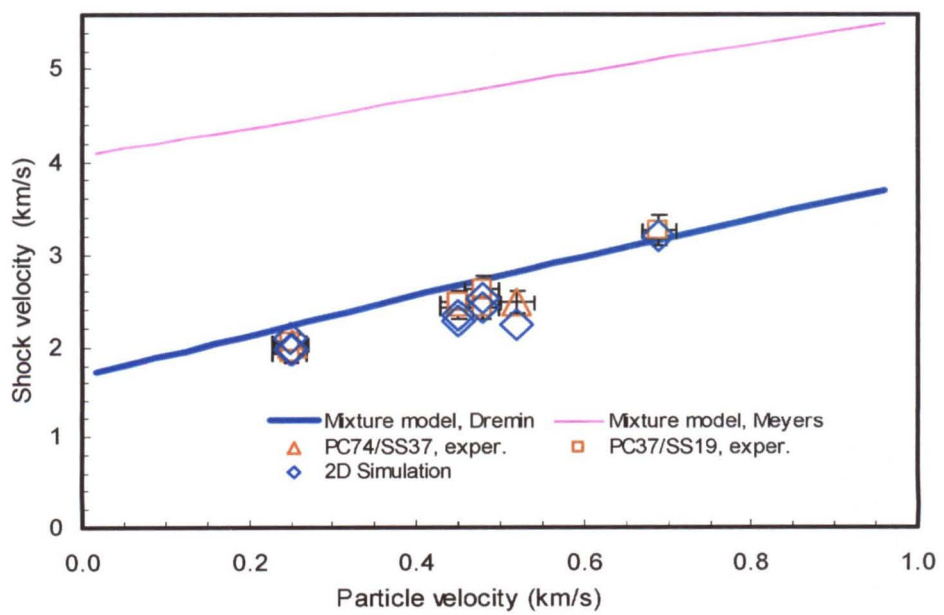

Figure 5.28 Shock Hugoniot data for PC/SS composites measured by experiments and predictions from two-dimensional numerical simulations and mixture models.

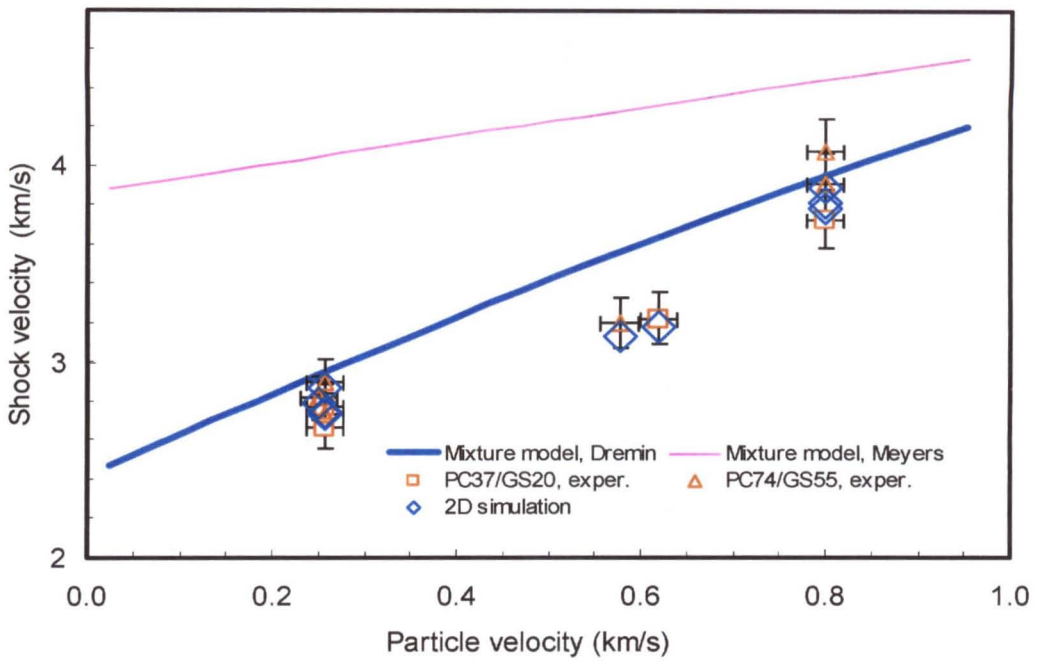

Figure 5.29 Shock Hugoniot data for PC/GS composites measured by experiments and predictions from by two-dimensional numerical simulations and mixture models.

Chapter 6

Suggested Future Work

6.1 Experimental Measurements

6.1.1 Stress Distribution in Each Component

The experimental data (Chapter 4) and numerical simulation results (Chapter 5) indicate that the layered composites can support steady structured shock waves. Nevertheless, the pattern of the steady state behind shock in layered composites is different from that in homogeneous solids. For a steady shock wave propagating in a layered composite, the stress or velocity profiles repeat periodically from unit to unit, but the profiles of stress or velocity within each layer are not uniformly distributed. There exists a maximum or minimum shock profile in each component layer. Furthermore, there may exist a steep stress gradient at the interface between the hard layer and soft layer depending on the mismatch of material properties of the components. As was pointed out, the reason for the resonant oscillations in the stress profile or particle velocity profile of the shock wave in the composite material is due to the interaction of the shock wave with multiple reflection waves in the layers. It will be very helpful to understand the scattering process if the detailed distribution of stress inside each layer can be experimentally measured. One way to do this is to embed several stress gages inside each layer of interest and measure the stress distribution of the layer (see Chapter 4). This is possible since the stress gage is very thin

(normally several tens of micrometers). Extreme care must be taken in bonding stress gage inside the metal or hard layer so that glue layer is as thin as possible.

6.1.2 Lateral Stress Measurement

Because of the inherent scattering effects existing in the composite material, the dynamic response of a composite to shock compression could be very different from that of a homogeneous material. It is very important to experimentally measure the shock velocity and shock stress history or particle velocity history so that appropriate constitutive model can be formulated for the composite. If the stress deviators in shocked composite materials can also be measured experimentally, it will be very helpful to understand the shock compression process in heterogeneous composites and to formulate a physically based, accurate constitutive model. Again, the manganin stress gage may be used for this purpose[1-5].

6.1.3 Stress-Strain Measurement

One of the most interesting stress regimes is the intermediate regime where the elastic-plastic properties dominate the compression process in the individual component material; it will be very useful to obtain the nominal stress-strain curve of layered composites at different strain rates to understand the 'strain hardening' effect and strain rate dependence. These experiments can be carried out using servo hydraulic testing machines and Kolsky (split Hopkinson) bars.

6.2 Theoretical Analysis

6.2.1 Interpretation of Stress Gage Measurements

In experiments, the stress gages are embedded at the interface between the hard layer and the soft layer. According to the numerical simulation results, the stresses in the hard layer and soft layer are not uniform and are different, and also, that steep gradients may exist at the interface. This raises following important questions which need to be investigated further. Whether the stress history measured by the stress gage represents the stress inside the soft layer or hard layer? If it represents the stress neither in the hard layer nor in the soft layer, does the stress history correspond to that of the adhesive used in bonding? If so, how can we understand the stress histories in components based on the experimental data? Can the problem be solved through numerical simulation by using finer size mesh?

6.2.2 Interface Viscosity

As discussed in Chapters 1 and 2, the widening of a shock front implies an increase in shock viscosity of the material under shock compression. Experimental results shown in Chapter 4 indicate that due to the interface scattering, the velocity of shock propagation in the composite slows down and, in general, the slope of the shock front decreases with the increase of interface impedance mismatch and the length scale of the heterogeneity of the components. Interface scattering affects both the shock velocity, the bulk response, and the structure of the shock profile, i.e., the deviatoric response of the composite. The existing EOS model for mixture can roughly, but not accurately, predict the experimental data. The future work in this area should address interface viscosity by relating the characteristic parameters associated with the heterogeneity, such as the component length scales and impedance mismatch, etc., to shock

viscosity, nonequilibrium stress relaxation time, so as to be able to develop a satisfactory model for describing the response of heterogeneous materials to shock compression. One way to proceed is to treat the interface scattering effects as an equivalent dissipative "viscous" process, and describe the interface by a spring and dashpot model, and the constituents by linear springs, and construct an effective medium model for composite subjected to impact loading.

6.2.3 Dispersion and Dissipation Mechanisms of Shock Energy

It is important to study how the shock energy is transported during shock compression of composites in order to understand the dispersion and dissipation of wave energy. Through computation, one can study the evolution of internal and kinetic energy of a shock wave, and to try to obtain the relation between the dissipation energy and dispersion energy. One needs to analyze the evolution of the frequency spectrum of internal energy as a function of distance for composites having different heterogeneity properties. This frequency spectrum needs to be connected with the normal modes of acoustic phonon energy induced by microstructure scattering. Controlled experiments are also needed for support and confirmation of such analyses.

6.3 Constitutive Modeling

Several of the existing phenomenological models for shock wave propagation in heterogeneous composites need to be evaluated by incorporating them into a finite element code and comparing the predicted results with experiment. They are Barker's nonlinear Maxwell model[6], Johnson's modified Barker model[7], and Kanel's empirical continuum anelasticity model[8]. Major effort should also be devoted to the verification and validation of Grady's physically based nonlinear

anelasticity model of wave propagation in heterogeneous media[9-10], and the exploration of the underlying physics and mechanisms of energy dispersion and momentum transport. The equilibrium response may be formulated based on the existing mixture model and experimental measurements of shock velocity in composites. Nonequilibrium stress may be determined based on the multimode theory and the understanding of dispersion and dissipation effects induced by microstructures.

6.4 Computational Modeling

In future computational modeling, several aspects need to be improved. The first is to consider the influence of friction on the interface between the hard and soft layers on the deformation process of composite materials under shock loading. The second is to further check the influence of finite mesh size on the accuracy of simulation results. Investigate the influence of the orientation of interfaces on scattering effects, so as to the shock wave propagation. Finally, three-dimensional simulations should be performed.

6.5 Optimal Composite

The problem of optimization of composites depends on which point of view one wants to pursue, i.e., in the sense of efficiently transporting shock energy/momentum from one point to another inside the composite, or efficiently dispersing or damping energy/momentum. It is clear that the dispersion of shock energy through a composite depends on the heterogeneity (geometric length scale) and the mechanical properties of its components. It is necessary to investigate the shock energy/momentum efficiency and/or distribution as a function of component length scale and the degree of interface impedance mismatch.

The composites are not necessary to be only two components system. For multiple component systems, the impedance mismatch can be described by some distribution function in the terms of distance from the external surface of the composite. Experiments can be designed to test some functionally layered specimens to address the energy transportation and damping issues. In this way, it may be possible to find a way to optimize the properties of composite for the desired function.

6.6 References

1. Rosenberg, Z. and Partom, Y. Lateral stress measurement in shock-loaded target with transverse piezoresistance gages, *J. Appl. Phys.* **58(8)**, 3072 (1985).
2. Rosenberg, Z. and Yaziv, D. Shear strength of shock-loaded alumina as determined with longitudinal and transverse mangnin gages, J. *Appl. Phys.* **62(3)**, 1120 (1987).
3. Rosenberg, Z., Brar, N.S., and Bless, S.J. Dynamic high-pressure properties of AIN ceramic as determined by flyer plate impact, *J. Appl. Phys.* **70(1)**, 167 (1991).
4. Feng, R., Gupta, Y.M., and Wong, M.K.W. Dynamic analysis of the response of lateral piezoresistance gauges in shocked ceramic, *J. Appl. Phys.* **82(6)**, 2845 (1997).
5. Feng, R. and Gupta, Y.M. Determination of lateral stresses in shocked solids: simplified analysis of piezoresistance gauge data, *J. Appl. Phys.* **83(2)**, 747 (1998).
6. Barker, L. M., A model for stress-wave propagation, J. *Comp. Mat.* **5**, 140 (1971).
7. Johnson, J.N., Hixson, R.S., and Gray, G.T. III Shock-wave compression and release of aluminum/ceramic composites, *J. Appl. Phys.* **76(10)**, 5706 (1994).
8. Kanel, G.I., Ivanov, M.F., and Parshikov, A.N. Computer simulation of the heterogeneous materials response to the impact loading, *Int. J. Impact Engng.* **17**, 455 (1995).
9. Grady, D.E. Physics and modeling of shock-wave dispersion in heterogeneous composite, *J. Phys IV FRANCE* **7**, C3-669 (1997).
10. Grady, D.E., Ravichandran, G., and Zhuang, S. Continuum and subscale modeling of heterogeneous media in the dynamic environment, in *Proceedings of the AIRPAT Conference*, Honolulu, Hawaii, edited by Manghani, M., Oxford University Press (1999).